UTS UNIVERSITY OF TECHNOLOGY SYDNEY

Microscale Investigations of Hydromechanical Failures of Granular Soils

by Shay Haq

Thesis submitted in fulfilment of the requirements for the degree of

Doctor of Philosophy

under the supervision of Distinguished Professor Buddhima Indraratna, Professor Cholachat Rujikiatkamjorn, and Dr. Thanh Nguyen

University of Technology Sydney
Faculty of Engineering and Information Technology

December 2022

CERTIFICATE OF ORIGINAL AUTHORSHIP

I, Shay Haq, declare that this thesis is submitted in fulfilment of the requirements for the award of Doctor of Philosophy in the School of Civil and Environmental Engineering, Faculty of Engineering and Information Technology, at the University of Technology Sydney.

This thesis is wholly my own work unless otherwise referenced or acknowledged. In addition, I certify that all information sources and literature used are indicated in the thesis.

This document has not been submitted for qualifications at any other academic institution.

This research is supported by the Australian Government Research Training Program.

Signature: Production Note:
Signature removed prior to publication.

Date: 9th December 2022

ACKNOWLEDGEMENTS

Thank you, ALLAH Almighty, for allowing me to collaborate with such talented researchers. My deepest gratitude goes to my supervisors Distinguished Professor Buddhima Indraratna, Professor Cholachat Rujikiatkamjorn, and Dr. Thanh Nguyen. They have provided me with endless inspiration and ideas throughout the past four years. Their enthusiasm for the research works has had an enormous impact on me. I want to thank them for all the support. I am also grateful to Dr. Jahanzaib Israr and Dr. Trung Ngo for their invaluable guidance throughout the period. Their prompt response to my emails and queries is especially appreciated.

I would like to thank numerous industry partners for their help, including the Australian Research Council (ARC) Industrial Transformation Training Centre for Advanced Technologies in Rail Track Infrastructure, the Australasian Centre for Rail Innovation (ACRI), and Sydney Trains. I thank the Transport Research Centre (TRC), University of Technology Sydney (UTS), for financial support. I would also like to thank my parents and my wife for their support. They were always there for me in good times and bad.

LIST OF PUBLICATIONS

1. Indraratna, B., Haq, S., Rujikiatkamjorn, C., & Israr, J. (2021). Microscale boundaries of internally stable and unstable soils. *Acta Geotechnica*. https://doi.org/10.1007/s11440-021-01321-7
2. Haq, S., Indraratna, B., Nguyen, T. T., & Rujikiatkamjorn, C. (2022). Hydromechanical state of soil fluidisation: a microscale perspective. *Acta Geotechnica*. https://doi.org/10.1007/s11440-022-01674-7
3. Haq, S., Indraratna, B., Nguyen TT., & Rujikiatkamjorn, C. (2022). Micromechanical analysis of internal instability during shearing. *ASCE, International Journal of Geomechanics* ***(Under Review)***
4. Haq, S., Indraratna, B., Rujikiatkamjorn, C., & Israr, J. (2022). Particle scale modelling of internal instability, *16th International Conference on Geotechnical Engineering, December 7-8, 2022, Lahore, Pakistan* ***(Accepted)***
5. Nguyen TT., Indraratna, B., Rujikiatkamjorn, C. & Haq, S. (2023). A comparative study on the performance of CFD/LBM-DEM coupling in predicting soil fluidization, *Geo-Congress, March 26-29, 2023, Los Angeles, California* ***(Accepted)***
6. Haq, S., Indraratna, B., Nguyen TT., & Rujikiatkamjorn, C. (2023). Microscale conditions of fluidisation – an LBM-DEM study, *ANZ Conference, July 2-5, 2023, Cairns Convention Centre, Queensland, Australia* ***(Abstract Accepted)***

TABLE OF CONTENTS

LIST OF FIGURES

LIST OF TABLES

LIST OF NOTATIONS

α = stress reduction factor,

α_d = shape coefficient,

ΔP = pressure drop across the particle bed,

Δx = lattice spacing,

δ_n = normal overlap,

δ_t = tangential overlap,

$\dot{\varepsilon}$ = strain rate,

ε_a = axial strain,

ε_s = solid fraction in the fluid cell volume,

ε_v = volumetric strain,

γ_w = unit weight of water,

γ'= submerged unit weight of soil,

χ = safety factor coefficient,

$\varpi_{i,o}$ = weight factor,

ρ_f = fluid density,

Ω_α = collision operator,

$\Omega_\alpha{}^{BGK}$ = collision operator of the BGK model,

$\Omega_\alpha{}^{S}$= additional collision term for solid fraction,

μ_s = coefficient of sliding friction,

μ_f = dynamic viscosity of the fluid,

σ'_{ij} = Cauchy effective stress tensor in the selected region,

$\sigma_{ij}^{p\prime}$= average stress tensor within a particle *p*,

σ'_{zz} = Cauchy effective stresses of the particles in a layer in the fluid flow direction at any time, and

σ'_{zzo} = initial Cauchy effective stresses of the particles in a layer in the fluid flow direction**,**

τ = relaxation time,

B = weighing function to correct the collision phase due to the presence of solid particles,

B_R = percentage of broken contacts,

$C_{d,i}$ = drag coefficient of the fluid-particle system,

C_u = coefficient of uniformity value,

c_L = lattice speed,

c_n = viscoelastic damping constant for normal contact,

c_s = sound celerity,

c_t = viscoelastic damping constant for tangential contact,

D_{c35}^{c} = constriction size that is 35% finer by surface area in the CSD of the coarser fraction,

D_{c35}^{cl} = controlling constriction size at the loosest state,

D_{15}^{c} = particle size that is 15% finer by mass in the PSD of the coarser fraction,

d_p = diameter of the particle,

d_{avg} = average diameter of the coarser fraction of PSD,

d_{50} = particle size that is 50% finer by mass in the PSD,

d_{85} = particle size that is 85% finer by mass in the PSD,

d_{85}^{f} = particle size that is 85% finer by surface area in the finer fraction's PSD,

E^* = equivalent Young's modulus,

e_{α}^{v} = microscopic fluid velocity,

e_{oi}^{k} = initial void ratio of the k^{th} layer,

e_{oi}^{avg} = initial void ratio of the entire sample considering all 10 Layers,

e_r = coefficient of restitution,

F = finer particles' fraction at any particle diameter D,

$F_{d,i}$ = drag force,

$F_{\nabla p,i}$ = pressure gradient force,

$F_{\nabla \tau,i}$ = viscous force,

$F_{vm,i}$ = virtual mass force,

$F_{B,i}$ = Basset force,

$F_{Saff,i}$ = Saffman force,

$F_{mag,i}$ = Magnus force,

f_{bu} = static buoyancy force on the particle,

f_{hyd}^{p} = total hydrodynamic force (including the static buoyancy force) on the particle p,

f_f = hydrodynamic forces on the particle without buoyancy force,

f_g^p = gravitational force on the particle p,

f_j^c = force vector in j^{th} direction at contact c,

f^T = tangential contact force,

f^N = normal contact force,

$f_\alpha(x,t)$ = particle distribution function,

$f_\alpha(x,t^*)$ = particle distribution function after the collision of fluid particles,

$f_\alpha^{eq}(x,t)$ = equilibrium distribution function,

G = shear modulus,

G^* = equivalent shear modulus,

H = incremental finer fraction between particle diameters D and $4D$,

I_n = Inertial number,

I^p = moment of inertia of the particle p,

i_o = overall applied hydraulic gradient,

$i_{o,cr}$ = critical overall hydraulic gradient of the soil specimen,

i_{hyd} = local hydraulic gradient in a layer,

k_n = elastic constant for normal contact,

k_t = elastic constant for tangential contact,

L = height of the particle bed,

M = Mach number,

M_s = fraction of mechanically stable particles,

m^p = mass of the particle p,

m^* = equivalent mass,

N = lattice resolution,

N_c = number of contacts,

N_d = number of degrees of freedom,

N_{ct} = number of constraints,

N_c^p = number of contacts on particle p,

$N_c^{coarse-coarse}$ = number coarse particle contacts,

$N_c^{fine-fine}$ = interparticle contacts of fine particles,

$N_c^{fine-coarse}$ = number of contacts between fine and coarse particles,

N_p = number of particles,

N_p^{coarse} = number of coarse particles,

$N_p^{\geq 4}$ = number of particles with at least 4 or more contacts,

n = overall porosity of the soil specimen,

n_c = skeleton's porosity,

$n_i^{c,p}$ = unit-normal vector from the centroid of the particle to the contact location,

n_L = number of layers,

O_i = initial centroidal location of particle i,

O_j = initial centroidal location of particle j,

O_j' = displaced centroidal location of particle j,

p^p = mean stress in the particle p,

p' = sample's effective mean stress equals the average of principal stresses,

p_f' = mean stress in the fines,

q = deviatoric stress,

R = constraint ratio for a three-dimensional particle system with only sliding resistance,

R_d = relative density,

R^* = equivalent radius,

Re_p = Reynold's number of the particle,

r_{min} = minimum particle radius,

S = variance in the void ratios,

S_i = slipping index,

S_c = fraction of slipping contacts,

T_f^p = fluid-particle interaction torque,

T_j^c = interparticle contact torque due to tangential force,

t = time,

t^* = time after the collision,

u = macroscopic fluid velocity,

$u_{f,o}$ = average fluid velocity of cell o,

$u_{p,i}$ = velocity of particle i residing in cell o,

u_{max} = maximum velocity of the fluid flow in physical units,

V = volume of the selected region or layer,

V^p = volume of particle p,

v_d = superficial or discharge velocity of the fluid,

v_f = kinematic viscosity of fluid,

v_n^{rel} = normal component of the relative velocity of two spherical particles,

v_t^{rel}= tangential component of the relative velocity of two spherical particles,

v^p = translational velocity of the particle p,

w^p = angular velocity of the particle p,

ω_α = weighing factor for the microscopic fluid velocity,

x^n = coordinate of the lattice cell,

x_i^c = location of the contact c,

x_i^p= centre of mass of the particle,

z = location of the particle,

Z = coordination number,

$Z^{fine-coarse}$ = fine-coarse coordination number,

$Z^{coarse-coarse}$ = coarse-coarse coordination number,

$Z_{avg.}$ = average coordination number,

LIST OF ABBREVIATIONS

ALE = Arbitrary Langrangian Eulerian,

BGK = Bhatnagar-Gross-Krook,

CF = Coarser Fraction,

CSD = Constriction Size Distribution,

CFD = Computational Fluid Dynamics,

DEM = Discrete Element Method,

DLM = Distributed Lagrange Multiplier,

DNS = Direct Numerical Simulations,

DSD = Deforming Spatial Domain,

FBM = Fictitious Boundary Method,

FD = Fictitious Domain,

FDM = Finite Difference Method,

FEM = Finite Element Method,

FF = Finer Fraction,

FVM = Finite Volume Method,

IBM = Immersed Boundary Method,

LAMMPS = Large-scale Atomic Molecular Massively Parallel Simulator,

LBM = Lattice Boltzmann Method,

LGA = Lattice Gas Automata,

LIGGGHTS = LAMMPS Improved for General Granular and Granular Heat Transfer Simulations,

MD = Molecular Dynamics,

MEM = Momentum Exchange Method,

NS = Navier-Stokes,

PCF = Pair Correlation Function,

PFC = Particle Flow Code,

PSD = Particle Size Distribution,

PSM = Partially Saturated Cells Method,

SA = Surface Area,

SST = Stabilised Space-Time,

USACE = United States Army Corps of Engineers,

μCT = Micro-Computed Tomography.

ABSTRACT

The Discrete Element Method (DEM) has proven useful to capture the micro and macro behaviour of soils. The complex micromechanical characteristics associated with hydromechanical failure of soils, such as internal instability and fluidisation, can be replicated with DEM. This research is divided into two parts, i.e., (i) microscale analysis of internal instability of cohesionless soils by using DEM under isotropic stress conditions and during shearing, and (ii) micromechanical analysis of fluidisation of granular soils by coupling DEM with the Lattice-Boltzmann Method (LBM).

Micromechanical analysis of the internal instability of cohesionless soils under isotropic stress state was carried out using DEM. The coordination number and the stress reduction factor were used to estimate the potential for internal instability of granular soils, and the clear boundaries between the samples that were internally stable and those that were unstable were delineated. Thereafter, the dense samples were sheared under drained conditions following a constant mean stress path to study the influence of shear deformation on internal instability. The simulation results showed that a dense sample could transition from internally stable to unstable soil as it dilates during shear.

Furthermore, microscale investigations on soil fluidisation were carried out using the DEM in combination with the LBM. The development of local hydraulic gradients, the distribution of contacts, and the associated fabric changes were examined. The microscale findings suggest that a critical hydromechanical state that induces fluid-like instability of a granular assembly can be described by a substantial and sudden increase in grain slippage combined with a decrease in interparticle contacts. Inspired by these results, a novel criterion is proposed to characterise the transformation of granular soil from a hydromechanically stable to a fluid-like state based on the constraint ratio,

representing the relative slippage between the particles and the loss of contacts between the particles within the granular mass. The constraint ratio of unity corresponds to zero effective stress, representing the critical hydromechanical state.

Keywords: Internal Instability, Discrete Element Method, Coordination Number, Stress Reduction Factor, Fluidisation, Constriction Size Distribution, Lattice Boltzmann Method, Constraint Ratio, Critical Hydraulic Gradient

CHAPTER 1 INTRODUCTION

1.1 BACKGROUND, SCOPE AND RESEARCH APPROACH

Railways are recognised as the most cost-effective and essential means of transport for people and freight worldwide. In the Australian mining and agriculture industry, railways are the predominant link between the source and distribution hubs (including ports); hence its secure and stable network is vital for an efficient supply chain across the country. With the increasing demand for faster rail networks, railway engineers face challenges in designing and maintaining a safe track environment.

Figure 1.1 shows the cross-section of a typical ballasted track in Australia. It consists of the rail and fastening system, the ballast layer, the capping layer, and the sub-grade. The sub-ballast/capping layer is the focus of this study, and it has two purposes: first, to safely transmit the load to the underlying subgrade, and second, to filter out the fine particles that can migrate from the subgrade to the overlying ballast layer (Israr 2016). In order to perform its intended functions, the capping layer, i.e., the uppermost compacted sandy-gravel layer of the sub-ballast, must be internally stable because it performs load distribution and also serves as a relatively impervious stratum which prevents fluidised subgrade soil (mud pumping) from contaminating the overlying ballast.

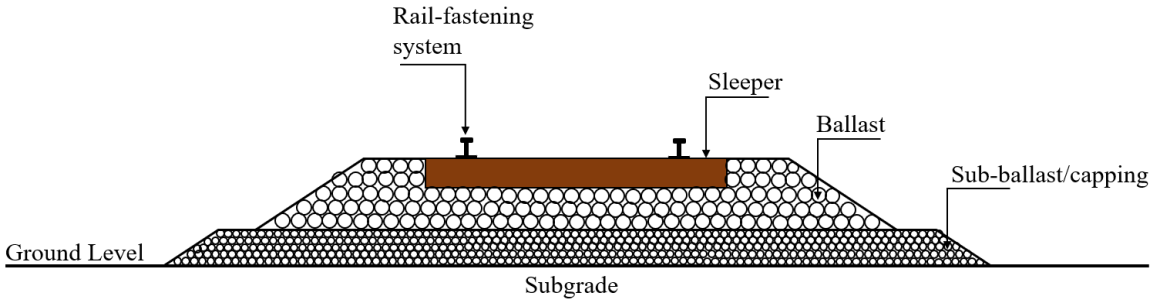

Fig. 1. 1 Typical cross-section of a ballasted track in Australia (modified after Indraratna & Ngo, 2018)

Internal instability implies that the coarser part of the Particle Size Distribution (PSD) curve cannot stop fine particles from migrating due to seepage flow (Fig. 1.2) (Kenney & Lau 1985; Skempton & Brogan 1994). Internal instability occurs in soils with a bimodal structure, i.e., the PSD curve can be split into coarser and finer fractions. Fine particles in a bimodal structure are much smaller than coarse particles, which makes them more vulnerable to erosion during seepage (Israr & Indraratna 2017; Mehdizadeh et al. 2017; Xiao & Shwiyhat 2012). Compared to hydraulic gradients that cause heave or piping, these fine particles can be eroded at much lower levels (Skempton & Brogan 1994), resulting in permanent changes to the original PSD of soil (Fig. 1.2) and also altering its hydraulic and mechanical properties.

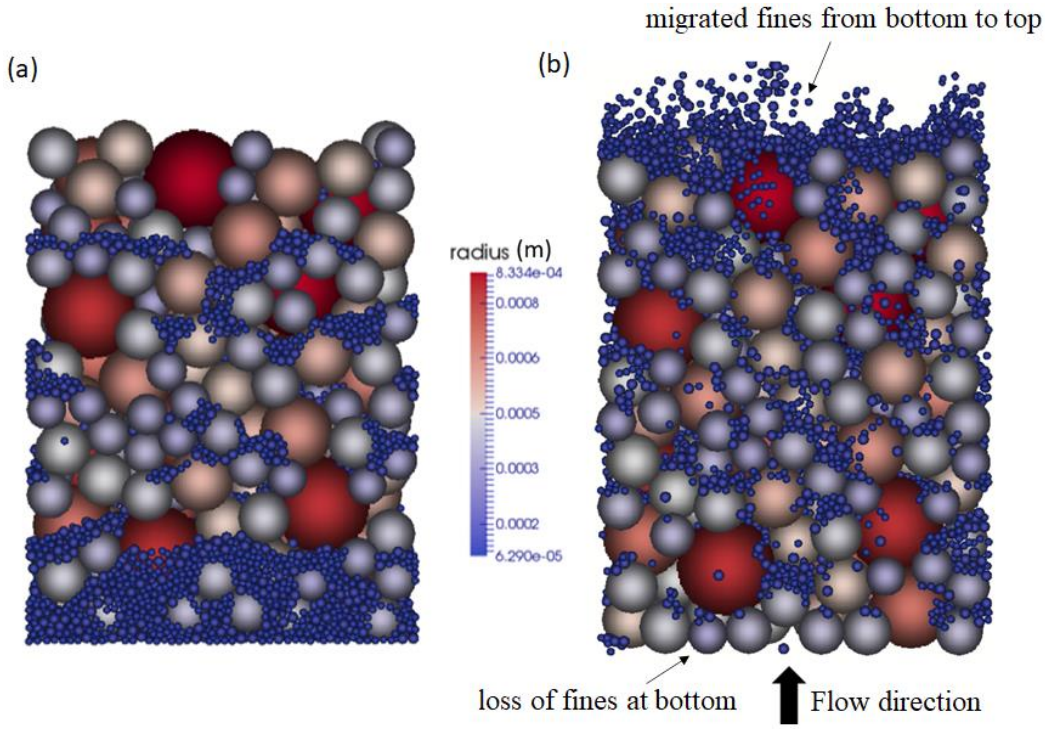

Fig. 1. 2 (a) before seepage flow, (b) after seepage flow, where fine particles have migrated from the bottom to the top of the soil specimen and show internal instability

To date, internal instability has been assessed using a number of criteria based on PSD and Constriction Size Distribution (CSD) (Indraratna, Israr & Rujikiatkamjorn 2015; Kenney & Lau 1985; Kezdi 1979; Li & Fannin 2008; To, Scheuermann & Williams

2018). Most of the criteria currently used to determine instability are based on macroscale laboratory tests, which unfortunately cannot capture any details of the micromechanisms. For example, how the fabric of internally stable and unstable soils differs at the microscale demands more insight. In view of the above, one may consider internal instability to be a problem at the particle scale, and therefore, the particulate Discrete Element Method (DEM) to be used to model and evaluate the extent of particle scale micromechanical problems (Cundall & Strack 1979; O'Sullivan 2011).

While the DEM is widely used in geomechanics to investigate the internal instability of cohesionless soils (Ahmadi et al. 2020, 2021; Shire et al. 2014; Shire & O'Sullivan 2013), no previous studies could demarcate clear boundaries between internally stable and unstable soils based on a micromechanical analysis. Therefore, this study attempts to delineate clear boundaries between internally stable and unstable soils by using the microscale parameters obtained directly from particle scale data, such as the coordination number (Z) and the stress reduction factor (α).

The coordination number (Z) is defined as the average number of contacts per particle in a granular assembly (Thornton 2000). The stress reduction factor means the ratio of effective stresses borne by fine particles to the mean effective stresses in the entire sample (Skempton & Brogan 1994). The coordination number (Z) and the stress reduction factor (α) were then compared to the criteria proposed by Kenney & Lau (1985) and Kezdi (1979) and the CSD-based criterion by Indraratna et al. (2011). After establishing the clear boundaries between internally stable and unstable soils under isotropic stress conditions, dense samples were sheared under drained conditions following a constant mean stress path so that the impact of shear-induced deformation on micromechanics could be assessed.

The second part of this thesis focuses on the micromechanics of subgrade fluidisation. In this regard, Figure 1.3 shows a typical problem at a site in NSW caused by an internally unstable capping layer, where unfavourable hydraulic gradients could cause the subgrade to initiate the condition of mud pumping. This is a major problem that leads to unstable railroads and substantial maintenance costs (Chawla & Shahu 2016; Duong et al. 2014; Hudson et al. 2016; Indraratna et al. 2020; Nguyen et al. 2019). Fluidisation is defined as a condition whereby saturated soils are subjected to excessive hydraulic gradients and lose their intergranular contacts as they transition to a fluid-like state. This slurry of fine particles then migrates (pumps) into the overlying coarser ballast layer, hence the commonly used term mud-pumping, as studied experimentally (Arivalagan et al. 2021; Duong et al. 2014; Indraratna et al. 2020).

Fig. 1. 3 Mud pumping of saturated subgrade soil (Picture Courtesy: Professor Buddhima Indraratna)

Experimental studies have enabled the hydromechanical behaviour of subgrade soils to be better understood, albeit at the macroscale. From a micromechanical perspective, i.e., at the grain level, the slippage and/or breakage of interparticle contacts and the resulting fabric evolution may initiate a transition from a hydromechanically stable to an unstable state that is still not fully understood. The DEM is a useful tool for

assessing the micromechanics of a granular medium (Cundall & Strack 1979; O'Sullivan 2011); it has been effectively used to study the evolution of interparticle contacts and fabric during shear by using the scalar and directional parameters (Barreto 2009; Thornton 2000). The coordination number is a fundamental microscale fabric descriptor for characterising granular medium (Fonseca et al. 2013; Thornton 2000). Despite these advances, the state of interparticle contacts and fabric during fluid flow has rarely been considered. In addition, the constraint ratio, as defined by the ratio of the number of constraints to the number of degrees of freedom within the particle system (Cundall & Strack 1983), can also be used to represent the relative slip and loss of interparticle contacts during instability.

The primary scope of this work includes an attempt to describe and quantify the critical hydromechanical conditions corresponding to the fluidisation phenomenon with special attention to granular soil at the microscale, adopting the concepts of the coordination number and the constraint ratio, as mentioned above. In this context, the DEM can be used in combination with Computational Fluid Dynamics (CFD) to study soil fluidisation in detail. For instance, Cui et al. (2014), Nguyen & Indraratna (2020) and Indraratna et al. (2021) examined the critical hydraulic gradients for internal erosion and fluidisation, taking into account the influence of the particle size distribution, the relative density, and the interparticle coefficient of friction. Neither of these studies could accurately quantify the critical hydromechanical conditions leading to potential fluidisation from a microscale perspective, so a more insightful microscale study of this instability process is needed.

Given the above, this study uses a combined Lattice Boltzmann Method (LBM)-DEM approach that is becoming increasingly popular in investigating fluid-particle interactions (Galindo-Torres et al. 2015; Han & Cundall 2017; Indraratna, Phan, et al.

2021; Wu et al. 2021). This study also offers another dimension to the expanding field of soil micromechanics, where soil-fluid interactions are analysed in a greater depth at a particulate level to interpret the effects of internal seepage and associated pore water pressure gradients, which traditional continuum mechanics fail to address.

The advantages of LBM over conventional CFD using the Navier-Stokes equations include (a) the ability to generate a much finer mesh size, i.e., finer than the particles that can simulate true experimental conditions, (b) a higher computational speed when executed on parallel computers and, (c) the relative feasibility of implementation in complex geometries of porous media (Han, Feng & Owen 2007a; Rettinger & Rüde 2017). In addition, the LBM is based on the kinetic theory of gases and represents a fluid through an assembly of particles that go through successive collision and propagation processes. This enables the calculation of the macroscopic fluid velocity and the pressure as a function of the momentum of these particles (Rettinger & Rüde 2017; Seil, Pirker & Lichtenegger 2018).

1.2 KEY OBJECTIVES OF THIS STUDY

The main aim of this doctoral thesis is to improve the longevity of railroads by proposing novel criteria that consider microscale perspectives for internal instability and fluidisation. This study considers the numerical aspects by using DEM/LBM-DEM to present an extended view of internal instability and fluidisation where the micromechanical factors are more insightfully discussed in relation to real-life observations with greater insight, as reflected in the following objectives.

i. To investigate the integrated concepts of granular mechanics, physics and hydromechanics which occur at the microscale for granular soils with DEM and to examine the validity of the current macroscale particle and constriction-based internal instability criteria from microscale investigations.

ii. To define the microscale boundaries for distinguishing internally stable and unstable soils using DEM and then compare the results of the internal instability assessment from the microscale investigations with experimental observations from the existing literature.

iii. To investigate the influence of shear-induced deformation on various concepts of the micromechanics of granular soils.

iv. To calibrate the LBM-DEM coupling with the experimental analysis of seepage flow and investigate the varying microscale parameters during the seepage flow.

v. To define a microscale boundary that distinguishes the solid-like and liquid-like states of a soil specimen and to study the fabric during seepage flow as the soil approaches fluidisation.

1.3 INNOVATION AND SALIENT OUTCOMES

This doctoral thesis introduces two novel criteria to assess internal instability and fluidisation in granular soils:

- The micromechanical parameters such as coordination number (Z) and stress reduction factor (α) were used to demarcate clear boundaries between internally stable and internally unstable soils. For instance, samples with the potential for internal instability simultaneously exhibit $Z \leq 1$, $\alpha \leq 0.5$. These two parameters can be used in practical design to assess the internal instability of the capping layer in railway sub-structures.
- A novel micromechanical criterion based on the constraint ratio has been proposed to assess whether the soil is fluidised, i.e., in a liquid-like state. The constraint ratio represents the relative slippage and breakage of the contacts between the particles. For instance, a granular assembly is hydromechanically stable when the constraint ratio > 1 and unstable (fluid-like) when the constraint ratio < 1; on this basis, the

microscale hydromechanical critical state is established at a constraint ratio of unity. The constraint ratio can then be used in practical design to assess the fluidisation of soils.

1.4 STRUCTURE OF THE THESIS

This thesis consists of seven chapters, which are briefly outlined as follows:

Chapter 1 has provided an introduction to internal instability and the scope of the work to be covered in this doctoral thesis, to be elaborated on in the remaining Chapters.

Chapter 2 presents a critical literature review where research gaps are identified in order to epitomize the importance of this study, including the geometric criteria for internal instability, the hydromechanical conditions, the numerical studies of internal instability and the fluid-particle interaction approaches currently available.

Chapter 3 describes the research approach and methodology, including the application of the discrete element method, the relevant governing equations and the solution of the Boltzmann equation, as well as details of the contact model used in the micromechanical simulations. The validation of the numerical approaches based on DEM and the LBM-DEM are also covered in this chapter.

Chapter 4 is dedicated to “microscale boundaries of internally stable and unstable soils”. Based on the microscale variables, a new DEM-inspired criterion is proposed to distinguish between internally stable and unstable soils. The microscale parameters are described and evaluated and compared with constriction size and particle size-based criteria, augmented with experimental results from the literature.

Chapter 5 focuses on the “micromechanical analysis of soil transition from an internally stable to an unstable state”. The influence of the shear-induced deformation on the micromechanics of the soil specimen is discussed in detail.

Chapter 6 is entitled “hydromechanical state of soil fluidisation – a microscale perspective”. This chapter describes the implementation of the lattice Boltzmann method in combination with the discrete element method to study soil fluidisation at a microscale. This chapter also introduces a novel approach to assessing the fluidisation of soil.

Chapter 7 summarises the findings of the previous chapters and makes recommendations for further studies. It is noteworthy that while the salient aspects of Chapters 4 and 5 have already been published in scholarly journals, these Chapters provide greater details for the benefit of other research students who shall continue this research in the future.

CHAPTER 2 LITERATURE REVIEW

2.1 INTRODUCTION

Internal instability is the phenomenon whereby fine particles pass through the constrictions of coarse particles under the action of seepage flow (Indraratna, Israr & Rujikiatkamjorn 2015; Kenney & Lau 1985). A much lower hydraulic gradient is needed for these fine particles to erode than is required to initiate heave or piping failure (Skempton & Brogan 1994). This can lead to a change in the PSD of soil and thus alter its hydromechanical properties. Hence, the soils used in railway substructures and dams may not serve their intended purpose if they are internally unstable. The types of soil that may be subject to internal instability are widely and gap-graded (Kenney & Lau 1985; Skempton & Brogan 1994).

Several researchers have examined the internal stability of cohesionless soils for over 70 years, beginning with the United States Army Corps of Engineers in 1953 (USACE 1953). The findings of previous studies are reviewed here, especially the geometric criteria used to verify internal instability, the hydromechanical conditions that trigger its onset, and the micromechanical analysis of internal instability using the Discrete Element Method (DEM), or DEM coupled with Computational Fluid Dynamics (CFD) using either the Navier-Stokes equations or the Boltzmann equation. The research gaps are identified in Section 2.7 of this Chapter.

2.2 TERMINOLOGIES USED FOR INTERNAL INSTABILITY

Many terms are used in literature to describe the internal instability of granular soils. Suffusion is a term used when fines are completely washed through granular soils without collapsing the structure of coarse particles (Indraratna, Nguyen & Rujikiatkamjorn 2011; Kezdi 1979). Suffosion refers to the washing out fine particles by collapsing the structure of coarse particles (Kenney & Lau 1985). Internal instability is a term used for both

suffusion and suffosion. The inherent instability and segregation pipe are two other terms used to describe internal instability (Skempton & Brogan 1994).

2.3 PROBLEMS CAUSED BY INTERNALLY UNSTABLE SOIL IN RAILWAYS

The following are the most common consequences of internally unstable soils found in railway substructures.

2.3.1 Ballast Fouling

Natural soils are weakened by the mechanical effects of dynamic loads at the boundary between sub-grade and sub-ballast. These attenuated particles can be conveyed to the top layers in a saturated sub-grade by strong hydrodynamic forces developed by excess pore pressures under cyclic loads (Figure 2.1). This causes the principal load-bearing ballast layer to become fouled, raising the possibility of undrained failure and reducing train speed limits (Trani & Indraratna 2010). It also reduces the free drainage capacity of ballast and decreases the interlocking of angular ballast particles (Indraratna et al. 2012). Fouled ballast has a lower hydraulic conductivity and shear strength than un-fouled ballast (Nguyen & Indraratna 2021). Despite the fact that most fouling occurs above the ballast layer, several investigations have found that about 18% of fouling is due to subgrade fines (Trani 2009); this means that a sub-ballast filter is needed to mitigate fouling from the subsurface.

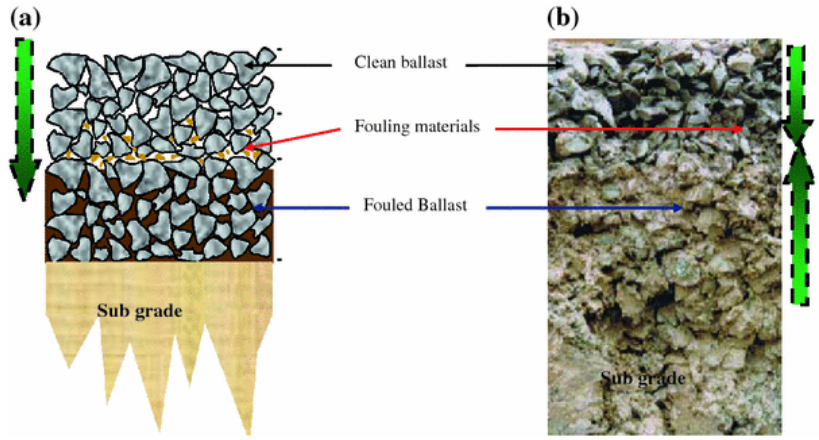

Fig. 2. 1 Ballast fouling in railway tracks (Anbazhagan et al., 2012, by permission)

2.3.2 Mud Pumping

Mud pumping, which causes attenuated fines to combine with the water and form a slurry in the subgrade, is another effect of severe erosion of subgrade soil (Hudson et al. 2016; Indraratna et al. 2020). Several research investigations into the generation of mud pumping have been conducted over the last few decades, but it is still not clear how subgrade fluidisation differs with different loads and soil conditions. According to Hudson et al. (2016), voids under sleepers, along with localised stress and cyclic deformation, promote mud pumping in railroad tracks. A similar phenomenon occurred in slab tracks, where gaps between the concrete slabs and subgrade caused fluidised subgrade and accelerated mud pumping near the base plate expansion joints during the next train loading (Cai et al. 2015).

According to Takatoshi (1997), suction causes mud pumping in four phases. As ballast degrades over time due to dilatation and breaking, gaps appear between the sleepers and the ballast layer. Trains cause significant excess pore pressures in the subgrade as they travel through the connectors. The vacuum created by the ties provides a suction during unloading, which drives fine particles in the subgrade up to the ballast layer. With cyclic loading, this suction force is repeated, causing particles to amass inside the ballast layer. Because the sleeper-ballast contact is weak, an upward suction is created in the ballast layer, which can suck fine particles into the ballast layer and foul the ballast.

According to Duong et al. (2014), the excess pore pressures under railway tracks in subgrade soils are generated by cyclic loads, which cause particles to migrate upwards through the surface layers. The fine particle migration results in 'interlayer creation,' or the formation of a layer of mixed materials at the subgrade and the ballast interface. Track subsidence occasionally occurs as this slurry is discharged at the track surface by strong hydrodynamic forces that have formed pipes through porous joints and interconnected

voids (Figure 2.2). Mud pumping can be greatly decreased using a sub-ballast filter that is internally stable and appropriately compacted (Indraratna, Singh & Nguyen 2020).

Fig. 2. 2 Mud pumping occurred along the east coast in NSW, Australia (Picture Courtesy: Prof. Buddhima Indraratna)

2.3.3 Erosion from Poor Drainage

The substructure of high-speed railways is prone to generating excessive pore pressures that lead to increased seepage forces and higher suction. Due to inadequate drainage, rainwater that collects under sleepers and inside the substructure may be propelled out under this extreme hydraulic pressure and erode sleepers and other track components. As a result, track maintenance costs increase, which jeopardises the ability of trains to operate at the established speed limits. Internally stable filters can effectively alleviate this problem (Israr 2016).

2.4 INTERNAL INSTABILITY ASSESSMENT

Several geometric criteria are presented in the literature to determine whether or not granular soils are internally unstable (Indraratna, Israr & Rujikiatkamjorn 2015; Kenney & Lau 1985; Kezdi 1979). These geometric criteria consider the diameters of the finer and coarser fractions of the Particle Size Distribution (PSD) curve of a soil specimen. Assuming a coarser fraction with a controlling constriction size larger than the largest

erodible finer particle allows fine particles to pass through these constrictions and alter the PSD, thus rendering the soil ineffective for its intended use. However, these geometric criteria do not take into consideration the hydraulic and stress conditions required to cause the erosion of fine particles (Israr 2016). A critical review of these different geometric approaches is as follows:

2.4.1 PSD-Based Criteria for Assessing Internal Instability

Most PSD-based criteria are derived directly from experimental investigations on granular soils and are based on semi-empirical relationships. The United States Army Corps of Engineers (USACE) was the first to use the term “inherent instability”. The USACE (1953) conducted experiments on mixtures of gravel and sand in order to determine which combination was internally stable and which was unstable. Four gravel-sand mixtures were tested in a constant-head permeameter apparatus. The soils were loose, and no surcharge loading information was available. The flow direction was downward, beginning with a hydraulic gradient of 0.5 and then gradually increasing to 16. Vibrations were applied during the experiments. The PSD curve was used before and after the test to determine instability. The results showed that soil Mixtures D (30% sand + 70% gravel) and A (50% sand +50% gravel) were internally unstable, while Mixtures C (90% sand +10% gravel) and B (70% sand + 30% gravel) were internally stable. Mixture B had a more suitable permeability than Mixture C and was therefore identified as a better filter material. However, they carried out these tests on limited soil samples, so no criterion was proposed to demarcate internally stable and unstable soils.

Istomina (1957, reported by Kovacs 1981) proposed a method to check inherent instability by using the uniformity coefficient (C_u). C_u is regarded as the primary index of the PSD curve. The soil is internally stable at $C_u \leq 10$, unstable at $C_u \geq 20$ and the soil is considered as transitional at $10 \leq C_u \leq 20$. However, this criterion has not yet proven itself

able to evaluate internal instability potential because it is based on theoretical investigations. In contrast, Lubochkov (1969) proposed that the shape of the PSD curve determines the movement of fine particles. Therefore, internal instability is independent of the C_u value. An analytical model has been proposed as follows:

$$\frac{1}{\chi^{0.6}}\frac{W(\chi d)-W(d)}{W(d)-W\left(\frac{d}{\chi}\right)}<1 \tag{2.1}$$

where d = any particle size obtained from the PSD curve, $W(x)$ = per cent passing by mass at particle size x, and χ = safety factor coefficient.

However, Lubochkov's (1969) criterion was not successful because it is also based on theoretical investigations. Kezdi (1979) proposed a method to determine whether granular soils have the potential for internal instability by splitting the PSD curve into finer and coarser components at any random particle size. The coarser component is considered as a filter material and is evaluated to retain the finer component. Soil is believed to be internally stable when $D_{15}^{c}/d_{85}^{f} \leq 4$ (Figure 2.3), where D_{15}^{c} is the 15% passing by mass of the PSD of the coarser fraction and d_{85}^{f} is the 85% passing by mass of the finer fraction's PSD. The D_{15}^{c} is considered the coarser fraction's controlling constriction size. Sherard (1979) later suggested that the threshold should be $D_{15}^{c}/d_{85}^{f} \leq 5$. Kezdi's (1979) criterion is simple and easy to implement but does not consider the relative density of the soil samples (Indraratna, Israr & Rujikiatkamjorn 2015).

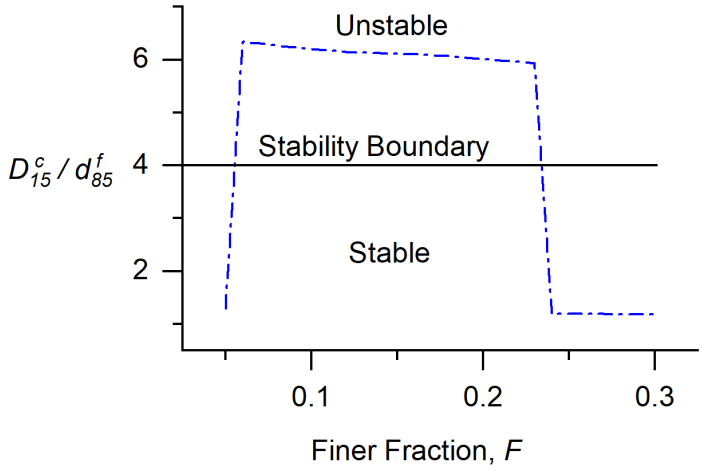

Fig. 2. 3 Kezdi's (1969) criterion (modified after Kezdi, 1979)

Fannin & Moffat (2006) experimented with five widely-graded and gap-graded soils in a seepage apparatus. The soil samples were 10 cm long and 10 cm in diameter and were held on a metal screen. A downward uni-directional flow was imposed along with vibrations. An overburden pressure of 25kPa was imposed. Variations in local hydraulic gradients and loss of fine particles were adopted to define the instability. They found that the value of $\left(D_{15}^{c}/d_{85}^{f}\right)_{max}$ increased, and the percentage loss of fine particles also increased. It was observed that the threshold of D_{15}^{c}/d_{85}^{f} = 4 is compatible with the experimental results. Li (2008) also carried out experimental investigations on various cohesionless soil samples, validated the criterion by Kezdi (1969), and came to similar conclusions. Indraratna et al. (2015) showed through their experimental investigations that the Kezdi (1969) criterion had had less success than the constriction-based criterion that considers the relative density of the soil samples.

Kenney & Lau (1985, 1986) tested 16 well-graded sandy gravels using a constant-head permeameter apparatus. Soil samples were 580 mm or 245 mm in diameter and 860 mm or 450 mm in length. A uni-directional downward flow was imposed with a surcharge pressure of 10 kPa. Vibrations that were induced by manual tamping significantly affected

the response of some PSD curves. Internal instability was evaluated by looking at the difference in PSD curves before and after the test.

The shape of the PSD curves was used to propose a criterion. The retention ratio from Kenney & Lau (1985) is $(H/F)_{min}$, where F is the finer particles' fraction at any particle diameter D, and H is the incremental finer fraction between particle diameters D and $4D$. The internally unstable soils have $(H/F)_{min} \leq 1$ (Figure 2.4), while the widely and uniformly graded samples were evaluated by considering particles finer than 20% and 30%, respectively. The boundary was originally defined as $(H/F)_{min} \leq 1.3$ but was modified to 1 after discussions with several researchers (Kenney & Lau 1986). The Kenney & Lau (1985) criterion is easy to use because the shape curve of the PSD is needed to verify whether or not a soil is internally stable or unstable. This could be achieved by implementing this criterion in a simple MATLAB code. The Kenney & Lau (1985) criterion applies only to narrowly graded and widely graded granular soils.

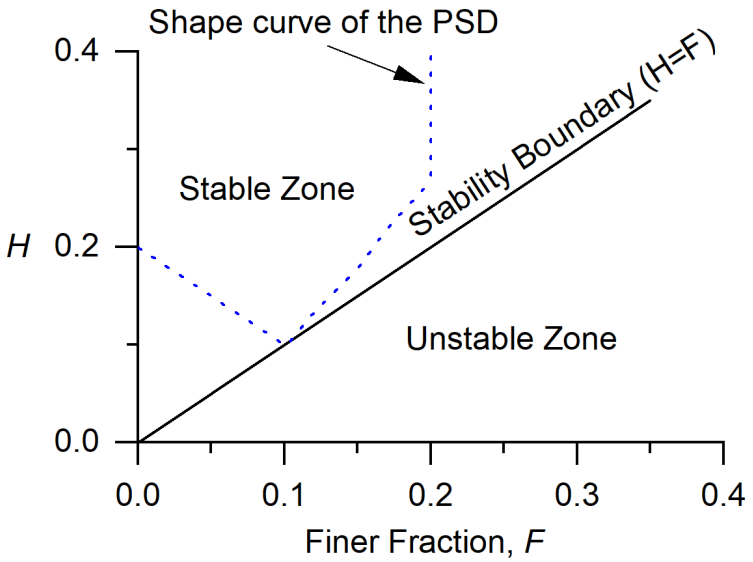

Fig. 2. 4 Kenney and Lau's (1985) criterion (modified after Kenney & Lau, 1985)

Kenney & Lau (1985) and Kezdi's (1979) criteria were compared by Chapuis (1992), who noted that both approaches could be described by comparable slope criteria. The likelihood of internal instability can be indicated by the secant slope of the PSD

curve. A slope of the secant line may be used to approximate the PSD curve's slope at any point. Therefore, Kenney and Lau's criterion corresponds to the following: in order to have internal instability, the slope per cycle of the particle size distribution curve must be less than y/log (4) for any particle size D_y (y ≤20). Likewise, Kezdi's (1969) criterion corresponds to the following: if the slope per cycle of the PSD curve is less than 0.15/log (4) for any particle diameter, it is considered unstable.

Subsequently, Burenkova (1993) presented a technique by conducting experiments on 22 samples with the largest particle size of 100 mm, and $C_u \leq 200$. Soils were separated into different size proportions and dried and blended in a container. The fundamental concept is that the finer proportion of the soil does not participate in the soil skeleton unless it causes an increase in volume when mixed with the coarser fraction. The conditional factors of uniformity have been proposed to characterise soil heterogeneity using the following two ratios:

$$h' = {}^{d_{90}}/_{d_{60}} \tag{2.2}$$

$$h' = {}^{d_{90}}/_{d_{15}} \tag{2.3}$$

Burenkova (1993) proposed the boundaries that distinguish "suffosive soils" from "non-suffosive soils" based on these two ratios (Fig. 2.5). Zones I and III indicate the suffosive soils; Zone II shows non-suffosive soils; Zone IV depicts artificial soils. The range for non-suffosive soils can be determined using the following equation:

$$0.76 \log(d_{90}/d_{15}) < d_{90}/d_{60} < 1.86 \log(d_{90}/d_{15}) + 1 \tag{2.4}$$

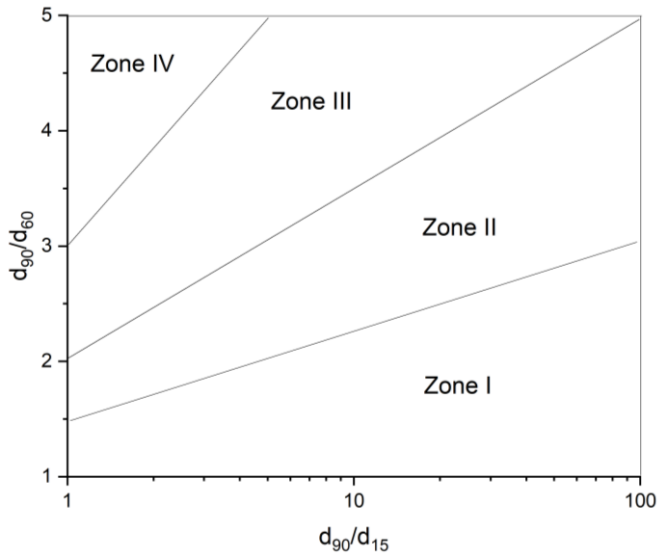

Fig. 2. 5 Burenkova's criterion (modified after Burenkova, 1993)

Honjo et al. (1996) experimented with gap-graded soils, primarily sand. A uni-directional downward flow was imposed with vibrations by gentle manual tamping and a surcharge pressure of 0.9 kPa. The loss of fine particles determined the presence of internal instability. As the gap ratio increased, the loss of fines increased, so they concluded that soils with a gap ratio> 4 are internally unstable, regardless of the number of fines in the soil. This criterion only applies to gap-graded soils.

Liu (2005) presented an approach to assess the internal instability of granular soils by dividing the soil gradation curve into coarser and finer fractions. The soil is internally stable when fine particles fill the voids created by coarser particles. Therefore, at any particle diameter for dividing the PSD curve, the percentage of the finer content by mass (P (%)) was used to check the internal instability. Based on the experimental investigations and theoretical analysis, the following criteria are proposed:

- P < 25%, internally unstable soils,
- P = 25 to 35%, transition conditions,
- P > 35%, internally stable soils.

The point at which the coarser and finer fractions are divided depends on the type of soil. These soils were classified as either continuously graded soils or gap-graded soils. For the continuously graded soils, P = percentage mass passing at the division diameter $d_f = \sqrt{d_{70}d_{10}}$, and for the gap-graded soils, P = mass passing (%) at the gap location for gap-graded soils.

Wan & Fell (2004) studied the internal instability of silt-sand-gravel and clay-silt-sand-gravel mixtures. Fourteen soil samples, each 300 mm in diameter by 300 mm long, were examined. The specimen was supported on a single-size 20 mm drainage aggregate. In order to break up the flow evenly over the top surface of the sample, a 25 mm aggregate was placed on top. The flow direction was downward, and the hydraulic gradients ranged from 10 to 18 across the specimen. The specimen was not subjected to vibrations. The occurrence of internal instability was checked using the PSD curve before and after each test. The soil samples were evaluated based on the available geometric methods and led to the following conclusions:

- The coefficient of uniformity (C_u) (Istomina, 1957) is not a good marker of internal instability,
- The methods used to split the PSD curve into a finer and coarser fraction (e.g., Kezdi, 1979) were too conservative in assessing internal instability,
- Kenney & Lau's (1985) method is conservative.

Li & Fannin (2008) contrasted the approaches of Kenney and Lau (1985, 1986) and Kezdi (1979). Based on an analysis of their experimental findings and literature data, they postulated that the criterion by Kezdi (1979) is the more conservative of the two when the per cent passing by mass F < 15%, while the criterion of Kenney and Lau (1985, 1986) is more conservative for F > 15%, as shown in Figure 2.6.

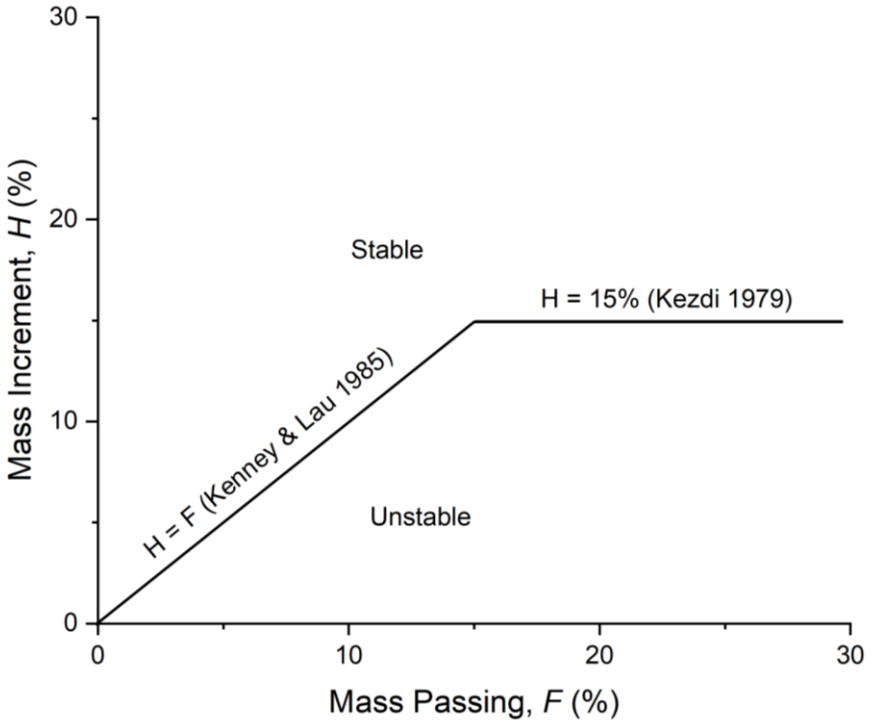

Fig. 2. 6 Comparative analysis of the two criteria (modified after Li & Fannin, 2008)

All the approaches discussed above take the PSD into account. However, it is not the PSD but the Constriction Size Distribution (CSD) that controls the instability. The constrictions of the coarser fraction control the movement of the fine particles through it. A soil sample has a large number of fines, but if the size of the controlling constriction is smaller due to its higher relative density, then the soil will be internally stable. However, at a lower relative density, the same sample exhibited larger constriction sizes and is therefore internally unstable.

2.4.2 CSD-Based Criteria for Assessing Internal Instability

The complex process of internal instability and the variables affecting it can be explained using geometric probabilistic approaches, which are useful analytical tools. The concept of CSD has gained popularity since it was initially proposed by Silveria (1965), who described the complications with particles being washed through dam filters. Until the CSD concept was introduced, it was assumed that internal instability was determined by considering the size of the filter and the base soils. However, in the 1980s, when attempts

were made to estimate the size of the controlling constriction, it attracted increased attention from researchers (Kenney et al. 1984). However, the fundamental problem remained because these studies were mainly aimed at approximating the CSD from the PSD (by mass).

In this regard, Kovacs (1981) presented a model to test internal instability of cohesionless soils. The model considers the collection of different parallel cylindrical tubes as the porous space or constrictions of the soil sample (Figure 2.7). The particle size distribution by mass was split at any arbitrary diameter (D_n). The effective diameter (D_h^c) of the coarser fraction was calculated using the D_n value. The following equation determines the average diameter of parallel tubes (d_o):

$$d_o = 4\frac{n_c}{1-n_c}\frac{D_h^c}{\alpha_d} \tag{2.5}$$

where α_d = shape coefficient; n_c = skeleton's porosity; and

$$D_h^c = \frac{1}{\sum\frac{\Delta F_i^c}{D_i^c}} \tag{2.6}$$

where D_i^c = average diameter in the i^{th} interval of the coarser fraction's PSD curve and ΔF_i^c = particle weight in the i^{th} interval of the coarser fraction's PSD curve.

Kovacs (1981) presented a criterion for internal instability as follows:

$$4\frac{n_c}{1-n_c}\frac{D_h^c}{\alpha_d} < d_{85}^f \tag{2.7}$$

The above model has not been widely used because experimental analysis was not performed to verify the model.

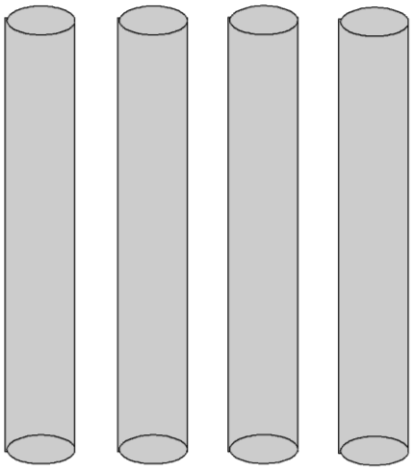

Fig. 2. 7 Capillary tube model (modified after Kovacs, 1981)

In the 1990s, researchers criticised using the PSD by mass and number for over-representing the finer and coarser fractions, respectively, and suggested using the PSD by surface area instead (Locke 2001). Locke et al. (2001) presented a model for estimating the CSD from PSD and R_d of the soil. Indraratna et al. (2007) presented an analytical approach for base-filter retention based on the study by Locke et al. (2001). They created a complete, user-friendly computer software made up of specific MATLAB subroutines that included the computation of CSD by surface area, number, and mass. Several CSD-based approaches that are available to assess internal instability are discussed below.

Indraratna et al. (2011) presented a method for checking the internal instability of granular soils. This criterion takes into account the relative density of the soil samples, which was neglected in the previous criteria. The PSD curve was divided into finer and coarser fractions, and the theory of Aberg (1992) was used. The CSD of the coarser portion and the PSD of the finer portion were plotted using the surface area method (Indraratna, Raut & Khabbaz 2007). The ratio of the governing constriction size (D_{c35}^{c}) and the largest erodible fine particle (d_{85}^{f}) was used as an index. Two boundaries proposed are given as follows:

- if $D_{c35}^{c}/d_{85}^{f} > 0.82$, the soil is internally unstable, and

- if $D_{c35}^{c}/d_{85}^{f} < 0.73$, the soil is internally stable; otherwise, it is in the transition zone (Figure 2.8).

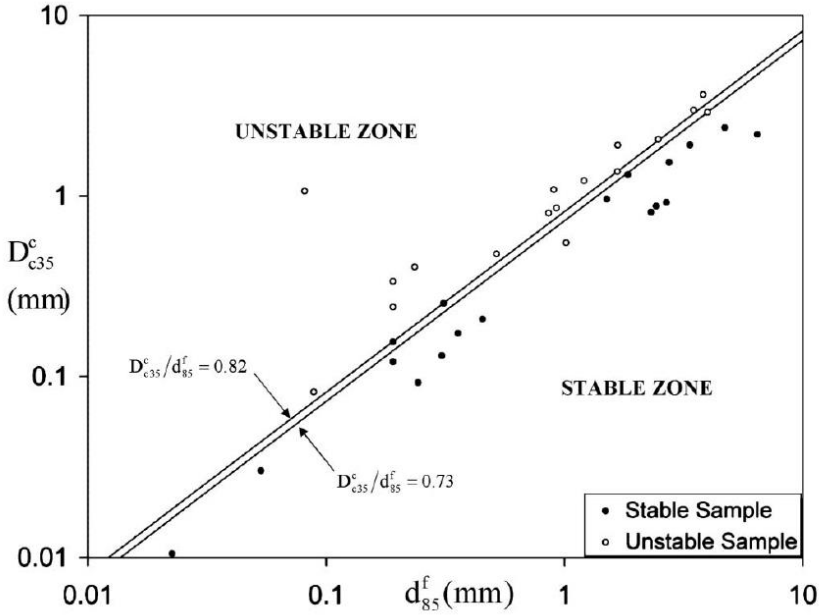

Fig. 2. 8 CSD-based method by Indraratna et al. (2011) (Indraratna et al. 2011, by permission)

Indraratna et al. (2015) carried out an experimental analysis on six granular soils with different uniformity coefficients and compacted to different relative densities. These test samples were 150 mm in diameter by 200 mm long. They extended the original criterion of Indraratna et al. (2011) by validating the model with their experimental analysis and data from the literature. At $(H/F)_{min}$, the PSD was split into coarser and finer fractions. The resulting coarser fraction was considered to be the filter, and the finer fraction was the base soil. The CSD of the coarser fraction and the PSD of the finer fraction were plotted using the surface area technique. The boundary proposed is given as follows: if $D_{c35}^{c}/d_{85}^{f} \leq 1$, the soil is considered internally stable (Figure 2.9). The criterion of Indraratna et al. (2015) has shown reasonable success in predicting the

internal instability of granular soils because it considered the PSD and relative density of the soil sample.

Israr & Indraratna (2017) performed hydraulic tests on four compacted granular materials under cyclic loading. These experiments revealed that the conventional criteria for static loading conditions did not work under cyclic loading conditions. Therefore, a revised geometric criterion was proposed to define the boundary between internally unstable and stable soils under cyclic loading conditions more precisely. The proposed boundary is: $D_{c35}^{cl}/d_{85}^{f} \leq 1$, where D_{c35}^{cl} is the controlling constriction size at the loosest state. The approaches described providing a review of the geometric factors. However, for internal instability to occur in the field, the hydraulic and stress conditions, i.e., the hydromechanical conditions, must be met.

Failure to meet the geometric criteria does not mean that fine particles travel through the constrictions of coarse particles because a relatively high gradient is required to initiate movement (Kovacs 1981). Therefore, in practice, some embankment dams constructed from potentially unstable materials may not suffer suffusion from seepage (Li 2008). So, if the hydraulic gradient is not a problem in a project, potentially unstable materials could be used. The following section provides an overview of the hydromechanical conditions presented in the previous studies.

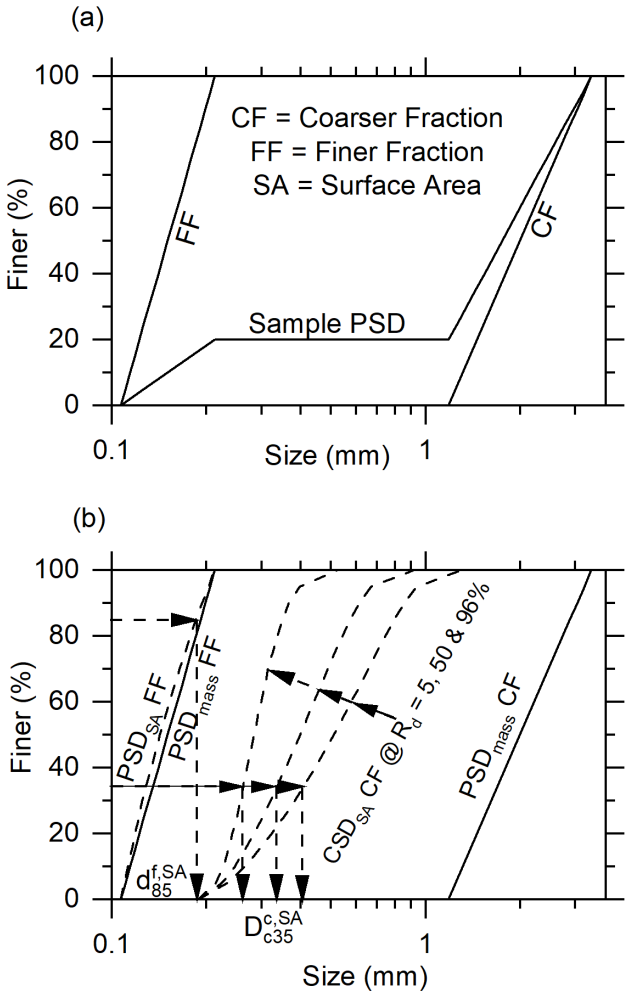

Fig. 2. 9 Illustration of the constriction-based criterion by Indraratna et al. (2015) (modified after Indraratna et al., 2015)

2.4.3 Hydromechanical Conditions of Internal Instability

Terzaghi (1943) first proposed a theory of uniform sand seepage failure. This theory is based on the submerged weight of soil particles and the upward seepage forces. Suppose the hydraulic gradient in a soil sample is increased to a zero effective stress state; in this case, heave failure occurs when the seepage pore water pressure becomes equal to the total overburden stress of the soil. The critical value of the hydraulic gradient (i_{cr}) is given by:

$$i_{cr} = \frac{\gamma'}{\gamma_w} \tag{2.8}$$

where γ_w = unit weight of water; γ' = submerged unit weight of soil.

Adel et al. (1988) performed experiments on three minestones. No overburden pressure was applied to the soil specimen, and each specimen was 105 cm long. In the horizontal direction, a uni-directional flow was imposed. A sand trap was used to collect the washout of fine particles. The critical hydraulic gradient was determined based on the rate at which fine particles were lost. Between $(H/F)_{min}$ and the critical hydraulic gradient, a linear relationship was found.

Skempton & Brogan (1994) conducted seepage experiments on different types of soil. The samples were 155 mm long and 139 mm in diameter. The soil sample was first saturated, and then upward flow was applied until the sample failed. They discovered that the critical hydraulic gradients for internally unstable materials could be about 1/3 to 1/5 of the normal value of 1 given by Terzaghi. The stability index $(H/F)_{min}$ and the critical hydraulic gradient were correlated (Figure 2.10). They interpreted a non-linear relationship between the $(H/F)_{min}$ and critical hydraulic gradient compared to the linear relationship of Adel et al. (1988). They concluded that the internal stress distribution could affect the piping potential.

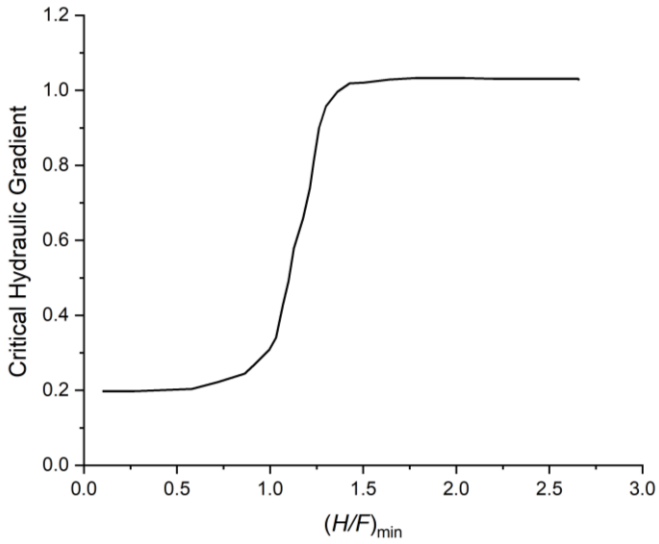

Fig. 2. 10 Relationship between $(H/F)_{min}$ and critical hydraulic gradient (modified after Skempton & Brogan, 1994)

Wan & Fell (2004) carried out experiments on 14 soil mixtures. These specimens were 250 mm long by 300 mm in diameter, and they were reconstituted by being compacted in a cylindrical cell. An upward hydraulic gradient was applied to the specimen and then increased until the specimen failed. Signs of the erosion of fines were noted by continuously observing the colour of the effluent. They concluded that:

(i) The internal instability of these soils commenced at critical hydraulic gradients of 0.5 or less,

(ii) No mathematical relationship was found between the coefficient of uniformity, the critical hydraulic gradient and Kenney & Lau's (1985) stability index or fines content,

(iii) A lower hydraulic gradient is required to erode high porosity soils,

(iv) A higher hydraulic gradient is required to erode clayey soils than soils with a similar proportion of fines but no cohesive fines,

(v) The i_{cr} is significantly affected by the density of the soil;

(vi) A lower hydraulic gradient is required for the failure of gap-graded soils compared to the continuously graded soils with a similar proportion of fines.

Liu (2005) conducted experiments in a vertical permeameter, where the diameters of the test samples were 200 mm to 300 mm. No overburden pressure was imposed on the soil specimen, and an upward uni-directional flow was induced. To define the critical hydraulic gradient (i_{cr}), the slope of the gradient versus seepage velocity was used. The i_{cr} increased as the proportion of particles increased, and they were non-linearly related. Moffat (2005) conducted experiments on 4 soil mixtures using a large permeameter. The test samples were 300 to 500 mm long and 279 mm in diameter. The influence of effective vertical stress on the commencement of internal instability was investigated. An

overburden pressure of 25 to 175 kPa was imposed. The critical hydraulic gradient was determined by differences in the local hydraulic gradients and visual observations. A linear relationship was discovered between the critical hydraulic gradient and the vertical effective stresses. A different hydromechanical boundary for each gradation marked the onset of internal instability.

Li & Fannin (2012) proposed the concept of a hydromechanical envelope to demonstrate the inception of suffusion in cohesionless soils (Figure 2.11). The hydromechanical envelope takes the form of a linear relationship in stress-gradient space. Its position depends on the magnitude of the stress imparted to the finer fraction of the PSD curve. Either heave or suffusion triggers the onset of instability following the observations of Terzaghi (1943) and Skempton & Brogan (1994), respectively.

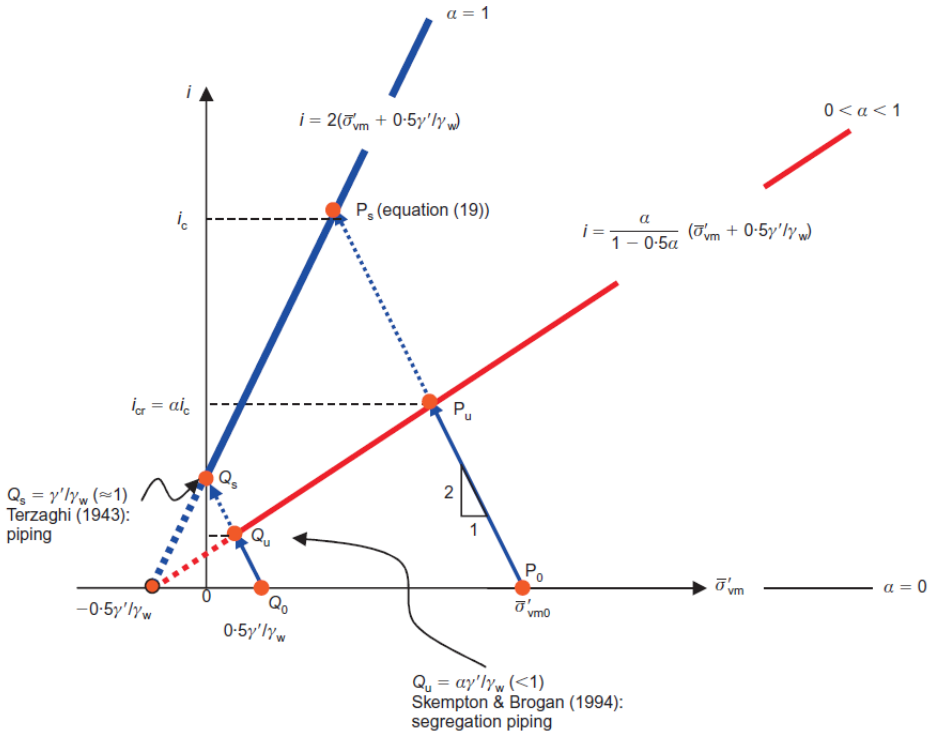

Fig. 2. 11 Theoretical hydromechanical envelope (modified after Li & Fannin, 2012)

Xiao & Shwiyhat (2012) investigated the effect of internal instability or suffusion on the geometric and mechanical properties of soils. The geometric and mechanical properties considered were volume change, permeability, PSD, and compressive strength.

The experimental tests were carried out using a triaxial device that allowed seepage through the soil, and the soil eroded during the tests was collected. After the seepage tests, the samples were sheared following consolidated undrained stress paths. The results showed that the internal instability influenced the geomechanical properties of the soil. Soil permeability was reduced because fine particles clogged the voids in the coarser particles. Similarly, the compressive strength and volume change properties were different before and after the suffusion tests. The changes in compressive strength were not captured very well, but some of the gap-graded soils showed that the compressive strength increased after internal instability. In contrast, the other soils showed lower compressive strength after erosion.

Chang & Zhang (2013) carried out laboratory investigations to study the critical hydraulic gradients of internal erosion under isotropic compression, drain triaxial compression, and extension stress paths. The influence of the stress state on the critical hydraulic gradient was studied. Stable, initiation, development, and failure were the four phases of erosion that they proposed. The hydraulic gradient for the initiation of particle motion first increased with the shear stress ratio and then decreased as the stress reached the failure point. Ke & Takahashi (2015) investigated the consequences of suffusion on the mechanical behaviour of cohesionless soils with different fines content and at different initial confining pressures. It was observed that the strength of the soil decreased after suffusion and at higher confining pressures; this drop in strength decreased. The volumetric strain was greater at lower confining pressure.

Indraratna et al. (2017) carried out experimental investigations on four cohesionless soils under cyclic loads. A uni-directional flow in an upward direction was induced. The relationship between the velocity of effluent and the hydraulic gradient was used to check the inception of instability (Figure 2.12). It was found that the critical

hydraulic gradient is influenced by the wall of the apparatus and particle-to-particle contact friction. It was also found that some samples that were stable under static loads became unstable under cyclic loads.

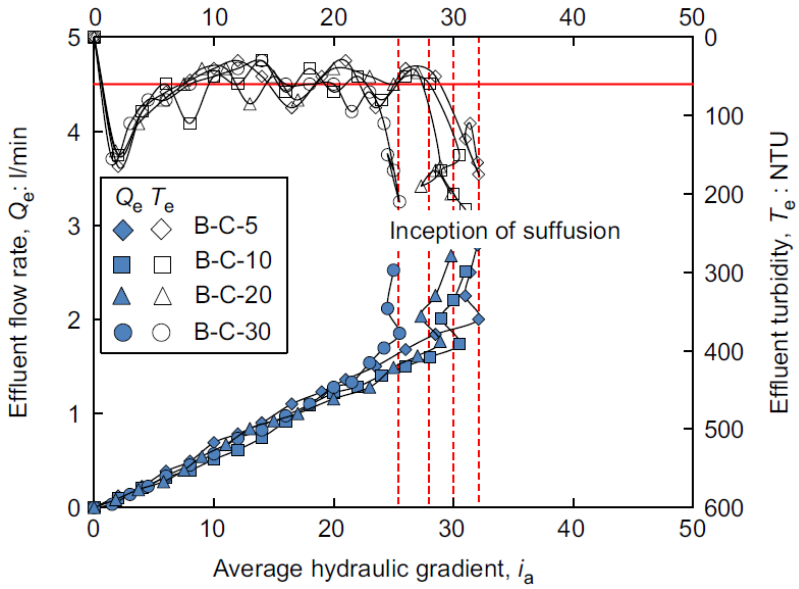

Fig. 2. 12 Relationship between effluent flow rate, turbidity and average hydraulic gradient (modified after Indraratna et al., 2017)

Mehdizadeh et al. (2017) investigated the post-erosion undrained behaviour of cohesionless soil under different loading paths. The undrained post-erosion shear strength increased under static and cyclic loading. The eroded samples showed higher resistance under cyclic loading, whereas the un-eroded sample liquefied immediately. The higher resistance of the eroded sample was due to effective contact between the coarser particles. Mehdizadeh et al. (2018) studied the effect of erosion on the geometric and mechanical properties of internally unstable soils and found that even a small percentage of eroded fine particles enhanced the mechanical behaviour.

Mehdizadeh et al. (2019) investigated the influence of the sample size on the internal erosion of the soil sample. As the sample increased in length, the likelihood of the particles becoming clogged increased, and fewer fines were eroded. The strain-softening behaviour became more pronounced as the residual fines content decreased.

The mechanical behaviour of the samples changed due to internal erosion, and the undrained peak strength increased with up to 15% of fine particle erosion.

Luo et al. (2020) studied the effect of deviatoric stress on the onset of soil suffusion. For this purpose, four internally unstable cohesionless soils were selected. The results showed that the deviatoric stress drastically affected the onset of suffusion of soils. A linear relationship was found between the shear stress ratio (ratio of deviatoric stress to mean stress) and the critical hydraulic gradient (i_{cr}). An empirical equation for determining the i_{cr} under complex loading conditions was developed. It was found that as the shear stress ratio increases, the i_{cr} first increases, peaks at the critical value of the shear stress ratio, and decreases significantly after the peak.

A mud pumping incident occurred at a railway site in NSW, leading to a research program at the University of Wollongong, Australia, to find the probable explanation. The internal instability of the subgrade soil at various points was identified as a possible mechanism. Geometrical constraints control the potential for internal instability, whereas hydromechanical constraints influence when instability occurs. Although empirical methods for checking the geometrical potential for internal instability do exist in the literature, their practical applicability is greatly limited by their applicability to soils of varied gradations and the utter lack of micromechanical conditions that lead to the onset of instability.

2.4.4 Effect of Cohesionless Fines on Internal Instability

This doctoral thesis also examines the influence of cohesionless fines content on the internal instability of soils because the hydromechanical threshold for the initiation of internal instability can alter as a result of variations in the fines content. The maximum proportion of mobile fines in the previously mentioned approaches was set at 20% to 30% of the total mass (Kenney & Lau 1985). The literature addressing the impact of fines on

the shear strength of cohesionless soils will now be compared to this proposed limit. In many geotechnical problems, the shear strength of soil with a proportion of sand and silt is a decisive factor because, according to experimental evidence, altering the fines fraction can change the shear strength of soil (Thevanayagam et al. 2002; Vallejo 2001). Apparently, this behaviour varies depending on the range of fines; in essence, the finer fraction influences the behaviour of gap-graded granular mixtures.

A correlation between the void ratio and the undrained shear strength was discovered in an experimental study by Thevanayagam et al. (2002). Their fundamental hypothesis was that soil behaves like an organised skeleton of particles where in some instances, the coarser fraction might carry most of the load, and the finer fraction contributes very little to transfer the load. The strength of the finer fraction is lower in this situation, so this finding must be considered in any limit equilibrium study of the particles (Skempton & Brogan 1994). When introducing non-plastic fines, Thevanayagam et al. (2002) recommended using a modified void ratio (inter-granular and inter-fine void ratio) to explain the change in shear strength. It was discovered that the inter-granular void ratio affects the large strain of the undrained shear strength. They also defined a threshold for fines at which strength of the soil is primarily controlled by fines. If the proportion of fines is low, the intergranular friction (the skeleton of the soil) plays an important role and the finer particles only play a secondary role.

Vallejo (2001) studied the stiffness and shear strength of mixtures of sand-gravel sizes of glass beads and mixtures of sand and silt. To ascertain its effect on the shear strength of these mixtures, the concentration of fines was varied. The variations in the shear strength of granular mixtures were attributed to variations in porosity. A change in porosity occurs with the weight percentage of fine particles. There is no longer room between the coarse grains for further fine grains once minimum porosity has been reached

because, beyond this stage, fine particles take over as the dominating component of the mixture as the coarse grains separate. It was demonstrated that between 25 and 30 per cent by weight of the finer fraction is responsible for differentiating the behaviour of the material. In soil migration studies, this percentage corresponds to the maximum anticipated "mobile" fines for material supported by the coarse fraction. It is comparable to how the peak shear strength changes in binary mixtures due to normal stress being applied in direct shear experiments.

As a result, the fines content of soil can affect a range of its behaviours, such as:

- The strength of the soil mixtures,
- The transfer of stress between coarser and finer particles,
- Mobile fines in the voids of coarse particles.

These factors are likely to influence the onset of internal stability under seepage flow (Moffat 2005).

2.4.5 Role of Particle Shape on Internal Instability

Although the shape strongly influences the behaviour of soils, little or no attention has been paid to this aspect when studying internal instability caused by seepage (Slangen 2015) due to the complex experimental and computational procedures. According to some research on the internal friction angles of granular soils, the internal friction angles for sub-angular particles significantly outperform those for sub-rounded particles when re-formed to the same void ratio. Youd (1973) showed that as the particles become more angular, the maximum and minimum index porosities and the difference between the maximum and minimum index porosities increase. Mitchell & Soga (2005) stated that rounded glass beads are less prone to breakage than angular glass beads.

According to Cho et al. (2006), compared to a similar packing of rounded particles, angular particles produce much looser packing that shows a lower stiffness at

small strains. Compression and decompression indices of rounded particles were lower than angular particles by intermediate strain response; this was associated with contact slippage or particle breaking. An increase in angularity was proposed to increase resistance at large strain response related to particle rotation and slip of contacts against particle rotation, resulting in greater shear resistance.

2.4.6 Decisive Factors for the Occurrence of Internal Instability

Based on the literature review given above, the initiation of internal instability is determined by the following factors:

- PSD (Indraratna, Israr & Rujikiatkamjorn 2015; Kenney & Lau 1985; Kezdi 1979),
- Relative density of soil (Israr & Indraratna 2017),
- Fines content (Liu, 2005),
- The shape of particles (Slangen 2015),
- Soil disturbance caused by vibration etc. (Kenney & Lau 1985; Skempton & Brogan 1994),
- The hydraulic gradient applied to the soil specimen (Indraratna, Israr & Li 2017; Li & Fannin 2012; Skempton & Brogan 1994),
- The effective stresses in the soil (Li & Fannin 2012).

Since all of the above literature focuses on the experimental investigations at the continuum scale, microscale perspectives could not be captured with these macroscale laboratory investigations. Internal instability is regarded as a problem at the particle scale (O'Sullivan 2011); therefore, numerical investigations using the Discrete Element Method (DEM) could be used for such particle scale problems. As mentioned in Chapter 1, this doctoral thesis focuses on the micromechanical modelling of internal instability

using DEM. Therefore, various studies on the numerical investigation of internal instability using DEM are first reviewed as follows.

2.5 MICROMECHANICAL ANALYSIS OF INTERNAL INSTABILITY AND FLUIDISATION

2.5.1 Micromechanical Analysis with the Discrete Element Method (DEM)

In order to solve rock mechanics problems, the numerical modelling method known as DEM was developed in the late 1970s (Cundall & Strack 1979). Since then, it has been widely used to address various engineering issues. DEM is a mesh-free method that, in contrast to more conventional numerical methods such as the Finite Element Method (FEM) or the Finite Difference Method (FDM), takes individual particles into account and records their behaviour. DEM makes it simpler than any conventional method in capturing the continuum response for problems where discrete units are needed to analyse their engineering response, such as simulating rockfall, railway sub-ballast, and ballast. DEM has been used to study internal instability (Ahmadi et al. 2020; Sufian et al. 2021).

Shire & O'Sullivan (2013) carried out DEM modelling of the internal instability of gap-graded granular soils. The samples considered showed different degrees of internal instability, which were evaluated according to the criterion of Kezdi (1979). The particles were spherical, and the periodic boundaries were used to minimize the boundary effects and achieve computational efficiency. The samples were compressed isotropically to a mean stress of 200 kPa, and no gravity force was applied to the samples in order to obtain an isotropic fabric. The micromechanical analysis considered the coordination number, the volume-weighted coordination number, the relative frequency of the contacts and the probability of the contact force. It was found that the coordination number and the volume-weighted coordination number decreased with increasing stability index by

Kezdi (1979) (Figure 2.13). However, there was no apparent distinction between samples that were internally stable and those that were unstable.

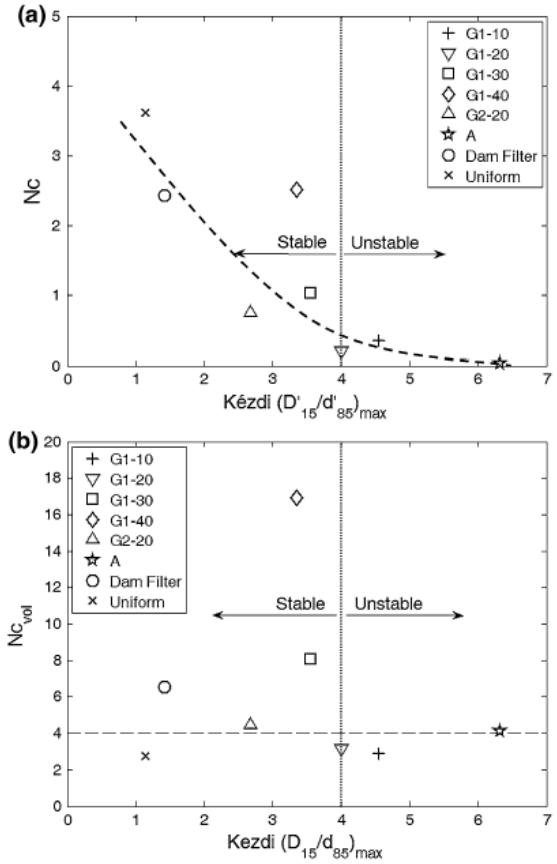

Fig. 2. 13 Variation in (a) coordination number, (b) volume-weighted coordination number with Kezdi's (1979) stability index (Shire & O'Sullivan 2013)

Shire et al. (2014) used DEM simulations to study the stress distribution in idealised gap-graded soils with different internal stability potentials. Samples of soil were created with particles having spherical shapes. No gravity force was applied to the particles, and the samples were compressed in an isotropic manner. The stress reduction factor (α) was quantified directly from the particle scale data using DEM variables. It was found that the stress distribution is affected by the particle size distribution, the relative density and the percentage of cohesionless fines.

The DEM data concluded that the soils are underfilled fabric, where the fines are loose in the voids of the coarse particles if the fines content < 25%. Therefore, soils with

fines content < 25% are not affected by the relative density of the soil. If the fines content > 35%, the soil is overfilled and considered to be internally stable. In soils with a fines fraction between 25% and 35%, the effective stress transferred to the fines is very sensitive to the relative density of the soil. The fabric of the soil sample was divided into 3 cases. In case 1 (Zone I), coarse particles dominate, while the fine particles sit loosely in the spaces between the coarse particles. In case 2 (Zone II), coarse particles are the dominant fabric while the fine particles are under-stressed and play a supporting role. In case 3 (Zone III), both fine and coarse particles participate in the transfer of stress (Figure 2.14). However, the samples could transition from one zone to another due to stress-induced anisotropy; this was not taken into account, but it will be considered in this doctoral thesis.

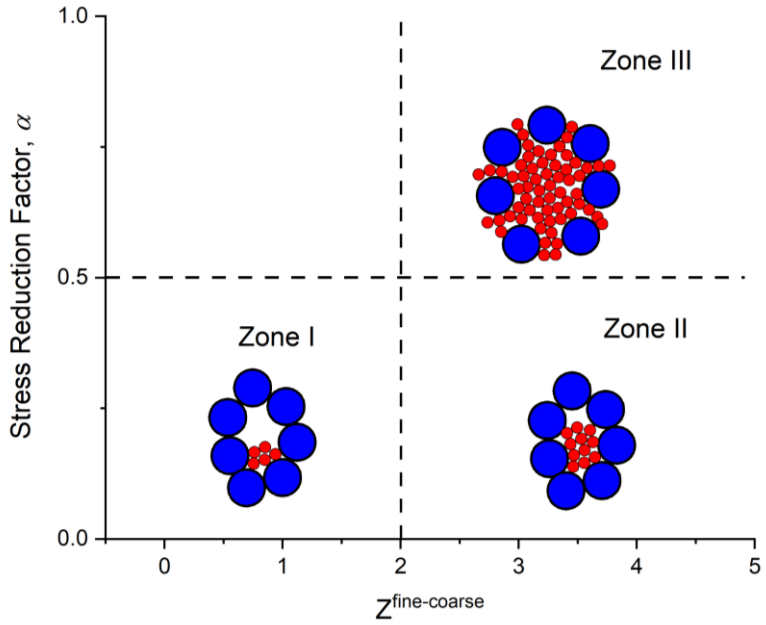

Fig. 2. 14 Zones of the various fabric cases (modified after Shire et al., 2014)

Langroudi et al. (2015) studied the micromechanical behaviour of internally stable and unstable soils using DEM. Linear, concave up, and gap graded were the three types of gradations chosen for the analysis. The numerical investigations showed that the gap-graded soil and concave up gradations exhibited low connectivity of the particles, whereas

the internally stable samples showed a more homogeneous network of contact forces than internally unstable soils. The macroscale criteria were compared to micromechanical parameters such as the mechanical coordination number, but there was no clear distinction between internally stable and unstable soils (Figure 2.15).

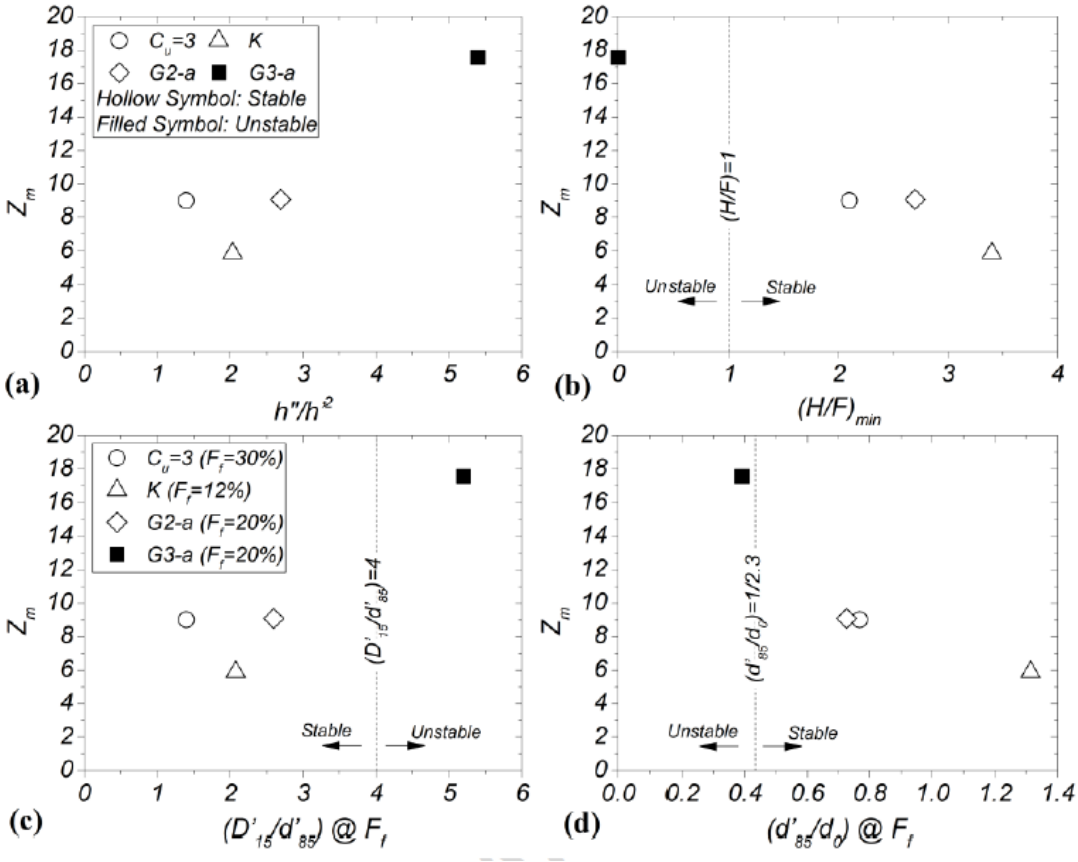

Fig. 2. 15 Mechanical coordination number versus various macroscale criteria (Langroudi et al., 2015, by permission)

Shire et al. (2016) studied the influence of the size ratio and fines content on the contact distribution and stress transfer in dense gap-graded soils. A mean stress of 50 kPa was imposed on the samples using the isotropic compression method. The periodic boundaries were used, and the gravity of the particles was not considered. It was discovered that the fines content and size ratio influence the stress reduction factor (Figure 2.16).

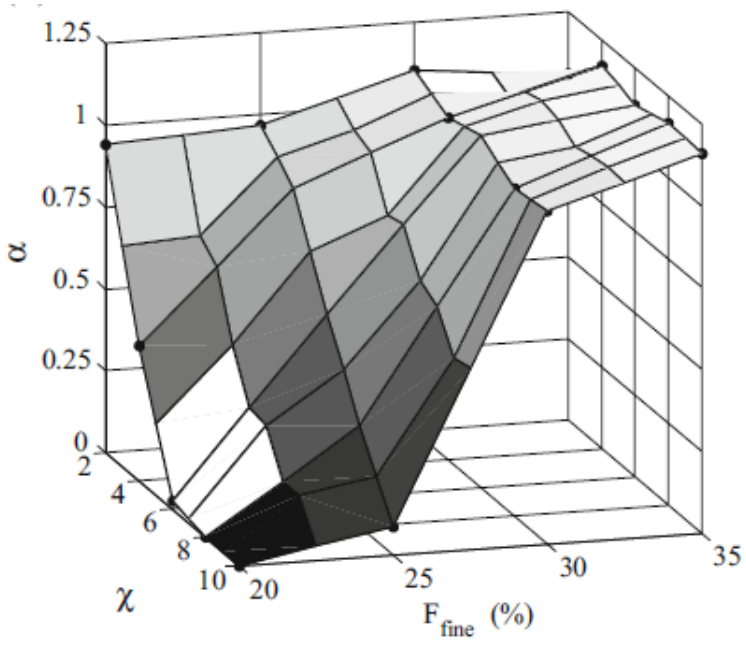

Fig. 2. 16 Relationship between stress reduction factor (α), size ratio (χ) and fines content (F_{fines}) (Shire, O'Sullivan & Hanley 2016)

Ahmadi et al. (2020) investigated the influence of the fine fraction, the relative density and the gap ratio on the internal instability of soils. A novel method was proposed to create the DEM samples with target relative densities. Spherical particles were used. The evolution of the stress reduction factor and the partial coordination number were checked at different relative densities; they found that gradations with gap ratios between 4-7 with 35% fines are internally unstable but can become stable as the relative density increases.

Ahmadi et al. (2021) studied the effect of soil structure on the internal instability of cohesionless gap-graded soils. The actual fabric of the soil was recorded using Micro-Computed Tomography (μCT) and then transferred to DEM using image processing techniques. The Pair Correlation Function (PCF) was used as a micro geometric parameter to assess the influence of image filters on the quality of the images from μCT. The numerical results from DEM showed a lower coordination number but a higher stress

reduction factor with the real fabric of the soil, which indicated that the fine particles are more involved in the transfer of stress in the structure of real soil.

Sufian et al. (2021) studied the influence of relative density and stress-induced anisotropy on the stress distribution in gap-graded soils using DEM. The particle shapes were spherical. Mean effective stress of 100 kPa was imposed on the samples, and then constant mean stress triaxial compression tests were carried out to investigate the effect of stress-induced anisotropy. A limiting value of the axial strain was set at 5% due to computational limitations. The presence of a single fines content threshold capable of distinguishing between coarse and fine dominating behaviour in gap-graded soils was refuted (Figure 2.17). Dense, transitional gap-graded soils showed less stress transferred to the finer fraction during shearing.

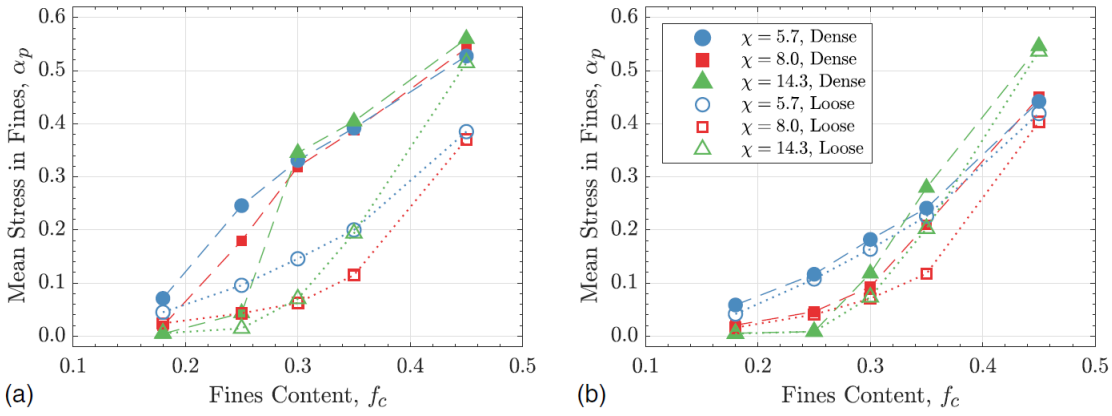

Fig. 2. 17 Distribution of mean stress in the fines (a) start (b) end of shearing (Sufian et al., 2021, by permission)

In the approaches presented above, spherical-shaped particles were assumed because the shape of particles affects internal instability. For example, spherical particles ought to be more prone to instability than angular particles. In the second case, an increase in the surface area leads to a large increase in the number of particles that make active contacts, which results in a more stable particle assembly. Angular particles have higher friction and more efficient stress transfer than spherical particles (Israr 2016). In addition,

the fluid part was ignored in all of the above studies. The following section discusses the coupled fluid-particle interaction methods used to assess internal instability.

2.5.2 Micromechanical Analysis with Coupled DEM-CFD/LBM

DEM is typically coupled with Computational Fluid Dynamics (CFD) using either the Navier-Stokes equations or the Boltzmann equation to model the interaction between the fluids and the particles. Modelling fluid-particle interaction is crucial when verifying internal instability or mud pumping. DEM-CFD has been used in the literature to study the internal instability and fluidisation of soils (Nguyen & Indraratna 2020b; Zhou et al. 2020; Zou, Chen & Zhang 2020).

Liu et al. (2020) investigated the migration of fines within the fabric of coarse particles in gap-graded soils using DEM coupled to CFD with the Navier Stokes equation. The influence of the confining pressure and the fines content was examined. The confining pressure at which the soil was compacted ranged from 50 kPa to 200 kPa, and the fines content ranged from 20% to 35%. For the analysis, micromechanical parameters such as the buckling of force chains and the release of strain energy under the influence of suffusion were considered. It was found that when fines contribute to the transfer of stress, i.e., fines content > 25%, the erosion of these fines causes the force chains to buckle and the original force transmission structure to collapse (Figure 2.18); this sudden collapse intensifies suffusion with the release of strain energy. These observations were more pronounced as the confining pressure increased. In contrast, samples with underfilled fabric and under-stressed fines were eroded through the soil fabric with little impact on the force network. In these structures, a higher confining pressure prevented suffusion from occurring.

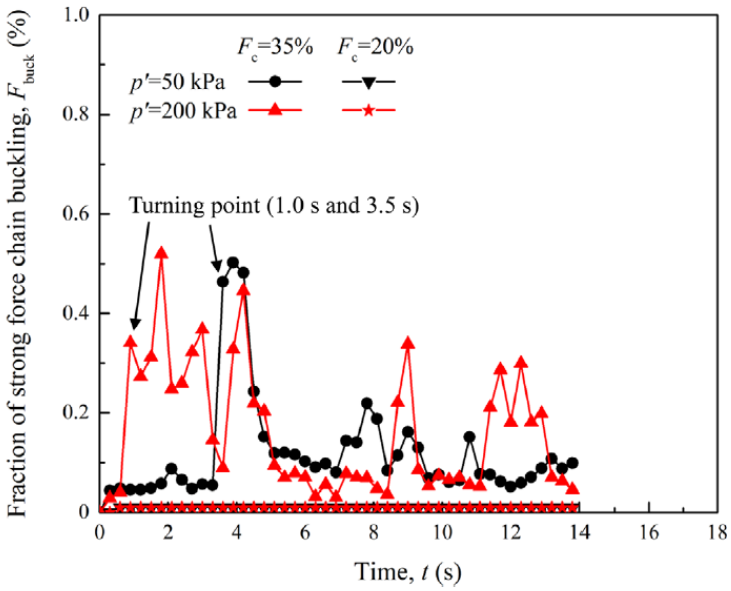

Fig. 2. 18 Percentage of buckling of strong force chains for samples with different fines content (Liu et al., 2020, by permission)

Hu et al. (2020) investigated the effect of suffusion on the undrained shear behaviour of an internally unstable soil using DEM-CFD coupling. Flow was induced in the upward direction through the granular assembly of the soil. Constant volume tests were carried out on the eroded and non-eroded specimens. Strain hardening and softening occurred in the non-eroded and eroded specimens. Shearing reduced the coordination number (Figure 2.19) and increased the equivalent intergranular void ratio. Fabric anisotropy was introduced through suffusion and shearing.

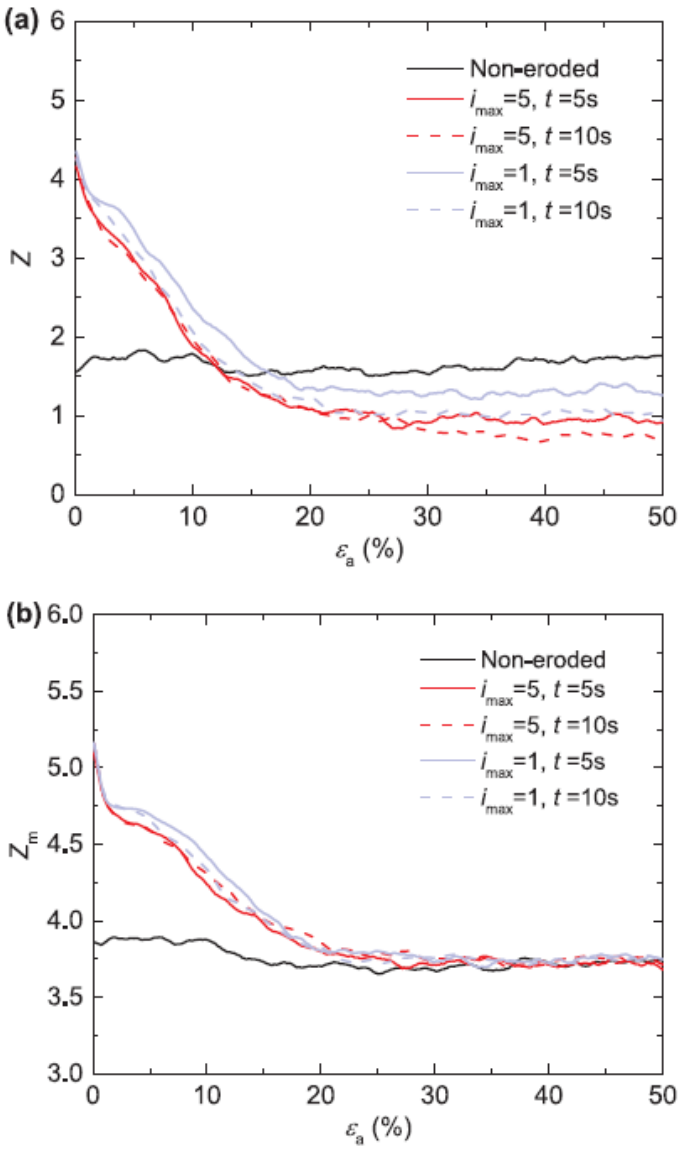

Fig. 2. 19 Evolution of (a) coordination number (b) mechanical coordination number during shearing (Hu et al. 2020, by permission)

Zou et al. (2020) studied the suffusion mechanism using coupled DEM-CFD. During suffusion with upward seepage, the varying flow rate, the evolution of distinct layers' porosity, and the temporal and spatial redistribution of particles in the sample were investigated. The results of the simulation showed that when Kenney and Lau's stability index was lower, the erosion ratio of fine particles was larger. The porosities across the layers of the sample changed continuously with the flow time (Figure 2.20). The fines

content of the lower layer decreased significantly, whereas the fines content of the upper layer decreased just somewhat.

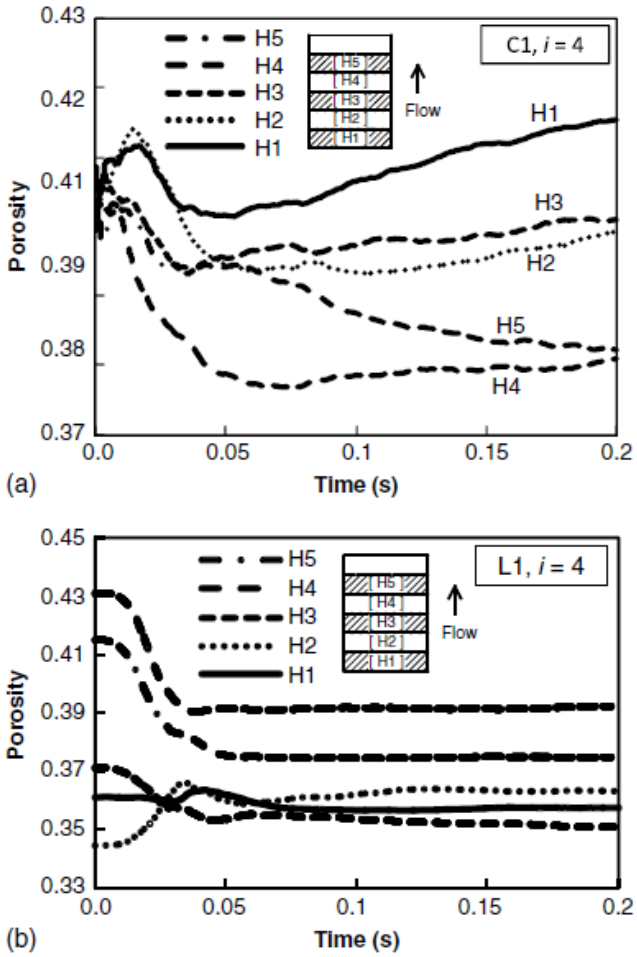

Fig. 2. 20 Porosities varying with time in different vertical layers across soil specimens (Zou et al., 2020, by permission)

Zhou et al. (2020) used coupled DEM and the Lattice Boltzmann Method (LBM) to study the evolution of internal erosion under various stress levels and hydraulic gradients. It was found that the hydraulic gradient and vertical stresses affect the porosities of the soils. Under hydraulic flow, granular materials were divided into erosion, stable, and compaction zones (Figure 2.21). As the hydraulic gradient was applied, the rattlers began to move with the flow, and the number of particles with a coordination number < 3 increased dramatically. Ballistic, caging, and diffusive erosion regimes were identified in the initial erosion phase. Indraratna et al. (2021) carried out investigations

with DEM coupled with LBM. They studied the number of contacts and the contact force distribution during fluid flow, but they did not propose a microscale criterion to distinguish soil from a stable to a liquid-like state.

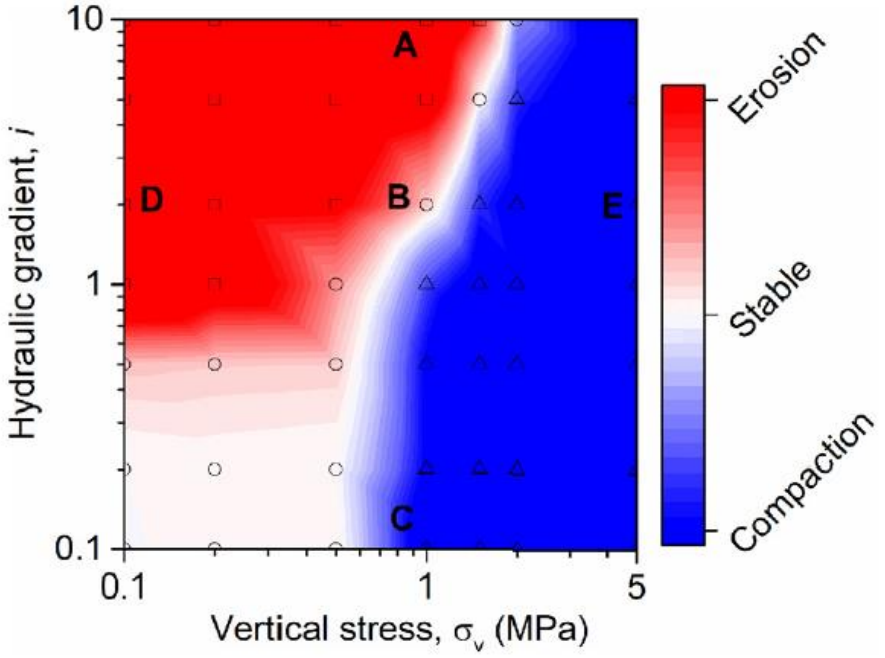

Fig. 2. 21 Three states of granular materials under hydraulic flow (Zhou et al. 2020, by permission)

Nguyen & Indraratna (2020) carried out simulations using DEM coupled to the Navier-Stokes equation. The hydraulic gradient was gradually applied to the soil specimen in an upward direction. The migration of particles, the rate of erosion, and the change in hydraulic conductivity during fluid flow were discussed. The influence of PSD, C_u, the friction coefficient, and the boundary conditions were evaluated; it was found that the onset of hydraulic failure was strongly influenced by the C_u, the friction coefficient, and the boundary conditions (Figure 2.22). Nguyen & Indraratna (2020b) further studied internal erosion through a novel concept of energy transformation. The DEM was coupled with CFD to model the fluid-particle interactions. The kinetic energies of the fluid and the particles were computed. They found that sufficient energy is lost as the fluid flows

through the soil, but a significant number of particles with low kinetic energy could migrate. The influence of PSD and porosity was also discussed.

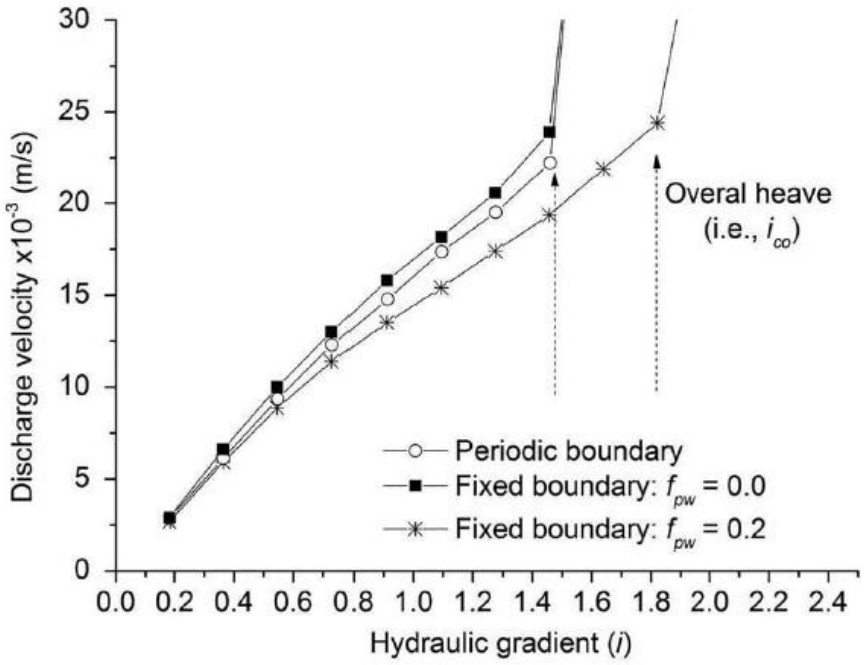

Fig. 2. 22 Influence of boundary conditions on the critical hydraulic gradient (Nguyen & Indraratna, 2020, by permission)

Although some of the studies discussed above have considered the micromechanical analysis of internal instability, the complex micromechanical behaviour of granular soils requires more insight. Furthermore, none of the studies could establish DEM-inspired criteria to evaluate fluidisation and internal instability. Table 2.1 summarises the various experimental and numerical studies on internal instability and fluidisation described above; this includes their limitations and whether or not they account for hydromechanical conditions and micromechanical analysis. The numerical studies described above usually combined the DEM to Navier-Stokes equations or the Boltzmann equation. These are the different approaches available to couple fluids to particles. Since it is vital to select an appropriate method for analysis in this study, the different approaches available are reviewed as follows:

Table 2. 1 Summary of various studies and their limitations

Reference	Macroscale criterion	Material susceptibility	Hydraulic conditions	Stress conditions	Microscale analysis
USACE (1953)	In a mixture of gravel and sand, a mixture with greater than 50% sand = stable	Yes	No	No	No
Istomina (1957)	$C_u \leq 10$, Stable $C_u \geq 20$, Unstable $10 \leq C_u \leq 20$, Transition	Yes	No	No	No
Lubochkov (1969)	The shape of the PSD curve determines the stability	Yes	No	No	No
Kezdi (1969)	Internal stability when $D_{15}^c/d_{85}^f \leq 4$	Yes	No	No	No
Kovacs (1981)	Capillary tube model	Yes	No	No	No
Kenney and Lau (1985)	Internal instability when $(H/F)_{min} \leq 1$	Yes	No	No	No
Chapuis (1992)	The slope of the PSD curve determines the stability	Yes	No	No	No
Burenkova (1993)	Different zones of internally stable and unstable soils	Yes	No	No	No
Honjo et al. (1996)	Internally unstable when gap ratio > 4	Yes	No	No	No
Liu (2005)	Fines < 25%, unstable Fines 25 to 35%, transition Fines > 35%, stable	Yes	No	No	No
Li & Fannin (2008)	Kezdi's ; finer content < 15% Kenney & Lau's; finer content > 15%	Yes	No	No	No
Indraratna et al. (2011)	if $D_{c35}^c/d_{85}^f > 0.82$, internally stable and if $D_{c35}^c/d_{85}^f < 0.73$, internally stable otherwise, transition zone.	Yes	No	No	No
Indraratna et al. (2015)	if $D_{c35}^c/d_{85}^f \leq 1$, internally stable	Yes	No	No	No
Israr & Indraratna (2017)	$D_{c35}^{cl}/d_{85}^f \leq 1$, internally stable	Yes	No	No	No

Reference	Macroscale criterion	Material susceptibility	Hydraulic conditions	Stress conditions	Microscale analysis
Terzaghi (1943)	$i_{cr} = \frac{\gamma'}{\gamma_w}$	No	Yes	Yes	No
Adel et al. (1988)	The critical hydraulic gradient was determined based on the loss rate of fine particles.	No	Yes	Yes	No
Skempton & Brogan (1994)	Relationship between $(H/F)_{min}$ and critical hydraulic gradient.	No	Yes	Yes	No
Wan & Fell (2004)	No mathematical relationship.	No	Yes	Yes	No
Liu (2005)	The slope of the hydraulic gradient and seepage velocity was used to define the critical hydraulic gradient.	No	Yes	Yes	No
Moffat (2005)	The critical hydraulic gradient was determined by local hydraulic gradient variations and visual observations.	No	Yes	Yes	No
Li & Fannin (2012)	The concept of a hydromechanical envelope was proposed.	No	Yes	Yes	No
Xiao & Shwiyhat (2012)	The geometric and mechanical properties considered were volume change, permeability, PSD and compressive strength.	No	Yes	Yes	No
Chang & Zhang (2013)	The hydraulic gradient for the particle motion initiation first increased with the shear stress ratio and then decreased as the stress reached the failure point.	No	Yes	Yes	No
Ke & Takahashi (2015)	No mathematical relationship.	No	Yes	Yes	No
Indraratna et al. (2017)	Critical hydromechanical envelopes were plotted.	No	Yes	Yes	No
Mehdizadeh et al. (2017)	N/A	No	Yes	Yes	No
Mehdizadeh et al. (2018)	N/A	No	Yes	Yes	No

Reference	Macroscale criterion	Material susceptibility	Hydraulic conditions	Stress conditions	Microscale analysis
Mehdizadeh et al. (2019)	N/A	No	Yes	Yes	No
Luo et al. (2020)	N/A	No	Yes	Yes	No
Shire & O'Sullivan (2013)	N/A	No	No	No	Yes
Shire et al. (2014)	N/A	No	No	Yes	Yes
Langroudi et al. (2015)	N/A	No	No	No	Yes
Shire et al. (2016)	N/A	No	No	Yes	Yes
Liu et al. (2020)	N/A	No	Yes	Yes	Yes
Hu et al. (2020)	N/A	No	Yes	Yes	Yes
Zou et al. (2020)	N/A	No	Yes	Yes	No
Zhou et al. (2020)	N/A	No	Yes	Yes	Yes
Nguyen & Indraratna (2020)	N/A	No	Yes	Yes	Yes
Nguyen & Indraratna (2020b)	N/A	No	Yes	Yes	Yes
Ahmadi et al. (2020)	N/A	No	No	Yes	Yes
Ahmadi et al. (2021)	N/A	No	No	Yes	Yes
Sufian et al. (2021)	N/A	No	No	Yes	Yes

2.6 FLUID-PARTICLE INTERACTION APPROACHES

Two approaches are available to couple fluids and particles; they are referred to as unresolved and resolved (Figure 2.23). A single fluid cell can hold multiple solid particles if a coupling is unresolved, i.e., the particle diameter is substantially less than the mesh size (Figure 2.23b). The interaction force between fluid and particles is calculated using the local porosity of the cell as well as the superficial slip velocity of the particles and the fluid (Hager 2014). Since the fluid phase has a low spatial resolution, it is challenging to compute the fluid-particle interactions directly. Therefore, these models require a closer relationship, so some correlations were used to compute the fluid-particle interaction forces. The biggest source of error with unresolved coupling is the average force experienced by the particles (Hager 2014; Third & Muller 2013). These unresolved approaches have been used in geomechanics (Nguyen & Indraratna 2016; Zhao & Shan 2013).

In resolved coupling, each solid particle contains several fluid cells, i.e., the particle diameter is larger than the mesh size and has several Langrangian points (Figure 2.23a). The hydrodynamic forces acting on the particle may be calculated by integrating the forces acting on the Langrangian points around the perimeter of the solid particle. The force on each particle is calculated separately. This resolved coupling can be a kind of Direct Numerical Simulation (DNS) (Hager 2014; Han, Feng & Owen 2007a; Third & Muller 2013).

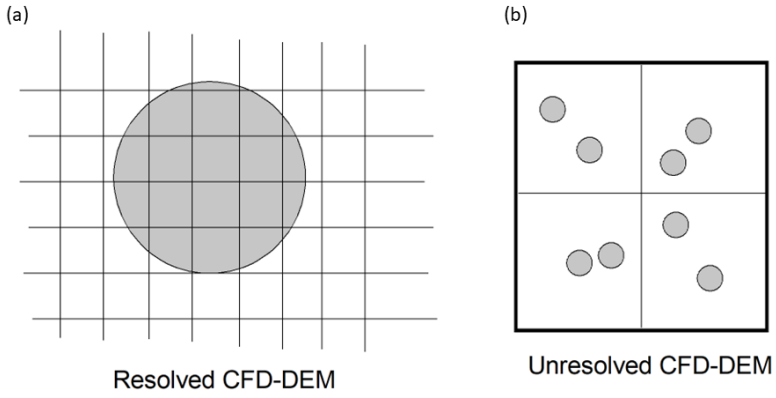

Fig. 2. 23 Resolved and unresolved approaches (modified after Hager, 2014)

2.6.1 Resolved Simulations

For the resolved simulations of the fluid-particle interaction, several methods based on the processing of the underlying mesh are available, namely (i) fixed mesh methods, and (ii) body-conformal mesh methods (Figure 2.24) (Haeri & Shrimpton 2012; Hager 2014). In the body-conformal mesh method, a discretization of space and time is first carried out. The solution is achieved by shifting it in time, starting from a certain initial state. With space discretization, the domain is sub-divided into control volumes; these control volumes are divided into two sub-groups, i.e., unstructured and structured meshes.

If the geometry is complex, then the unstructured mesh is the best choice, but it is complicated to generate. If the particles are stationary, the unstructured mesh is generated once around each particle, and then the solution is carried out. However, the entire domain is re-meshed at each time step when the particles are in motion. Re-meshing is a slow and complicated technique. Various other methods are also available in this category, namely Deforming-Spatial-Domain/Stabilized Space-Time (DSD/SST), Arbitrary-Langrangian-Eulerian (ALE), and Fictitious Boundary Method (FBM) (Figure 2.24). These methods are not suitable for simulating high-resolution 3D particular flow with many particles (Haeri & Shrimpton 2012). Note that this doctoral thesis only introduced the Body Conforming Mesh Methods, and the details are not elaborated here.

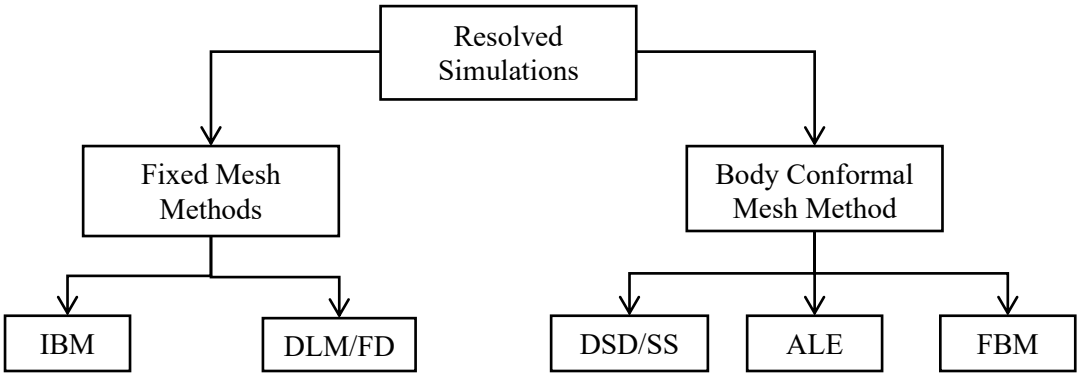

Fig. 2. 24 Categories of resolved simulations based on the treatment of underlying mesh (modified after Haeri & Shrimpton, 2012)

The fixed mesh methods are further divided into two categories, i.e., Immersed Boundary Method (IBM) and Distributed Lagrange Multiplier/Fictitious Domain (DLM/FD) (Figure 2.24). In the fixed mesh methods, the flow equations are solved on either a structured or unstructured mesh but with a stationary Eulerian grid. The object within the Eulerian domain is defined by adding Langrangian points to the surfaces of the objects; these Langrangian points may or may not coincide with the Eulerian grid, and they can move freely over the Eulerian mesh (Peskin 1972).

A non-slip condition at the boundary of the submerged object is considered to simulate the flow around them, regardless of whether the object is stationary or in motion. The fluid node has the same velocity as the solid node at the solid boundary for the moving objects, whereas with stationary objects, the fluid and solid nodes have zero velocity in all directions at the boundary of the object. An additional source term called the forcing term is introduced into the governing equations of fluid flow at these surface points of the object (Haeri & Shrimpton 2012). Coupling between the Langrangian marker points of the surface within the Eulerian grid is achieved by the force that the flow exerts on the marker points and the reaction force that the marker points exert on the fluid (Peng & Luo 2008).

2.6.1.1 Immersed boundary method (IBM)

IBM was originally introduced by Peskin (1972) to simulate fluid-particle interactions. In this method, the solid object within the fluid domain cuts through the fluid's mesh, so only the governing equations of the fluid near the boundary are modified. Therefore, a body force term is introduced into the fluid flow governing equation at predefined boundary points to enforce the boundary conditions at those points. IBM offers a number of benefits, including quick solutions due to the structured mesh; unstructured meshes are not required to discretize complicated geometries. Imagine a stream of liquid flowing around a body, as shown in Figure 2.25. The volume of the body is Ω_b with boundary Γ_b and the surrounding fluid is represented by Ω_f.The governing equations for the fluid are written in terms of Navier-Stokes equations as (Mittal & Iaccarino 2005):

$$\frac{\partial \vec{u}}{\partial t} + \vec{u}.\nabla\vec{u} + \frac{1}{\rho}.\nabla p - \frac{\mu}{\rho}\nabla^2\vec{u} = 0 \tag{2.9}$$

$$\nabla\vec{u} = 0 \tag{2.10}$$

The above equations only apply to the fluid domain represented by Ω_f. To include the boundary of the immersed object, the following equations must be modified at the boundary Γ_b as:

$$\vec{u} = \vec{u}_\Gamma \tag{2.11}$$

where $\vec{u}$ = the fluid velocity, p = the pressure, and ρ and μ = the density and viscosity, respectively.

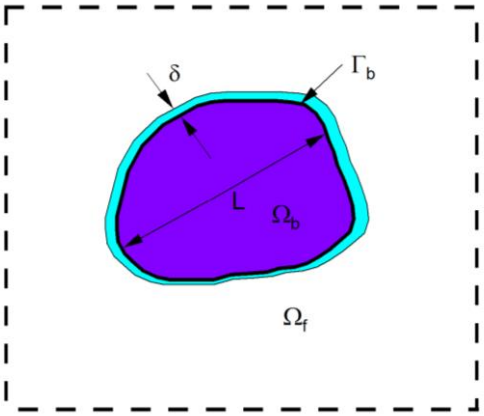

Fig. 2. 25 Schematic diagram showing a generic body around which the flow is to be simulated (modified after Mittal & Iaccarino, 2005)

In the Body Conformal Mesh Methods, Equations 2.9 and 2.10 are discretized for the fluid domain and the boundary conditions, i.e., Equation 2.11 at the immersed boundary Γ_b is enforced directly. While in the immersed boundary method, Equations 2.9 and 2.10 are discretized on a Cartesian grid. By changing these equations, the boundary conditions can be enforced indirectly. In most cases, this adjustment takes the form of a source term in the governing equation called a forcing term that reproduces the boundary effect. There are two approaches to applying these forcing terms. The "continuous forcing approach" is the first approach; the forcing element is incorporated into the continuous governing Equations 2.9 and 2.10, resulting in equations of the form:

$$\mathcal{L}\underline{U} = \underline{f_b} \tag{2.12}$$

where $\mathcal{L}$ = the operator representing the Navier-Stokes equations as in Equations 2.9 and 2.10. Equation 2.12 is then applied to the entire domain, i.e., $\Omega_b + \Omega_f$. Note that $\underline{f_b} = (f_m, f_p)$, where f_m and f_p = the forcing term applied to the momentum and pressure, respectively. Equation 2.10 is then discretized on a Cartesian grid, which can be written as:

$$\{L\}\{\underline{U}\} = \left\{\underline{f_b}\right\} \tag{2.13}$$

The system of equations, i.e., Equation 2.13, is then solved over the entire domain.

The discrete forcing technique is the second method, and it involves discretizing the governing equations on a Cartesian grid without taking into account the immersed boundary, as follows:

$$\{L\}\{\underline{U}\} = 0 \tag{2.14}$$

After discretization, the equations near the immersed boundary are adjusted to account for its presence resulting in a modified system of equations as follows:

$$\{L'\}\{\underline{U}\} = \{\underline{r}\} \tag{2.15}$$

which are then solved on the Cartesian grid, where $\{\underline{r}\}$ represents the known terms associated with the boundary condition on the immersed surface.

The two approaches are connected; the above equation is written as follows:

$$\{L\}\{\underline{U}\} = \{\underline{f_b}'\} \tag{2.16}$$

where,

$$\{\underline{f_b}'\} = \{\underline{r}\} + \{L\}\{\underline{U}\} - \{L'\}\{\underline{U}\} \tag{2.17}$$

2.6.2 Resolved Simulations Using the Lattice Boltzmann Method (LBM)

Fluid flows can be simulated at different scales, i.e., microscopic, mesoscopic, and macroscopic. The Navier-Stokes (NS) equations are the basis of fluid flows at the macroscopic scale and can be solved using either the Finite Element Method (FEM), the Finite Difference Method (FDM), or the Finite Volume Method (FVM) because they are complicated to be solved by analytical methods (Bao & Meskas 2011). The simulation of fluid flows can be done at the microscopic scale by Molecular Dynamics (MD) by solving Hamilton's equation. However, identifying the location and velocity of each particle by the MD method is complex and requires enormous computations. The Lattice Boltzmann Method (LBM) closes the gap between macro and micro scales; it is a modern method in

Computational Fluid Dynamics (CFD) and is based on the kinetic theory of gases and models the system on a mesoscopic scale.

The macroscopic fluid behaviour results from the collective behaviour of microscopic particles (Bao & Meskas 2011; Chen & Doolen 1998). LBM has evolved from the Lattice Gas Automata (LGA) method, which is a simplified fictitious MD model in which space, time, and particle velocities are all discrete. Unlike standard CFD techniques, LBM models the fluid as a collection of notional particles that propagate and collide sequentially (Chen & Doolen 1998). LBM does not mimic detailed particle motion like particle-based approaches such as MD and Direct Simulation Monte Carlo (Chen & Doolen 1998; Noble & Torczynski 1998). In NS equations, fluid is described in terms of macroscopic quantities, e.g., velocity and pressures, while in LBM, the velocity and pressure are computed as the momentum of particles. The NS equations can be recovered from Lattice Boltzmann (LB) equations using the Chapman-Enskog expansion (Bhatnagar, Gross & Krook 1954).

The Lattice Boltzmann Method (LBM) has been effectively employed for Direct Numerical Simulations (DNS) (i.e., resolved simulations) of particle flow systems, unlike the standard Computational Fluid Dynamics (CFD). Researchers have used several thousand to millions of spherical particles with LBM. This approach may also be used to address non-spherical objects, such as the movement of blood cells and the motion of elongated particles (Rettinger & Rüde 2017). Several approaches are available for fluid-particle coupling with LBM, (i) Partially Saturated Cells Method (PSM), (ii) Momentum Exchange Method (MEM), and (iii) methods based on Langrangian marker points such as IBM.

2.6.2.1 Momentum exchange method (MEM)

Ladd (1994) proposed the momentum exchange method with the basic idea that when solid particles are placed within the fluid domain, some links between the lattice nodes are cut by the boundary surface. The fluid particles travelling down these links interact with the solid surface at the boundary nodes, which are situated halfway along these links. This results in a discrete representation of the particle surface that becomes increasingly precise as the particle size grows. This method maps the particles at each time step when they are in motion. The approach used in this method is similar to the bounce-back boundary condition where the particles travelling from the fluid node to the solid node are bounced back with additional momentum, depending on particle velocity. The force and torque on the particle are then computed by summing over the momentum transfer across the boundary. This method is computationally efficient, but when a particle travels, the cells originally covered with the solid domain that convert back to the fluid require a consistent reconstruction of missing particle distribution function information. As a result, the interaction forces and pressures oscillate (Rettinger & Rüde 2017).

2.6.2.2 Partially saturated cells method (PSM)

PSM was first proposed by Noble & Torczynski (1998) and was then used by Seil & Pirker (2016) to develop an open-source code called LBDEM coupling. Han & Cundall (2017) used the same method to couple the Particle Flow Code (PFC) 2D and 3D with LBM. The Immersed Moving Boundary (IMB) technique, which differs from the momentum exchange method, is another name for this methodology.

At each time step, instead of mapping the object, the local solid volume percentages for each computational cell are determined. The LBM collision operator is then modified, and the hydrodynamic forces are evaluated using this solid volume fraction (Noble & Torczynski 1998; Rettinger & Rüde 2017). The involvement of solid particles

within the fluid can be achieved by introducing an additional collision term into the original LBM equation to account for the interaction of fluid particles with nodes that overlap with solids. This approach shifts the hydrodynamics very smoothly between the fluid and solid nodes.

Each time step is divided into two further sub-steps in the LBM: collision and streaming/propagation. In the collision phase, the particles in a lattice collide and transfer momentum to one another. The distribution function of each particle carries the momentum transfer information. While the streaming/propagation phase is the post-collision phenomenon, the new distribution functions of the particles have shifted to the neighbouring nodes.

2.6.3 Unresolved Simulations

When the behaviour of a large number of particles is of interest, unresolved simulations are chosen. The mesh cell is much larger than the particle sizes, and a cell can contain several particles (Tsuji, Tanaka & Ishida 1992). Coupling the fluid to the particle is achieved by a particle-fluid interaction force at a continuum scale for the fluid and individual particle levels for the solid phase. The Discrete Element Method (DEM) describes the motion of particles (Cundall & Strack 1979). The flow of the fluid by the local averaged Navier-Stokes equations. Two formulations are available; they are referred to as model *A* and model *B*. The decrease in pressure is distributed by the fluid and the particle in model *A*, but only the fluid phase in model B. However, both models do not provide many different results. Model *A* is explained here which is given as follows (Zhou et al. 2010):

Conservation of mass equation:

$$\frac{\partial n}{\partial t} + \nabla.\left(nu_f\right) = 0 \tag{2.18}$$

Conservation of momentum equation:

$$\frac{\partial(\rho_f n u_f)}{\partial t} + \nabla.\left(\rho_f n u_f u_f\right) = -n\nabla p - f_p + \nabla.(n.\tau) + \rho_f n g \tag{2.19}$$

where n = porosity of the cell, u_f = fluid velocity, p = fluid pressure, τ = viscous fluid stress tensor, ρ_f = fluid density, f_p = force exerted on the fluid cell by the particles. The computation of f_p can be obtained as follows:

$$f_{p,o} = \sum_{i=1}^{n_{p,o}} \varpi_{i,o}\left(\frac{F_{p,i}}{V_{c,o}}\right) \tag{2.20}$$

where $n_{p,o}$ = total number of particles in cell o, $\varpi_{i,o}$ = weight factor, which is the ratio of the volume of the particle i to the cell's total volume o; it has values ranging from 0 to 1; if the particle covers the cell completely, then its value would be 1, and $F_{p,i}$ = total force acting on particle i.

The particle-fluid interaction force on the individual particle i can be written as (Zhou et al., 2010)

$$F_{f,i} = F_{d,i} + F_{\nabla p,i} + F_{\nabla \tau,i} + F_{vm,i} + F_{B,i} + F_{Saff,i} + F_{mag,i} \tag{2.21}$$

where $F_{pf,i}$ = total fluid-particle interaction force, $F_{d,i}$ = drag force, $F_{\nabla p,i}$ = pressure gradient force, $F_{\nabla \tau,i}$ = viscous force, $F_{vm,i}$ = virtual mass force, $F_{B,i}$ = Basset force, $F_{Saff,i}$ = Saffman force and $F_{mag,i}$ = Magnus force. Different authors have proposed different correlations to compute the various forces in the above equation, summarized in Zhou et al. (2010). The correlations of some of the most common forces are given as:

De Felice's solution gives the drag force on the particle and is given as (Nguyen & Indraratna 2016):

$$F_{d,i} = \frac{1}{8} C_{d,i} \rho_f \pi D_{p,i}^2 n_o^2 \left(u_{f,o} - u_{p,i}\right)\left|u_{f,o} - u_{p,i}\right| n_o^{-\chi} \tag{2.22}$$

where $C_{d,i}$ = drag coefficient of the fluid-particle system, ρ_f = fluid density, D_p = diameter of the particle, $u_{f,o}$ = average fluid velocity of cell o, $u_{p,i}$ = velocity of particle i residing

in cell o, $n_o^{-\chi}$ = a porosity function which considers the presence of other particles in the cell with power factor χ being a function of Reynold's number and is given as:

$$\chi = 3.7 - 0.65\, exp\left[-\frac{\left(1.5 - log_{10} R_{e_{p,i}}\right)^2}{2}\right] \tag{2.23}$$

The Reynold's number can be given by:

$$R_{e_{p,i}} = \frac{n_o \rho_f D_{p,i} \left|u_{f,o} - u_{p,i}\right|}{\mu_f} \tag{2.24}$$

$C_{d,i}$ is also related to the particle Reynolds number and can be given as follows:

$$C_{d,i} = \left(0.63 + \frac{4.8}{\sqrt{R_{e_{p,i}}}}\right)^2 \tag{2.25}$$

The pressure gradient force can be divided into (i) the buoyancy force $F_{b,i}$ (ii) and the acceleration pressure gradient force $F_{\nabla p,i}$ due to difference in pressure of flowing fluid:

$$F_{b,i} = -\rho_f g V_{p,i} \tag{2.26}$$

$$F_{\nabla p,i} = -(\nabla . p) V_{p,i} \tag{2.27}$$

where ρ_f = fluid density, g = gravitational acceleration, $V_{p,i}$ = volume of particle i.

Viscous forces can be computed by using the following relationship:

$$F_{\nabla \tau,i} = -(\nabla . \tau) V_{p,i} \tag{2.28}$$

The motion of individual particles is governed by the DEM proposed by Cundall & Strack (1979) and is given as follows:

$$m^p \frac{dv^p}{dt} = f_g^p + \sum_{c=1}^{N_c^p} f_j^c \tag{2.29}$$

$$I^p \frac{dw^p}{dt} = \sum_{c=1}^{N_c^p} T_j^c \tag{2.30}$$

where m^p and I^p are the mass and the moment of inertia of the particle p, and v^p and w^p are the translational and angular velocities of the particle p, N_c^p is the total number of contacts on the particle p, f_j^c is the contact force vector in the j^{th} direction at contact c on the particle p, T_j^c is the torque that acts on the particle p due to the tangential contact force at contact c, and f_g^p is the gravitational force on the particle p.

This discussion shows that since the biggest error source in unresolved simulations is the average force experienced by the particles from the fluid; therefore, the resolved simulations with the Lattice Boltzmann Method (LBM) are used in this study. LBM is considered to be a modern approach that is relatively new to the field of geomechanics; as such, it has only been used in a limited number of studies (Han & Cundall 2017; Indraratna, Phan, et al. 2021).

2.7 IDENTIFICATION OF RESEARCH GAPS

Various macroscale criteria for evaluating the internal instability potential based on the experimental investigations have been proposed in the literature. Micromechanical analyses have also been carried out using DEM or DEM-CFD/LBM. However, the complex micromechanical analysis of internally stable and unstable soils demands further insights; none of these studies could address the following research gaps:

- Internal instability was studied at the continuum scale using experimental investigations, and several empirical methods were proposed. However, internal instability is a problem at the micro/particle scale. Several studies were conducted to investigate internal instability at the particle scale using DEM, but none of them could demarcate the clear boundaries between internally stable and unstable soils based on parameters such as the coordination number and stress reduction factor that are obtained directly from the particle scale data. Therefore, there is a need to delineate

distinct boundaries to distinguish internally stable and unstable soils based on these microscale parameters using DEM.

- Several studies carried out microscale analyses of internally stable and unstable soils but under isotropic stress conditions using DEM. Limited microscale analyses under anisotropic stress state due to shear-induced deformation were carried out, but none of them investigated how the samples could transition from an internally stable to an unstable state due to shear-induced deformation by taking soil micromechanics into account. This is why this study investigates parameters such as the coordination number, the partial coordination number, sliding contacts, and the stress reduction factor due to shear-induced deformation of the soil specimen and gives a whole new perspective.
- Fluidisation or mud pumping was studied at a macroscale level using traditional experimental investigations. However, the changes in the fabric at a microscale could trigger the fluidisation of soil, and that has not yet been studied. Therefore, DEM, coupled with LBM, considered an emerging fluid-particle interaction approach, can be used to model the initiation of fluidisation at the microscale using parameters such as the coordination number and constraint ratio. Therefore, this study uses DEM-LBM and considers microscale parameters such as the coordination number, constraint ratio, sliding index, lost contacts, and contact force distribution to model the initiation of fluidisation at a microscale.

2.8 SUMMARY AND CURRENT RESEARCH FOCUS

In summary, internal instability is a phenomenon that changes the hydraulic and mechanical properties of soils. Since internal instability is a particle scale phenomenon, the DEM (Cundall & Strack 1979) can be used to study this phenomenon. DEM has previously been used to study internal instability (Hu, Zhang & Yang 2019; Langroudi,

Soroush & Shourijeh 2015; Nguyen & Indraratna 2020b; Shire et al. 2014; Zou, Chen & Zhang 2020). Shire et al. (2014) studied the stress distribution in gap-graded soils using DEM simulations. The stress distribution was affected by the PSD, relative density and the percentage of cohesionless fines. Langroudi et al. (2015) studied the micromechanical behaviour of internally stable and unstable soils using DEM. The gap-graded and concave-up gradations exhibited low connectivity of the particles.

Similarly, Liu et al. (2020) investigated the migration of fine particles within the fabric of coarse particles in gap-graded soils using DEM coupled to Computational Fluid Dynamics (CFD) with the Navier Stokes equation. Hu et al. (2020) investigated the effect of suffusion on the undrained shear behaviour of internally unstable soil using DEM-CFD. Zou et al. (2020) studied the suffusion mechanism using coupled DEM-CFD. The simulation results showed that the erosion ratio of the fine particles was larger when Kenney and Lau's stability index was lower. Nguyen & Indraratna (2020) studied internal erosion through a novel concept of energy transformation. Sufian et al. (2021) studied the effect of stress-induced anisotropy on the gap-graded bimodal samples using DEM. The main focus of this thesis is to establish micromechanically inspired criteria for checking the internal instability and fluidisation of soils. DEM combined with LBM is used in this study to achieve the objectives outlined in Chapter 1, based on the research gaps mentioned above.

CHAPTER 3 RESEARCH METHODOLOGY

3.1 INTRODUCTION

Literature reveals that extensive laboratory investigations have been carried out to check the internal instability and fluidisation of cohesionless soils (Indraratna et al. 2020; Israr & Indraratna 2017; Mehdizadeh et al. 2017; Xiao & Shwiyhat 2012). Although these tests were usually used to study the behaviour of soils at the continuum scale, microscale particle interactions have not been studied in detail. Soil is a particulate material, so it should be modelled at particle scale or microscale to gain further insights (O'Sullivan 2011) because microscale interactions between particles strongly influence soil behaviour at a continuum scale.

Recent advances in computational modelling have helped simulate soil at the microscale using the Discrete Element Method (DEM) (Cundall & Strack 1979). DEM is a viable tool for modelling soil at the microscale and has been widely used (Ahmadi et al. 2020; Shire et al. 2014). DEM is typically coupled with Computational Fluid Dynamics (CFD) to model the interaction between the fluid and the particles (Nguyen & Indraratna 2020b). Several approaches available for coupling fluids and particles have been described in detail in Chapter 2. The analyses in this doctoral thesis were carried out using DEM and its coupling to the Lattice Boltzmann Method (LBM), a comparatively new fluid-particle interaction tool used in geomechanics. The fluid-particle interaction was carried out using the method proposed by Noble & Torczynski (1998), who modified the fluid equation to account for the solid fraction of the particles. This chapter describes the DEM, the fundamental characteristics of the contact model, boundary conditions, the governing equations and their numerical approximations, and the coupling between DEM and LBM.

3.2 DISCRETE ELEMENT METHOD

The Discrete Element Method (DEM) was originally proposed by Cundall & Strack (1979) to solve rock mechanics problems. It considers the particulate nature of soil, where particles are modelled in a discrete manner, and it can reproduce the macroscale response of the soil. It also provides microscale parameters that are not easy to determine from the experimental investigations. It uses an explicit finite difference system as a numerical scheme in which particle interaction is treated as a transient problem. The contact forces are found from the force-displacement law using the particle displacements. The motion of the particles resulting from the contact forces is obtained by Newton's 2nd law as follows:

$$m^p \frac{dv^p}{dt} = f_g^p + \sum_{c=1}^{N_c^p} f_j^c \tag{3.1}$$

$$I^p \frac{dw^p}{dt} = \sum_{c=1}^{N_c^p} T_j^c \tag{3.2}$$

where m^p and I^p are the mass and the moment of inertia of the particle p, v^p and w^p are the translational and angular velocities of the particle p, N_c^p is the total number of contacts on the particle p, f_j^c is the contact force vector in the j^{th} direction at contact c on the particle p, T_j^c is the torque that acts on the particle p due to the tangential contact force at contact c, and f_g^p is the gravitational force on the particle p. Figure 3.1 shows the flow chart of the DEM algorithm. The parameters required to run a DEM simulation are listed in Table 3.1.

Table 3. 1 Required parameters to run a DEM simulation

	Parameter	**Units**
Geometric parameters	Number of particles	-
	Particle Size Distribution	-
	Dimensions and shape of the domain	m
Contact Parameters	Young's modulus	N/m^2
	Density of particles	Kg/m^3
	Poisson's ratio	-
	Coefficients of friction	-
Characteristic times	Strain rate	s^{-1}
Other parameters	Applied pressure	N/m^2

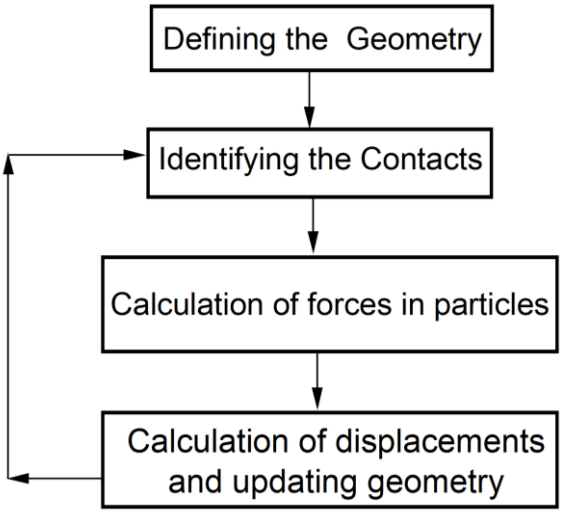

Fig. 3. 1 Flow chart of the DEM algorithm

3.2.1 Time Step and Stability

The DEM is conditionally stable because it uses a finite-difference integration scheme, and therefore the time step must be small enough to achieve stability. Various approaches are available to define a critical time step. According to Cundall & Strack (1979), the

critical time step (Δt_{crit}) is estimated based on a system with a single degree of freedom of mass m that is connected to the ground by a stiffness spring K, it is given as follows:

$$\Delta t_{crit} = 2\sqrt{\frac{m}{K}} \tag{3.3}$$

Moreover, according to ITASCA, a safety factor of 0.8 should be multiplied by the critical time step, which was re-calculated by O'Sullivan (2011) using Rayleigh's theorem, as follows:

$$\Delta t_{crit} = 0.22\sqrt{\frac{m}{K}} \tag{3.4}$$

The mass of the soil particles can be scaled up to increase the time step, but this increases particles inertia. Mass scaling is not advised if a high frequency response is needed (O'Sullivan 2011), which is why this thesis never used mass or density scaling. Strain rates are selected by having the inertial number less than 7.9 x 10^{-5} (Perez et al. 2016). The capability of the contact detection algorithm to effectively detect the formation and loss of contacts between particles is also related to the appropriate choice of the time step. Having a large time-step means variations in the current contact of the particle assembly may alter dramatically, and the contact detection algorithm may not identify them; as a result, the predicted particle response may be altered.

3.2.2 Fundamental Characteristics of Contact Model

Figure 3.2 shows the rheological scheme and schematic sketch of the Hertz-Mindlin contact model used to simulate the internal instability and fluidisation of soil. The tangential contact force (f^T) is based on the work of Mindlin & Deresiewicz (1989) and Hertzian contact theory is the basis of the normal contact force (f^N). The f^N and f^T have nonlinear spring and damping components. The normal and tangential damping coefficients (c_n and c_t) are related to the restitution coefficient, as reported by Tsuji et al. (1992).

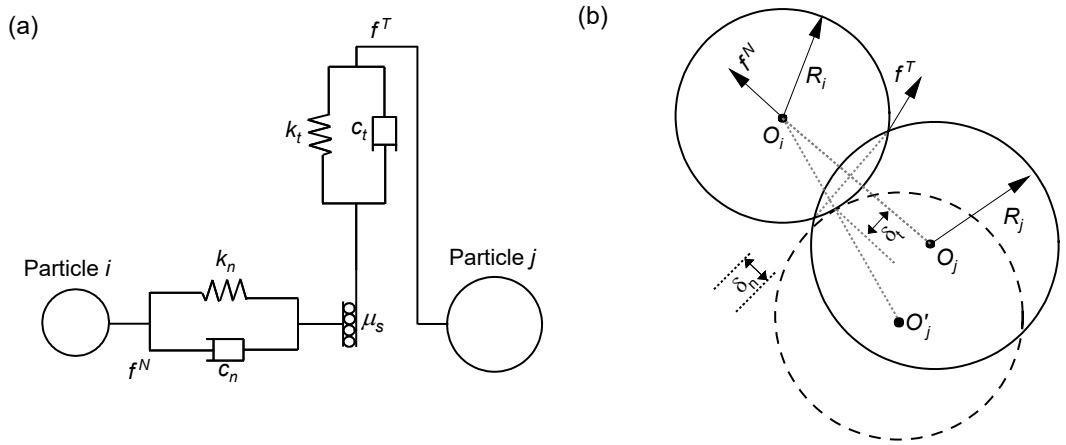

Fig. 3. 2 (a) Rheological scheme and (b) schematic sketch of the Hertz-Mindlin contact model used to simulate soil specimen fluidisation and internal instability

The tangential frictional force follows Coulomb's friction law (Cundall & Strack 1979).

$$f^N = k_n \delta_n - c_n v_n^{rel} \tag{3.5}$$

Where c_n is the viscoelastic damping constant for normal contact, k_n is the elastic constant for normal contact, δ_n is the normal component of the displacement at the contact, as represented by the overlap distance, v_n^{rel} is the normal component of the relative velocity of two spherical particles, and k_n is given by:

$$k_n = \frac{4}{3} E^* \sqrt{R^* \delta_n} \tag{3.6}$$

where E^* is the equivalent Young's modulus and R^* is the equivalent radius which can be written as follows:

$$\frac{1}{R^*} = \frac{1}{R_i} + \frac{1}{R_j} \tag{3.7}$$

$$\frac{1}{E^*} = \frac{1 - \nu_i^2}{E_{y_i}} + \frac{1 - \nu_j^2}{E_{y_j}} \tag{3.8}$$

where R_i and R_j are the radius, E_{y_i} and E_{y_j} are Young's modulus, and ν_i and ν_j are the Poisson's ratio of each neighbouring sphere in contact. The viscoelastic damping constant (c_n) is given by:

$$c_n = -2\sqrt{\frac{5}{6}}\ \beta\sqrt{S_n\, m^*} \quad \geq 0 \tag{3.9}$$

where, m^* is the equivalent mass and is given by:

$$\frac{1}{m^*} = \frac{1}{m_i} + \frac{1}{m_j} \tag{3.10}$$

β and S_n are given by:

$$\beta = \frac{ln\, e_r}{\sqrt{ln^2 e_r + \pi^2}} \tag{3.11}$$

$$S_n = 2E^*\sqrt{R^*\delta_n} \tag{3.12}$$

where e_r is the coefficient of restitution. The tangential contact force (f^T) is given by:

$$f^T = k_t\delta_t - c_t v_t^{rel} \tag{3.13}$$

where k_t is the elastic constant for tangential contact, c_t is the viscoelastic damping constant for tangential contact, δ_t is the tangential overlap, and v_t^{rel} is the tangential component of the relative velocity of two spherical particles, and k_t is given by:

$$k_t = 8G^*\sqrt{R^*\delta_n} \tag{3.14}$$

with G^* as the equivalent shear modulus, and c_t is written as follows:

$$c_t = -2\sqrt{\frac{5}{6}}\ \beta\sqrt{k_t\, m^*} \quad \geq 0 \tag{3.15}$$

The f^T is limited by:

$$f^T = \mu_s\, f^N \tag{3.16}$$

where μ_s is the coefficient of sliding friction.

3.2.3 Types of Boundary Conditions Used

The boundary conditions that a soil sample experiences in the field or during laboratory tests can be simulated with a variety of boundary types. In this current study, rigid frictional walls and periodic boundary conditions were used (Figure 3.3). Frictional walls are used to simulate the fluidisation of soil specimens using DEM coupled with LBM. The most commonly used boundary types are rigid boundaries with frictional walls (O'Sullivan 2011). These rigid boundaries might be flat or curved, and they are analytically specified surfaces. Inclusions or machinery interacting with the granular material can also be simulated using rigid boundaries. Periodic boundaries are used to simulate internal instability using DEM. Since boundary effects are neglected when using periodic boundaries, the number of particles can be reduced, which means computing time can be saved because smaller samples are required. Second, the uniform strain field is intended to prevent the formation of localization during shear, thus ensuring the samples remain homogeneous until they reach a critical state.

3.2.4 The Quasi-Static Condition

When the response of the particle system becomes independent of the rate of loading, quasistatic conditions are reached. Under quasi-static conditions, the inertial forces are negligible compared to the contact forces from the applied loads. Therefore, in order to achieve quasi-static conditions, the kinetic energy of the particle systems should be small enough to ensure it does not affect the overall mechanical behaviour. A dimensionless inertial number (I_n) is used to confirm the quasi-static conditions (Da Cruz et al. 2005).

$$I_n = \dot{\varepsilon}\, d_{avg} \sqrt{\frac{\rho}{p'}} \tag{3.17}$$

where $\dot{\varepsilon}$ is the strain rate, d_{avg} is the average diameter of the PSD, and p' is the effective mean stress. The limiting value of I_n for the quasi-static isotropic compression should be less than 7.9 x 10^{-5} (Perez et al. 2016).

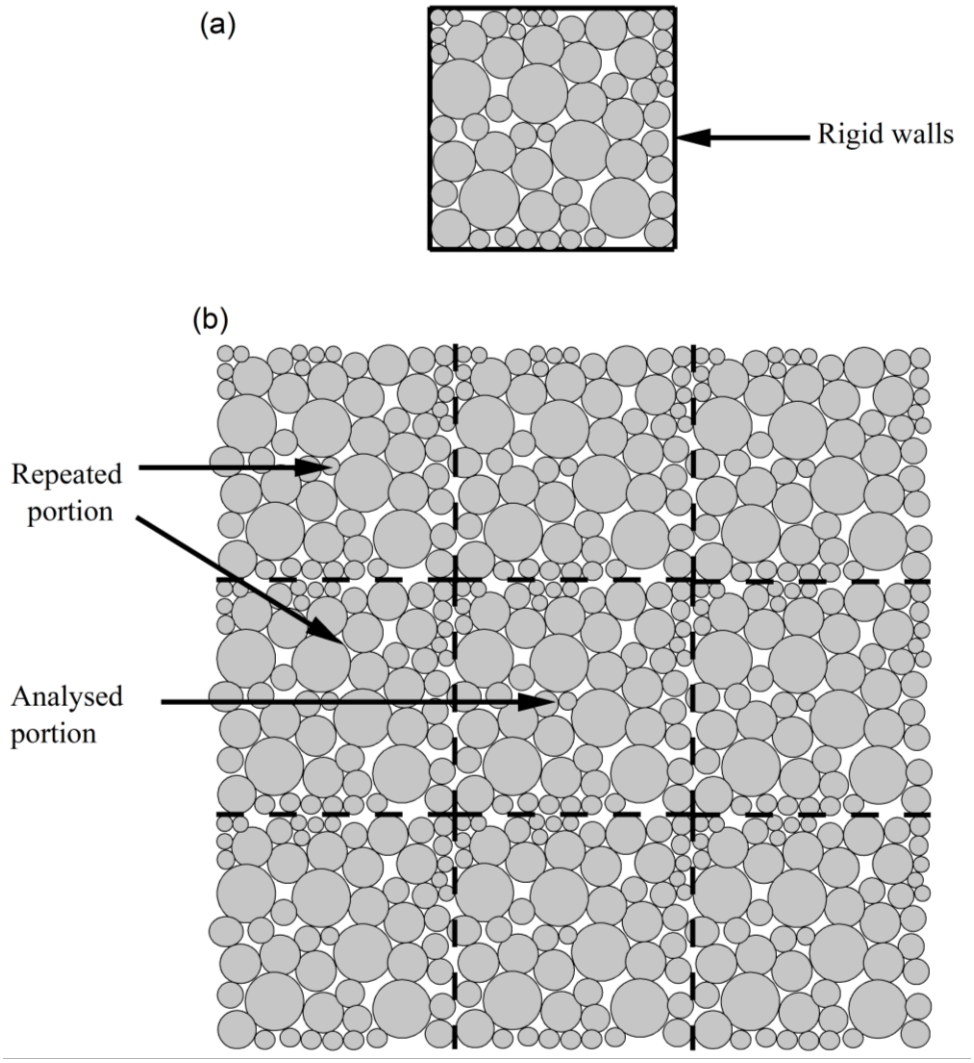

Fig. 3. 3 (a) Rigid boundaries, (b) periodic boundaries (modified after O'Sullivan, 2011)

3.3 DEM COUPLED WITH THE LATTICE BOLTZMANN METHOD

In order to simulate fluid-particle interaction, the DEM is coupled to the Lattice Boltzmann Method (LBM). The Navier-Stokes' (NS) equations are the basis of fluid flows at a macroscopic scale, which can be solved by either the finite element, finite difference or finite volume method. The Lattice Boltzmann Method (LBM), which is considered to be a modern approach in Computational Fluid Dynamics (CFD), bridges

the gap between macro and micro scales because it is based on the kinetic theory of gases and models the fluid on a mesoscopic scale. Macroscopic fluid behaviour is the result of the collective behaviours of microscopic particles (Bao & Meskas 2011; Chen & Doolen 1998). Unlike molecular dynamics, LBM does not simulate detailed particle motion (Chen & Doolen 1998; Noble & Torczynski 1998). The theoretical formulations of the LBM coupled with the DEM approach are described as follows:

3.3.1 Fluid Equations

The governing Boltzmann equation is written as (Chen, Martínez & Mei 1996):

$$\frac{\partial f_\alpha(x,t)}{\partial t} + e_\alpha^v \nabla f_\alpha(x,t) = \Omega_\alpha \qquad (\alpha = 1,2,\dots\dots\dots\dots,N) \tag{3.18}$$

where $f_\alpha(x,t)$ is the particle distribution function in the α direction, e_α^v is the microscopic fluid velocity and Ω_α is the collision operator which considers the transfer of momentum between the particles during collision, and t is the time. Equation (3.18) can be discretized on a regular lattice using a unique finite difference method, and the lattice-Boltzmann equation with the Bhatnagar-Gross-Krook (BGK) collision operator for a Newtonian fluid is written as (Bhatnagar, Gross & Krook 1954; Chen, Martínez & Mei 1996):

$$f_\alpha(x + e_\alpha^v \Delta t, t + \Delta t) - f_\alpha(x,t) = {\Omega_\alpha}^{BGK} \tag{3.19}$$

where ${\Omega_\alpha}^{BGK}$ is the BGK collision operator, and Δt is the time-step. Equation (3.19) ensures the conservation of mass and momentum at each lattice node. For each direction of the lattice nodes, the particle distribution function ($f_\alpha(x,t)$) defines the proportion of particles moving with velocity e_α^v at time t along the α direction of the node at position x.

Each time step is split into streaming and collision sub-steps, where the collision step is written as:

$$f_\alpha(x,t^*) = f_\alpha(x,t) + {\Omega_\alpha}^{BGK} \tag{3.20}$$

$f_\alpha(x, t^*)$ and $f_\alpha(x, t)$ are the particle distribution functions after and before the collision, respectively, and t^* is the time after the collision. In the streaming step, the $f_\alpha(x, t^*)$ is propagated over the lattice grid as follows:

$$f_\alpha(x + e_\alpha^v \, \Delta t, t + \Delta t) = f_\alpha(x, t^*) \tag{3.21}$$

The ${\Omega_\alpha}^{BGK}$, through which momentum transfer occurs between the particles when they collide, is given by (Bhatnagar, Gross & Krook 1954):

$${\Omega_\alpha}^{BGK} = -\frac{\Delta t}{\tau}\left(f_\alpha(x, t) - f_\alpha^{eq}(x, t)\right) \tag{3.22}$$

where $f_\alpha^{eq}(x, t)$ is the equilibrium distribution function, τ is the relaxation time, and is related to the kinematic viscosity (ν_f) of the fluid, the lattice spacing (Δx), and the time step (Δt) by the following relationship:

$$\nu_f = \frac{1}{3}\left(\tau - \frac{1}{2}\right)\frac{\Delta x^2}{\Delta t} \tag{3.23}$$

Equation (3.23) implies that the τ value should be greater than 0.5. For a given value of ν_f and τ, the Δt is defined according to the chosen Δx by:

$$\Delta t \; = \frac{1}{3\nu_f}\left(\tau - \frac{1}{2}\right)\Delta x^2 \tag{3.24}$$

The $f_\alpha^{eq}(x, t)$ for the BGK model is given by (Bhatnagar, Gross & Krook 1954):

$$f_\alpha^{eq}(x, t) = \omega_\alpha \rho_f \left(1 + \frac{3}{{c_L}^2} e_\alpha^v \, u + \frac{9}{2{c_L}^4}(e_\alpha^v \, u)^2 - \frac{3}{2{c_L}^2} u^2\right) \tag{3.25}$$

where, ω_α is the weighting factor for the velocity vectors, ρ_f is the fluid density, e_α^v is the microscopic fluid velocity, u is the macroscopic fluid velocity, and c_L is the lattice speed given by:

$$c_L = \frac{\Delta x}{\Delta t} \tag{3.26}$$

In the lattice Boltzmann computations, $c_L = \Delta x = \Delta t = 1$, and the discretisation schemes in LBM are labelled as *DdQq,* where *d* is the number of dimensions, and *q*

represents the number of velocity vectors. This study used *D3Q19*, a three-dimensional scheme with 19 velocity vectors, including one at rest.

Figure 3.4 shows the directions of the velocity vectors (e_α^v) for the *D3Q19* scheme and, for the sake of simplicity, their magnitudes are already defined by:

$$e_\alpha^v = \begin{cases} (0,0,0) & i = 0 \\ (\pm c_L, 0,0), (0, \pm c_L, 0), (0,0, \pm c_L) & i = 1,2,3,4,5,6 \\ (\pm c_L, \pm c_L, 0), (\pm c_L, 0, \pm c_L), (0, \pm c_L, \pm c_L) & i = 7,8,9,10,11, \dots ,18 \end{cases} \quad (3.27)$$

and the weighing factors are $\omega_0 = 1/3$, $\omega_{1,2,3,4,5,6} = 1/18$ and $\omega_{7,8,\dots,18} = 1/36$.

The macroscopic fluid properties, i.e., fluid density (ρ_f) and velocity (u) can be retrieved at each node and are given by (Han & Cundall 2017; Seil & Pirker 2016):

$$\rho_f\,(x,t) = \sum_{\alpha=0}^{q-1} f_\alpha(x,t) \quad (3.28)$$

$$u\,(x,t) = \frac{1}{\rho_f} \sum_{\alpha=0}^{q-1} f_\alpha(x,t) e_\alpha^v \quad (3.29)$$

To determine the fluid pressure p_f, it is assumed that the fluid is slightly compressible, and thus the following state equation is used:

$$p_f = c_s^2 \rho_f \quad (3.30)$$

where c_s is the sound celerity, defined as follows:

$$c_s = \frac{c_L}{\sqrt{3}} \quad (3.31)$$

Fluid modelled with LBM requires a slight variation in spatial density. An approximate incompressibility situation can only be achieved when the Mach number (M) is small; it is therefore kept below 0.1 (Han, Feng & Owen 2007b) and is defined as follows:

$$M = \frac{u_{max}}{c_L} \quad (3.32)$$

u_{max} is the maximum velocity in the fluid flow in physical units. Fluids with lower viscosity and turbulent flows can also be simulated with LBM using the Smagorinsky Large Eddy Simulation approach (Han, Feng & Owen 2007a; Seil, Pirker & Lichtenegger 2018).

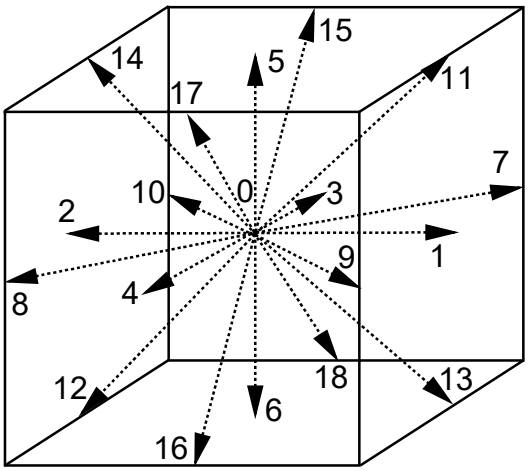

Fig. 3. 4 Directions of the 19 (0-18) velocity vectors of the D3Q19 discretisation scheme used in this study

3.3.2 Fluid-Particle Interaction

For fluid-particle interaction, the partially saturated cells method was introduced by Noble & Torczynski (1998) and implemented by Seil & Pirker (2016) to couple open-source DEM code, which is the LAMMPS Improved for General Granular and Granular Heat Transfer Simulations (LIGGGHTS) (Kloss et al. 2012) with LBM code Palabos (Parallel Lattice Boltzmann Solver). This thesis has further modified the implementation of Seil & Pirker (2016). Han & Cundall (2017) also used the same model to couple LBM with PFC2D and PFC3D. The advantage of this method is the smooth variation of forces acting on the particles. The method is also called the Immersed Moving Boundary (IMB) (Rettinger & Rüde 2017). The participation of solid particles in the fluid is achieved by introducing an additional collision term (Ω_α^s) in Equation (3.19) (Noble & Torczynski 1998):

$$f_\alpha(x, t^*) = f_\alpha(x, t) + [1 - B\,]{\Omega_\alpha}^{BGK} + B{\Omega_\alpha}^{s} \tag{3.33}$$

$$B = \frac{\varepsilon_s\left({}^{\tau}/_{\Delta t} - {}^{1}/_{2}\right)}{(1 - \varepsilon_s) + \left({}^{\tau}/_{\Delta t} - {}^{1}/_{2}\right)} = (0,1) \tag{3.34}$$

where ε_s is the solid fraction in the fluid cell volume, B is a weighting function for correcting the collision phase of the lattice-BGK equation due to the presence of solid particles, and τ is the relaxation time. The critical part of this algorithm is to evaluate the solids fraction in each lattice over time while taking into account the moving particles. In a three-dimensional case, the volume of the fluid cell can be divided into a number of sub-cells, and then it can be evaluated whether these sub-cells are located inside or outside the solid object. The solid fraction can then be computed from the ratio of the sub-cells within the solid object to the total number of sub-cells in a lattice (Rettinger & Rüde 2017; Seil, Pirker & Lichtenegger 2018).

The non-equilibrium part of the particle distribution function is bounced back and ${\Omega_\alpha}^{s}$ is computed using:

$${\Omega_\alpha}^{s} = f_{-\alpha}(x, t) - f_\alpha(x, t) + {f_\alpha}^{eq}\left(\rho_f, v^p\right) - {f_{-\alpha}}^{eq}\left(\rho_f, u\right) \tag{3.35}$$

where v^p is the velocity of solid particle p at time $t + \Delta t$ at the node, u is the macroscopic fluid velocity, and the notation $f_{-\alpha}$ is the rebound state obtained by reversing all microscopic fluid velocities, i.e., e_α^v to $e_{-\alpha}^v$.

The force (f_f) (without the static buoyancy force) and the torque (T_f) acting on a particle through the fluid can then be computed by (Noble & Torczynski 1998; Seil, Pirker & Lichtenegger 2018):

$$f_f = \frac{\Delta x^3}{\Delta t}\left[\sum_n B_n \sum_\alpha {\Omega_\alpha}^{s}\, e_\alpha^v\right] \tag{3.36}$$

$$T_f = \frac{\Delta x^3}{\Delta t}\left[\sum_n B_n\,(x^n - x^p) \sum_\alpha {\Omega_\alpha}^{s}\, e_\alpha^v\right] \tag{3.37}$$

B_n is the weighting function in the cell, x^n is the coordinate of the lattice cell, and x^p is the centre of mass of the particle. Since Equation (3.19) does consider acceleration due to the force of gravity of the fluid, Equation (3.36) does not include the static buoyancy forces; therefore, they are applied separately to the particles and the total hydrodynamic force (f_{hyd}) on the particle, including the static buoyancy force (f_{bu}) is given by:

$$f_{hyd} = f_f + f_{bu} \tag{3.38}$$

3.3.3 Governing Equations of Particle Motion

The governing equations of the motion of solid particles given by Cundall & Strack (1979), with the additional fluid-particle interaction force (f_{hyd}^p) and the torque (T_f^p), are as follows:

$$m^p \frac{dv^p}{dt} = f_g^p + f_{hyd}^p + \sum_{c=1}^{N_c^p} f_j^c \tag{3.39}$$

$$I^p \frac{dw^p}{dt} = T_f^p + \sum_{c=1}^{N_c^p} T_j^c \tag{3.40}$$

where m^p and I^p are the mass and the moment of inertia of the particle p, v^p and w^p are the translational and angular velocities of the particle p, N_c^p is the total number of contacts on the particle p, f_j^c is the contact force vector in the j^{th} direction at contact c on the particle p, T_j^c is the torque that acts on the particle p due to the tangential contact force at contact c, and f_g^p is the gravitational force on the particle p. Figure 3.5 shows the flowchart of the LBM-DEM approach described above. The DEM calculation cycles are within the LBM cycles. A suitable interval for the information transfer was chosen so that the accuracy of the simulation could not be impaired.

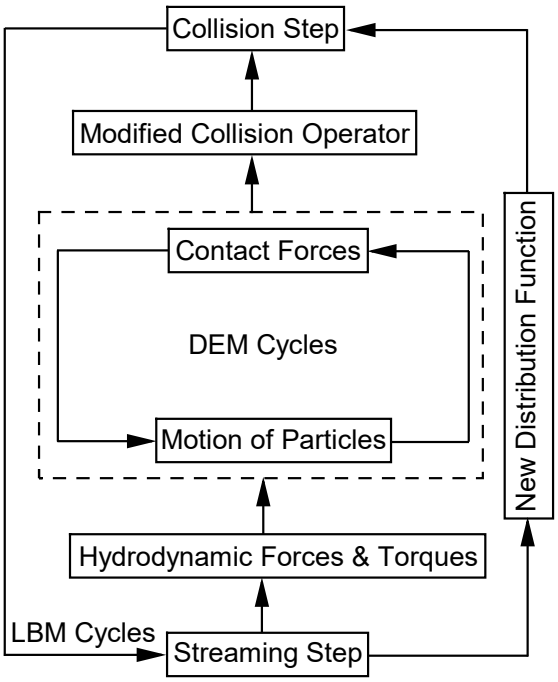

Fig. 3. 5 Flowchart of the Lattice Boltzmann Method (LBM) combined with the Discrete Element Method (DEM)

3.4 VALIDATION

3.4.1 Drag Force on A Single Fixed Particle

Figure 3.6a shows a schematic sketch of the problem where a single fixed particle (sphere) with diameter D (where $D = L_x/10$) is in the centre of a 3D region of dimensions L_x, L_y and L_z (where $L_x = L_z$, and $L_y = 20D$). The drag force on the particle was investigated under creeping flow conditions by maintaining smaller values of the particle Reynold's number (R_{ep}). The numerical results of the drag coefficient (c_D) were compared at different R_{ep} values from 0.01 to 1 with analytical solution and experimental results by Yang et al. (2015). Each simulation was run until the flow conditions stabilized. The analytical solution for the drag coefficient (c_D) is given as follows (Hoerner 1965; Yang et al. 2015):

$$c_D = \frac{24}{R_{ep}} = \frac{8F_D}{\rho v^2 \pi D^2} \tag{3.41}$$

where F_D is the Stoke's drag force and v is the velocity of the fluid.

Figure 3.6b shows the analytical, experimental and numerical c_D at different R_{ep} values. For the numerical analysis, the lattice resolution (N) and relaxation time (τ) were 5 and 0.59, respectively. An N value of 5 means the particle consists of 5 cells along its diameter. While the value of τ is chosen close to but greater than its lower limit of 0.5. Figure 3.6b shows that the numerically determined c_D values agree very well with the analytical and experimental values.

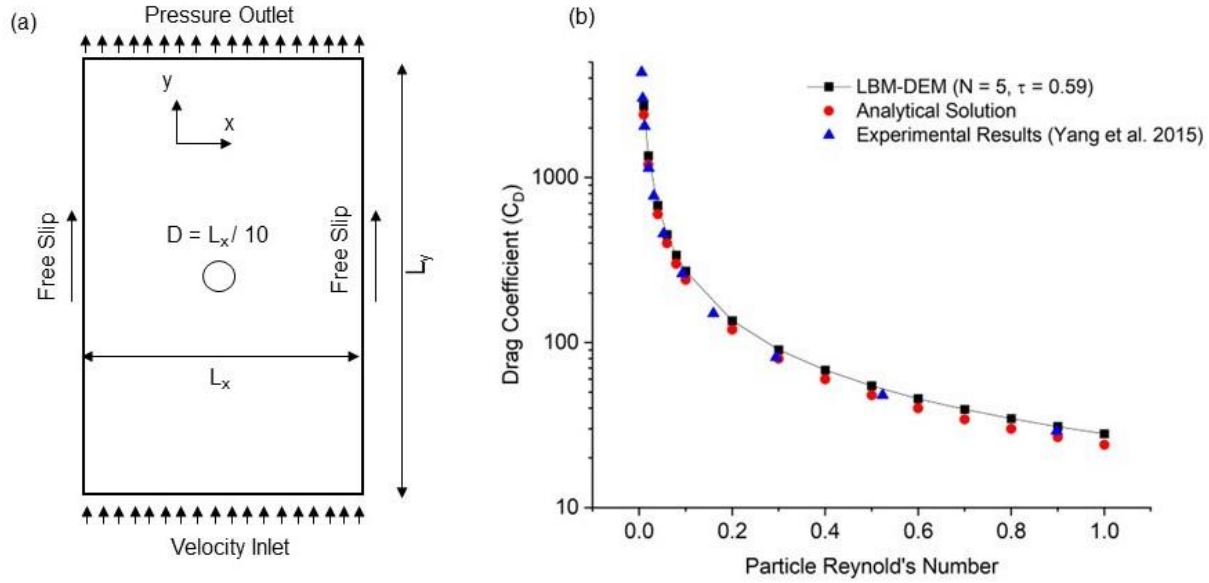

Fig. 3. 6 Validation of drag force on a single fixed particle

3.4.2 Single-Particle Falling into The Fluid

The transient motion of the particles in the fluid also needs to be validated with LBM-DEM coupling. In this regard, an attempt is made in this study to validate the motion of a single particle falling into the fluid with different particle Reynold's numbers (Re_p). The validation was carried out by comparing the numerical results with the experimental observations by Ten Cate et al. (2002). Figures 3.7(a) and 3.7(b) show the schematic sketch and the modelled problem using the LBM-DEM approach.

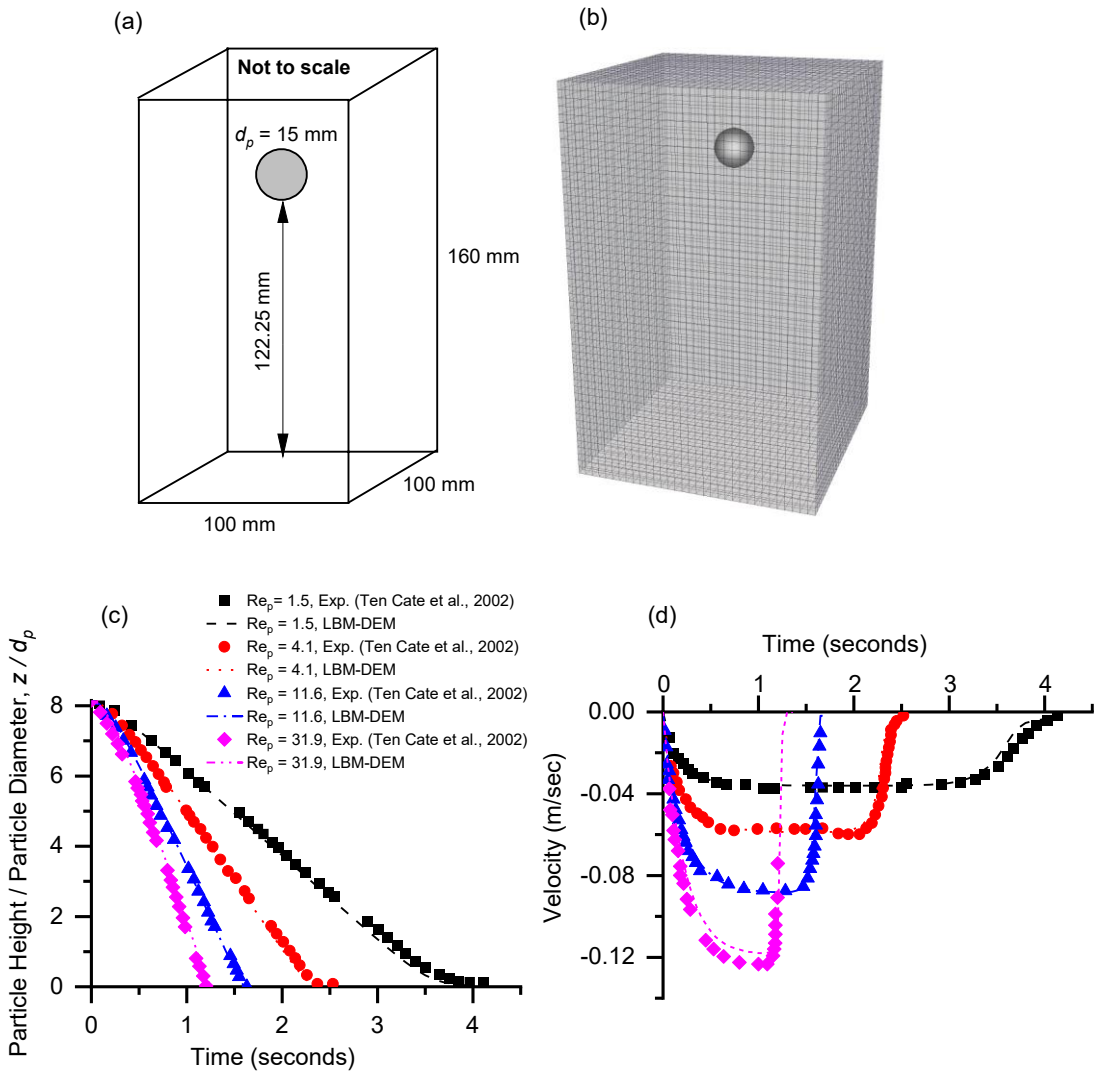

Fig. 3. 7 (a) Schematic representation of a single sphere with a diameter (d_p) = 15 mm falling into the fluid; (b) the modelled particle in the fluid mesh using LBM-DEM; (c) comparison of the numerical and experimental results of particle position over time; (d) comparison of experimental and numerical results of particle velocity over time

Table 3.2 shows the fluid properties used with lattice resolution (N) = 5 (particle diameter corresponds to 5 fluid cells) and the relaxation time (τ) = 0.53. Figures 3.7(c) and 3.7(d) show an excellent agreement between the numerical and experimental results of the position and velocity of the falling particle over time at different Reynold's numbers. Hence, it could be justified with confidence that the LBM-DEM approach can

reasonably predict the transient motion of the particles in the fluid with these selected numerical parameters.

Table 3. 2 Fluid properties for simulating the single-particle falling into the fluid using the LBM-DEM approach (after Ten Cate et al. 2002)

Case	Density (ρ_f) (kg/m^3)	Kinematic Viscosity (υ_f) (m^2/s)
Re_p = 1.5	970	3.845 x 10^{-4}
Re_p = 4.1	965	2.197 x 10^{-4}
Re_p = 11.6	962	1.175 x 10^{-4}
Re_p = 31.9	960	6.042 x 10^{-5}

3.4.3 Fluidisation of Granular Soils

The minimum fluidization velocity and the pressure drop through a three-dimensional particle bed were investigated in this case. The particles were placed in a 3D rectangular domain with a velocity inlet, a pressure outlet, and free-slip side boundaries (Figure 3.8a). Buoyancy force was applied to each particle separately, while the gravity of the fluid was not considered. The semi-analytical solution for the pressure drop through a packed particle bed is given by (Ergun 1952):

$$\frac{\Delta P}{L} = \frac{150\mu_f v_d (1-n)^2}{d_p^2\, n^3} + \frac{1.75\rho_f v_d^2 (1-n)}{d_p\, n^3} \tag{3.42}$$

where ΔP is the drop in pressure across the bed of particles, L is the height of the bed, d_p is the particle size, and it is selected equal to d_{50} (particle size corresponding to 50% finer in the particle size distribution), n is the overall porosity, μ_f is the fluid's dynamic viscosity, and v_d is the superficial or discharge velocity of the fluid.

Figures 3.8b and 3.8c show the analytically and numerically determined pressure drops and minimum fluidization velocities while considering different values of N and τ. The inlet velocity was gradually increased, and the pressure drop continued to drop as the

velocity increased. A continuous increase in the flow velocity leads to a condition where particles begin to migrate with a constant drop in pressure. This state is called a fluidised state, where the effective stresses tend to zero, and the particulate medium acts like a fluid. Numerical analyses were performed for $N = 2$ and $N = 5$. When $N = 2$, the results deviated greatly from the analytical solution, and there was a considerable difference in the results with various τ values. Therefore, it is necessary to increase the N value to better resolve the fluid-particle interaction.

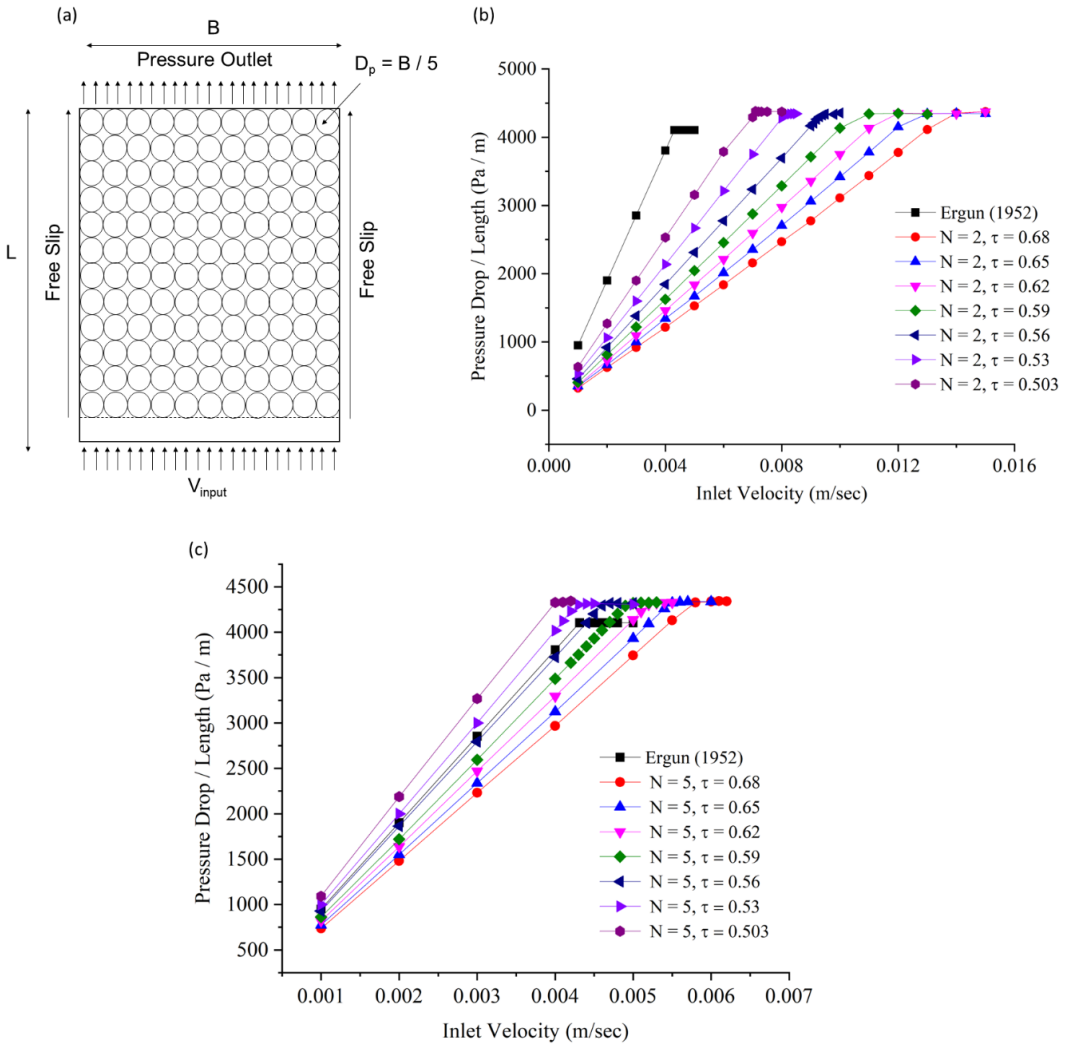

Fig. 3. 8 Validation of fluidisation of particles

Figure 3.8 shows that when $N = 5$ and $\tau = 0.56$, the numerical results are comparable to the analytical solution, and as the τ value is further increased, the minimum

fluidization velocity increases. The values of τ affect these results in two ways, namely the fluid compressibility error and the fluid-particle interaction force error. A lower value of τ close to but greater than the limiting value of 0.5 reduced errors in the fluid compressibility and fluid-particle interaction. The effect of the τ value on the fluid-particle interaction forces is easily explained using Figures 3.8b and 3.8c. As the τ value increased, the minimum fluidization velocity also increased, showing that the forces of the fluid on the particles became smaller for larger values of τ. Therefore, a smaller value of τ ($\geq$0.5) leads to smaller errors in the fluid-particle interaction forces. In Figure 3.8c, where $N = 5$, the variation in τ value did not affect the results as much as when $N = 2$.

3.4.4 Hydraulic Conductivity Prediction

Figure 3.9 shows the results of the hydraulic conductivity prediction given by the LBM-DEM method compared to available semi-empirical solutions, i.e., Hazen (1892), Carman (1939) and Indraratna et al. (2012). The lattice resolution (N) was kept equal to 5 with a relaxation time of 0.56. There is a good agreement between the current study and other works, which indicates reasonable success in predicting the hydraulic conductivity of granular materials using DEM coupled with LBM.

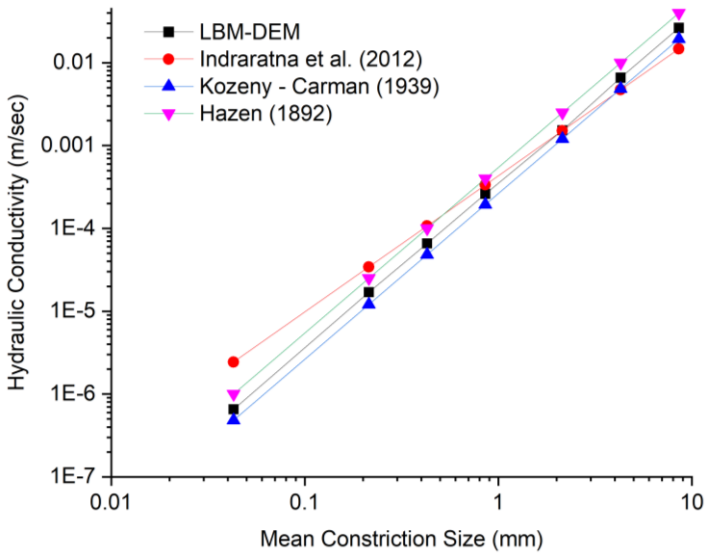

Fig. 3. 9 Validation of hydraulic conductivity through the particle bed

3.4.5 Stress-Strain Behaviour

The parameters used for the analysis with DEM are listed in Table 3.3. The samples were first compressed isotropically to different confining pressures using a strain-controlled approach that considered quasi-static conditions; the samples were then sheared. Figure 3.10a shows the stress-strain curves of the samples sheared under drained conditions at constant confining pressures of 50 kPa, 100 kPa, and 200 kPa. The stress-strain curves from the numerical simulations are in a reasonable comparison to that of the experimental ones by Hazzar et al. (2020). Figure 3.10b also compares the volumetric strain with axial strain well.

The experimental investigations were carried out on glass beads by a series of drained triaxial compression tests. The dense specimens with a diameter of 38 mm and a height of 76 mm were produced using the air pulviation method. The required bulk density was achieved by compacting each layer of glass beads. The specimens were saturated using the back pressure, and the sample saturation was verified using Skempton's pore-pressure parameter *B*. The cell pressure was then increased by keeping the back pressure constant until the difference between the two reached the desired consolidated pressures of 50 kPa, 100 kPa, and 200 kPa. After consolidation, each specimen was sheared under drained condition.

Table 3. 3 Parameters used for the DEM simulations

Parameter	Value
Young's modulus	70 GPa (Thornton 2000)
Poisson's ratio	0.30 (Shire et al. 2014)
Friction coefficient during isotropic compression	0 (Thornton 2000)
Friction coefficient during shearing	0.30 (Shire et al. 2014)

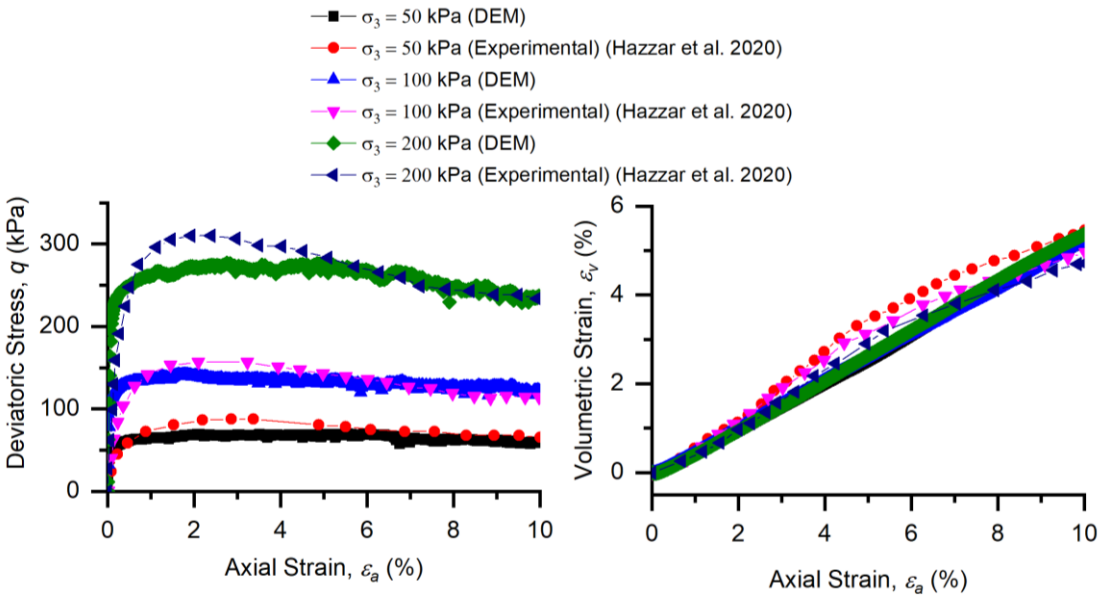

Fig. 3. 10 Validation of the (a) deviatoric stress versus axial strain, (b) volumetric strain versus axial strain

3.5 SUMMARY

This chapter describes the numerical approaches used in this thesis. This includes the governing equation of the DEM, the choice of the appropriate time step, details of the contact model, the assumed boundary conditions, and the quasi-static conditions. This chapter also described the Boltzmann equation and its solution using the finite difference scheme and its coupling to DEM. The DEM-LBM coupling was further validated by using the results for the drag force on a single fixed particle, a single particle falling into the fluid, the fluidisation of a bed of cohesionless soils, and the hydraulic conductivity and the stress-strain behaviour. A good comparison of the results showed that the approaches selected are suitable for the micromechanical investigations of soil.

CHAPTER 4 MICROSCALE BOUNDARIES OF INTERNALLY STABLE AND UNSTABLE SOILS

4.1 INTRODUCTION

Internal instability is the inability of coarse particles to prevent fine particles from being eroded during seepage flow. Soil can become internally unstable due to changes in Particle Size Distribution (PSD), and this can affect its hydraulic and mechanical properties (Mehdizadeh, Disfani & Shire 2019; Xiao & Shwiyhat 2012). To evaluate the likelihood of internal instability, several proven criteria based on the PSD and Constriction Size Distribution (CSD) are available (Indraratna, Israr & Rujikiatkamjorn 2015; Kenney & Lau 1985; Kezdi 1979). However, these criteria are based on macroscale laboratory modelling, while internal instability is a problem at the micro/particle scale. Hence, internal instability may be better assessed at particle scale using the Discrete Element Method (DEM) (O'Sullivan 2011).

Prior studies have used DEM to examine internal instability (Ahmadi et al. 2020; Shire et al. 2014; Shire & O'Sullivan 2013), but internally stable and unstable soils have yet to be delineated at the microscale. In order to differentiate between internally unstable and stable soil, this chapter focuses on the internal instability of non-cohesive soils at the micro/particle scale using DEM under isotropic stress conditions. With 21 particle size distribution curves, 63 DEM simulations were carried out at three different relative densities. The findings demonstrate a new method of examining the likelihood of internal instability in cohesionless soils. The coordination number and stress reduction factor, taken directly from the particle scale data, were considered. The results were compared to the available macroscale criteria based on PSD and CSD. This analysis demonstrates that CSD-based criteria could anticipate the possibility of internal instability more accurately, and thus it could be used to evaluate the internal instability of cohesionless

soils. This Chapter has been adapted from the following published article and is reproduced with permission from Springer Nature:

Indraratna, B., Haq, S., Rujikiatkamjorn, C., & Israr, J. (2021). Microscale boundaries of internally stable and unstable soils. *Acta Geotechnica*. https://doi.org/10.1007/s11440-021-01321-7

4.2 PARTICLE SIZE DISTRIBUTION CURVES AND INTERNAL INSTABILITY ASSESSMENT USING EXISTING CRITERIA

Figure 4.1 shows a total of 21 PSD curves selected for numerical analysis from previously published experimental research (Crawford-Flett 2014; Honjo, Haque & Tsai 1996; Indraratna, Raut & Khabbaz 2007; Israr 2016; Slangen 2015). Since soils with more than 35% of fines are always internally stable (Skempton & Brogan 1994), only soils with less than 35% of fines were included in this study. The PSDs of Samples 1,2,3,4, and 5 are in the range of the typical size of sub-ballast in Australian railroads (Israr 2016). Although samples 1,2,3,4, and 5 are uniformly graded and well-graded soils, they could exhibit internal instability under certain conditions (Israr & Indraratna 2017). Other samples are gap-graded soils, which are also used for practical purposes, such as embankment dams (Skempton & Brogan 1994).

Figure 4.2 shows the use of PSD-based approaches by Kenney & Lau (1985) and Kezdi (1979) to evaluate the internal instability of the selected specimens. The retention ratio of Kezdi (1979) is given by $(D_{15}^{c}/d_{85}^{f})_{max}$, where D_{15}^{c} is the 15% passing by mass of the PSD of the coarser fraction and d_{85}^{f} is the 85% passing by mass of the PSD of the finer fraction. Soils are internally unstable when $(D_{15}^{c}/d_{85}^{f})_{max} \geq 4$. The retention ratio from Kenney & Lau (1985) is given by $(H/F)_{min}$, where F is the finer fraction at any particle diameter D, and H is the incremental finer fraction between particle diameters D and $4D$. The soils with the potential for internal instability have $(H/F)_{min} \leq 1$, while the

widely and uniformly graded samples were evaluated by considering particles finer than 20% and 30%, respectively.

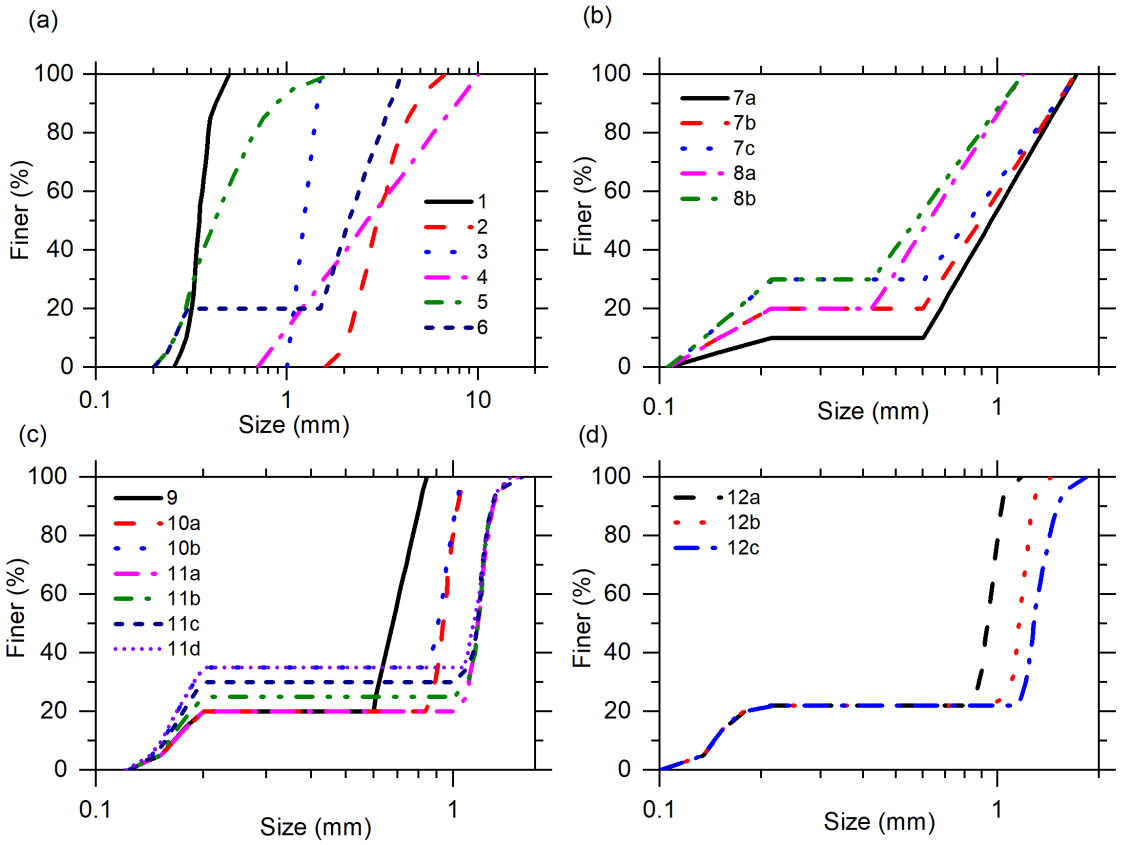

Fig. 4. 1 Particle size distribution of soils investigated (Indraratna, Haq, et al. 2021) (reproduced with permission from Springer Nature)

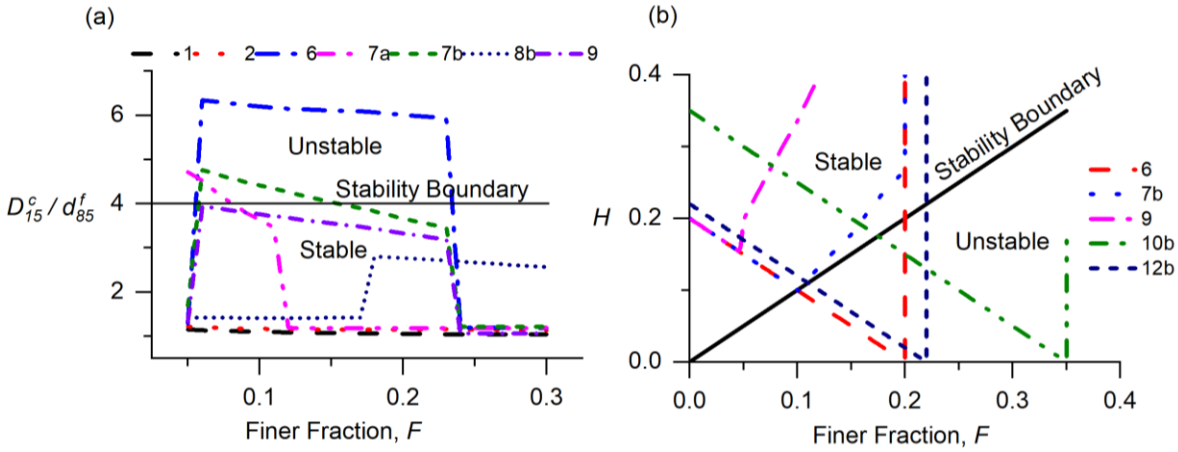

Fig. 4. 2 Evaluation of the likelihood for internal instability of selected samples using the methods of (a) Kezdi (1979) (b) Kenney and Lau (1985) (Indraratna, Haq, et al. 2021) (reproduced with permission from Springer Nature)

Table 4.1 summarises the results of the internal instability assessment by considering the CSD-based retention ratio presented by Indraratna et al. (2011). The CSD-based retention ratio is $D_{c35}^{c^*}/d_{85}^{f^*}$, where $D_{c35}^{c^*}$ is the 35% finer of the CSD of the coarser fraction and $d_{85}^{f^*}$ is the 85% finer of PSD of the finer fraction, both plotted using the surface area method (Indraratna, Raut & Khabbaz 2007). The soil specimens with $D_{c35}^{c^*}/d_{85}^{f^*} \geq 0.73$ are internally unstable. In the CSD-based method, the PSD of soil was split into coarser and finer fractions at the ratio $(H/F)_{min}$ for continuously-graded soils and percentage finer corresponding to the almost horizontal part of the PSD of gap-graded soils, following the method proposed by Indraratna et al. (2015). The gradations of soils with a fines content ≥ 25% were divided into finer and coarser fractions at the 25% finer point on the respective PSD curves for loose and medium states and the 20% finer point for the dense state.

The CSD can be determined accurately from a given particle gradation using the mathematical approach introduced by Indraratna et al. (2007, 2015) and Indraratna & Raut (2006), from which the controlling constriction size ($D_{c35}^{c^*}$) and the largest erodible fine particle ($d_{85}^{f^*}$) are readily obtained by using the relative density of the soil and exploiting the surface area approach (e.g., using MATLAB). The use of the CSD-based method in real life design to assess internal instability, and for instance to evaluate the effectiveness of base-filter combinations for rail substructures and embankment dam materials has been described elsewhere (Indraratna, Israr & Rujikiatkamjorn 2015; Indraratna & Raut 2006; Indraratna, Raut & Khabbaz 2007).

Table 4. 1 Evaluation of internal instability (Indraratna, Haq, et al. 2021)

(reproduced with permission from Springer Nature)

ID	R_d [a]	$(D_{15}^c/d_{85}^f)_{max}$ [b]	D_{c35}^{c*}/d_{85}^{f*} [c]	$(H/F)_{min}$ [d]	N_p [e]	n [f]	Z [g]	α [h]	Exp. [i]
1	Loose	1.150	0.270	N/A	10000	0.415	4.317	1.111	Stable
	Medium	1.150	0.227	N/A		0.391	5.182	1.124	Stable
	Dense	1.150	0.175	N/A		0.358	5.736	1.138	Stable
2	Loose	1.220	0.322	N/A	10000	0.387	3.733	1.210	Stable
	Medium	1.220	0.270	N/A		0.366	4.778	1.244	Stable
	Dense	1.220	0.205	N/A		0.337	5.456	1.336	Stable
3	Loose	1.070	0.276	N/A	10000	0.397	4.290	1.090	Stable
	Medium	1.070	0.232	N/A		0.393	5.210	1.123	Stable
	Dense	1.070	0.177	N/A		0.361	5.470	1.128	Stable
4	Loose	1.500	0.462	1.740	41000	0.275	2.160	1.277	Stable
	Medium	1.500	0.385	1.740		0.271	3.680	1.475	Stable
	Dense	1.500	0.283	1.740		0.251	4.630	1.758	Stable
5	Loose	1.280	0.344	2.200	10000	0.364	3.410	1.250	Stable
	Medium	1.280	0.288	2.200		0.343	4.530	1.340	Stable
	Dense	1.280	0.217	2.200		0.317	5.170	1.422	Stable
6	Loose	6.340	1.750	0	82000	0.239	0.040	0.255	-
	Medium	6.340	1.467	0		0.221	0.050	0.073	-
	Dense	6.340	1.113	0		0.185	0.090	0.007	Unstable
7a	Loose	4.720	1.096	0.970	15000	0.317	0.154	0.279	-
	Medium	4.720	0.916	0.970		0.286	0.187	0.134	-
	Dense	4.720	0.737	0.970		0.266	0.206	0.044	Stable
7b	Loose	4.760	1.111	0.980	35000	0.234	0.111	0.392	-
	Medium	4.760	0.930	0.980		0.216	0.239	0.224	-
	Dense	4.760	0.703	0.980		0.185	2.059	0.399	Stable
7c	Loose	3.990	0.668	0.790	55000	0.218	1.566	0.857	-
	Medium	3.990	0.550	0.790		0.212	3.872	1.133	-
	Dense	3.990	0.398	0.790		0.198	5.141	1.810	Stable
8a	Loose	3.330	0.777	2.700	12000	0.267	0.464	0.772	-
	Medium	3.330	0.650	2.700		0.243	1.361	0.777	-
	Dense	3.330	0.491	2.700		0.222	3.058	1.116	Stable
8b	Loose	2.810	0.595	1.590	20000	0.253	1.748	1.111	-
	Medium	2.810	0.492	1.590		0.248	3.780	1.372	-
	Dense	2.810	0.361	1.590		0.231	4.814	1.789	Stable
9	Loose	3.940	0.887	3.290	12000	0.296	0.362	0.473	Unstable

	Medium	3.940	0.745	3.290		0.268	0.551	0.452	-
	Dense	3.940	0.567	3.290		0.234	1.708	0.758	-
10a	Loose	5.490	1.213	0	27000	0.281	0.124	0.252	Unstable
	Medium	5.490	1.019	0		0.251	0.163	0.148	-
	Dense	5.490	0.777	0		0.212	0.244	0.119	-
10b	Loose	4.940	0.666	0.160	56000	0.246	3.256	1.120	Stable
	Medium	4.940	0.545	0.160		0.242	4.593	1.363	-
	Dense	4.940	0.247	0.160		0.226	5.382	1.756	-
11a	Loose	6.620	1.524	0	53000	0.276	0.055	0.204	Unstable
	Medium	6.620	1.281	0		0.245	0.064	0.037	-
	Dense	6.620	0.977	0		0.209	0.082	0.003	-
11b	Loose	6.420	1.528	0	69000	0.252	0.060	0.287	Unstable
	Medium	6.420	1.284	0		0.206	0.330	0.124	-
	Dense	6.420	0.432	0		0.187	4.630	0.701	-
11c	Loose	6.240	0.717	0	90000	0.220	0.110	0.522	Unstable
	Medium	6.240	0.574	0		0.213	4.100	0.884	-
	Dense	6.240	0.419	0		0.200	5.350	1.564	-
11d	Loose	6.360	0.677	0.160	116000	0.231	3.550	1.099	Stable
	Medium	6.360	0.564	0.160		0.227	4.750	1.292	-
	Dense	6.360	0.250	0.160		0.212	5.520	1.807	-
12a	Loose	5.960	1.341	0	44000	0.263	0.080	0.282	Stable
	Medium	5.960	1.126	0		0.234	0.090	0.104	-
	Dense	5.960	0.859	0		0.193	0.380	0.061	-
12b	Loose	7.260	1.671	0	85000	0.258	0.040	0.283	Unstable
	Medium	7.260	1.405	0		0.224	0.050	0.061	-
	Dense	7.260	1.071	0		0.190	0.120	0.001	-
12c	Loose	8.220	1.873	0	120000	0.258	0.030	0.250	Unstable
	Medium	8.220	1.573	0		0.231	0.040	0.031	-
	Dense	8.220	1.199	0		0.189	0.110	0.0003	-

[a] relative density; [b] retention ratio by Kezdi (1979); [c] retention ratio by Indraratna et al. (2011); [d] retention ratio by Kenney and Lau (1985); [e] number of particles simulated; [f] sample's porosity; [g] coordination number; [h] stress reduction factor, [i] experimental assessments of the samples from the previous studies (Crawford-Flett 2014; Honjo, Haque & Tsai 1996; Indraratna, Israr & Rujikiatkamjorn 2015; Indraratna, Raut & Khabbaz 2007; Israr 2016; Israr & Indraratna 2019; Slangen 2015)

4.3 SIMULATION APPROACH

Three-dimensional simulations were carried out on cubical samples using an open-source particulate Discrete Element Method (DEM) code developed by Kloss et al. (2012). The periodic boundary conditions were used, thus negating the need to account for boundary effects while still allowing for an infinite sample size (Thornton 2000). The Young's modulus and Poisson's ratio of the particles were set to 70 GPa and 0.3, respectively, with a particle density of 2650 kg/m^3 (Thornton 2000). The spherical shapes of the particles were simulated. The literature has considered a broad range of friction coefficient (μ_s) values. Senetakis et al. (2013) used a micromechanical inter-particle loading apparatus and found that sand particles are in the range of $0.12 < \mu_s < 0.35$. Since Huang et al. (2014) found that using $\mu_s > 0.5$ for element tests in geomechanics leads to implausible findings, so $\mu_s < 0.5$ was assumed in this study. Since it is not always possible to mimic the void ratios observed in experiments with spherical particles in DEM samples, the relative density (R_d) was matched in order to draw comparisons with experimental observations (Salot, Gotteland & Villard 2009). The minimum and maximum void ratios in the numerical samples were determined by varying the coefficient of inter-particle friction (μ_s) under isotropic compression, and they are a function of the mean effective stress (p') (Abbireddy & Clayton 2010; Sazzad, Biswas & Toufiq-E-Alahy 2014; Thornton 2000). During isotropic compression, dense, medium, and loose states were achieved by setting μ_s = 0, 0.1, and 0.3, respectively. Thereafter, the samples were equilibrated through sufficient cycles with μ_s = 0.3 (Shire et al. 2014).

When identifying fine particles that do not help to transmit stresses, gravity was disabled, and periodic boundaries were used. The representative volume element (RVE) was also checked for periodic boundaries. In order to achieve an RVE, it was ensured that at least 500 particles were present in the coarser fraction of PSD (Shire et al. 2014). The

particles were initially produced in the periodic cell without any contact between them. The boundaries were then isotropically compressed to the desired stress level using a strain-controlled approach. A strain rate was chosen to ensure a quasi-static compression of the samples. After the target stress was reached, the strain rate went to zero, and the system stabilized. A sufficient number of simulation cycles were run to guarantee equilibrium at the target stress level. The simulations were then stopped as the mean stress (p') and the coordination number (Z) remained constant for 20,000 cycles. Shire et al. (2014) and Thornton (2000) followed a similar simulation approach.

The average Cauchy stress tensor ($\bar{\sigma}_{ij}$) of the samples after isotropic compression to the desired stress level was calculated using the following equation (Potyondy & Cundall 2004):

$$\bar{\sigma}_{ij} = \frac{1}{V} \sum_{N_p} \bar{\sigma}_{ij}^{p} V^{p} \tag{4.1}$$

where V is the sample volume, V^p is the volume of particle p, N_p is the number of particles, and $\bar{\sigma}_{ij}^{p}$ is the average stress tensor within a particle p and is given by:

$$\bar{\sigma}_{ij}^{p} = \frac{1}{V^{p}} \sum_{N_{c,p}} \left| x_i^c - x_i^p \right| n_i^{c,p} f_j^c \tag{4.2}$$

where f_j^c is the force at the contact c with the location x_i^c, x_i^p is the location of particle centroid, $n_i^{c,p}$ is the unit-normal vector from the centroid of particle to contact location, and $N_{c,p}$ is the contact numbers on particle p.

The stress reduction factor (α) was calculated using the approach given by Shire et al. (2014):

$$p'_f = \alpha \, p' \tag{4.3}$$

where p'_f is the mean stress in fines and p' is the mean stress of the sample, it is given as follows:

$$p' = \frac{1}{V}\sum_{N_p}(p^p V^p) \tag{4.4}$$

where p^p is the mean stress in the particle p, and p'_f is given as follows:

$$p'_f = \frac{(1-n)}{\sum_{N_p^{fines}} V^p}\sum_{N_p^{fines}}(p^p V^p) \tag{4.5}$$

where N_p^{fines} is the number of fine particles, and n is the porosity of the sample.

The coordination number (Z) is a microscale parameter that describes the packing of particles as given by (Thornton 2000):

$$Z = \frac{2N_c}{N_p} \tag{4.6}$$

where N_c and N_p are the number of contacts and particles in the samples, respectively. Eq. 4.6 also includes those particles that are not involved in the stress transmission (i.e., with less than two contacts). Here, Z can be less than 1 since gravity has been omitted.

Figure 4.3 shows the isotropically compressed DEM modelled samples 1 and 11b in their dense states to the target mean stress (p') of 200 kPa. The concept of relative density was used to model the experimental conditions because the precise values of the numerically simulated void ratios are not always directly comparable to those found experimentally (e.g., Salot et al., 2009). For example, the loose, medium, and dense states of numerical samples correspond to relative densities of 10%, 50%, and 95%, respectively.

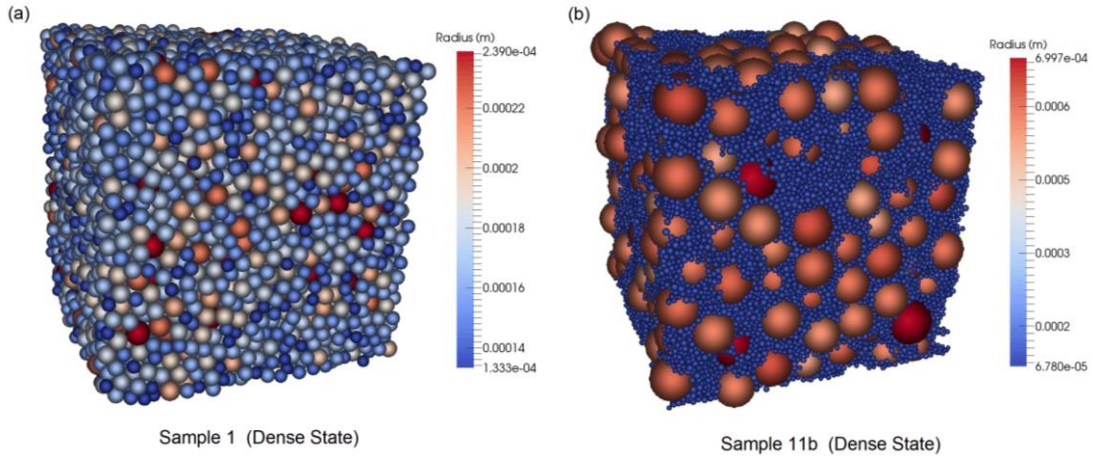

Fig. 4. 3 Isotropically compressed DEM modelled samples to the target mean stress of 200 kPa in their dense states, (a) Sample 1, (b) Sample 11b (Indraratna, Haq, et al. 2021) (reproduced with permission from Springer Nature)

4.4 RESULTS AND DISCUSSION

4.4.1 Microscale Parameters versus CSD-Based Criterion

The number of particles (N_p), the porosity (n), the coordination number (Z), and the stress reduction factor (α) of each sample are shown in Table 4.1. Figures 4.4a and 4.4b illustrate the microscale parameters Z and α, together with the CSD-based retention ratio introduced by Indraratna et al. (2011). It was possible to discern distinct boundaries between the samples that were internally stable and those that were unstable. There is a high probability that the samples that have the potential for internal instability concurrently show $Z \leq 1$, $\alpha \leq 0.5$ and $D_{c35}^{c^*}/d_{85}^{f^*} \geq 0.73$, whereas particle erosion could not occur until a certain level of the hydraulic gradient is applied. In order to determine whether internal instability could occur, the microscale parameters Z and α must be examined. If a sample does not satisfy either of the two stability limits listed below, then the sample is considered to be internally unstable: $Z > 1$ or $\alpha > 0.5$.

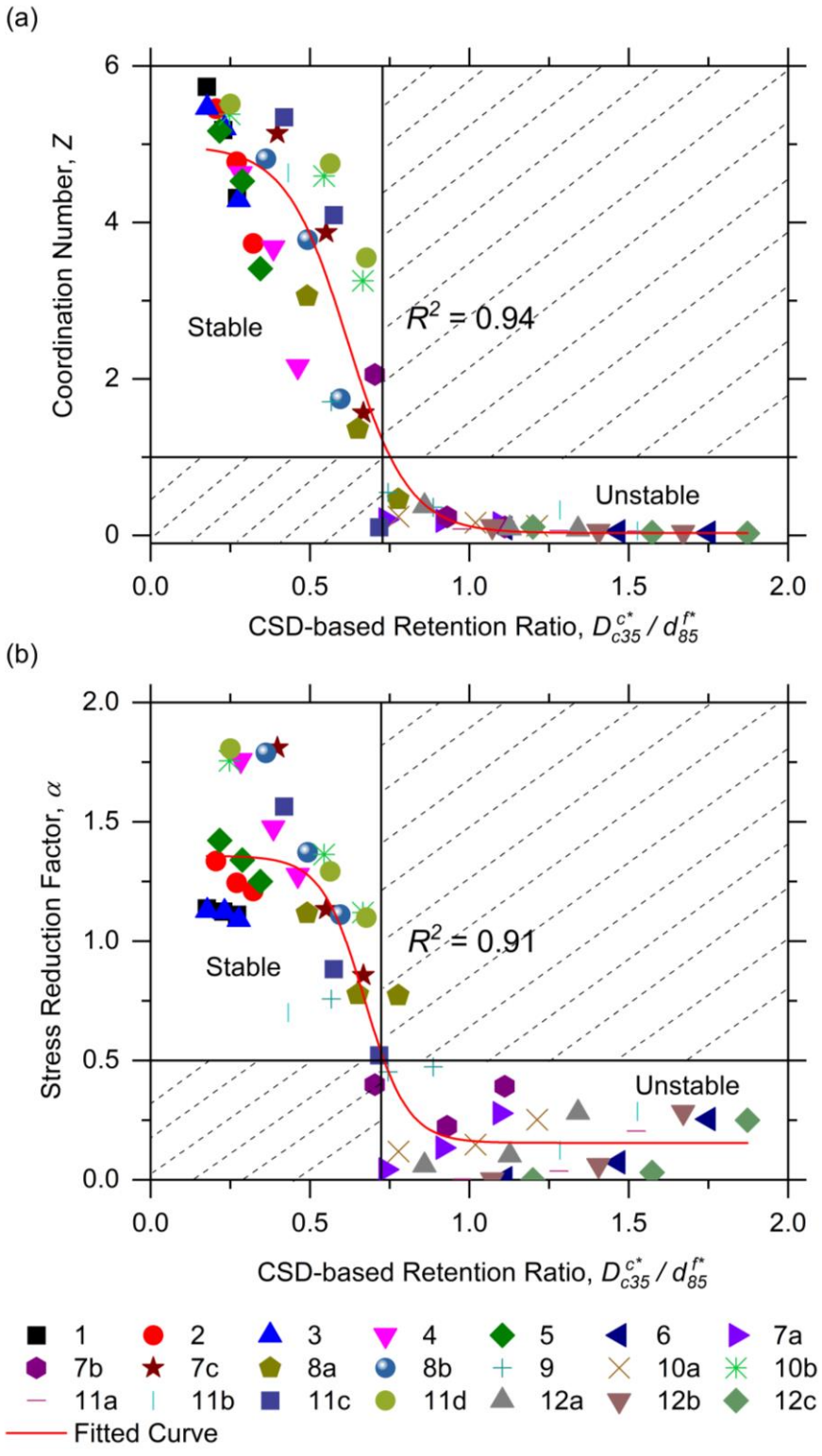

Fig. 4. 4 Evolution of (a) coordination number with CSD-based retention ratio and (b) stress reduction factor with CSD-based retention ratio (Indraratna, Haq, et al. 2021) (reproduced with permission from Springer Nature)

Following the above explanations, Sample 8a is found to be unstable according to the CSD-based criterion because, in its loose state, it has the values of Z = 0.464 and α = 0.772, and the ratio $D_{c35}^{c^*}/d_{85}^{f^*}$ = 0.777. Moreover, it does not meet one of the microscale stability boundaries, Z >1. Therefore, based on the microscale evaluation, this sample is regarded as internally unstable. Similarly, Sample 7b is also unstable in its dense state with values of Z = 2.059 and α = 0.399. Despite the dense state value of $D_{c35}^{c^*}/d_{85}^{f^*}$ = 0.703 for Sample 7b, the microscale assessment would be overly cautious to label it as unstable. In addition, according to the methods of Kenney & Lau (1985) and Kezdi (1979), this sample is also anticipated to be unstable (Table 4.1). It is noteworthy that Sample 8a, in its loose state, and Sample 7b, in its dense state, are very close to the CSD-based boundary of 0.73. Due to the distinct fabric categories of these two samples, their Z and α values contradict one another (e.g., Shire et al., 2014). For all other samples, the boundaries of Z and α coincide with the boundary of $D_{c35}^{c^*}/d_{85}^{f^*}$. As an overall trend, Z and α decrease as $D_{c35}^{c^*}/d_{85}^{f^*}$ increases.

Figure 4.4 shows that Sample 11b has values of $Z \leq 1$, $\alpha \leq 0.5$, and $D_{c35}^{c^*}/d_{85}^{f^*} \geq$ 0.73 in the loose and medium states, so it is regarded as internally unstable. However, this sample formed more contacts and became stable in its dense state with the boundaries Z >1, $\alpha > 0.5$, and $D_{c35}^{c^*}/d_{85}^{f^*} < 0.73$. This compaction of Sample 11b into its dense state eliminated the void spaces between the coarser particles by allowing the fine particles to fit in, making Z >1 and $\alpha > 0.5$. This demonstrates the significance of taking relative density (R_d) into account while evaluating internal instability. Similar experimental findings were reported by Indraratna et al. (2015), with some of the unstable samples becoming stable at higher R_d values. Given that Sample 11b has a fines content of 25%, the internal instability is sensitive to the value of R_d for samples with a fines content ≥

25%. In addition, the variation in α at different R_d for samples with a gap ratio (the ratio of the minimum particle size in the coarser fraction to the maximum particle size in the finer fraction of the particle size distribution curve of a gap-graded soil) ≥ 4 and fines content < 25% was insignificant, as in 12a, 12b, and 12c, among other samples.

Sample 7a represents the bounds where $Z \leq 1$, $\alpha \leq 0.5$, and $D_{c35}^{c^*}/d_{85}^{f^*} \geq 0.73$ at all compaction states, characterised as internally unstable. In contrast, Sample 7c is stable since it has bounds that are $Z > 1$, $\alpha > 0.5$, and $D_{c35}^{c^*}/d_{85}^{f^*} < 0.73$ for all values of R_d. Interestingly, Samples 7a and 7c have identical gap ratios but with 10% and 30% fines, respectively. This shows that the unstable samples filled the voids left by the coarser particles and became stable as the fines content increased. Higher values of Z and α occur because the finer particles become well-connected as they fill the voids left by coarser particles. The case with Samples 10a, 10b, 11a, and 11d is similar.

Similarly, Sample 9 is found to be stable in its dense state with values of $Z > 1$, $\alpha > 0.5$, and $D_{c35}^{c^*}/d_{85}^{f^*} < 0.73$ (Table 4.1), whereas Samples 10a and 11a are unstable. It is noteworthy that Samples 9, 10a, and 11a have a comparable proportion of fines despite different gap ratios. The fines in the voids become looser as the gap ratio rises, which decreases the magnitude of Z and α. As a result, the coarser fraction subsequently begins to transfer the principal stresses. Therefore, in internally stable soils, fine particles mainly act as *void fillers* because they occupy the pore spaces between the coarse particles.

Figure 4.4 depicts that the Z values decreased as the proportion of loose or disconnected fine particles increased with the coefficient of uniformity (C_u) in the continuously-graded Samples 1, 2, 3, 4, and 5. In fact, Z could drop below 1 after a specific value of C_u, which would make the samples internally unstable. Figure 4.4 also

shows the trend line relating the Z and α with $D_{c35}^{c^*}/d_{85}^{f^*}$. The values of Z and α varied systematically with $D_{c35}^{c^*}/d_{85}^{f^*}$, and were correlated by the following equations:

$$Z = \frac{5}{1 + \exp\left(10\frac{D_{c35}^{c^*}}{d_{85}^{f^*}} - 6.2\right)} \tag{4.7}$$

$$\alpha = 0.16 + \frac{1.2}{1 + \exp\left(14\frac{D_{c35}^{c^*}}{d_{85}^{f^*}} - 9.5\right)} \tag{4.8}$$

4.4.2 Microscale Parameters versus PSD-Based Criteria

Figure 4.5 shows the excessive scatter between the parameters Z and α with the retention ratio defined by Kezdi (1979) as $(D_{15}^c/d_{85}^f)_{\max}$. The ratio $(D_{15}^c/d_{85}^f)_{\max}$ does not take the R_d and the fines content into account, so it may not offer a more accurate prediction of internal instability for the samples with fines ≥ 25%, where R_d has a significant impact. For instance, Sample 11b is unstable in its loose and medium states where $Z \leq 1$ and $\alpha \leq 0.5$ but becomes stable in its dense state where $Z > 1$ and $\alpha > 0.5$. However, the ratio $(D_{15}^c/d_{85}^f)_{\max} > 4$ predicts that it would be unstable in the loose, medium, and dense states. Consequently, the ratio $(D_{15}^c/d_{85}^f)_{\max}$ incorrectly predicts that Sample 11b is unstable in its dense state.

Similarly, Samples 10b and 11d have 35% of fines and are stable at all relative density levels, although the ratio $(D_{15}^c/d_{85}^f)_{\max} > 4$ predicts these stable samples to be unstable. In Figure 4.5, except for the sample with fines content ≥ 25%, the other data points follow a clear relationship between Z and α with an increasing magnitude of $(D_{15}^c/d_{85}^f)_{\max}$. The samples that do not follow the trend of decreasing magnitude of Z as the value of $(D_{15}^c/d_{85}^f)_{\max}$ increases are also marked in Fig. 4.5. Therefore, the CSD-based

retention ratio is the only macroscale approach that considers all three factors, i.e., PSD, R_d, and the fines content affecting internal instability.

Considering Figure 4.6, there is no convincing evidence of a clear relationship between Z, α, and the retention ratio from Kenney & Lau (1985), i.e., $(H/F)_{min}$. For example, according to the Kenney & Lau (1985) criterion, Sample 7c is internally unstable because its $(H/F)_{min} < 1$ at all R_d (Table 4.1). However, it has boundaries where $Z > 1$, $\alpha > 0.5$ and $D_{c35}^{c*}/d_{85}^{f*} < 0.73$ at loose, medium, and dense states and is therefore stable. Honjo et al. (1996) also found this sample stable in their experimental investigations. Accordingly, in contrast to the PSD-based criteria, the experimental studies are consistent with the microscale boundaries and CSD-based criterion.

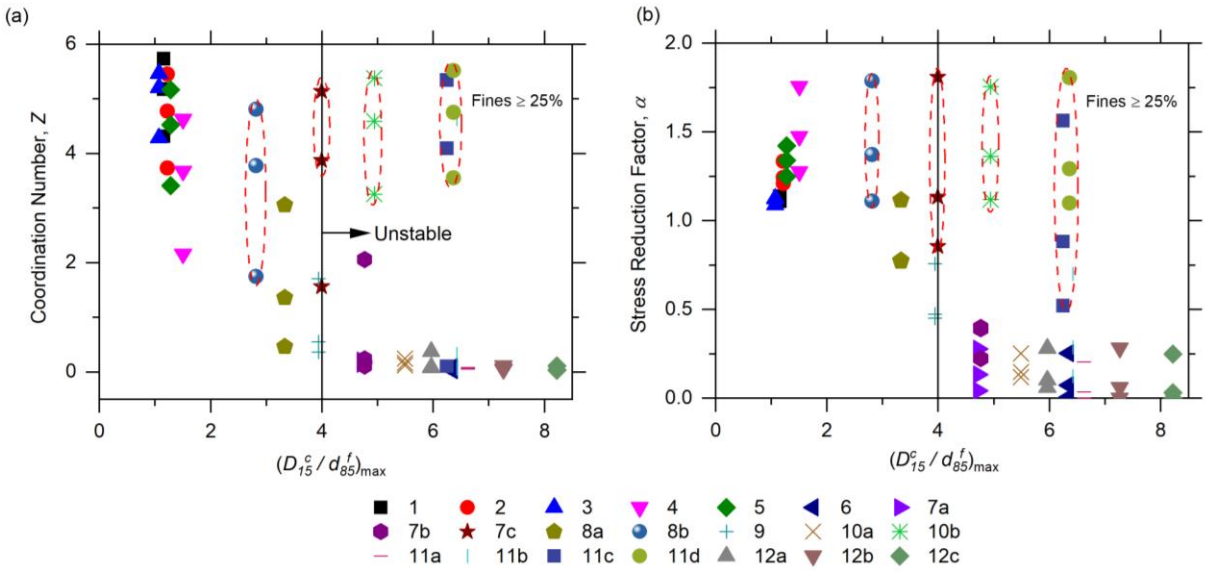

Fig. 4. 5 Variation of (a) coordination number with Kezdi's (1979) retention ratio and (b) stress reduction factor with Kezdi's (1979) retention ratio (Indraratna, Haq, et al. 2021) (reproduced with permission from Springer Nature)

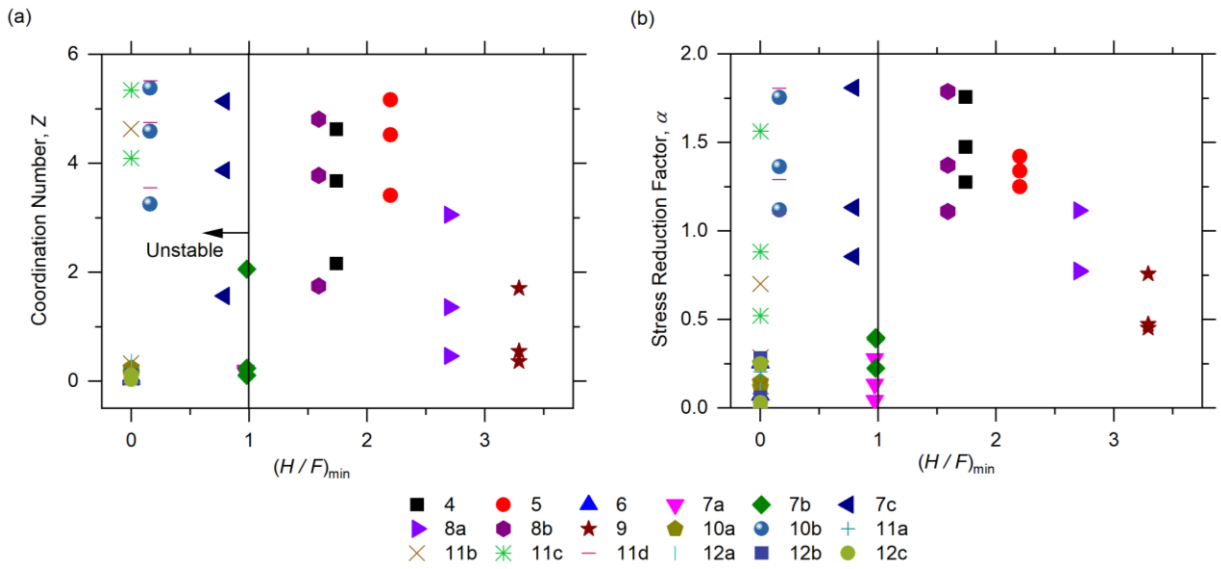

Fig. 4. 6 Variation of (a) coordination number with Kenney & Lau's (1985) retention ratio and (b) stress reduction factor with Kenney & Lau's (1985) retention ratio (Indraratna, Haq, et al. 2021) (reproduced with permission from Springer Nature)

4.5 SUMMARY

This chapter described internal instability at the microscale level using the DEM. A total of 63 DEM simulations were carried out on 21 different PSD curves at three different density levels. The microscale parameters, i.e., the coordination number (Z) and the stress reduction factor (α), were used to mark the boundaries between internally stable and unstable samples. The samples showed internal instability when $Z \leq 1$ or $\alpha \leq 0.5$. These microscale boundaries showed consistent results when compared to the constriction-based retention ratio. However, excessive scattering of the data occurred when the microscale parameters were plotted against particle-size-based criteria. Therefore, criteria based on particle size could not accurately predict internal instability because they do not take the relative density of soil into account in a quantifiable manner. In addition, samples with higher fines, i.e., more than 35%, could not be analyzed due to high computational cost, which can be considered a limitation of the current study.

CHAPTER 5 MICROMECHANICAL ANALYSIS OF SOIL TRANSITION FROM AN INTERNALLY STABLE TO AN UNSTABLE STATE

5.1 INTRODUCTION

Chapter 4 presented a novel approach to check the internal instability potential of cohesionless soils under an isotropic stress state. However, the stresses under railroad structures and on the downstream side of an embankment dam are anisotropic. Previous experimental studies examined internal instability under different stress paths (Chang & Zhang 2013; Ke & Takahashi 2015; Luo, Luo & Xiao 2020; Xiao & Shwiyhat 2012). Meanwhile, these laboratory tests only assessed the behaviour of granular soils at a continuum scale; hence the underlying micro mechanism is not yet fully understood. Therefore, the internal instability under anisotropic stress conditions could be modelled at a microscale using the Discrete Element Method (DEM) (O'Sullivan 2011).

This Chapter describes a series of simulations using DEM to check the internal instability of soil samples under anisotropic loading conditions. The novel findings of this Chapter show how shear-induced deformation can cause some samples that were internally stable under an isotropic stress state to become internally unstable under an anisotropic stress state. This Chapter also shows the different stages of evolution of the stress reduction factor due to shear-induced deformation of dense soil specimens; this has not previously been reported in recent studies (e.g., Sufian et al. 2021). It is noted that much of the contents of this Chapter have been submitted for publication:

Haq, S., Indraratna, B., Nguyen TT., & Rujikiatkamjorn, C. (2022). Micromechanical analysis of internal instability during shearing. *ASCE, International Journal of Geomechanics* ***(UNDER REVIEW)***

5.2 PARTICLE SIZE DISTRIBUTION CURVES AND SIMULATION APPROACH

Figure 5.1 shows a set of 10 particle size distribution (PSD) curves of the soil samples considered for analysis from a previous experimental study (Honjo, Haque & Tsai 1996). These samples show varying degrees of internal instability (Table 5.1). In order to replicate all fabric types, from underfilled to overfilled, two values for gap ratios, 2 and 3, were chosen from previous experimental studies (Honjo, Haque & Tsai 1996), and the fines content ranged from 10% to 40%. Gap-graded soils are used in numerous geotechnical engineering applications such as alluvial sediment deposits, moraines, glacial tills, mining waste, rockfill-soil mixtures used in embankment dams, fouled ballast under railroads, and geological hazards such as debris flows and landslides that cause the formation of gap-graded soils (Langroudi et al. 2013; Zhu et al. 2020). Table 5.1 shows the gap ratios, fines contents, initial void ratios, initial coordination numbers, initial stress reduction factors, and the number of particles considered.

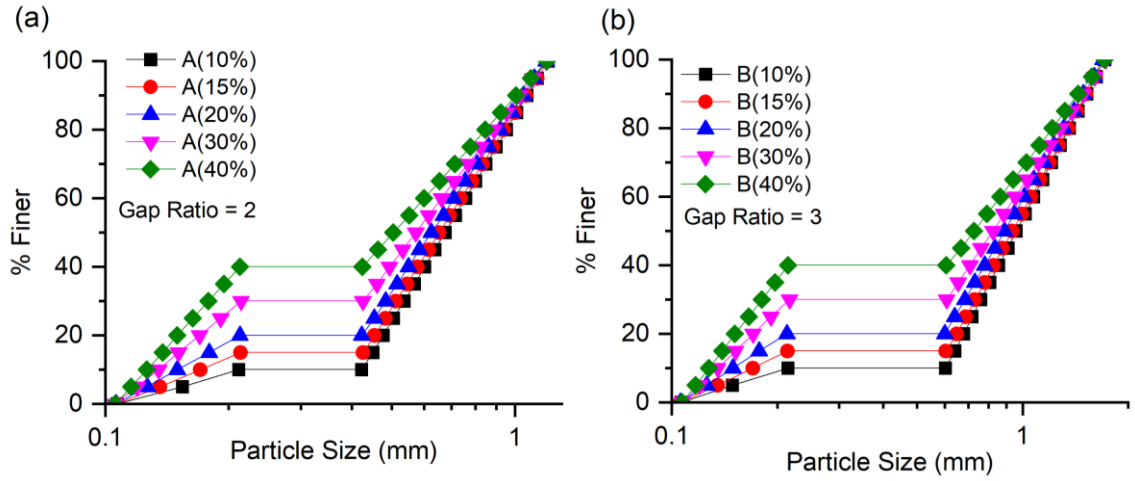

Fig. 5. 1 Particle size distribution curves (10 numbers) of soils analysed with the discrete element method

Table 5. 1 Properties of the particle size distribution curves used in the analysis

S. No.	Sample ID	Gap Ratio	FC (%)	R_d (%)	Initial Void Ratio (e_o)	Number of Particles	Initial Coordination Number (Z_o)	Initial Stress Reduction Factor (α_o)	Internal Instability*
1	A	2	10	95	0.3713	5000	0.719	0.459	Unstable
2			15	95	0.3131	10,000	0.858	0.337	Unstable
3			20	95	0.2854	12,000	3.058	1.116	Stable
4			30	95	0.3004	20,000	4.814	1.665	Stable
5			40	95	0.3203	30,000	5.202	1.616	Stable
6	B	3	10	95	0.3619	15,000	0.206	0.044	Unstable
7			15	95	0.2911	25,000	0.146	0.062	Unstable
8			20	95	0.2277	35,000	2.156	0.400	Unstable
9			30	95	0.2470	55,000	5.141	1.655	Stable
10			40	95	0.2851	85,000	5.419	1.739	Stable

*Assessment of internal instability using microscale criterion proposed by (Indraratna, Haq, et al. 2021)

Three-dimensional DEM simulations were carried out using an open-source code developed by Kloss et al. (2012). To avoid boundary effects, periodic boundaries were applied to the cubical samples during the simulation (Thornton 2000). The Hertz-Mindlin contact model was adopted. Spherical shapes were simulated with a particle density of 2650 kg/m^3. Young's modulus and Poisson's ratio of the particles were assumed to be 70 GPa and 0.3 (Thornton 2000).

In order to identify the fine particles not assisting in the transfer of stresses, periodic boundaries were used with the gravity of the particles switched off. Each sample had at least 500 particles in the coarser fraction of the particle size distribution curve, which was enough to attain a representative element volume (REV) (Shire et al. 2014). The samples were created in a dense state that was achieved through isotropic compression by setting the coefficient of friction (μ_s) = 0. The μ_s value was changed to

0.3 once the requisite stress level was reached, and then the samples were given enough cycles to equilibrate (Shire et al. 2014).

A strain-controlled method was used to compress a non-interacting cloud of particles to the target confining pressure = $p' = (\sigma_1' + \sigma_2' + \sigma_3')/3$ = 200 kPa. To assure the samples' quasi-static deformation, a strain rate was selected by maintaining the low inertial number (I_n) determined after the sensitivity analysis. The strain rate dropped to zero at p' = 200 kPa, thereby bringing the system into a state of equilibrium. The simulations were run for additional cycles sufficient to confirm equilibrium. As shown in Figure 5.2, the samples were then sheared under a constant p' stress path. Shearing was terminated when the axial strain reached 15%. The target stress at each time step was estimated at the constant p' drained loading conditions by assuming that the stresses in the *x* and *y* directions were equal. The p' is given as follows:

$$p' = \frac{\sigma_1' + \sigma_2' + \sigma_3'}{3} \tag{5.1}$$

Since $\sigma_2' = \sigma_3'$ therefore,

$$\sigma_2' = \sigma_3' = \frac{1}{2}(3p' - \sigma_1') \tag{5.2}$$

$$\sigma_{1,t+\Delta t}' = \sigma_{1,t}' + \left(\sigma_{1,t}' - \sigma_{1,t-\Delta t}'\right) \tag{5.3}$$

The desired stresses in the *x* and *y* directions at $t + \Delta t$ can be given by:

$$\sigma_{2,t+\Delta t}' = \sigma_{3,t+\Delta t}' = \frac{1}{2}\left(3p' - \sigma_{1,t+\Delta t}'\right) \tag{5.4}$$

The strain rates in the *x* and *y* directions can be determined using the following equation:

$$\dot{\varepsilon_2} = \dot{\varepsilon_{i2}} \left(\frac{\sigma_{2,t+\Delta t}' - \sigma_{2,t}'}{\sigma_{2,t+\Delta t}'}\right) \tag{5.5}$$

$$\dot{\varepsilon_3} = \dot{\varepsilon_{i3}} \left(\frac{\sigma_{3,t+\Delta t}' - \sigma_{3,t}'}{\sigma_{3,t+\Delta t}'}\right) \tag{5.6}$$

where $\dot{\varepsilon}_2$ and $\dot{\varepsilon}_3$ are the strain rates in the x and y directions, and $\dot{\varepsilon}_{i2}$ and $\dot{\varepsilon}_{i3}$ are the initial strain rates in the x and y directions.

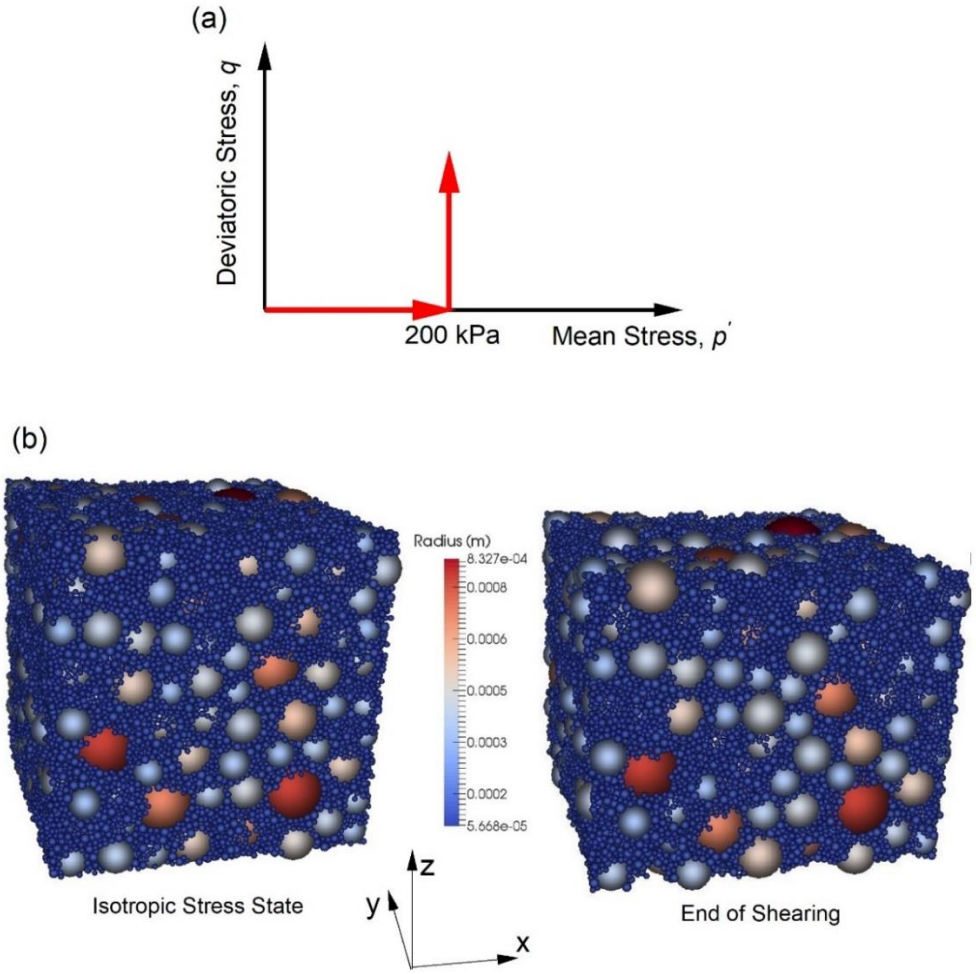

Fig. 5. 2 Constant mean stress path followed in the simulations; (b) isotropically compressed and sheared Sample B (30%) (fines content are given in brackets)

5.3 RESULTS AND DISCUSSION

5.3.1 Justification for smaller gap widths

At the isotropic stress state, Fig. 5.3a shows a plot of the percentage (by number) of unconnected cohesionless fine particles within the voids of the coarse particles for different gap widths and fines content. For a given particle size distribution curve, the gap width is the ratio of the minimum particle size in the coarser fraction to the maximum particle size in the finer fraction. It is shown that with 10% (by mass) fines, the

percentage of unconnected (suspended) fine particles by number is greater than 90% for both gap widths (i.e., 2 and 3) considered within the scope of this study. With 20% (by mass) fines, the proportion of unconnected fines by number is around 50% for both gap widths. In contrast, with higher proportions of fines corresponding to 30% and 40% (by mass), the percentage of fine particles (by number) for both gap widths is less than 20%. A lower percentage (by number) of unconnected fines at a higher percentage (by mass) of fines indicates that the fines occupy the voids between the coarse particles, thereby establishing contact with one another. From this, it can be concluded that at 10% and 20% of the fines with gap widths of 2 and 3, a notable number of unconnected fines can still be present in the voids of the coarse particles.

Figure 5.3b shows the percentage of unconnected particles with the percentage of fines. With an increasing proportion of fines, the unconnected particles decrease. This is because the fine particles occupy the voids between the coarse particles and remain connected to each other as the proportion increases. The decrease in unconnected particles is insignificant when the fines content is ≥ 30%. Therefore, a fine content = 30% can be considered as the threshold required to connect the unconnected particles in voids for gap ratios 2 and 3.

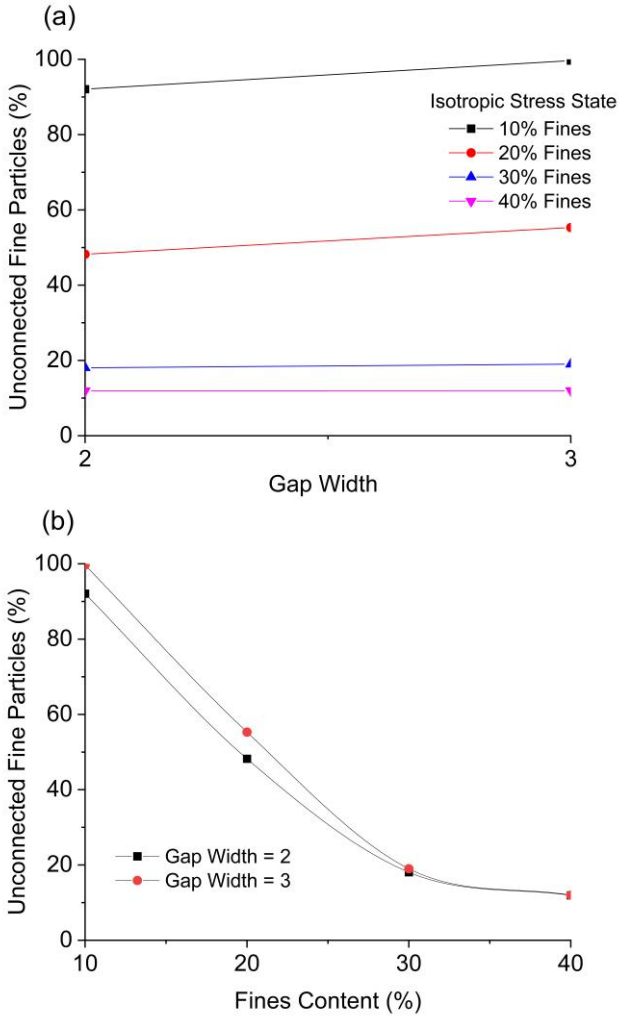

Fig. 5. 3 Percentage (by number) of unconnected fines with different gap widths and fines content

5.3.2 Stress-Strain Behaviour

Figure 5.4 shows the macroscopic stress-strain behaviour of the sample after being sheared under drained conditions with a constant mean stress path. When shearing, the contacts do not engage, which causes the stress-strain curves to oscillate (Sufian et al. 2021). How the contacts engage during shearing is determined by the initial fabric of the sample. Selected examples include the stress-strain curves of Samples A (40%) and B (40%), with the fines indicated in brackets, showing more subtle variations than the other samples in their respective groups. At relatively low axial strains (< 2%), all samples

show a noticeable peak deviatoric stress (q_{peak}), indicating that the samples were stiff (dense).

Figure 5.4 also shows that the gap ratio and fines influence the macroscopic stress-strain behaviour. All samples show post-peak strain softening; however, samples with higher fines show a significant drop in post-peak deviatoric stress, i.e., indicating a greater degree of post-peak strain softening than those with lower fines content. For example, at the end of the shear, the post-peak deviatoric stress of Sample B (30%) is less than Sample B (20%). The relative densities of both samples are the same; however, the fine contents are different; hence the post-peak deviatoric stresses of Samples B (30%) and B (20%) are different. For Sample A with a gap ratio of 2 and different fines, the stress-strain curves are similar because the difference in size of the coarse and fine particles is insignificant due to a smaller gap ratio. While for Sample B with a gap ratio of 3 and different fines, the stress-strain curves are different because the sizes of the coarse and fine particles are significantly different.

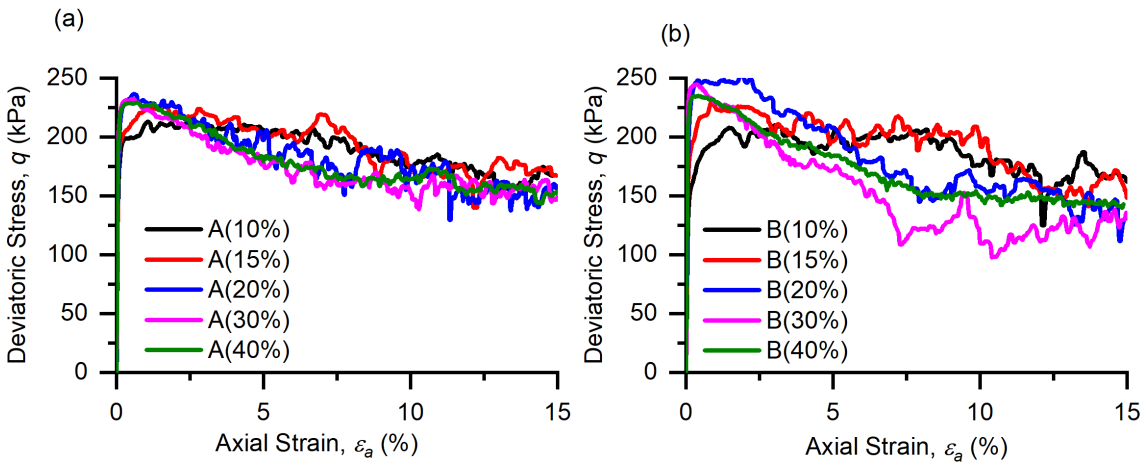

Fig. 5. 4 Stress-strain curves of all specimens under drained shearing with a constant mean stress path

5.3.3 Volumetric Strain versus Axial Strain

Figure 5.5 shows the development of volumetric strain (ε_v) with axial strain. A positive value of ε_v implies that the specimen has dilated. The magnitude of ε_v first increases until it reaches a critical value and then remains relatively constant. This is considered to be the critical state, where shear deformation continues without changing the sample volume. The samples with a higher proportion of fines reach the critical value of ε_v at lower axial strains than those with a lower proportion of fines. For example, in Sample A(30%), ε_v becomes constant at about 6% of axial strain, whereas in Sample A(20%), ε_v becomes constant at about 10% of axial strain. Similarly, Sample B (30%) reaches the critical ε_v level at about 5% axial strain, but Sample B (20%) shows no apparent convergence of strain to a constant value. For both the gap ratios = 2 and 3, specimens with 30% fines undergo the least amount of dilation than the other specimens because of the filled fabric, i.e., fine particles completely fill the voids between the coarse particles, restricting the dilation of the specimens.

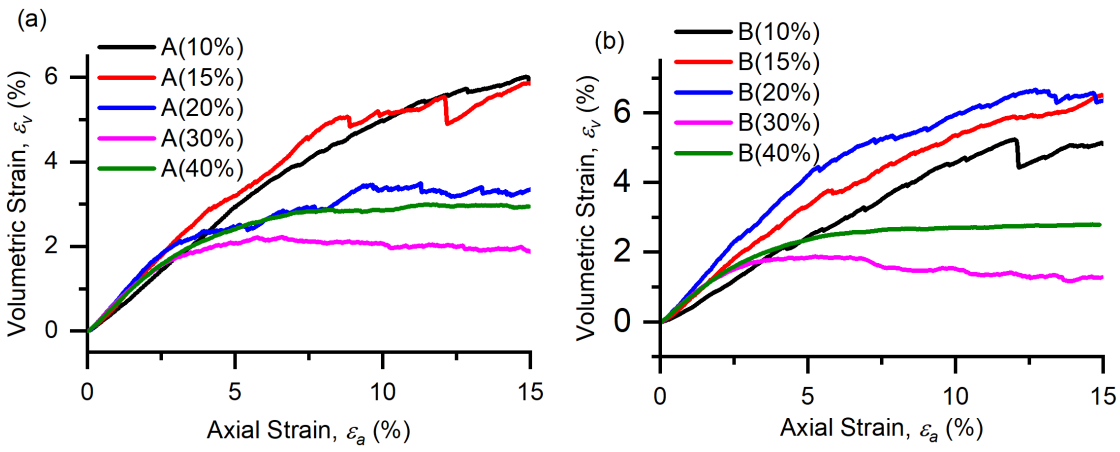

Fig. 5. 5 Evolution of the volumetric strain (ε_v) with axial strain

5.3.4 Varying Initial Void Ratio and Peak Strength with Fines Content

Figure 5.6a shows the correlation between the fines content and the initial void ratio (e_o) for each gap ratio. Initial void ratio (e_o) is affected by fines, gap ratio and density. e_o

decreases as the proportion of fine increases because the fine particles occupy the voids between the coarse particles. At a certain fines content, the voids are completely occupied by fine particles, whereby the void ratio reaches a minimum value; in this particular case (Figure 5.6b), there is no more space between the coarse particles to accommodate further fine particles. As additional fines are introduced, the coarse particles must be separated, and the fine particles become more dominant in the mixture. As a result, coarse particles float in the matrix of fine particles, which is known as an overfilled fabric (Figure 5.6b). The void ratio increases after reaching the overfilled fabric. The proportion of fines needed to achieve the lowest value of e_o is determined by the gap ratio; a sample with a higher gap ratio requires more fines to fill the voids. Figure 5.6c shows the development of the peak deviatoric stress (q_{peak}) for different fines content. As the proportion of fines increases, e_o decreases, causing the q_{peak} value to increase. The highest value of q_{peak} is reached at the lowest value of e_o. After the maximum of q_{peak}, the value of q_{peak} decreases as e_o increases with increasing fines.

The numerical results show that the influence of the gap ratio on q_{peak} is insignificant at 10-15% fines. However, this influence becomes more pronounced when the fines content exceeds 15%. The larger the gap ratio, the larger q_{peak}; in particular, the largest q_{peak} is about 254 kPa at a gap ratio of 3 but decreases to about 237 kPa as the gap ratio decreases to 2. As fines continue to increase and the soil becomes overfilled, the difference between the two curves narrows due to the increasing role of fines in shear strength. It is to be expected that the two curves, which represent different gap ratios, will converge with an increasing proportion of fines (>40%) and will have a significant influence on the shearing behaviour of the soil.

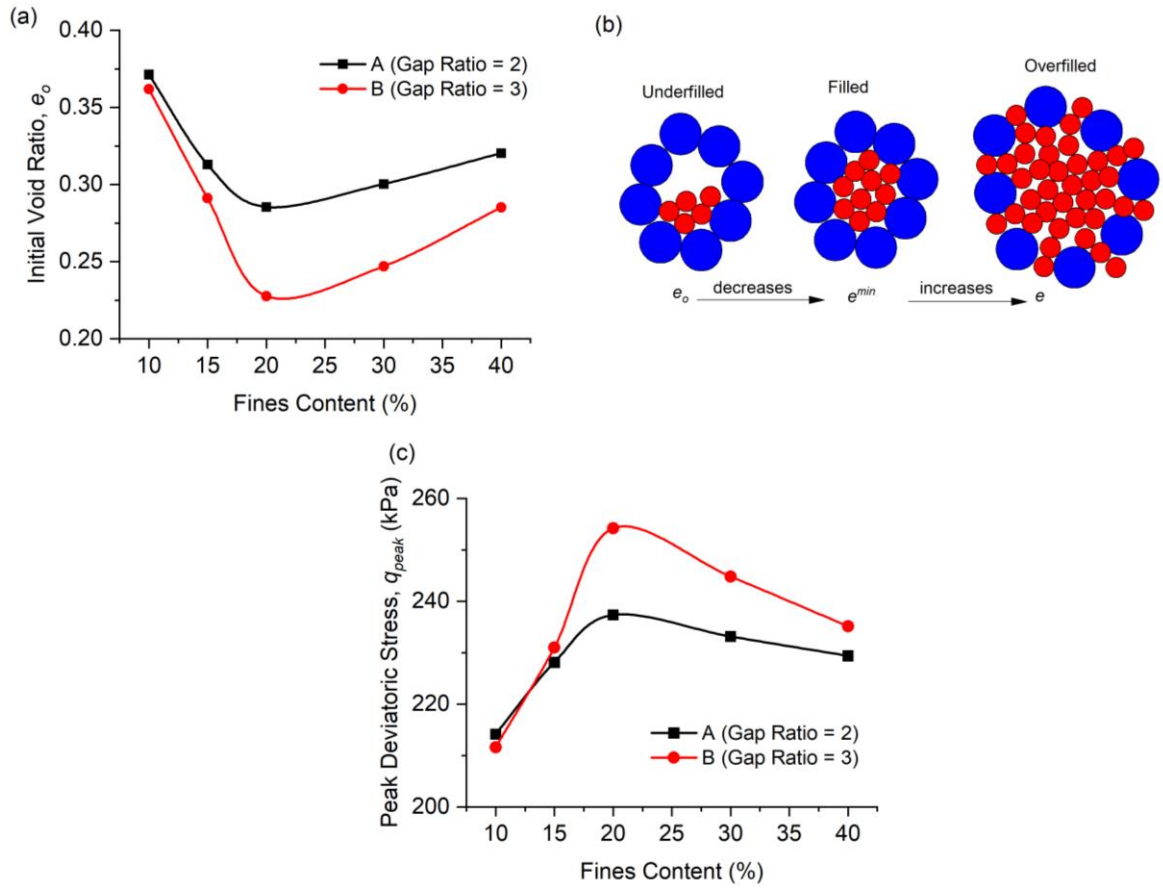

Fig. 5. 6 (a) Relationship between the fines content and the initial void ratio, (b) schematic sketch of different fabric cases, (c) relationship between the fines content and the peak deviatoric stress

5.3.5 Evolution of Coordination Number during Shearing

Figure 5.7 shows the variations in coordination number (Z) with axial strain. Z is a microscale parameter that describes the average number of contacts per particle and is given as follows (Thornton 2000).

$$Z = \frac{2N_c}{N_p} \tag{5.7}$$

where N_c = the number of contacts, and N_p = the number of particles in the specimen.

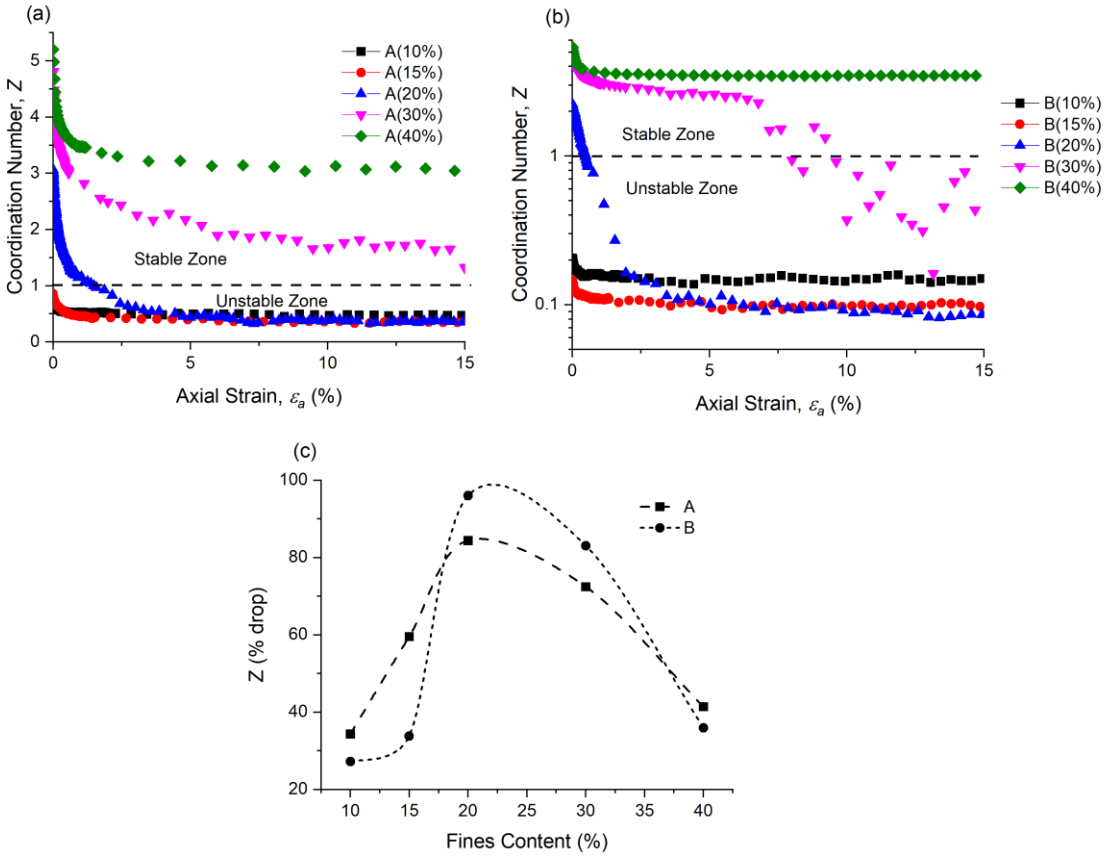

Fig. 5. 7 (a), (b) Development of the coordination number (Z) with axial strain for specimens A and B, and (c) percentage of drop in Z values with fines content

During the early shearing phase, the value of Z changes rapidly until it reaches a critical value that remains constant thereafter. The decrease in Z values can be attributed to the shear strain breaking the particle contacts. The initial rapid decline in coordination number implies that the rate of contact breakage exceeds the rate at which new contacts are formed. In the critical state, this rate of breakage and formation of new contacts becomes equal (Rothenburg & Kruyt 2004). It is apparent that the critical coordination number is a function of the PSD and the proportion of fines. For Sample B(30%), the Z value suddenly falls below the critical value. These fluctuations in Z values are caused by local instability and increasing particle mobility (Thornton 2000). If actual boundaries were used, strain localisation and shear band formation could occur, but when the uniform strain field is applied, strain localisation cannot occur in periodic cells (Thornton 2000).

Figure 5.7c shows the percentage decrease of Z during the shear-induced deformation with the fines content. The overall behaviour can be divided into three categories: (i) the decrease in Z value is less for samples with a low fines content, (ii) the value of Z decreases dramatically for samples with 20 to 30% fines, but the percentage of decrease is also affected by the gap ratio, (iii) the decrease in Z is again lower for overfilled samples with a higher proportion of fines, and this is consistent across different gap ratios. In Fig. 5.7c, it is noticeable that the decrease in the value of Z is greater than 80% for samples that change from an internally stable to an unstable state, i.e., Samples A (20%), B (20%), and B (30%).

5.3.6 Development of Stress Reduction Factor during Shearing

Figure 5.8 shows a three-dimensional plot of the stress reduction factor (α), the axial strain, and the stress ratio (q/p'). The α is the ratio of the mean stress carried by the fines to the overall mean stress, which was determined using the method described by Shire et al. (2014). The value of α indicates how much the fine particles contribute to stress transfer and the overall stress-strain response; hence, it can be used as an index to determine internal instability. A low value of α indicates a significant likelihood of internal instability (Shire et al. 2014). The samples can be divided into two distinct groups based on their behaviour. The first group consists of samples with a low fines content and underfilled fabric, i.e., Samples A(10%), A(15%), B(10%), and B(15%). Because the fine particles do not contribute to the deviatoric stress and remain loose in the voids of the coarse particle fractions, the values of α with the axial strain and stress ratio remain constant, albeit with minor fluctuations. After the peak stress ratio, the α value for Sample B (15%) increases slightly.

The second group consists of samples with a higher proportion of fines, i.e., Samples A(20%), A(30%), A(40%), B(30%), and B(40%). During shearing, α changes

significantly. In Sample B (30%), the α value drops dramatically from 1.655 to 0.751; likewise, in Sample A (30%), it decreases from 1.665 to 0.964. The drop in α of Samples A (40%) and B(40%) is not as significant as that of Samples A(30%) and B(30%). In this sense, the development of α for samples in the second group can be divided into three stages. In stage 1, α remains constant up to a stress ratio = 0.80 with a low axial strain value; in stage 2 α decreases slightly as it approaches the peak stress ratio, and stage 3 is the post-peak region, where the value of α falls dramatically. For example, in Samples A(20%), A(30%), A(40%), B(30%), and B(40%), α remains practically constant until the peak stress ratio is reached with a small axial strain value; thereafter, the value of α gradually decreases until it reaches the peak stress ratio. The value of α then drops dramatically after the peak stress ratio.

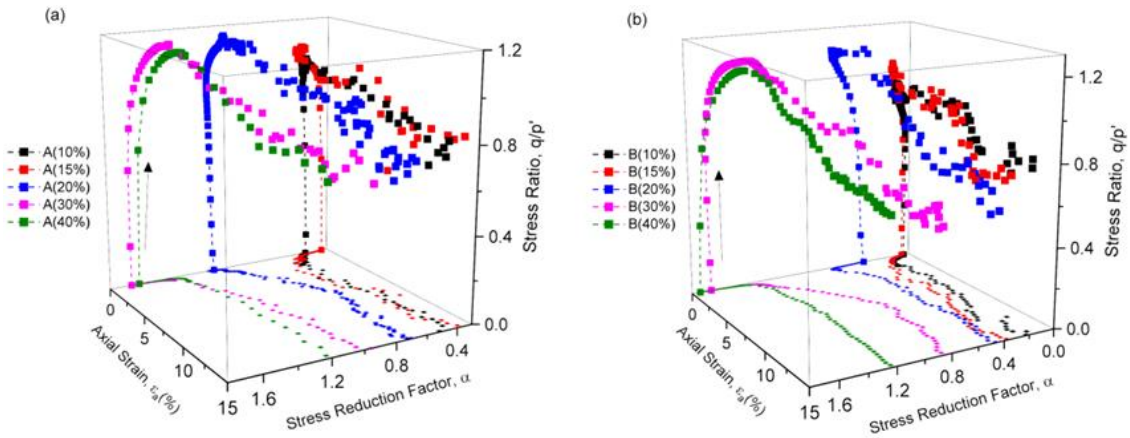

Fig. 5. 8 Three-dimensional plot between the stress reduction factor ($\boldsymbol{\alpha}$), the axial strain ε_a (%) and the stress ratio (q/p')

For a certain axial strain and stress ratio, the α value of both gap ratios increases with the proportion of fines. Fine particles begin to intervene in the load-carrying process as their proportion increases; however, the magnitude of their contribution varies with the gap ratio. For example, with the same proportion of fines, e.g., at 30% fines, the value of α drops with an increasing gap ratio. Because as the gap ratio increases, fines can easily fit into the voids between the coarse particles. With a higher proportion of fines, i.e., 40%,

α increases with the gap ratio because a larger number of fine particles separate the coarse particles and are now accessible to carry and distribute the stresses (Sufian et al. 2021). For example, at the isotropic stress state, Sample A(20%) has a α value of 1.116 while Sample B(20%) has a α value of 0.40. In contrast, the α value of Sample A(40%) is 1.616, while that of Sample B(40%) is 1.740.

The coordination number (Z) and the stress reduction factor (α) were used to assess the internal instability of granular soils, as explained elsewhere by Indraratna et al. (2021). The Z and α values are used to define the boundaries between internally stable and unstable soils (Figures 5.7 and 5.8). For instance, samples with the potential for internal instability exhibit $Z \leq 1$ or $\alpha \leq 0.5$. Sample A(20%) has an initial value of Z = 3.06 and α = 1.116; however, the critical value of Z becomes less than 1, and the sample becomes internally unstable. Similarly, Sample B(30%) has an initial $Z > 1$ and $\alpha > 0.50$, and thereafter, the value of Z becomes less than unity. As a result, it transforms from internally stable to unstable materials with dilation.

5.3.7 Development of the Stress Reduction Factor with Fine-Fine and Fine-Coarse Coordination Number

Figure 5.9 shows the progression of α with fine-fine and fine-coarse coordination numbers ($Z^{fine\text{-}coarse}$) during shearing, where $Z^{fine\text{-}coarse}$ is defined by (Minh & Cheng 2013):

$$Z^{fine-coarse} = \frac{2(N_c^{fine-fine} + N_c^{fine-coarse})}{N_p^{fines}} \tag{5.8}$$

where $N_c^{fine-fine}$ is the number of contacts between the fine particles, $N_c^{fine-coarse}$ is the number of contacts between the fine and coarse particles and N_p^{fines} is the total number of fine particles. Although their percentage is lower, the fine particles outnumber the coarse particles.

Fabrics are classified into three categories (Shire et al. 2014; Thevanayagam et al. 2002). (i) Type 1 includes Case I and Case IV (Fig. 5.9), where mainly the coarse particles are in contact with each other. In Case I, the fine particles are loose in the voids of the coarse particles, and their erosion does not appreciably disturb the structure of the coarse particles. In Case IV, fine particles get stuck between the coarser particles and are overstressed. (ii) Type 2 is Case II, where coarse particles are primarily in contact with each other, and the fine particles serve as a support. In this case, both the coarse and fine particles affect stress transfer, but the coarse particles govern the transfer of stresses. The loss of fines can cause the fabric of the coarse particles to disintegrate, (iii) Type 3, i.e., Case III represents the situation where the fine particles are mainly in contact with each other, and the coarse particles are dispersed in the mixture (overfilled by fines). In this scenario, both coarse and fine particles transmit equal amounts of stress. Each case with different intergranular contacts may show a distinct drained shear response. During the shear-induced dilation of the samples, a transition in the microstructure between different cases can occur.

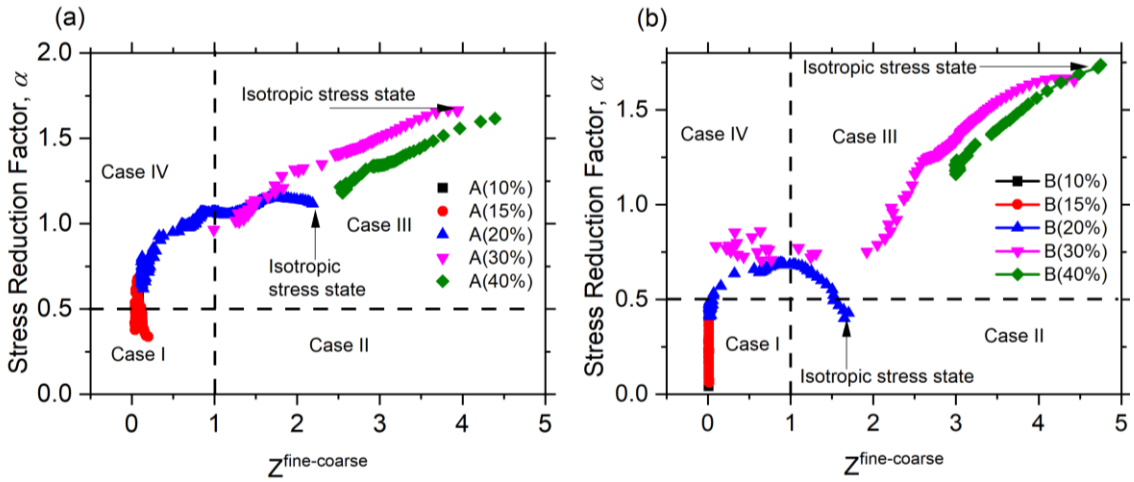

Fig. 5. 9 Evolution of the stress reduction factor (α) with fine-coarse coordination number ($Z^{fine\text{-}coarse}$)

Figure 5.9 shows the development of the fabrics of various samples with dilation during shearing. For instance, Sample A(20%) begins with the overfilled fabric in Case

III with $Z^{fine-coarse} > 1$ and $\alpha > 0.5$; however, it moves from Case III to Case IV with $Z^{fine-coarse} < 1$ and $\alpha > 0.5$ towards the end of shearing due to sample dilation. This means that the fine particles were once in contact with each other but have already lost contacts. Similarly, Sample B(20%) shows Case II with $Z^{fine-coarse} > 1$ and $\alpha < 0.5$ at the isotropic stress state and transitions to Case I with $Z^{fine-coarse} < 1$ and $\alpha < 0.5$ at the end of shearing, indicating that fines are now loosely seated between the coarse particles and can be eroded without affecting the coarse particles. These findings have practical implications since the samples with overfilled fabric could be internally stable at the isotropic stress state; however, due to shear-induced deformation, they could transition from internally stable to unstable soils with underfilled fabric.

5.3.8 Variation of the Coarse-Coarse Coordination Number with Deviatoric Stress

Figure 5.10 shows the evolution of the coarse-coarse coordination number ($Z^{coarse\text{-}coarse}$) with the deviatoric stress. The value of $Z^{coarse-coarse}$ is defined as (Minh & Cheng 2013):

$$Z^{coarse-coarse} = \frac{2N_c^{coarse-coarse}}{N_p^{coarse}} \tag{5.9}$$

where $N_c^{coarse-coarse}$ is the number of coarse particles contacts, and N_p^{coarse} is the number of coarse particles.

$Z^{coarse\text{-}coarse}$ decreases rapidly until the peak deviatoric stress is reached and then increases slightly. Consequently, the stress reduction factor (α) remains constant until the stress ratio reaches the peak value (Figure 5.8). As a result, in the early phase of shearing up to the peak of the deviatoric stress, the coarse particles are separated by dilation. However, the stresses they carry remain constant (constant α), overstressing the reduced coarser contacts. The loss of contacts for coarse particles ceases after the peak deviatoric stress, whereas α continues to drop. Consequently, the coarser particles are subjected to

increased stress as the α lowers. Because coarse particles carry significant stresses, they re-establish some contacts after the peak when the $Z^{coarse\text{-}coarse}$ value increases slightly in some samples (e.g., A(20%), A(30%), A(40%), and B(30%). This behaviour of $Z^{coarse\text{-}coarse}$ is consistent across different samples, although the initial value of $Z^{coarse\text{-}coarse}$ changes with fines content.

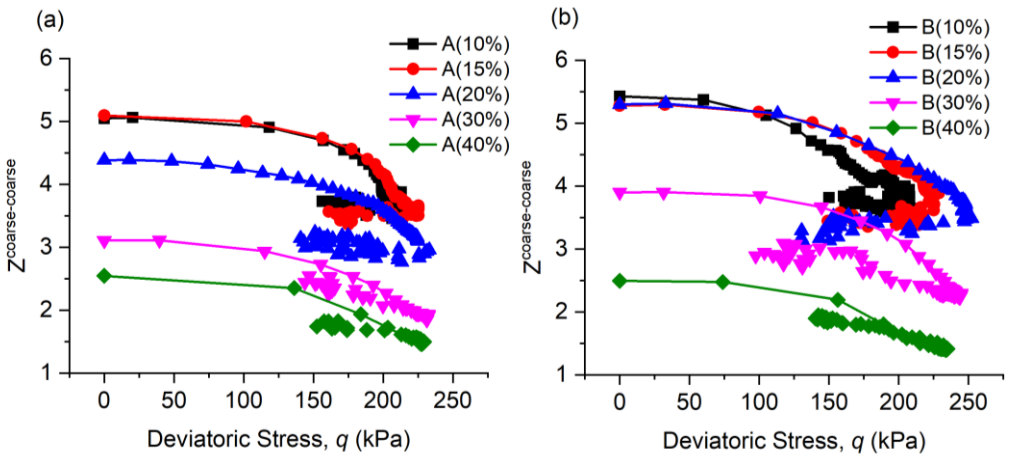

Fig. 5. 10 Variation of the coarse-coarse coordination number ($Z_{coarse\text{-}coarse}$) with deviatoric stress

5.3.9 Development of Sliding Contacts with Axial Strain

Figure 5.11 shows the development of sliding contacts with axial strain. The sliding contacts are identified using the following equation:

$$S_i = \frac{f^T}{\mu_s f^N} \tag{5.10}$$

where S_i represents the sliding index, f^T represents the tangential contact force, and f^N represents the normal contact force. When f^T fully mobilises the friction, sliding contacts occur, i.e., $S_i = 1$.

The percentage of sliding contacts increases first, reflecting the initial shear stage where the deviatoric stress increases rapidly (see Fig. 5.4). After reaching a peak value, it decreases and then remains constant, which is when the critical state takes place with constant volumetric strain. It is worth noting that the percentage of sliding contacts

increases after the peak (axial strain > 3%) in Sample B (30%). This can be attributed to the local instability and significant particle mobility, consistent with the evolution of the coordination number with axial strain for this sample, as mentioned previously (see Fig. 5.7).

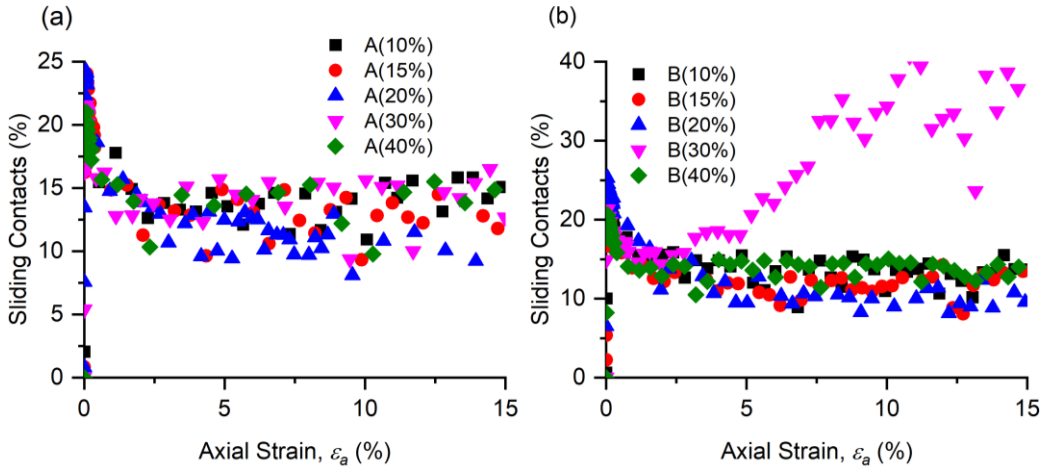

Fig. 5. 11 Development of the proportion of sliding contacts with axial strain.

5.3.10 Directional Distribution of Contacts

Figure 5.12 shows the directional distribution of contacts (rose histograms) in selected Samples A(10%), B(10%), and B(15%) at the isotropic stress state and at the end of shear. These results only apply to the x-z plane as the distribution of contacts in the y-z plane is similar. The distribution of the contacts is the same in all directions at the isotropic stress state, as shown in Fig. 5.12. However, at the end of the shear, anisotropy develops in the contact networks, and the contact distribution is not equal in all directions. Therefore, shear deformation of soil due to contact separation leads to structural anisotropy. The number of contacts in the major principal stress direction is higher than that of minor principal stress. Consequently, the major contact losses occur during shear deformation in the lateral strain direction perpendicular to the direction of major principal stress.

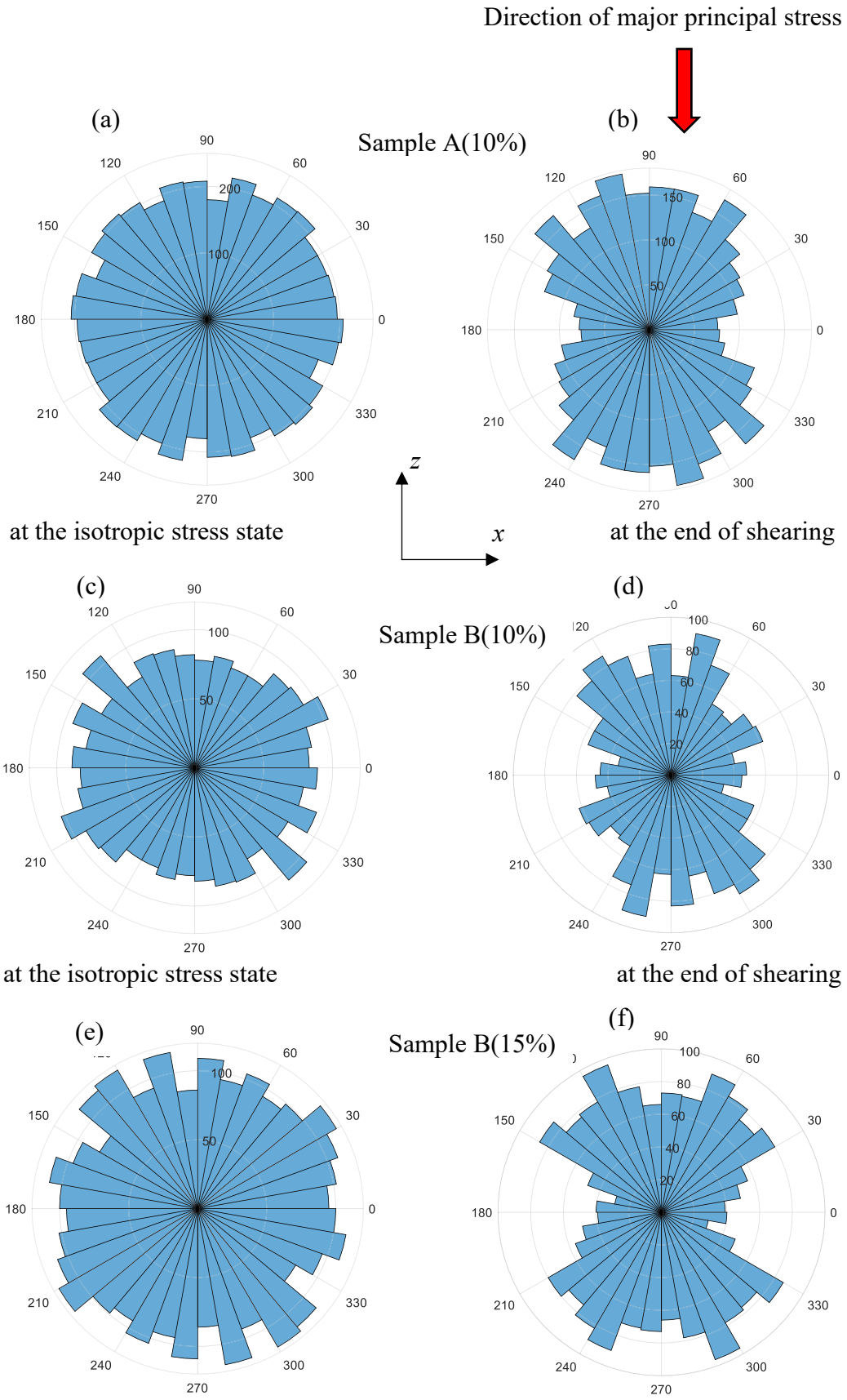

Fig. 5. 12 Rose histograms of the contacts for selected Samples 1(10%), 2(10%) and 2(15%)

5.4 SUMMARY

A total of 10 DEM simulations were carried out on 10 particle size distribution curves. The specimens were prepared in a dense state and sheared under drained conditions along a constant mean stress path to study the influence of stress anisotropy on micromechanics. The development of microscale parameters such as the coordination number, partial coordination number, sliding contacts, and stress reduction factor was observed. The simulations showed that certain internally stable samples could become unstable during shear-induced dilation. This was confirmed by observing the evolution of the coordination number and stress reduction factor due to shear-induced deformation of soil samples.

The coordination number initially decreased rapidly, showing that the contact breaking rate was higher than the contact forming rate. It then remained constant, with the rate of breakage and the formation of contacts remaining the same. In addition, three distinct stages in the development of the stress reduction factor were observed in the dense, overfilled fabric samples. Stage 1 was characterised by α remaining constant when the stress ratio (q/p') was less than 0.80 at a low axial strain value. Stage 2 was characterised by a slight decrease in α as it approached the peak q/p', and Stage 3 was characterised by a significant decrease in α due to shear-induced dilation in the post-peak region.

CHAPTER 6 HYDROMECHANICAL STATE OF SOIL FLUIDISATION – A MICROSCALE PERSPECTIVE

6.1 INTRODUCTION

Chapters 4 and 5 included the use of the Discrete Element Method (DEM) to describe how hydromechanical instability of granular soils could occur. However, the fluid part was ignored in the previous chapters; therefore, the hydraulic conditions could not be considered. Since it is vital to consider the hydraulic conditions, this chapter addresses the fluid-particle interaction and examines an important hydromechanical failure mode called fluidisation that implies the transition of a stable soil to a slurry-like state due to loss of contacts between soil particles, often known as mud pumping or subgrade fluidisation in railway terminology. Mud pumping occurs when soil slurry penetrates the overlying coarser ballast layer of rail tracks. While literature reveals that experiments have been carried out to study fluidisation and mud pumping (Hudson et al., 2016; Indraratna et al., 2020), these laboratory investigations only provide a macroscale response, whereas the evolution of fabric at the microscale may reveal the mysteries associated with fluidisation. This means the Discrete Element Method (DEM) could be used to evaluate the fabric of soil during fluidisation.

This chapter aims to study soil fluidisation at the microscale through the discrete element concepts of (i) coordination number (average number of contacts per particle) and (ii) constraint ratio (ratio of number of constraints to the number of degrees of freedom in the particle system). In this study, the DEM was coupled with the Lattice Boltzmann Method (LBM) to simulate fluid-particle interaction. An upward hydraulic gradient was applied to the specimen, and the evolution of effective stress was noted as the hydraulic gradient increased. A novel criterion based on microscale parameters was proposed to characterise the transformation of granular soil from stable to liquid-like

material. A significant part of this Chapter has been adapted from the following work and reproduced with permission from Springer Nature:

Haq, S., Indraratna, B., Nguyen, T. T., & Rujikiatkamjorn, C. (2022). Hydromechanical state of soil fluidisation: a microscale perspective. Acta Geotechnica. https://doi.org/10.1007/s11440-022-01674-7

6.2 SIMULATION APPROACH

Three-dimensional LBM-DEM simulations were carried out using the Hertz-Mindlin contact model with Young's modulus and Poisson's ratio of particles set as 70 GPa and 0.3, respectively (Thornton 2000). The particle density was set to 2650 kg/m^3, and rigid boundary walls were used. The gravitational deposition method was used for sample preparation (Abbireddy & Clayton 2010), whereby the acceleration due to the force of gravity of the particles was set to 9.81 m/s^2. The particles were initially created in a larger volume with no overlap, and then particles were dropped under gravity. The particles were allowed to settle until equilibrium was reached, thereby ensuring that the coordination number remained constant for a sufficient number of numerical cycles.

Since it is not always possible to simulate the actual void ratios and fabric with an assembly of purely spherical particles, the notion of relative density was utilised to simulate the experimental conditions, as suggested by Salot et al. (2009). The sample was prepared in a dense state by setting the coefficient of friction (μ_s) to 0 (Abbireddy & Clayton 2010; Cundall 1988). Subsequently, μ_s was changed to 0.30, and the particles were re-equilibrated with a sufficient number of numerical cycles before they became saturated with fluid (Cundall 1988; Thornton 2000). The value of μ_s used here was in the range of real quartz particles that can be determined experimentally with a micromechanical interparticle loading apparatus (e.g., Senetakis et al., 2013). The

particle-wall contact parameters were assumed to correspond to the particle-to-particle contact parameters (Hu, Zhang & Yang 2019).

The fluid density was set to 1000 kg/m^3 with a kinematic viscosity of 1 x 10^{-6} m^2/s according to pure water properties at 20 ^{o}C and 1 atmosphere (101 kPa). The resolution of the fluid lattice was chosen with at least 5 lattices in each particle, i.e., the diameter of the smallest particle corresponds to at least 5 fluid cells based on the validation of a single-particle displaced downwards into the fluid that was described previously. A relaxation parameter close to but greater than 0.50 was chosen, and the Mach number was kept below 0.1, inspired by the need for improved accuracy, as explained elsewhere by Han et al. (2007). Fluid flow was initiated with the relevant inlet and outlet pressure boundary conditions, and no-slip conditions were imposed on the boundaries perpendicular to the flow. For each hydraulic gradient applied, the flow was continued over a sufficient period of time until a steady-state condition was attained.

6.3 PARTICLE SIZE DISTRIBUTION AND HOMOGENEITY OF THE SAMPLE

Figure 6.1(a) illustrates the particle size distribution of the sample selected from an experimental study carried out by Indraratna et al. (2015). Figure 6.1(b) shows the three-dimensional DEM-based sample with 17607 particles, and the direction of flow of the fluid is also shown, i.e., the *z*-direction. Figure 6.1(c) shows the sample after being divided into 10 different inner layers. The ratio of the lateral dimension of the simulation domain to the maximum particle diameter was greater than 12 in order to obtain a representative elementary volume (REV) and avoid the boundary effects. A local decrease in the void ratio occurred near the rigid boundaries (O'Sullivan, 2011), so the bottom boundary layer (besides the rigid bottom boundary) was omitted in order to nullify the boundary effects (Huang, Hanley, O'Sullivan & F. C. Y. Kwok 2014). The thickness of each layer was more than twice the maximum particle diameter in order to define a

REV (Huang, Hanley, O'Sullivan & F. C. Y. Kwok 2014). The stresses at the boundaries do not reflect the actual material response, so the interaction of the particles in each layer with the lateral boundaries was not considered.

Figure 6.1(c) shows the similar initial void ratios of all layers, indicating the REV in each layer. The initial homogeneity of the sample was further confirmed by considering the variances in the void ratios as reported by Jiang et al. (2003):

$$S^2 = \frac{1}{n_L - 1} \sum_{k=1}^{n_L} (e_{oi}^k - e_{oi}^{avg})^2 \tag{6.1}$$

where S is the variance of the void ratios, n_L is the total number of layers, e_{oi}^k is the initial void ratio of the k^{th} layer, and e_{oi}^{avg} is the initial void ratio of the entire sample. The S^2 value for the sample in Fig. 6.1(c) is 2.72 x 10^{-5}, which is low enough to classify the sample as homogenous with respect to the REV in each layer. The overall void ratio of the numerical sample is the same as the experimental sample. Note that the void ratio only considers the volume of the voids and solid particles, not the particulate structure of the granular medium. Figure 6.1(d) shows an enlarged view of the particles modelled in the fluid mesh. It is noteworthy that the mesh is much smaller than the particle and pore sizes, unlike the conventional unresolved approach with the Navier-Stokes equation.

6.4 CALIBRATION

Figure 6.2 shows the calibration of the numerical model of soil fluidisation by comparing the flow curves obtained from the LBM-DEM approach, an earlier experimental study (Indraratna, Israr & Rujikiatkamjorn 2015), and a semi-analytical solution (Ergun 1952) as follows:

$$\frac{\Delta P}{L} = \frac{150\mu_f v_d (1-n)^2}{d_p^2\, n^3} + \frac{1.75\rho_f v_d^2 (1-n)}{d_p\, n^3} \tag{6.2}$$

where ΔP is the pressure drop across the particle bed, L is the height of the bed, d_p is the particle size and in this study is selected equal to d_{50} (the particle size that is 50% finer by mass in the particle size distribution), n is the overall porosity, μ_f is the dynamic viscosity of the fluid, and v_d is the superficial or discharge velocity of the fluid.

The flow curves obtained from the LBM-DEM approach, experimental, and semi-analytical methods agree with each other. The overall critical hydraulic gradient ($i_{o,cr}$) predicted by the LBM-DEM approach was 1.050, while the semi-analytical and experimental values of $i_{o,cr}$ were 1.133 and 1.180, respectively. These values are in acceptable agreement with one another.

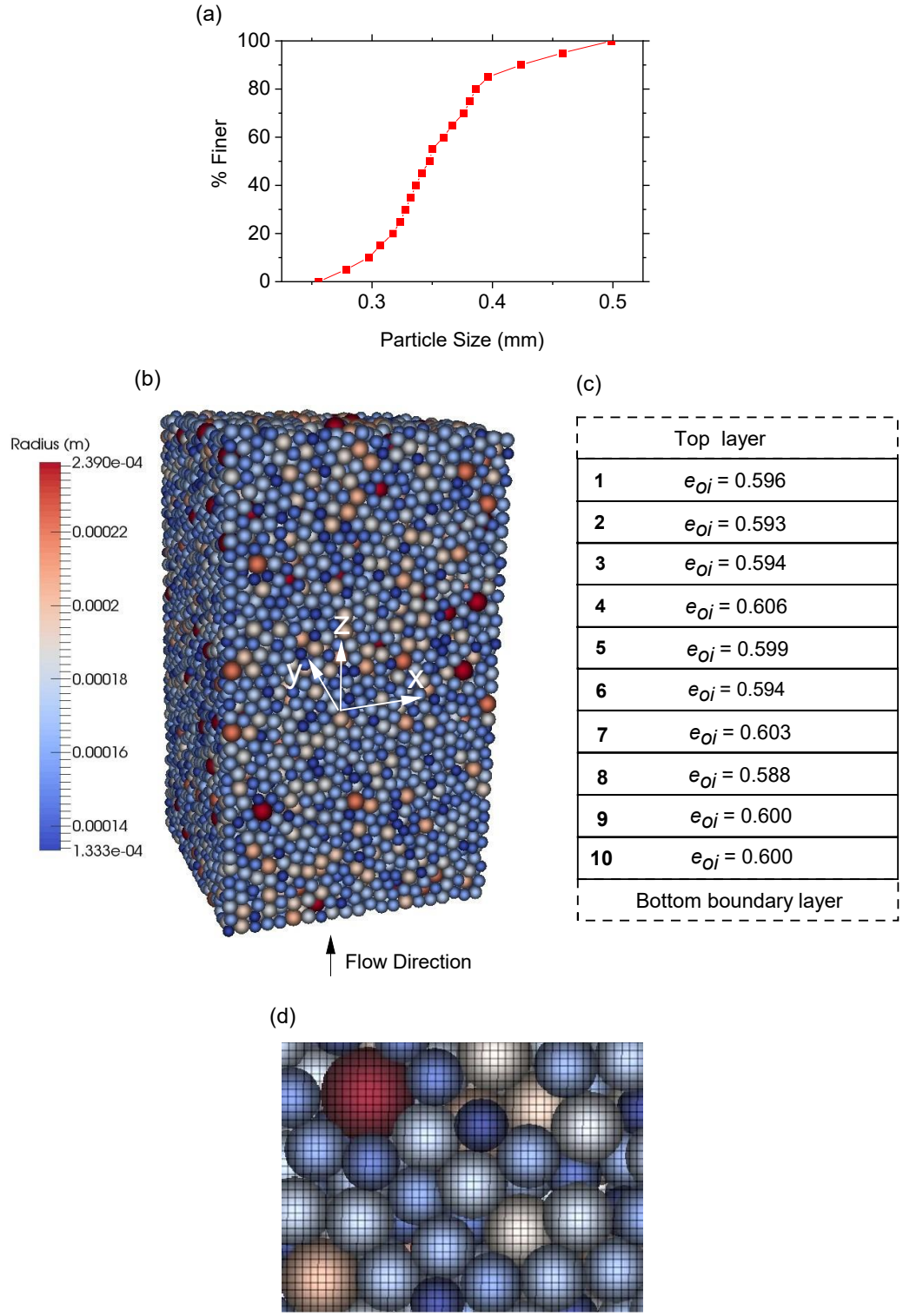

Fig. 6. 1 (a) Particle size distribution of the sample selected for modelling in DEM; (b) three-dimensional sample modelled in DEM; (c) division of the sample into different layers with the mentioned layer numbers and initial void ratios (e_{oi}); (d) a close-up view of the particles modelled in the fluid mesh using the LBM-DEM approach (Haq et al. 2022) (reproduced with permission from Springer Nature)

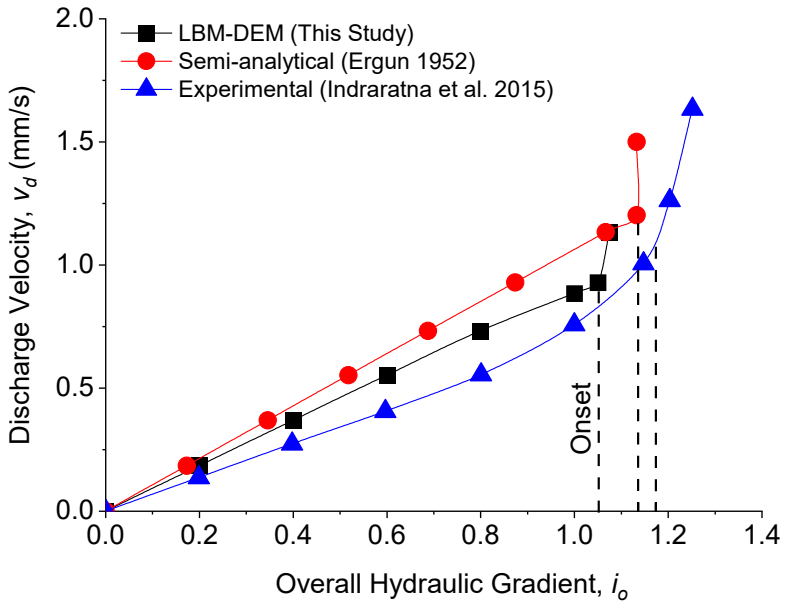

Fig. 6. 2 Calibration of the soil specimen fluidisation model by comparing the flow curves obtained from the LBM-DEM, the documented experimental, and semi-analytical solution (Haq et al. 2022) (reproduced with permission from Springer Nature)

6.5 RESULTS AND DISCUSSION

6.5.1 Stress-Hydraulic Gradient Evolution

Figure 6.3 shows the stress-hydraulic gradient space where the local hydraulic gradients (i_{hyd}) are plotted against the normalised Cauchy effective stresses ($\sigma'_{zz}/\sigma'_{zzo}$) of particles in a given layer in the fluid flow direction at any time, where σ'_{zz} is the Cauchy effective stresses of the particles in a layer at any time, and σ'_{zzo} is the initial Cauchy effective stresses of the particles in that particular layer. The σ'_{zz} is obtained using particle-based stresses via the following second-order stress tensor equation (Potyondy & Cundall 2004).

$$\sigma'_{ij} = \frac{1}{V}\sum_{p=1}^{N_p} \sigma_{ij}^{p\prime} V^p \tag{6.3}$$

where V is the volume of the layer or the selected region, V^p is the volume of particle p in the region, N_p is the number of particles in the layer, and $\sigma_{ij}^{p\prime}$ is the average stress tensor within a particle p, and it is given by:

$$\sigma_{ij}^{p\prime} = \frac{1}{V^p} \sum_{c=1}^{N_c^p} \left| x_i^c - x_i^p \right| n_i^{c,p} f_j^c \tag{6.4}$$

where f_j^c is the force vector in the j^{th} direction at contact c with the location x_i^c, x_i^p is the location of the particle's centroid, $n_i^{c,p}$ is the unit normal vector from the centroid of the particle to the contact location and N_c^p is the number of contacts on particle p. Note that Equations (6.3) and (6.4) compute the effective stresses directly from the contact moments and not according to Terzaghi's concept used in the macroscale laboratory studies. Reynold's stresses are negligible and are not taken into account.

The onset of soil fluidisation is associated with hydraulic and stress conditions, i.e., hydromechanical conditions. The effective stresses decrease as the local hydraulic gradients increase in each layer, and fluidisation occurs at a critical hydraulic gradient when the effective stresses drop to zero. The evolution of the stress-gradient of each layer is not the same. The stress-gradient paths of Layers 1-6 are approximately linear with a slope of -1. In contrast to the theoretical linear stress-gradient paths presented by Li and Fannin (2012), the stress-gradient paths of Layers 7-10 (lower layers) are nonlinear until failure, and failure commences when the effective stress of Layer 10 approaches zero. At the same time, Layers 1-9 show residual stresses due to the motion of particles in the form of clusters. These residual stresses decrease as the particles in the cluster lose further contacts over time after onset until complete fluidisation occurs. The inception of failure at Layer 10 under all layers is consistent with the experimental investigations (Indraratna, Israr & Li 2017; Indraratna, Israr & Rujikiatkamjorn 2015).

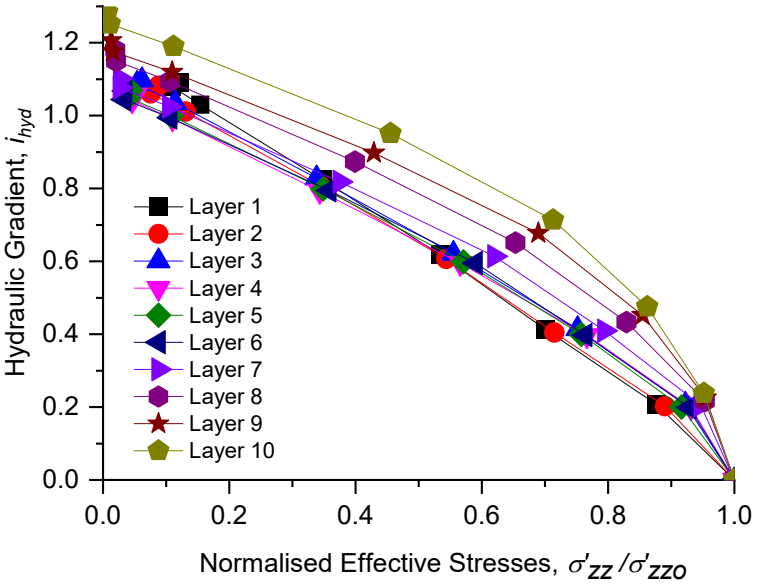

Fig. 6. 3 Evolution of the local hydraulic gradient and normalised effective stresses (Haq et al. 2022) (reproduced with permission from Springer Nature)

6.5.2 Distribution of Normal Contact Forces

Figure 6.4 shows the Probability Density Function (PDF) of the normalised contact forces ($f^N/f_o^{N,avg}$) of the selected layers, where f^N is the normal contact force at any time and $f_o^{N,avg}$ is the average normal contact force in a layer at a hydrostatic state. Given that two types of contact networks are present, the strong and the weak contacts. The strong contacts that carry the primary load are those with above-average normal contact forces ($f^N \geq f_o^{N,avg}$); otherwise, they correspond to weak contacts (Thornton & Antony 1998). The average normal contact force at the hydrostatic state (when the particles are saturated with fluid and the overall hydraulic gradient across the soil specimen is zero) is used for subsequent stages as the overall hydraulic gradient is increased until the soil is fluidised.

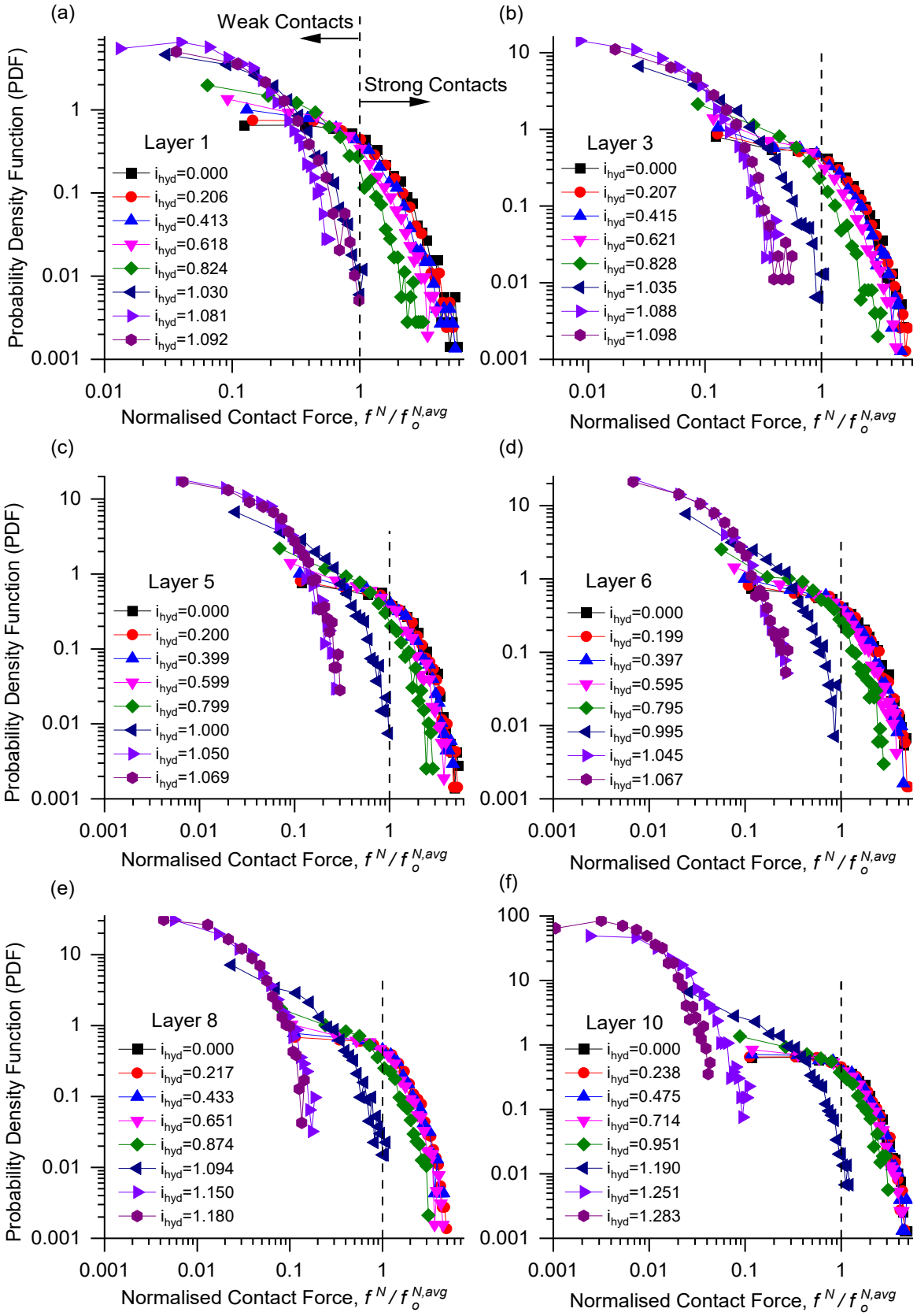

Fig. 6. 4 Probability density function (PDF) of the normalised contact forces ($\boldsymbol{f^N/f_o^{N,avg}}$) of the selected layers at the different local hydraulic gradients (i_{hyd})

The PDF decreases exponentially as the magnitude of normalised normal contact force increases. In almost all layers at the hydrostatic state, the strong forces have a broad tail that is up to 5 times the average normal contact force. The seepage forces alleviate the normal contact forces between particles in a granular medium with increasing local hydraulic gradients. As a result, the tail of the strong forces shifts to the left, and the head of the weak forces becomes wider, showing that the strong contacts fade into weak ones. It is noteworthy that the strong contacts at the critical hydraulic gradient disappear entirely, which indicates the onset of fluidisation of the soil layers. On this basis, these PDF plots can be used to distinguish soil that has changed from a hydromechanically stable into a fluid-like state. Note that Fig. 6.4 only considers the active contacts, so those particles with contacts that have already been lost are not involved.

Figure 6.5 shows the evolution of normalised effective stresses with strong contacts across all layers as the local hydraulic gradients increase. The strong contacts decrease, and consequently, the normalised effective stresses diminish. When the percentage of strong contacts becomes zero, the normalised effective stresses decrease to minimum values, i.e., about 10% of the effective stresses remain in each layer. The proportion of strong contacts in all layers at the hydrostatic state is 40%, which is about a third of the total contacts; this observation was also reported by Thornton and Antony (1998). This lower proportion of contacts that transmit strong forces is evidence of the arching effect and heterogeneity of the force network in the granular assembly due to the gravitational force on the particles. This also shows that only 40% of the contacts in each layer are available to contribute to the 90% of effective stresses to resist the incipient fluidisation of the soil layers. The contribution made by the weak contacts and tangential forces (with a coefficient of friction of 0.30) to the effective stresses remains marginal, i.e., less than or equal to 10%.

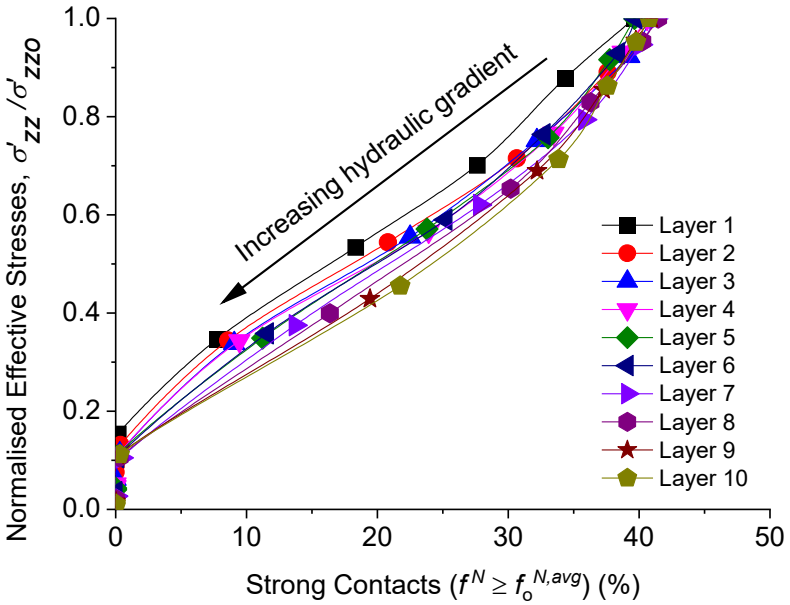

Fig. 6. 5 Varying normalised effective stresses ($\sigma'_{zz}/\sigma'_{zzo}$) with strong contacts ($f^N \geq f_o^{N,avg}$)

6.5.3 Evolution of Broken Contacts

Figure 6.6 shows the development of broken contacts (B_R) compared to the normalised effective stresses ($\sigma'_{zz}/\sigma'_{zzo}$). B_R is the percentage of interparticle contact losses in the initial number of contacts in the corresponding layer. The value of B_R increases with an increasing hydraulic gradient and decreasing effective stresses. Contact is lost when the normal contact force due to hydrodynamic forces becomes zero. When the fluid flows, the contacts break off, and new contacts are formed in the layer. The sharp turn in B_R represents the critical hydromechanical state where the contacts are notably lost. The granular assembly would become a fully fluid-like material when the number of unconnected particles increases to a maximum due to contact breakage, i.e., most particles would simply float without making any contact. It is noteworthy that the contact losses in the lower layers are greater than in the upper layers, which shows that more particles lose contact at the bottom and migrate upwards with the fluid flow if the constrictions are wide enough. The B_R at the critical hydraulic gradient is about 5% in Layer 1 and 17% in Layer

10, but it increases substantially when a further slight increase in the hydraulic gradient is applied across the soil specimen.

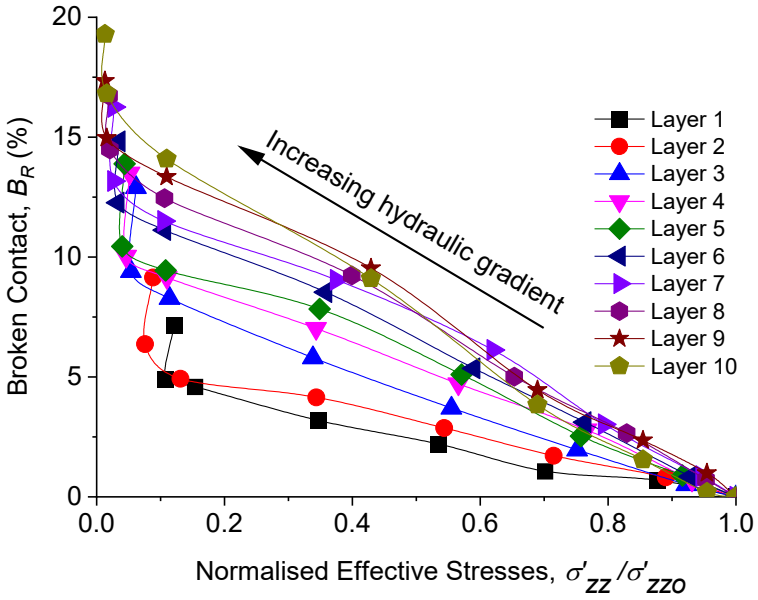

Fig. 6. 6 Evolution of broken contacts with the normalised effective stresses (Haq et al. 2022) (reproduced with permission from Springer Nature)

6.5.4 Variation of Mechanically Stable Particles

Figure 6.7 shows the evolution of the fraction of mechanically stable particles (M_s) with normalised effective stresses ($\sigma'_{zz}/\sigma'_{zzo}$) under increasing hydraulic gradients. The mechanically stable particles are those that participate in the stable network of force transmission. Since soil approaching fluidisation would continuously lose those particles involved in the stable force transmission network, it is essential to examine their development with decreasing effective stresses. The value of M_s is defined by (Imole et al. 2012):

$$M_s = \frac{N_p^{\geq 4}}{N_p} \tag{6.5}$$

where $N_p^{\geq 4}$ is the number of particles with at least 4 or more contacts. Particles with zero contacts that do not take part in the stable network of force transmission are called rattlers

or unconnected particles, so they are excluded. Those particles with 1, 2, and 3 contacts are temporarily stable for a limited time, so they are also neglected in the above equation.

It should be noted that the values of M_s are always smaller than 1 across all layers because temporarily stable particles are also present at a hydrostatic state. The lower levels have higher initial M_s values than the top layers. The values of M_s decrease across all layers with a decrease in the values of the effective stresses. This reduction becomes significant under critical hydromechanical conditions that indicate the breakup of clusters of mechanically stable particles. The results show that a critical value of $M_s \approx 0.75$ is found for all layers, below which the fluid-like behaviour of the soil is observed.

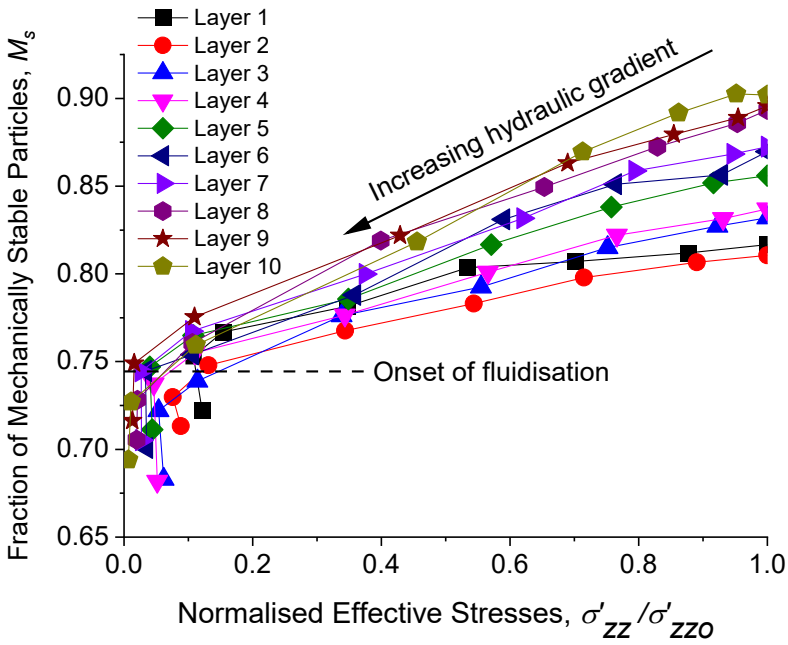

Fig. 6. 7 Evolution of the fraction of mechanically stable particles with normalised effective stresses (Haq et al. 2022) (reproduced with permission from Springer Nature)

6.5.5 Change of the Soil Fabric

Figure 6.8 shows a conceptual model that describes the differences in the fabrics of two-particle systems where particles with two different geometrical arrangements are placed. Note that the void ratios of both arrangements are the same. However, the number

of interparticle contacts is different due to the dissimilarity of the fabrics of the particulate systems. It is noteworthy that the geometric arrangement of the particles is more important than the void ratio when it comes to the strength of the granular assembly (Cundall & Strack 1983). The similar initial void ratios of all layers indicate that the number of particles in each layer is the same. However, the number of interparticle contacts can vary due to the different geometrical configurations of the particles. During fluid flow, the number of particles in each layer remains unchanged until fluidisation begins, while the geometrical rearrangement of the particles can occur, mainly due to the fact that the interparticle contacts within the layer slip and/or break. To assess the evolution of soil fabric under fluid flow, this study uses a scalar approach (e.g., Fonseca et al., 2013) to quantify the fabric with a scalar fabric descriptor called the coordination number (Z) (Thornton 2000). Figure 6.9 shows the distribution of Z at the hydrostatic state and the onset of soil fluidisation, taking into account three distinct cases:

(a) all particles

(b) particles with diameters (d_p) $\geq d_{50}$ (where d_{50} is the particle size that is 50% finer by mass), and

(c) particles with $d_p \geq d_{85}$ (where d_{85} is the particle size that is 85% finer by mass)

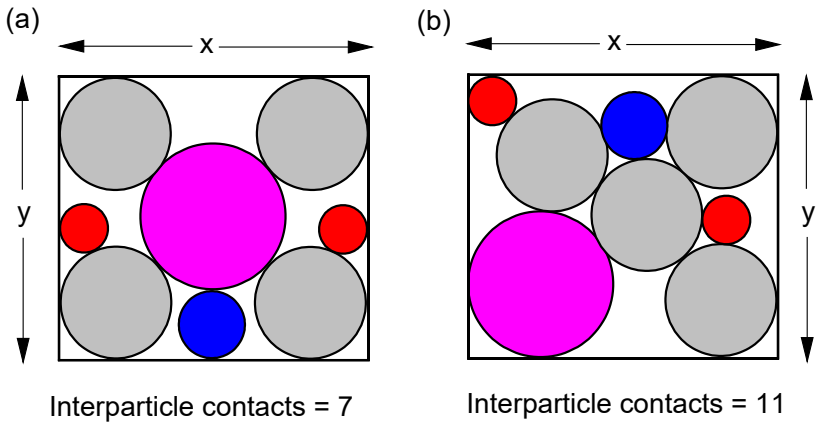

Fig. 6. 8 Conceptual model showing differences in the fabrics of particles with the same void ratios (Haq et al. 2022) (reproduced with permission from Springer Nature)

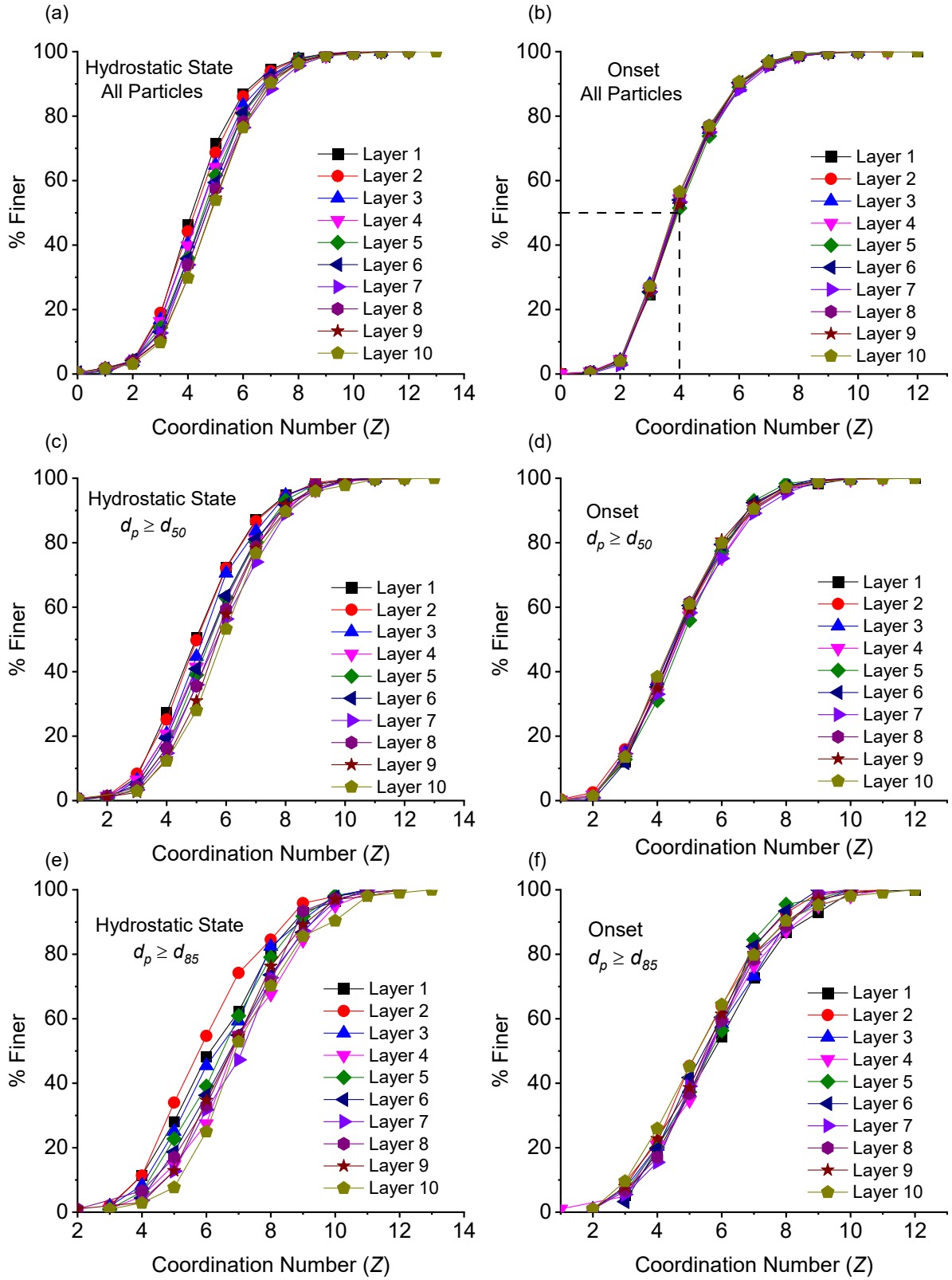

Fig. 6. 9 Distribution of the coordination number at the hydrostatic state and the onset of fluidisation of soil specimen (Haq et al. 2022) (reproduced with permission from Springer Nature)

Figure 6.9(a) shows that the distribution of the coordination numbers at the hydrostatic state across different layers is somewhat dissimilar when all particles are considered. This difference is enhanced when larger particle sizes are considered (Figures 6.9(c) & 6.9(e)), which shows a dissimilarity in the fabric of all layers despite the similar void ratios. This fabric dissimilarity is ascribed to the influence of gravity during the sample preparation phase. The curves of the lower layers are on the right-hand side and show higher values of the coordination numbers than those of the upper layers. The slight difference in the evolution of local hydraulic gradients and effective stresses through each layer, as described previously, is due to the slight dissimilarity of the particles' fabric in the layers. It is appealing to note that at the onset of fluidisation, the distributions of the coordination numbers of all layers converge and become similar (Figures 6.9(b), 6.9(d), & 6.9(f)). The median value of the coordination number (Z_{50}) is 4 when all particles in the granular medium of the layer are taken into account (Figure 6.9(b)). Thus, at the onset of fluidisation, the distributions of the interparticle contacts are uniform and show a similar fabric for all soil layers.

Figure 6.10 shows average coordination numbers (Z_{avg}) versus normalised effective stresses ($\sigma'_{zz}/\sigma'_{zzo}$), where the initial (at the hydrostatic state) average coordination of Layer 10 is the highest (i.e., $Z_{avg} = 5.405$), while Layer 1 has the lowest (i.e., $Z_{avg} = 4.811$). As the normalised effective stresses decrease, the values of Z_{avg} decrease across all layers, and so does the difference between them. Although each layer initially had a different fabric, the Z_{avg} of all layers has evolved to become the same, i.e., 4.6 at the critical hydromechanical state.

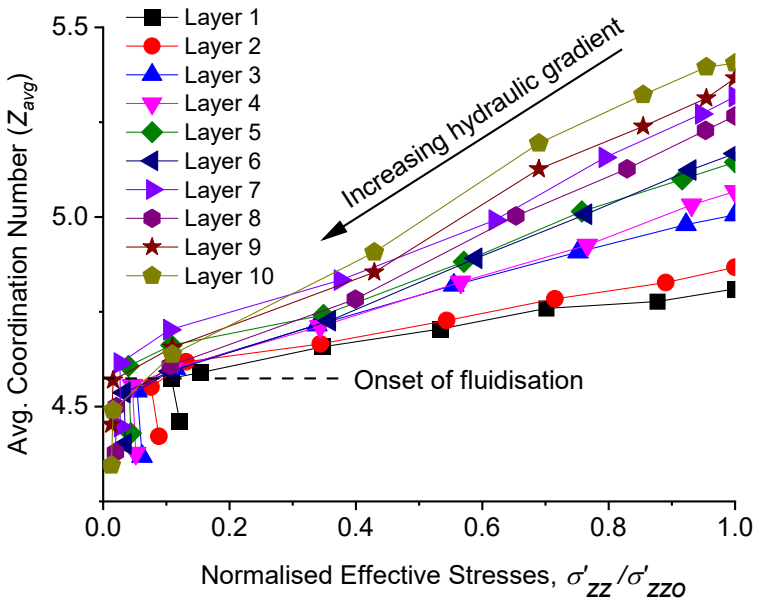

Fig. 6. 10 Development of the average coordination number with normalised effective stresses (Haq et al. 2022) (reproduced with permission from Springer Nature)

6.5.6 Distribution of Slipping Index

The distribution of the slipping index (S_i) of the selected Layer 10 is shown in Figure 6.11. Note that all layers show an almost similar development in the slipping index as the local hydraulic gradient increases. The slipping index (S_i) is defined by (Imole et al. 2012):

$$S_i = \frac{f^T}{\mu_s f^N} \tag{6.6}$$

Slipping or plastic contacts occur when the tangential contact force (f^T) has fully mobilised the friction, i.e., S_i = 1. The contacts with S_i < 1 are elastic contacts and f^T is independent of f^N in such contacts. Note that contacts that have already been lost are omitted when calculating S_i.

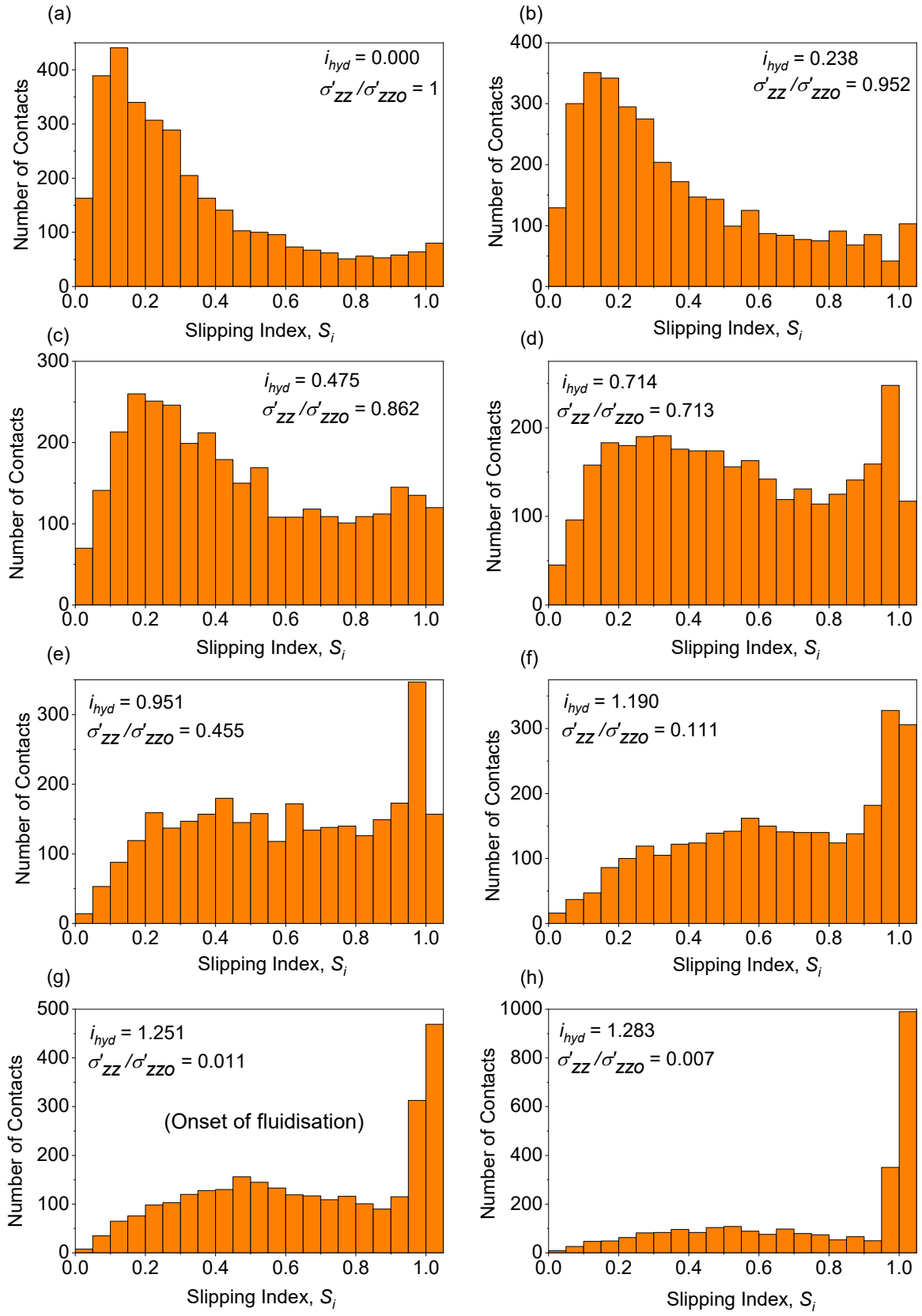

Fig. 6. 11 Distribution of the slipping index (S_i) of the selected Layer 10 at different local hydraulic gradients (i_{hyd}) (Haq et al. 2022) (reproduced with permission from Springer Nature)

The results show that a small proportion of contacts slip even at the hydrostatic state since the static buoyancy forces would be acting on the particles when they are saturated with the fluid. As the local hydraulic gradients increase, the elastic contacts decrease, and the slipping contacts increase. The hydrodynamic forces from the seepage flow tend to move the particles, causing a change in the magnitudes of the resisting tangential and normal contact forces. As a result, a slip is caused when the elastic tangential contact force reaches the Coulomb cut-off, i.e., $f^T = \mu_s f^N$ and this slipping of the particles occurs in the weak contacts ($f^N < f_o^{N,avg}$) (Cundall, Drescher & Strack 1982). At $i_{hyd} \leq 1$, the proportion of slipping contacts in the total number of contacts in the layer is ≤ 10%, while it is around 17% at the critical i_{hyd} =1.251 (Figure 6.11(g)). Thereafter, this proportion of slipping contacts increases sharply with a further, albeit slight, increase in the hydraulic gradient. It is noteworthy that the maximum tangential force is controlled by the value of μ_s. Therefore, the value of μ_s has a profound influence on the proportion of slipping contacts and consequently on the macroscale behaviour of the granular assembly.

6.5.7 Evolution of Constraint Ratio

Figure 6.12 shows a three-dimensional representation of the constraint ratio (R) versus local hydraulic gradients (i_{hyd}) and normalised effective stresses ($\sigma'_{zz}/\sigma'_{zzo}$). The constraint ratio for a three-dimensional particle system that only considers the sliding resistance is given by (Cundall & Strack 1983):

$$R = \frac{N_{ct}}{N_d} = \frac{N_c(3 - 2S_c)}{6N_p} \tag{6.7}$$

where N_{ct} is the number of constraints, N_d is the number of degrees of freedom, and S_c is the fraction of slipping contacts in the total number of contacts at a given point in time. For an idealised granular medium with $\mu_s = \infty$, $N_{ct} = 3N_c$ and $N_d = 6N_p$. The realistic

granular medium, however, would have a finite value of μ_s; therefore, the two tangential force constraints on contacts subject to slipping vanish and are excluded from the total number of constraints given in Equation (6.7). Theoretically, if $N_{ct} > N_d$, the granular assembly is considered to be over-constrained or mechanically stable, and if $N_{ct} = N_d$, it is considered to be in a critical or transitional state; otherwise, it is unstable. Note that R represents both slipping and loss of contacts in the particle systems, whereas the coordination number (Thornton 2000) does not consider the slipping of particles.

The constraint ratio in each layer decreases according to the nonlinear power laws when the normalised effective stresses decrease, and it decays exponentially after the onset of the soil fluidisation. The initial mild slope shows that at relatively low i_{hyd} values, i.e., $i_{hyd} < 1$, the particles slip less and have minimal loss of contacts. The abrupt change in slope after onset is triggered by substantial slipping and the associated rapid loss of interparticle contacts. The point at which the slope values change represents the critical microscale hydromechanical state or the onset of soil fluidisation. This point is marked as a transition line from a hydromechanically stable to a fluid-like state, as shown in Fig. 6.12(b). This critical hydromechanical state corresponds to $R \approx 1$, with effective stresses ≈ 0 at the critical hydraulic gradient. Therefore, the soil is hydromechanically stable when R is greater than 1. It is in a transition state from a hydromechanically stable to a fluid-like state when R is 1; otherwise, it corresponds to a slurry or fluid-like state. Complete fluidisation of the soil specimen occurs when almost all interparticle contacts are lost, with a constraint ratio well below 1.

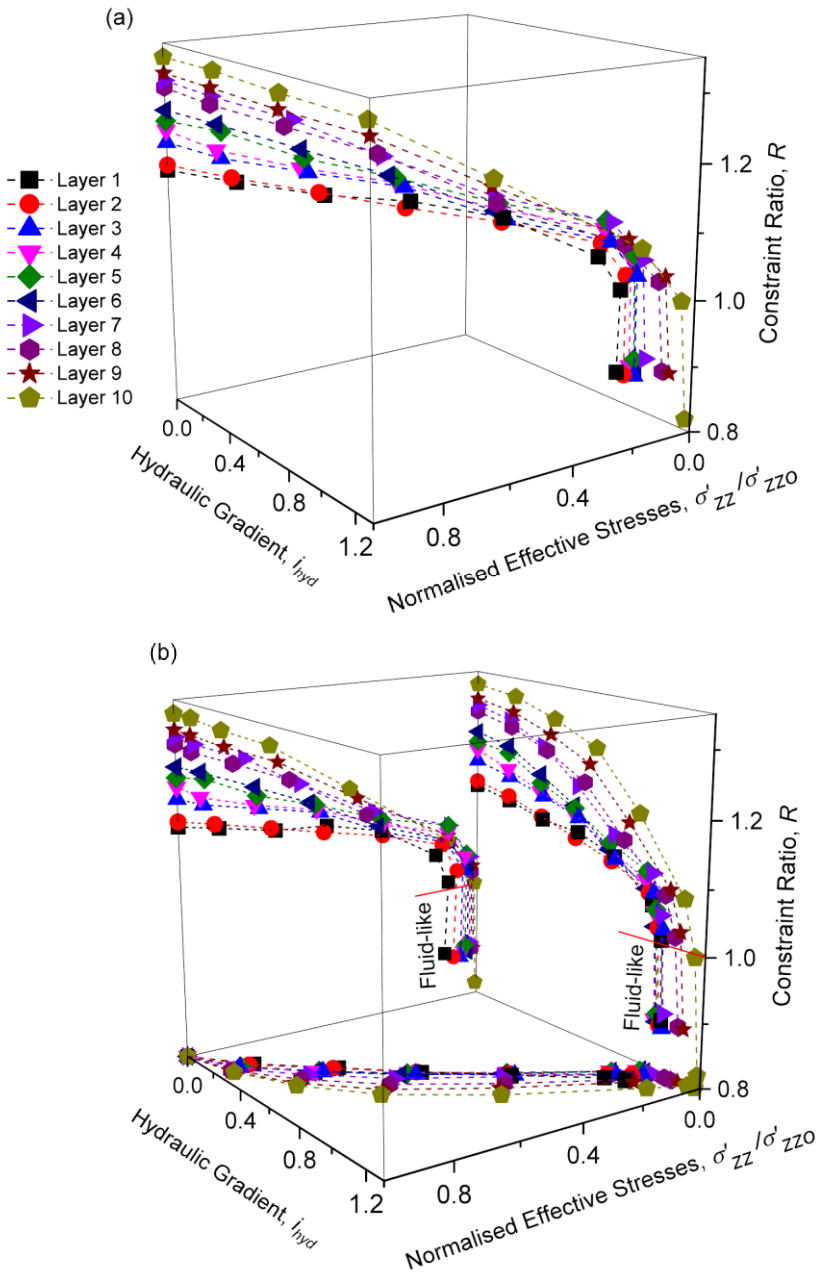

Fig. 6. 12 (a) Three-dimensional plot of the hydraulic gradient, the normalised effective stresses, and the constraint ratio; (b) projections of the three-dimensional plot of hydraulic gradient, the normalised effective stresses, and the constraint ratio (Haq et al. 2022) (reproduced with permission from Springer Nature)

6.6 SUMMARY

DEM coupled with LBM was used to study the fluidisation of soils at the microscale. The sample was prepared in a dense state by dropping the particles under the action of gravity

into a cuboid domain. Microscale parameters such as the coordination number, broken contacts, fraction of mechanically stable particles, sliding index, and the constraint ratio were observed. The percentage of interparticle contact losses compared to the initial number of contacts was non-uniform at the critical hydraulic gradient and ranged from 5 to 17 per cent across the depth of the specimen. The breakage of interparticle contacts then appeared to accelerate, even with a small increase in hydraulic gradients. At the onset of fluidisation, the coordination number distributions became more uniform across all layers of the soil specimen, with a median value of 4 and an average value of 4.6, thus indicating a more uniform granular fabric across the soil layers. The results also showed that soil changes from a solid-like substance to a liquid-like material when the constraint ratio falls below 1.

CHAPTER 7 CONCLUSIONS

7.1 INTRODUCTION

The scope of this doctoral thesis was to describe and quantify the critical hydromechanical conditions corresponding to internal instability and fluidisation with particular attention to granular soil at the microscale, adopting the concepts of various microscale parameters such as coordination number, constraint ratio, stress reduction factor, partial coordination number, and sliding contacts etc. The primary objective of this thesis was to propose novel criteria considering the microscale parameters to assess the potential for internal instability and fluidisation of soil.

In order to present a comprehensive understanding of internal instability and fluidisation, this study considered the numerical aspects by combining the Discrete Element Method (DEM) with the Lattice Boltzmann Method (LBM), and the micromechanical factors were discussed with greater insight. Based on this 4-year PhD study (also contributing to 3 peer-reviewed journal papers), the following salient Conclusions are drawn.

7.2 SALIENT FINDINGS

7.2.1 Microscale Boundaries of Internally Stable and Unstable Soils

The internal instability of granular soils was assessed from a microscale perspective using the DEM. A total of 21 Particle Size Distribution (PSD) curves were analysed at three different relative density levels. The key findings of this study are listed below:

- Clear boundaries were drawn between internally unstable and stable soils with parameters obtained directly from the particle scale data, i.e., the coordination number (Z) and the stress reduction factor (α). For instance, samples with the potential for internal instability showed $Z \leq 1$ and $\alpha \leq 0.5$.

- The influence of relative density on the microscale parameters was minimal in soils with a gap ratio ≥ 4 and a fines content < 25% and became noticeable for soils with a fines content ≥ 25%. The coordination number (Z) and stress reduction factor (α) increased as the relative density increased, making the samples internally stable.
- For a soil to be internally stable, fines must fully occupy the voids formed by the coarse particles. As the percentage of fines increased, there were more contacts with a higher coordination number (Z), a higher stress reduction factor (α), and increased internal stability. Similarly, reducing the gap ratio increased the internal stability.
- The significant scatter of the results between the microscale parameters and particle size-based criteria showed that the particle-size-based criteria could not predict internal instability very well.
- The microscale boundaries closely matched the criterion based on Constriction Size Distribution (CSD). This proved beyond doubt that the CSD-based criterion could appropriately predict internal instability with greater accuracy. For brevity, soils with $Z \leq 1$, $\alpha \leq 0.5$ and $D_{c35}^{c^*}/d_{85}^{f^*} \geq 0.73$ (where $D_{c35}^{c^*}$ is the 35% finer of the CSD of the coarser fraction and $d_{85}^{f^*}$ is the 85% finer of PSD of the finer fraction, both plotted using the surface area method) were considered internally unstable, which is consistent with the experimental results of internal instability. This consistency of results increases confidence in using microscale and CSD-based criteria in practical design.

7.2.2 Micromechanical Analysis of Soil Transition from an Internally Stable to an Unstable State

Simulations with DEM were carried out to investigate the influence of shear-induced deformation on internal stability under drained conditions subjected to a constant mean stress path. Based on the findings of this study, the following conclusions could be drawn:

- The numerical analysis showed that the coordination number initially dropped rapidly because the rate at which the contacts disintegrated was higher than the rate at which new contacts could form. The coordination number then remained unchanged, as the rate of disintegration and the formation of contacts were the same. This leads to the conclusion that the development of the coordination number was strongly influenced by shear-induced deformation.
- Internally stable samples, e.g., Sample A (20%) (where the percentage of fines is given in brackets) with an initial coordination number (Z) = 3.06 and a stress reduction factor (α) = 1.116, transitioned into internally unstable soil with $Z < 1$ and $\alpha > 0.5$ at the end of shearing. Similarly, Sample B (30%) with an initial $Z > 1$ and $\alpha > 0.50$ became internally unstable with $Z < 1$ and $\alpha > 0.50$. The percentage drop in the Z-values of the samples that transition from internally stable to unstable soils was greater than 80%. In addition, at the macroscale, the volumetric strain increased due to the shear-induced dilation of the dense samples. Based on these results, it was evident that the decrease in microscale parameters, such as the Z and α, would be linked to the volumetric response of the samples at the macroscale.
- It was found that the initially overfilled fabric of Sample A (20%) with a fine-coarse coordination number ($Z^{fine-coarse}$) > 1 and $\alpha > 0.5$ was found to convert to an underfilled fabric with $Z^{fine-coarse} < 1$ and $\alpha > 0.5$ upon shearing. Similarly, Sample B (20%) with partially filled fabric ($Z^{fine-coarse} > 1$ and $\alpha < 0.5$) at the isotropic

stress state changed to underfilled fabric ($Z^{fine-coarse} < 1$ and $\alpha < 0.5$) at the end of shearing. This leads to the conclusion that the fabric of the soil may change significantly due to shear-induced deformations, thus altering the internal stability of the soil.

- The stress reduction factor (α) of samples with underfilled fabric, i.e., A (10%), A (15%), B (10%), B (15%), and B (20%), remained almost unchanged with the axial strain and the stress ratio. For samples with a higher fines content, α dropped significantly during shearing. For instance, in Sample B (30%), α decreased significantly from 1.655 to 0.751. Three distinct stages were observed in the development of α, namely: Stage 1, where α was constant when the stress ratio (q/p') ≤ 0.80 at a small value of axial strain; Stage 2 represented the slight decrease in α as it approached the peak q/p' and Stage 3 where α dropped significantly in the post-peak region caused by shear-induced dilation. This implies that the stress distribution is a function of the soil fabric, the stress ratio (q/p') and the axial strain.

7.2.3 Hydromechanical State of Soil Fluidisation – A Microscale Perspective

The hydromechanical state of soil fluidisation was evaluated from a micromechanical point of view using the hybrid LBM-DEM approach. The excellent agreement between the model predictions and the experimental observations regarding particle motion, fluid flow curves, and the critical hydraulic gradients confirms the capability and reliability of this hybrid numerical method. Based on the findings of this study, the following salient outcomes could be drawn:

- At comparatively low values of the local hydraulic gradient (i_{hyd}), i.e., $i_{hyd} \leq 1$, the proportion of slipping contacts in the total number of contacts of the selected Layer 10 (bottom of the specimen) was ≤ 10%, while it was about 17% at the critical i_{hyd}

=1.251. The magnitude of the slipping contacts increased with a further increase in the hydraulic gradient applied across the soil specimen.

- At the critical hydraulic gradient, the percentage of interparticle contact losses relative to the initial number of contacts was non-uniform and varied between 5 and 17% across the depth of the specimen. Thereafter, even with a slight increase in the hydraulic gradients, the breakage of the interparticle contacts appeared to exacerbate.
- At the onset of fluidisation, the coordination number distributions became more uniform across all layers of the soil specimen, with a median value of 4 and an average value of 4.6; this indicated a more uniform granular fabric across the soil layers.
- The granular assembly was hydromechanically stable when the constraint ratio > 1 and unstable (fluid-like) when the constraint ratio < 1, thereby establishing the microscale hydromechanical critical state at the constraint ratio of unity.

7.3 RESEARCH IMPACTS

The following are the implications of this research work:

- Microscale investigations enabled a better understanding of the mechanism of internal instability and the fluidisation of soil, which can be helpful in the design and construction of substructures in railways.
- To demarcate internally unstable and stable soils, a microscale criterion based on the coordination number and the stress reduction factor was proposed that can be used to estimate the probability of internal instability in the field. The microscale criterion was shown to agree with the constriction-based criterion; therefore, it could be used to reduce the maintenance cost of railway substructures.
- Fluidisation or mud pumping is a problem in railways that results in significant maintenance costs. A microscale criterion based on the constraint ratio was proposed

to determine the onset of soil fluidisation, and this proposed criterion could be used to avoid this problem.

7.4 LIMITATIONS AND RECOMMENDATIONS

7.4.1 Limitations

The following are some of the limitations of this study:

- The shapes of the particles were spherical as opposed to the actual irregular shapes of the particles. Non-spherical shapes of the particles could create more contacts and thus an increased coordination number, and the hydraulic gradient required to initiate movement of the fine particles is also increased, resulting in greater internal stability.
- The fluidisation of granular soils was simulated under upward flow conditions, although these simulations could have been carried out under cyclic loading conditions. The cyclic loading causes a continuous change in the fabric and pore structure of the granular medium and thus changes the fluidisation resistance of the soil, while this cannot be simulated in simple upward flow conditions.
- The microscale experimental investigations could have been carried out to evaluate the internal instability of non-cohesive soils using micro-CT scanning and image analysis techniques.
- A pore network analysis could have been carried out to check internal instability. This could be achieved by extracting the constriction size distribution of coarser particles from the DEM data and comparing it to the particle size distribution of the finer particles.

7.4.2 Recommendations

The following are some recommendations for future studies:

- The microscale boundaries proposed in this study apply under static loads. This work could be extended to check the validity of the presented methods under cyclic loading conditions. In this regard, DEM coupled with LBM can be incorporated under cyclic loading conditions to examine the internal instability and fluidisation of soils.
- The shear behaviour of the samples was checked by considering the constant mean stress path, but various stress paths can also be used to investigate this behaviour. Stress paths that could be used for further investigations are (i) conventional triaxial compression with increasing mean stress, (ii) triaxial extension etc. These triaxial compression and extension stress paths are used to simulate the conditions of loading and unloading in the field.
- Particles with different shapes can be utilised to observe the effect of their shapes on the micromechanics of the samples. The real shapes of the particles can first be scanned and then incorporated into DEM simulations by clumping the particles together.
- DEM investigations can be extended to capture the behaviour of broadly-graded soils with a coefficient of uniformity (C_u) > 10, which are used in various practical applications and are not studied in detail in the literature.
- Micro-CT scan can be used to determine the internal structure of soil and compare it to the DEM results; this should be carried out to compare the microscale parameters from the DEM simulations with experimental observations of real soil specimens. This can be accomplished by carrying out the image analysis of the CT-scanned samples.

REFERENCES

Abbireddy, C.O.R. & Clayton, C.R.I. 2010, 'Varying initial void ratios for DEM simulations', *Geotechnique*, vol. 60, no. 6, pp. 497–502.

Aberg, B. 1992, 'Void Ratio of Noncohesive Soils and Similar Materials', *Journal of Geotechnical and Geoenvironmental Engineering*, vol. 118, no. 9, pp. 1315–34.

Adel, H.D., Bakker, K.J. & Breteler, M.K. 1988, 'Internal stability of minestones', *Modelling Soil-Water-Structure Interactions: SOWAS 88, Kolman et al (eds), Rotterdam: A.A. Balkema*, pp. 225–31.

Ahmadi, M., Madadi, M., Disfani, M., Shire, T. & Narsilio, G. 2021, 'Reconstructing the microstructure of real gap-graded soils in DEM: Application to internal instability', *Powder Technology*, vol. 394, pp. 504–22.

Ahmadi, M., Shire, T., Mehdizadeh, A. & Disfani, M. 2020, 'DEM modelling to assess internal stability of gap-graded assemblies of spherical particles under various relative densities, fine contents and gap ratios', *Computers and Geotechnics*, vol. 126.

Anbazhagan, P., Bharatha, T.P. & Amarajeevi, G. 2012, 'Study of Ballast Fouling in Railway Track Formations', *Indian Geotechnical Journal*, vol. 42, no. 2, pp. 87–99.

Arivalagan, J., Rujikiatkamjorn, C., Indraratna, B. & Warwick, A. 2021, 'The role of geosynthetics in reducing the fluidisation potential of soft subgrade under cyclic loading', *Geotextiles and Geomembranes*.

Bao, Y.B. & Meskas, J. 2011, 'Lattice Boltzmann Method for Fluid Simulations', *Department of Mathematics, Courant Institute of Mathematical Science, New York*.

Barreto, D. 2009, 'Numerical and experimental investigation into the behaviour of granular materials under generalised stress states', PhD. Thesis, University of London.

Bhatnagar, P.L., Gross, E.P. & Krook, M. 1954, 'A Model for Collision Processes in Gases .I. Small Amplitude Processes in Charged and Neutral One-Component Systems', *Physical Review*, vol. 94, no. 3, pp. 511–25.

Burenkova, V.V. 1993, 'Assessment of suffosion in non-cohesive and graded soils', *Filters in geotechnical and hydraulic engineering*, pp. 357–60.

Cai, Xiaopei, Cai, Xianghui, Liu, K., Wang, H. & Guo, L. 2015, 'Study on Mud Pumping Mechanism of Subgrade Surface Layer in Slab Ballastless Track Zone', *Sensors and Transducers*, vol. 186, no. 3, pp. 154–60.

Carman, P.C. 1939, 'Permeability of saturated sands, soils and clays', *The Journal of Agricultural Science*, vol. 29, no. 2, pp. 262–73.

Ten Cate, A., Nieuwstad, C.H., Derksen, J.J. & Van den Akker, H.E.A. 2002, 'Particle imaging velocimetry experiments and lattice-Boltzmann simulations on a single sphere settling under gravity', *Physics of Fluids*, vol. 14, no. 11, pp. 4012–25.

Chang, D.S. & Zhang, L.M. 2013, 'Critical Hydraulic Gradients of Internal Erosion under Complex Stress States', *Journal of Geotechnical and Geoenvironmental Engineering*, vol. 139, no. 9, pp. 1454–67.

Chapuis, R.P. 1992, 'Similarity of internal stability criteria for granular soils', *Canadian Geotechnical Journal*, vol. 29, no. 4, pp. 711–3.

Chawla, S. & Shahu, J.T. 2016, 'Reinforcement and mud-pumping benefits of geosynthetics in railway tracks: Model tests', *Geotextiles and Geomembranes*, vol. 44, no. 3, pp. 366–80.

Chen, S. & Doolen, G.D. 1998, 'Lattice Boltzmann Method for Fluid Flows', *Annu. Rev. Fluid Mech.*, vol. 30, pp. 329–64.

Chen, S., Martínez, D. & Mei, R. 1996, 'On boundary conditions in lattice Boltzmann methods', *Physics of Fluids*, vol. 8, no. 9, pp. 2527–36.

Cho, G.-C., Dodds, J. & Santamarina, J.C. 2006, 'Particle Shape Effects on Packing Density, Stiffness, and Strength: Natural and Crushed Sands', *Journal of Geotechnical and Geoenvironmental Engineering*, vol. 132, no. 5, pp. 591–602.

Crawford-Flett, K. 2014, 'An improved hydromechanical understanding of seepage-induced instability phenomena in soil', Ph.D. Thesis: The University of British Columbia.

Da Cruz, F., Emam, S., Prochnow, M., Roux, J.N. & Chevoir, F. 2005, 'Rheophysics of dense granular materials: Discrete simulation of plane shear flows', *Physical Review E - Statistical, Nonlinear, and Soft Matter Physics*, vol. 72, no. 2, pp. 1–17.

Cui, X., Li, J., Chan, A. & Chapman, D. 2014, 'Coupled DEM-LBM simulation of internal fluidisation induced by a leaking pipe', *Powder Technology*, vol. 254, pp. 299–306.

Cundall, P.A. 1988, 'Computer Simulations of Dense Sphere Assemblies', *Studies in Applied Mechanics*, vol. 20, no. C, pp. 113–23.

Cundall, P.A., Drescher, A. & Strack, O.D.L. 1982, 'Numerical experiments on granular assemblies; measurements and observations.', *Deformation and failure of granular materials. IUTAM symposium, Delft*, pp. 355–70.

Cundall, P.A. & Strack, O.D.L. 1979, 'A discrete numerical model for granular assemblies', *Géotechnique*, vol. 29, no. 1, pp. 47–65.

Cundall, P.A. & Strack, O.D.L. 1983, 'Modeling of microscopic mechanisms in granular material', *Studies in Applied Mechanics*, vol. 7, no. C, pp. 137–49.

Duong, T.V., Cui, Y.J., Tang, A.M., Dupla, J.C., Canou, J., Calon, N. & Robinet, A. 2014, 'Investigating the mud pumping and interlayer creation phenomena in railway sub-structure', *Engineering Geology*, vol. 171, pp. 45–58.

Ergun, S. 1952, 'Fluid Flow through Randomly Packed beds', *Chemical Engineering*

Progress, vol. 48, pp. 89–94.

Fannin, R.J. & Moffat, R. 2006, 'Observations on internal stability of cohesionless soils', *Geotechnique*, vol. 56, no. 7, pp. 497–500.

Fonseca, J., O'Sullivan, C., Coop, M.R. & Lee, P.D. 2013, 'Quantifying the evolution of soil fabric during shearing using scalar parameters', *Geotechnique*, vol. 63, no. 10, pp. 818–29.

Galindo-Torres, S.A., Scheuermann, A., Mühlhaus, H.B. & Williams, D.J. 2015, 'A micro-mechanical approach for the study of contact erosion', *Acta Geotechnica*, vol. 10, no. 3, pp. 357–68.

Haeri, S. & Shrimpton, J.S. 2012, 'On the application of immersed boundary, fictitious domain and body-conformal mesh methods to many particle multiphase flows', *International Journal of Multiphase Flow*, vol. 40, pp. 38–55.

Hager, A. 2014, 'CFD–DEM on Multiple Scales–An Extensive Investigation of Particle–fluid Interactions', PhD Thesis: Johannes Kepler University Linz.

Han, K., Feng, Y.T. & Owen, D.R.J. 2007a, 'Coupled lattice Boltzmann and discrete element modelling of fluid-particle interaction problems', *Computers and Structures*, vol. 85, no. 11–14, pp. 1080–8.

Han, K., Feng, Y.T. & Owen, D.R.J. 2007b, 'Numerical simulations of irregular particle transport in turbulent flows using coupled LBM-DEM', *CMES - Computer Modeling in Engineering and Sciences*, vol. 18, no. 2, pp. 87–100.

Han, Y. & Cundall, P. 2017, 'Verification of two-dimensional LBM-DEM coupling approach and its application in modeling episodic sand production in borehole', *Petroleum*, vol. 3, no. 2, pp. 179–89.

Haq, S., Indraratna, B., Nguyen, T.T. & Rujikiatkamjorn, C. 2022, 'Hydromechanical state of soil fluidisation: a microscale perspective', *Acta Geotechnica*.

Hazzar, L., Nuth, M. & Chekired, M. 2020, 'DEM simulation of drained triaxial tests for glass-beads', *Powder Technology*, vol. 364, pp. 123–34.

Hoerner, S.F. 1965, *Fluid-dynamic drag : practical information on aerodynamic drag and hydrodynamic resistance*, 2nd edn, Midland Park, N.J. : Dr.-Ing. S.F. Hoerner, 1958.

Honjo, Y., Haque, M.A. & Tsai, K.A. 1996, 'Self-filtration behaviour of broadly and gap-graded cohesionless soils.', *Geofilters' 96, BiTech Publishers, Montreal, Canada*, pp. 227–36.

Hu, Z., Yang, Z.X. & Zhang, Y.D. 2020, 'CFD-DEM modeling of suffusion effect on undrained behavior of internally unstable soils', *Computers and Geotechnics*, vol. 126, no. June.

Hu, Z., Zhang, Y. & Yang, Z. 2019, 'Suffusion-induced deformation and microstructural change of granular soils: a coupled CFD–DEM study', *Acta Geotechnica*, vol. 14, no. 3, pp. 795–814.

Huang, X., Hanley, K.J., O'Sullivan, C. & Kwok, C.Y. 2014, 'Exploring the influence of interparticle friction on critical state behavior using DEM', *International Journal for Numerical and Analytical Methods in Geomechanics*, no. 38, pp. 1276–97.

Huang, X., Hanley, K.J., O'Sullivan, C. & Kwok, F.C.Y. 2014, 'Effect of sample size on the response of DEM samples with a realistic grading', *Particuology*, vol. 15, pp. 107–15.

Hudson, A., Watson, G., Le Pen, L. & Powrie, W. 2016, 'Remediation of Mud Pumping on a Ballasted Railway Track', *Procedia Engineering*, vol. 143, no. ICTG, pp. 1043–50.

Imole, O.I., Kumar, N., Magnanimo, V. & Luding, S. 2012, 'Hydrostatic and shear behavior of frictionless granular assemblies under different deformation conditions',

KONA Powder and Particle Journal, vol. 30, no. 30, pp. 84–108.

Indraratna, B., Haq, S., Rujikiatkamjorn, C. & Israr, J. 2021, 'Microscale boundaries of internally stable and unstable soils', *Acta Geotechnica*.

Indraratna, B., Israr, J. & Li, M. 2017, 'Inception of geohydraulic failures in granular soils – an experimental and theoretical treatment', *Géotechnique*, vol. 68, no. 3, pp. 233–48.

Indraratna, B., Israr, J. & Rujikiatkamjorn, C. 2015, 'Geometrical Method for Evaluating the Internal Instability of Granular Filters Based on Constriction Size Distribution', *Journal of Geotechnical and Geoenvironmental Engineering*, vol. 141, no. 10, p. 04015045.

Indraratna, B. & Ngo, T. 2018, *Ballast Railroad Design: SMART-UOW Approach*, *Ballast Railroad Design: SMART-UOW Approach*.

Indraratna, B., Nguyen, V.T. & Rujikiatkamjorn, C. 2011, 'Assessing the Potential of Internal Erosion and Suffusion of Granular Soils', *Journal of Geotechnical and Geoenvironmental Engineering*, vol. 137, no. 5, pp. 550–4.

Indraratna, B., Phan, N.M., Nguyen, T.T. & Huang, J. 2021, 'Simulating Subgrade Soil Fluidization Using LBM-DEM Coupling', *ASCE International Journal of Geomechanics*, vol. 21, no. 5, pp. 1–14.

Indraratna, B. & Raut, A.K. 2006, 'Enhanced Criterion for Base Soil Retention in Embankment Dam Filters', *Journal of Geotechnical and Geoenvironmental Engineering*, vol. 132, no. 12, pp. 1621–7.

Indraratna, B., Raut, A.K. & Khabbaz, H. 2007, 'Constriction-Based Retention Criterion for Granular Filter Design', *Journal of Geotechnical and Geoenvironmental Engineering*, vol. 133, no. 3, pp. 266–76.

Indraratna, B., Singh, M. & Nguyen, T.T. 2020, 'The mechanism and effects of subgrade

fluidisation under ballasted railway tracks', *Railway Engineering Science*, vol. 28, no. 2, pp. 113–28.

Indraratna, B., Singh, M., Nguyen, T.T., Leroueil, S., Abeywickrama, A., Kelly, R. & Neville, T. 2020, 'Laboratory study on subgrade fluidization under undrained cyclic triaxial loading', *Canadian Geotechnical Journal*, vol. 57, no. 11, pp. 1767–79.

Indraratna, B., Tennakoon, N., Nimbalkar, S. & Rujikiatkamjorn, C. 2012, 'Behaviour of clay-fouled ballast under drained triaxial testing', *Geotechnique*, vol. 63, no. 5, pp. 1–10.

Indraratna, B., Vafai, F. & Dilema, E.L.G. 1996, 'An experimental study of the filtration of a lateritic clay slurry by sand filters', *Proc. Instn Civ. Engrs Goetech. Engng.*, pp. 75–83.

Israr, J. 2016, 'Internal instability of granular filters under cyclic loading', Ph.D. Thesis : University of Wollongong, Wollongong, Australia.

Israr, J. & Indraratna, B. 2017, 'Internal Stability of Granular Filters under Static and Cyclic Loading', *Journal of Geotechnical and Geoenvironmental Engineering*, vol. 41, no. 1.

Israr, J. & Indraratna, B. 2019, 'Study of Critical Hydraulic Gradients for Seepage-Induced Failures in Granular Soils', *Journal of Geotechnical and Geoenvironmental Engineering*, vol. 145, no. 7, pp. 1–15.

Jiang, M.J., Konrad, J.M. & Leroueil, S. 2003, 'An efficient technique for generating homogeneous specimens for DEM studies', *Computers and Geotechnics*, vol. 30, no. 7, pp. 579–97.

Ke, L. & Takahashi, A. 2015, 'Drained Monotonic Responses of Suffusional Cohesionless Soils', *Journal of Geotechnical and Geoenvironmental Engineering*, vol. 141, no. 8, p. 04015033.

Kenney, T.C., Chahal, E., Chiu, E., Ofoegbu, G.I., Omange, G.N. & Ume, C.A. 1984, 'Controlling constriction sizes of granular filters', *Canadian Geotechnical Journal*, vol. 22, pp. 32–43.

Kenney, T.C. & Lau, D. 1985, 'Internal stability of granular filters.', *Canadian Geotechnical Journal*, vol. 22, no. 2, pp. 215–25.

Kenney, T.C. & Lau, D. 1986, 'Internal stability of granular filters: Reply', *Canadian Geotechnical Journal*, vol. 23, no. 3, pp. 420–3.

Kezdi, A. 1979, *Soil Physics - selected topics*, Elsevier Scientific, Amsterdam, the Netherlands.

Kloss, C., Goniva, C., Hager, A., Amberger, S. & Pirker, S. 2012, 'Models, algorithms and validation for opensource DEM and CFD-DEM', *Progress in Computational Fluid Dynamics, An International Journal*, vol. 12, no. 2/3, p. 140.

Kovacs, G. 1981, *Seepage Hydraulics*, Elsevier Scientific Publishing Company, Amsterdam.

Ladd, A.J.C. 1994, 'Numerical simulations of particulate suspensions via a discretized Boltzmann equation. Part 1. Theoretical foundation', *Journal of Fluid Mechanics*, vol. 271, pp. 285–309.

Langroudi, F.M., Soroush, A. & Shourijeh, P.T. 2015, 'A comparison of micromechanical assessments with internal stability/instability criteria for soils', *Powder Technology*, vol. 276, pp. 66–79.

Langroudi, F.M., Soroush, A., Tabatabaie Shourijeh, P. & Shafipour, R. 2013, 'Stress transmission in internally unstable gap-graded soils using discrete element modeling', *Powder Technology*, vol. 247, pp. 161–71.

Li, M. 2008, 'Seepage Induced Instability in Widely Graded Soils', PhD Thesis: University of British Columbia, Vancouver, Canada.

Li, M. & Fannin, R.J. 2008, 'Comparison of two criteria for internal stability of granular soil', *Canadian Geotechnical Journal*, vol. 45, no. 9, pp. 1303–9.

Li, M. & Fannin, R.J. 2012, 'A theoretical envelope for internal instability of cohesionless soil', *Géotechnique*, vol. 62, no. 1, pp. 77–80.

Liu, J. 2005, 'Seepage control of earth-rock dams: theoretical basis, engineering experiences and lessons (in Chinese)', *China Waterpower Press, Beijing*, p. 219p.

Liu, Y., Wang, L., Hong, Y., Zhao, J. & Yin, Z.Y. 2020, 'A coupled CFD-DEM investigation of suffusion of gap graded soil: Coupling effect of confining pressure and fines content', *International Journal for Numerical and Analytical Methods in Geomechanics*, vol. 44, no. 18, pp. 2473–500.

Locke, M. 2001, 'Analytical and laboratory modelling of granular filters for embankment dams', Ph.D. Thesis : University of Wollongong, Wollongong, Australia.

Locke, M., Indraratna, B. & Adikari, G. 2001, 'Time-Dependent Particle Transport through Granular Filters', *Journal of Geotechnical and Geoenvironmental Engineering*, vol. 127, no. 6, pp. 521–9.

Lubochkov, E.A. 1969, 'The calculation of suffosion properties of noncohesive soils when using the non-suffosion analog (in Russian)', *International Conference on Hydraulic Research, Brno, Czechoslovakia*, pp. 135–48.

Luo, Y., Luo, B. & Xiao, M. 2020, 'Effect of deviator stress on the initiation of suffusion', *Acta Geotechnica*, vol. 15, no. 6, pp. 1607–17.

Mehdizadeh, A., Disfani, M.M., Evans, R. & Arulrajah, A. 2018, 'Progressive Internal Erosion in a Gap-Graded Internally Unstable Soil : Mechanical and Geometrical Effects', *International Journal of Geomechanics*, vol. 18, no. 3, pp. 1–14.

Mehdizadeh, A., Disfani, M.M., Evans, R., Arulrajah, A. & Ong, D. 2017, 'Mechanical Consequences of Suffusion on Undrained Behaviour of a Gap-graded Cohesionless

Soil - An Experimental Approach', *Geotechnical Testing Journal*, vol. 40, no. 6, pp. 1026–42.

Mehdizadeh, A., Disfani, M.M. & Shire, T. 2019, 'Post-erosion mechanical response of internally unstable soil of varying size and flow regime', *Canadian Geotechnical Journal*, vol. 58, no. 4, pp. 531–9.

Mindlin, R.D. & Deresiewicz, H. 1989, 'Elastic Spheres in Contact Under Varying Oblique Forces', *The Collected Papers of Raymond D. Mindlin Volume I*, pp. 269–86.

Minh, N.H. & Cheng, Y.P. 2013, 'A DEM investigation of the effect of particle-size distribution on one-dimensional compression', *Geotechnique*, vol. 63, no. 1, pp. 44–53.

Mitchell, J.K. & Soga, K. 2005, *Fundamentals of Soil Behavior*, 3rd edn, JOHN WILEY & SONS, INC.

Mittal, R. & Iaccarino, G. 2005, 'Immersed Boundary Methods', *Annual Review of Fluid Mechanics*, vol. 37, no. 1, pp. 239–61.

Moffat, R. 2005, 'Experiments on the internal stability of widely graded cohesionless soils', PhD thesis, the University of British Columbia, Vancouver, Canada.

Nguyen, T.T. & Indraratna, B. 2016, 'Hydraulic behaviour of parallel fibres under longitudinal flow : a numerical treatment', *Canadian Geotechnical Journal*, vol. 1092, no. January, pp. 1081–92.

Nguyen, T.T. & Indraratna, B. 2020a, 'A Coupled CFD–DEM Approach to Examine the Hydraulic Critical State of Soil under Increasing Hydraulic Gradient', *ASCE International Journal of Geomechanics*, vol. 20, no. 9, p. 04020138.

Nguyen, T.T. & Indraratna, B. 2020b, 'The energy transformation of internal erosion based on fluid-particle coupling', *Computers and Geotechnics*, vol. 121, no.

February, p. 103475.

Nguyen, T.T. & Indraratna, B. 2021, 'Rail track degradation under mud pumping evaluated through site and laboratory investigations', *International Journal of Rail Transportation*, vol. 10, no. 1, pp. 44–71.

Nguyen, T.T., Indraratna, B., Kelly, R., Phan, N.M. & Haryono, F. 2019, 'Mud pumping under railtracks: Mechanisms, assessments and solutions', *Australian Geomechanics Journal*, vol. 54, no. 4, pp. 59–80.

Noble, D.R. & Torczynski, J.R. 1998, 'A Lattice-Boltzmann Method for Partially Saturated Computational Cells', *International Journal of Modern Physics C*, vol. 09, no. 08, pp. 1189–201.

O'Sullivan, C. 2011, *Particulate Discrete Element Modelling - A Geomechanics Perspective*, London: Spon Press/Taylor & Francis.

Peng, Y. & Luo, L.S. 2008, 'A comparative study of immersed-boundary and interpolated bounce-back methods in LBE', *Progress in Computational Fluid Dynamics, An International Journal*, vol. 8, no. 1/2/3/4, p. 156.

Perez, J.C.L., Kwok, C.Y., Sullivan, C.O., Huang, X. & Hanley, K.J. 2016, 'Assessing the quasi-static conditions for shearing in granular media within the critical state soil mechanics framework', *Soils and Foundations*, vol. 56, no. 1, pp. 152–9.

Peskin, C.S. 1972, 'Flow patterns around heart valves: A numerical method', *Jounral of Computational Physics*, vol. 271, no. 10, pp. 252–71.

Potyondy, D.O. & Cundall, P.A. 2004, 'A bonded-particle model for rock', *International Journal of Rock Mechanics and Mining Sciences*, vol. 41, no. 8 SPEC.ISS., pp. 1329–64.

Rettinger, C. & Rüde, U. 2017, 'A comparative study of fluid-particle coupling methods for fully resolved lattice Boltzmann simulations', *Computers and Fluids*, vol. 154,

pp. 74–89.

Rothenburg, L. & Kruyt, N.P. 2004, 'Critical state and evolution of coordination number in simulated granular materials', *International Journal of Solids and Structures*, vol. 41, no. 21, pp. 5763–74.

Salot, C., Gotteland, P. & Villard, P. 2009, 'Influence of relative density on granular materials behavior: DEM simulations of triaxial tests', *Granular Matter*, vol. 11, no. 4, pp. 221–36.

Sazzad, M., Biswas, S. & Toufiq-E-Alahy 2014, 'Determination of relative density of a granular assembly in DEM based modeling', *Proceedings of the 2nd International Conference on Civil Engineering for Sustainable Development (ICCESD-2014), 14~16 February 2014, KUET, Khulna, Bangladesh*.

Seil, P. & Pirker, S. 2016, 'LBDEMcoupling : Open-Source Power for Fluid-Particle Systems', *The 7th International Conference on Discrete Element Methods, Dalian, China*, pp. 1–8.

Seil, P., Pirker, S. & Lichtenegger, T. 2018, 'Onset of sediment transport in mono- and bidisperse beds under turbulent shear flow', *Computational Particle Mechanics*, vol. 5, no. 2, pp. 203–12.

Senetakis, K., Coop, M.R. & Todisco, M.C. 2013, 'Tangential load-deflection behaviour at the contacts of soil particles', *Geotechnique Letters*, vol. 3, no. APRIL/JUN, pp. 59–66.

Sherard, J.L. 1979, 'Sinkholes in dams of coarse broadly graded soils', *Proceedings of 13th ICOLD, New Delhi, India*, pp. 25–35.

Shire, T. & O'Sullivan, C. 2013, 'Micromechanical assessment of an internal stability criterion', *Acta Geotechnica*, vol. 8, no. 1, pp. 81–90.

Shire, T., O'Sullivan, C. & Hanley, K.J. 2016, 'The influence of fines content and size-

ratio on the micro-scale properties of dense bimodal materials', *Granular Matter*, vol. 18, no. 3, pp. 1–10.

Shire, T., O'Sullivan, C., Hanley, K.J. & Fannin, R.J. 2014, 'Fabric and effective stress distribution in internally unstable soils', *Journal of Geotechnical and Geoenvironmental Engineering*, vol. 140, no. 12, pp. 1–11.

Skempton, A.W. & Brogan, J.M. 1994, 'Experiments on piping in sandy gravels', *Géotechnique*, vol. 44, no. 3, pp. 449–60.

Slangen, P. 2015, 'On the influence of effective stress and micro-structure on suffusion and suffosion', Ph.D. Thesis: The University of British Columbia.

Sufian, A., Artigaut, M., Shire, T. & O'Sullivan, C. 2021, 'Influence of Fabric on Stress Distribution in Gap-Graded Soil', *Journal of Geotechnical and Geoenvironmental Engineering*, vol. 147, no. 5, p. 04021016.

Takatoshi, I. 1997, 'Measure for the stabilization of railway earth structure', *Japan Railway Technical Service*, vol. 20.

Terzaghi, K. 1943, *Theoretical Soil Mechanics*, John Wiley and Sons, New York.

Thevanayagam, S., Shenthan, T., Mohan, S. & Liang, J. 2002, 'Undrained Fragility of Clean Sands, Silty Sands, and Sandy Silts', *Journal of Geotechnical and Geoenvironmental Engineering*, vol. 128, no. 10, pp. 849–59.

Third, J.R. & Muller, C.R. 2013, 'Coupled LBM-DEM Simulations of Gas Fluidised Beds', *The 14th International Conference on Fluidization - From Fundamentals to Products*.

Thornton, C. 2000, 'Numerical simulations of deviatoric shear deformation of granular media', *Geotechnique*, vol. 50, no. 1, pp. 43–53.

Thornton, C. & Antony, S.J. 1998, 'Quasi-static deformation of particulate media', *Philosophical Transactions of the Royal Society A: Mathematical, Physical and*

Engineering Sciences, vol. 356, no. 1747, pp. 2763–82.

To, P., Scheuermann, A. & Williams, D.J. 2018, 'Quick assessment on susceptibility to suffusion of continuously graded soils by curvature of particle size distribution', *Acta Geotechnica*, vol. 13, no. 5, pp. 1241–8.

Trani, L.D.O. 2009, 'Application of constriction size based filtration criteria for railway subballast under cyclic conditions', PhD Thesis: University of Wollongong, Wollongong, Australia.

Trani, L.D.O. & Indraratna, B. 2010, 'The use of particle size distribution by surface area method in predicting the saturated hydraulic conductivity of graded granular soils', *Géotechnique*, vol. 60, no. 12, pp. 957–62.

Tsuji, Y., Tanaka, T. & Ishida, T. 1992, 'Lagrangian numerical simulation of plug flow of cohesionless particles in a horizontal pipe', *Powder Technology*, vol. 71, no. 3, pp. 239–50.

Vallejo, L.E. 2001, 'Interpretation of the limits in shear strength in binary granular mixtures', *Canadian Geotechnical Journal*, vol. 38, no. 5, pp. 1097–104.

Wan, C.F. & Fell, R. 2004, 'Experimental investigation of internal erosion by the process of suffusion in embankment dams and their foundations', *ANCOLD Bulletin No. 126*, pp. 69–78.

Wu, S., Chen, Y., Zhu, Y., Zhang, P., Scheuermann, A., Jin, G. & Zhu, W. 2021, 'Study on filtration process of geotextile with LBM-DEM-DLVO coupling method', *Geotextiles and Geomembranes*, vol. 49, no. 1, pp. 166–79.

Xiao, M. & Shwiyhat, N. 2012, 'Experimental investigation of the effects of suffusion on physical and geomechanic characteristics of sandy soils', *Geotechnical Testing Journal*, vol. 35, no. 6, pp. 1–11.

Yang, H., Fan, M., Liu, A. & Dong, L. 2015, 'General formulas for drag coefficient and

settling velocity of sphere based on theoretical law', *International Journal of Mining Science and Technology*, vol. 25, no. 2, pp. 219–23.

Youd, T.L. 1973, 'Factors Controlling Maximum and Minimum Densities of Sands.', *ASTM Special Technical Publication*, no. October, pp. 98–112.

Zhao, J. & Shan, T. 2013, 'Coupled CFD-DEM simulation of fluid-particle interaction in geomechanics', *Powder Technology*, vol. 239, pp. 248–58.

Zhou, W., Ma, Q., Ma, G., Cao, X. & Cheng, Y. 2020, 'Microscopic investigation of internal erosion in binary mixtures via the coupled LBM-DEM method', *Powder Technology*, vol. 376, pp. 31–41.

Zhou, Z.Y., Kuang, S.B., Chu, K.W. & Yu, A.B. 2010, 'Discrete particle simulation of particle-fluid flow: Model formulations and their applicability', *Journal of Fluid Mechanics*, vol. 661, pp. 482–510.

Zhu, Y., Nie, Z., Gong, J., Zou, J., Zhao, L. & Li, L. 2020, 'An analysis of the effects of the size ratio and fines content on the shear behaviors of binary mixtures using DEM', *Computers and Geotechnics*, vol. 118, no. October 2019.

Zou, Y., Chen, C. & Zhang, L. 2020, 'Simulating Progression of Internal Erosion in Gap-Graded Sandy Gravels Using Coupled CFD-DEM', *International Journal of Geomechanics*, vol. 20, no. 1, p. 04019135.

APPENDIX A - SOURCE CODE FOR ISOTROPICALLY COMPRESSING THE SAMPLES USING THE DISCRETE ELEMENT METHOD (DEM)

The following code was used in LIGGGHTS (LAMMPS Improved for General Granular and Granular Heat Transfer Simulations) to isotropically compress the samples to constant mean stress of 200 kPa. The code also shows that samples were equilibrated with a sufficient number of numerical cycles after isotropic compression to the desired stress level.

```
variable run1 equal 1000
variable reqstress equal 2e5
variable ratei equal 0.90
variable rho_s equal 2650
variable v_limit equal 1e-14
variable n_particles equal 20000
variable dmp_stp equal 1e7
variable timestep equal 5.95e-9

#Dimensions of the domain
variable dx equal 0.0058
variable dy equal 0.0058
variable dz equal 0.0058

variable  r1   equal     0.000574232
variable  r2   equal     0.000533125
variable  r3   equal     0.000494961
```

```
variable  r4   equal     0.000460306
variable  r5   equal     0.000428076
variable  r6   equal     0.000398104
variable  r7   equal     0.000369605
variable  r8   equal     0.000343147
variable  r9   equal     0.000319121
variable  r10  equal     0.000296777
variable  r11  equal     0.000275998
variable  r12  equal     0.00025624
variable  r13  equal     0.000238299
variable  r14  equal     0.00022124
variable  r15  equal     0.000101256
variable  r16  equal     9.01E-05
variable  r17  equal     8.01E-05
variable  r18  equal     7.14E-05
variable  r19  equal     6.35E-05
variable  r20  equal     5.62E-05

units          si
atom_style     granular
atom_modify    map array
hard_particles yes

communicate    single vel yes

boundary  p p p
```

```
newton          off
processors * * *
region          box block 0 ${dx} 0 ${dy} 0 ${dz} units box
create_box      1 box

variable  skin equal 5e-6
neighbor  ${skin} bin
neigh_modify   delay 0

fix       m1 all property/global youngsModulus peratomtype
70e9
fix       m2 all property/global poissonsRatio peratomtype
0.3
fix       m3  all  property/global  coefficientRestitution
peratomtypepair 1 0.70
fix       m4   all   property/global   coefficientFriction
peratomtypepair 1 0

pair_style      gran model hertz tangential history
pair_coeff      * *

#fix xwalls1 all wall/gran model hertz tangential history
primitive type 1 xplane 0
#fix xwalls2 all wall/gran model hertz tangential history
primitive type 1 xplane ${dx}
#fix ywalls1 all wall/gran model hertz tangential history
```

```
primitive type 1 yplane 0
#fix ywalls2 all wall/gran model hertz tangential history
primitive type 1 yplane ${dy}
#fix zwalls1 all wall/gran model hertz tangential history
primitive type 1 zplane 0
#fix zwalls2 all wall/gran model hertz tangential history
primitive type 1 zplane ${dz}

timestep        ${timestep}

fix       1 all nve/sphere

fix  pts1 all  particletemplate/sphere  11593     atom_type
     1    density   constant  ${rho_s}  volume_limit
     ${v_limit}     radius    constant  ${r1}
fix  pts2 all  particletemplate/sphere  11701     atom_type
     1    density   constant  ${rho_s}  volume_limit
     ${v_limit}     radius    constant  ${r2}
fix  pts3 all  particletemplate/sphere  11807     atom_type
     1    density   constant  ${rho_s}  volume_limit
     ${v_limit}     radius    constant  ${r3}
fix  pts4 all  particletemplate/sphere  11897     atom_type
     1    density   constant  ${rho_s}  volume_limit
     ${v_limit}     radius    constant  ${r4}
fix  pts5 all  particletemplate/sphere  11969     atom_type
     1    density   constant  ${rho_s}  volume_limit
```

```
     ${v_limit}     radius    constant  ${r5}
fix  pts6 all  particletemplate/sphere  12071     atom_type
     1    density   constant  ${rho_s}  volume_limit
     ${v_limit}     radius    constant  ${r6}
fix  pts7 all  particletemplate/sphere  12157     atom_type
     1    density   constant  ${rho_s}  volume_limit
     ${v_limit}     radius    constant  ${r7}
fix  pts8 all  particletemplate/sphere  12253     atom_type
     1    density   constant  ${rho_s}  volume_limit
     ${v_limit}     radius    constant  ${r8}
fix  pts9 all  particletemplate/sphere  12347     atom_type
     1    density   constant  ${rho_s}  volume_limit
     ${v_limit}     radius    constant  ${r9}
fix  pts10     all  particletemplate/sphere  12437
     atom_type 1    density   constant  ${rho_s}
     volume_limit   ${v_limit}     radius    constant
     ${r10}
fix  pts11     all  particletemplate/sphere  12517
     atom_type 1    density   constant  ${rho_s}
     volume_limit   ${v_limit}     radius    constant
     ${r11}
fix  pts12     all  particletemplate/sphere  12601
     atom_type 1    density   constant  ${rho_s}
     volume_limit   ${v_limit}     radius    constant
     ${r12}
fix  pts13     all  particletemplate/sphere  12689
```

```
     atom_type 1    density   constant  ${rho_s}
     volume_limit   ${v_limit}     radius    constant
     ${r13}
fix  pts14     all  particletemplate/sphere  12791
     atom_type 1    density   constant  ${rho_s}
     volume_limit   ${v_limit}     radius    constant
     ${r14}
fix  pts15     all  particletemplate/sphere  12899
     atom_type 1    density   constant  ${rho_s}
     volume_limit   ${v_limit}     radius    constant
     ${r15}
fix  pts16     all  particletemplate/sphere  12973
     atom_type 1    density   constant  ${rho_s}
     volume_limit   ${v_limit}     radius    constant
     ${r16}
fix  pts17     all  particletemplate/sphere  13049
     atom_type 1    density   constant  ${rho_s}
     volume_limit   ${v_limit}     radius    constant
     ${r17}
fix  pts18     all  particletemplate/sphere  13159
     atom_type 1    density   constant  ${rho_s}
     volume_limit   ${v_limit}     radius    constant
     ${r18}
fix  pts19     all  particletemplate/sphere  13249
     atom_type 1    density   constant  ${rho_s}
     volume_limit   ${v_limit}     radius    constant
```

```
     ${r19}
fix  pts20     all  particletemplate/sphere  13339
     atom_type 1    density   constant  ${rho_s}
     volume_limit   ${v_limit}     radius    constant
     ${r20}

fix pdd1 all particledistribution/discrete 32452843 20 pts1
0.05 pts2 0.05 pts3 0.05 pts4 0.05 pts5 0.05 pts6 0.05 pts7
0.05 pts8 0.05 pts9 0.05 pts10 0.05 pts11 0.05 pts12 0.05
pts13 0.05 pts14 0.05 pts15 0.05 pts16 0.05 pts17 0.05 pts18
0.05 pts19 0.05 pts20 0.05

region  insreg block 0 ${dx} 0 ${dy} 0 ${dz} units box

fix ins all insert/pack seed 32452867 distributiontemplate
pdd1 insert_every once &
                      overlapcheck                    yes
particles_in_region  ${n_particles}  region  insreg  ntry_mc
50000

fix    stress    all    ave/euler    nevery    ${dmp_stp}
cell_size_relative 3 parallel no

compute             cpgl all pair/gran/local pos id force
force_normal force_tangential contactArea contactPoint
```

```
run 1

compute               peratom all stress/atom pair
compute            p all reduce sum c_peratom[1] c_peratom[2]
c_peratom[3]
variable            press              equal              -
(c_p[1]+c_p[2]+c_p[3])/(3*vol)
#variable           sigmaxx equal -(c_p[1])/vol
#variable           sigmayy equal -(c_p[2])/vol
#variable           sigmazz equal -(c_p[3])/vol

# thermo settings
fix       ts all check/timestep/gran 10000 0.1 0.1
compute        contacts all contact/atom
thermo_style   custom ke step v_press
thermo         50000
thermo_modify  lost ignore norm no
#compute_modify     thermo_temp dynamic yes

##########################################
#Dumping
##########################################

dump dmp_LIG all custom ${dmp_stp} output/post/d_*.liggghts
id type type x y z ix iy iz vx vy vz fx fy fz omegax omegay
omegaz   radius   c_contacts   c_peratom[1]   c_peratom[2]
```

```
c_peratom[3] c_peratom[4] c_peratom[5] c_peratom[6]

dump dmp_cpgl all local ${dmp_stp} output/CPGL/cpgl*.dump
c_cpgl[1] c_cpgl[2] c_cpgl[3] c_cpgl[4] c_cpgl[5] c_cpgl[6]
c_cpgl[7]  c_cpgl[8]  c_cpgl[9]  c_cpgl[10]  c_cpgl[11]
c_cpgl[12]  c_cpgl[13]  c_cpgl[14]  c_cpgl[15]  c_cpgl[16]
c_cpgl[17]  c_cpgl[18]  c_cpgl[19]  c_cpgl[20]  c_cpgl[21]
c_cpgl[22]

dump      dmp_euler      all      euler/vtk      ${dmp_stp}
output/euler/eulerdump*.vtk

run 1

##########################################
#application of strain rate
##########################################

variable      rate      equal      ${ratei}*(${reqstress}-
v_press)/(${reqstress})

fix       iso all deform 1 z erate -${rate} x erate -${rate}
y erate -${rate} remap x units box

#######################################
#printing some data
```

```
########################################

#fix printingdata all print 20000 "$(step) $(v_press)
$(v_sigmaxx) $(v_sigmayy) $(v_sigmazz) $(v_rate)" screen no
file stresses.txt

############################################################
###
#if statement to desired stress level and changing the
coefficient of friction
############################################################
###

label loop
if '$(v_press) >= ${reqstress}' then 'jump in.lbdem endloop'
run ${run1}
jump in.lbdem loop
label endloop

unfix iso
unfix m4
fix m4 all property/global coefficientFriction
peratomtypepair 1 0.30

dump_modify dmp_LIG every 50000
dump_modify dmp_cpgl every 50000
```

```
dump_modify dmp_euler every 50000

run 500000

write_restart restart.file
```

APPENDIX B - SOURCE CODE FOR SHEARING THE SAMPLES USING THE DEM

The following code was used in LIGGGHTS (LAMMPS Improved for General Granular and Granular Heat Transfer Simulations) to first isotropically compress the samples to constant mean stress of 200 kPa, and then the samples were sheared using a constant mean stress path.

```
variable run1 equal 1000

variable reqstress equal 2e5

variable ratei equal 0.55

variable rho_s equal 2650

variable v_limit equal 1e-14

variable n_particles equal 53000

variable dmp_stp equal 1e8
```

```
variable timestep equal 7.25e-9

#Dimensions of the domain
variable dx equal 0.01124
variable dy equal 0.01124
variable dz equal 0.01124
#particle sizes

variable  r1   equal     6.82E-05
variable  r2   equal     7.92E-05
variable  r3   equal     8.64E-05
variable  r4   equal     9.50E-05
variable  r5   equal     0.000522185
variable  r6   equal     0.000550642
variable  r7   equal     0.000558669
variable  r8   equal     0.000569553
variable  r9   equal     0.000578785
variable  r10  equal     0.000583457
variable  r11  equal     0.000590062
variable  r12  equal     0.000598663
variable  r13  equal     0.000604467
variable  r14  equal     0.000607389
variable  r15  equal     0.000612292
variable  r16  equal     0.000622217
variable  r17  equal     6.31E-04
```

```
variable  r18  equal     6.40E-04
variable  r19  equal     6.57E-04
variable  r20  equal     7.12E-04

#Percentage increments

variable  pts1 equal     0.05
variable  pts2 equal     0.05
variable  pts3 equal     0.05
variable  pts4 equal     0.05
variable  pts5 equal     0.05
variable  pts6 equal     0.05
variable  pts7 equal     0.05
variable  pts8 equal     0.05
variable  pts9 equal     0.05
variable  pts10     equal     0.05
variable  pts11     equal     0.05
variable  pts12     equal     0.05
variable  pts13     equal     0.05
variable  pts14     equal     0.05
variable  pts15     equal     0.05
variable  pts16     equal     0.05
variable  pts17     equal     0.05
variable  pts18     equal     0.05
variable  pts19     equal     0.05
variable  pts20     equal     0.05
```

```
units           si
atom_style      granular
atom_modify     map array
hard_particles yes
communicate     single vel yes

boundary  p p p
newton          off
processors * * *
region          box block 0 ${dx} 0 ${dy} 0 ${dz} units box
create_box      1 box

variable  skin equal 7e-6
neighbor  ${skin} bin
neigh_modify   delay 0

fix       m1 all property/global youngsModulus peratomtype
   70e9
fix       m2 all property/global poissonsRatio peratomtype
   0.3
fix       m3  all  property/global  coefficientRestitution
   peratomtypepair 1 0.70
fix       m4   all   property/global   coefficientFriction
   peratomtypepair 1 0
```

```
pair_style     gran model hertz tangential history
pair_coeff     * *

#fix xwalls1 all wall/gran model hertz tangential history
   primitive type 1 xplane 0
#fix xwalls2 all wall/gran model hertz tangential history
   primitive type 1 xplane ${dx}
#fix ywalls1 all wall/gran model hertz tangential history
   primitive type 1 yplane 0
#fix ywalls2 all wall/gran model hertz tangential history
   primitive type 1 yplane ${dy}
#fix zwalls1 all wall/gran model hertz tangential history
   primitive type 1 zplane 0
#fix zwalls2 all wall/gran model hertz tangential history
   primitive type 1 zplane ${dz}

timestep        ${timestep}

fix  1 all nve/sphere

fixpts1   all  particletemplate/sphere  11593     atom_type
     1    density   constant  ${rho_s}  volume_limit
     ${v_limit}     radius    constant  ${r1}
fixpts2   all  particletemplate/sphere  11701     atom_type
     1    density   constant  ${rho_s}  volume_limit
     ${v_limit}     radius    constant  ${r2}
```

```
fix pts3   all  particletemplate/sphere  11807     atom_type
     1    density   constant  ${rho_s}  volume_limit
     ${v_limit}     radius    constant  ${r3}
fix pts4   all  particletemplate/sphere  11897     atom_type
     1    density   constant  ${rho_s}  volume_limit
     ${v_limit}     radius    constant  ${r4}
fix pts5   all  particletemplate/sphere  11969     atom_type
     1    density   constant  ${rho_s}  volume_limit
     ${v_limit}     radius    constant  ${r5}
fix pts6   all  particletemplate/sphere  12071     atom_type
     1    density   constant  ${rho_s}  volume_limit
     ${v_limit}     radius    constant  ${r6}
fix pts7   all  particletemplate/sphere  12157     atom_type
     1    density   constant  ${rho_s}  volume_limit
     ${v_limit}     radius    constant  ${r7}
fix pts8   all  particletemplate/sphere  12253     atom_type
     1    density   constant  ${rho_s}  volume_limit
     ${v_limit}     radius    constant  ${r8}
fix pts9   all  particletemplate/sphere  12347     atom_type
     1    density   constant  ${rho_s}  volume_limit
     ${v_limit}     radius    constant  ${r9}
fix pts10  all  particletemplate/sphere  12437     atom_type
     1    density   constant  ${rho_s}  volume_limit
     ${v_limit}     radius    constant  ${r10}
fix pts11  all  particletemplate/sphere  12517     atom_type
     1    density   constant  ${rho_s}  volume_limit
```

```
     ${v_limit}     radius    constant  ${r11}
fixpts12  all  particletemplate/sphere  12601     atom_type
     1    density   constant  ${rho_s}  volume_limit
     ${v_limit}     radius    constant  ${r12}
fixpts13  all  particletemplate/sphere  12689     atom_type
     1    density   constant  ${rho_s}  volume_limit
     ${v_limit}     radius    constant  ${r13}
fixpts14  all  particletemplate/sphere  12791     atom_type
     1    density   constant  ${rho_s}  volume_limit
     ${v_limit}     radius    constant  ${r14}
fixpts15  all  particletemplate/sphere  12899     atom_type
     1    density   constant  ${rho_s}  volume_limit
     ${v_limit}     radius    constant  ${r15}
fixpts16  all  particletemplate/sphere  12973     atom_type
     1    density   constant  ${rho_s}  volume_limit
     ${v_limit}     radius    constant  ${r16}
fixpts17  all  particletemplate/sphere  13049     atom_type
     1    density   constant  ${rho_s}  volume_limit
     ${v_limit}     radius    constant  ${r17}
fixpts18  all  particletemplate/sphere  13159     atom_type
     1    density   constant  ${rho_s}  volume_limit
     ${v_limit}     radius    constant  ${r18}
fixpts19  all  particletemplate/sphere  13249     atom_type
     1    density   constant  ${rho_s}  volume_limit
     ${v_limit}     radius    constant  ${r19}
fixpts20  all  particletemplate/sphere  13339     atom_type
```

```
      1    density   constant  ${rho_s}  volume_limit
      ${v_limit}     radius    constant  ${r20}

fix pdd1 all particledistribution/discrete 32452843 20 pts1
   ${pts1} pts2 ${pts2}  pts3 ${pts3}  pts4 ${pts4}  pts5
   ${pts5}  pts6 ${pts6}  pts7 ${pts7}  pts8 ${pts8}  pts9
   ${pts9}  pts10 ${pts10}  pts11 ${pts11}  pts12 ${pts12}
   pts13 ${pts13} pts14 ${pts14}  pts15 ${pts15}  pts16
   ${pts16}  pts17 ${pts17}  pts18 ${pts18}  pts19 ${pts19}
   pts20 ${pts20}

region  insreg block 0 ${dx} 0 ${dy} 0 ${dz} units box

fix ins all insert/pack seed 32452867 distributiontemplate
   pdd1    insert_every    once    &    overlapcheck    yes
   particles_in_region ${n_particles} region insreg ntry_mc
   50000

fix    stress    all    ave/euler    nevery    ${dmp_stp}
   cell_size_relative 3 parallel no

compute   cpgl all pair/gran/local pos id force force_normal
   force_tangential contactArea contactPoint

run 1
```

```
compute               peratom all stress/atom pair
compute           p all reduce sum c_peratom[1] c_peratom[2]
   c_peratom[3]
variable            press              equal              -
   (c_p[1]+c_p[2]+c_p[3])/(3*vol)
#variable           sigmaxx equal -(c_p[1])/vol
#variable           sigmayy equal -(c_p[2])/vol
#variable           sigmazz equal -(c_p[3])/vol

# thermo settings
fix  ts all check/timestep/gran 10000 0.1 0.1
compute        contacts all contact/atom
thermo_style   custom ke step v_press
thermo         50000
thermo_modify  lost ignore norm no

##########################################
#Dumping
##########################################

dump dmp_LIG all custom ${dmp_stp} output/post/d_*.liggghts
   id type type x y z ix iy iz vx vy vz fx fy fz omegax
   omegay    omegaz    radius    c_contacts    c_peratom[1]
   c_peratom[2]   c_peratom[3]   c_peratom[4]   c_peratom[5]
   c_peratom[6]
```

```
dump dmp_cpgl all local ${dmp_stp} output/CPGL/cpgl*.dump
   c_cpgl[1]  c_cpgl[2]  c_cpgl[3]  c_cpgl[4]  c_cpgl[5]
   c_cpgl[6]  c_cpgl[7]  c_cpgl[8]  c_cpgl[9]  c_cpgl[10]
   c_cpgl[11] c_cpgl[12] c_cpgl[13] c_cpgl[14] c_cpgl[15]
   c_cpgl[16] c_cpgl[17] c_cpgl[18] c_cpgl[19] c_cpgl[20]
   c_cpgl[21] c_cpgl[22]

dump      dmp_euler      all      euler/vtk      ${dmp_stp}
   output/euler/eulerdump*.vtk

run 1

##########################################
#application of strain rate
##########################################

variable      rate      equal      ${ratei}*(${reqstress}-
   v_press)/(${reqstress})

fix       iso all deform 1 z erate -${rate} x erate -${rate}
   y erate -${rate} remap x units box

#######################################
#printing some data
#######################################
```

```
#fix printingdata all print 20000 "$(step) $(v_press)
   $(v_sigmaxx) $(v_sigmayy) $(v_sigmazz) $(v_rate)" screen
   no file stresses.txt

##############################################################
   ###
#if statement to desired stress level and changing the
   coefficient of friction
##############################################################
   ###

label loop
if '$(v_press) >= ${reqstress}' then 'jump in.lbdem endloop'
run ${run1}
jump in.lbdem loop
label endloop

unfix iso
unfix m4
fix m4 all property/global coefficientFriction
   peratomtypepair 1 0.30

dump_modify dmp_LIG every 50000
dump_modify dmp_cpgl every 50000
dump_modify dmp_euler every 50000
```

```
run 500000

write_restart restart.file

read_restart restart.file

variable run1 equal 1000

variable lo equal  0.0089361908

variable reqstress equal 2e5

variable reqstresszz equal 1e6

variable ratexi equal -0.55

variable rateyi equal -0.55

variable ratezi equal -0.55

variable ratezshear equal -0.11

variable v_limit equal 1e-14

variable dmp_stp equal 200000
```

```
hard_particles yes

communicate    single vel yes

newton         off

variable  skin equal 7e-6
neighbor  ${skin} bin
neigh_modify   delay 0

fix       m1 all property/global youngsModulus peratomtype
   70e9
fix       m2 all property/global poissonsRatio peratomtype
   0.3
fix       m3  all  property/global  coefficientRestitution
   peratomtypepair 1 0.70
fix       m4   all   property/global   coefficientFriction
   peratomtypepair 1 0.30

pair_style     gran model hertz tangential history
pair_coeff     * *

fix  1 all nve/sphere

fix    stress    all    ave/euler    nevery    ${dmp_stp}
   cell_size_relative 3 parallel no
```

```
compute             cpgl all pair/gran/local pos id force
   force_normal force_tangential contactArea contactPoint

run 1

compute              peratom all stress/atom pair
compute           p all reduce sum c_peratom[1] c_peratom[2]
   c_peratom[3]
variable            press              equal              -
   (c_p[1]+c_p[2]+c_p[3])/(3*vol)
variable       sigmaxx equal -(c_p[1])/vol
variable       sigmayy equal -(c_p[2])/vol
variable       sigmazz equal -(c_p[3])/vol

# thermo settings
fix  ts all check/timestep/gran 10000 0.2 0.2
compute        contacts all contact/atom
thermo_style   custom ke step v_sigmaxx v_sigmayy v_sigmazz
   v_press vol lx ly lz
thermo         ${run1}
thermo_modify  lost ignore norm no
#compute_modify     thermo_temp dynamic yes

run 20000
```

```
#############################################################
   ###
#Application of strain rate to bring the system back into
   the required mean stress after the equilibrium
#############################################################
   ###

label loop1

fix       iso1  all  deform  1  z  erate  ${ratezi}  x  erate
   ${ratexi} y erate ${rateyi} remap x units box

#############################################################
   ###
#If statement to desired stress level
#############################################################
   ###

if  '$(v_press)  >=  ${reqstress}'  then  'jump  in2.lbdem
   endloop1'
run ${run1}

jump in2.lbdem loop1

label endloop1
```

```
unfix iso1

run 20000

##########################################
#Dumping
##########################################

dump dmp_LIG all custom ${dmp_stp} output2/post/d_*.liggghts
   id type type x y z ix iy iz vx vy vz fx fy fz omegax
   omegay omegaz radius c_contacts c_peratom[1]
   c_peratom[2] c_peratom[3] c_peratom[4] c_peratom[5]
   c_peratom[6]

dump dmp_cpgl all local ${dmp_stp} output2/CPGL/cpgl*.dump
   c_cpgl[1] c_cpgl[2] c_cpgl[3] c_cpgl[4] c_cpgl[5]
   c_cpgl[6] c_cpgl[7] c_cpgl[8] c_cpgl[9] c_cpgl[10]
   c_cpgl[11] c_cpgl[12] c_cpgl[13] c_cpgl[14] c_cpgl[15]
   c_cpgl[16] c_cpgl[17] c_cpgl[18] c_cpgl[19] c_cpgl[20]
   c_cpgl[21] c_cpgl[22]

dump dmp_euler all euler/vtk ${dmp_stp}
   output2/euler/eulerdump*.vtk

run 1
```

```
##############################################
#Printing some data
##############################################

fix printingdata all print ${dmp_stp} "$(step) $(v_sigmaxx)
   $(v_sigmayy)  $(v_sigmazz)  $(v_press)  $(vol)  ${ebs1}
   ${ebs2} ${ebs3}" screen no file data.txt

##############################################
#Application of strain rate
##############################################

label loop3

label loop2

variable ebs1 equal 100*(${lo}-$(lz))/(${lo})

variable ebs2 equal 100*(${lo}-$(ly))/(${lo})

variable ebs3 equal 100*(${lo}-$(lx))/(${lo})

variable reqstressxx equal 0.50*(3*${reqstress}-v_sigmazz)

variable reqstressyy equal 0.50*(3*${reqstress}-v_sigmazz)
```

```
variable     ratex     equal     ${ratexi}*(${reqstressxx}-
   v_sigmaxx)/(${reqstressxx})

variable     ratey     equal     ${rateyi}*(${reqstressyy}-
   v_sigmayy)/(${reqstressyy})

variable    ratez    equal    ${ratezshear}*(${reqstresszz}-
   v_sigmazz)/(${reqstresszz})

fix      iso all deform 1 z erate ${ratez} x erate ${ratex}
   y erate ${ratey} remap x units box

if '${ebs1} > 2' then 'jump in2.lbdem endloop2'

run ${run1}

jump in2.lbdem loop2

label endloop2

dump_modify dmp_LIG every 5000000
dump_modify dmp_cpgl every 5000000
dump_modify dmp_euler every 5000000

if '${ebs1} > 15' then 'jump in2.lbdem endloop3'
```

```
run ${run1}

jump in2.lbdem loop3

label endloop3

unfix iso

run 1

write_restart restart2.file
```

APPENDIX C - SOURCE CODE FOR SIMULATING FLUIDISATION OF SOIL

The following code was used in LIGGGHTS (LAMMPS Improved for General Granular and Granular Heat Transfer Simulations) coupled with PALABOS (Parallel Lattice Boltzmann Solver) to simulate the fluidisation of samples.

```
*/
#include "palabos3D.h"
#include "palabos3D.hh"

#include "plb_ib.h"

#include <vector>
#include <cmath>
```

```
#include <iostream>
#include <fstream>
#include <sstream>
#include <ctime>

// necessary LAMMPS/LIGGGHTS includes
#include "lammps.h"
#include "input.h"
#include "library.h"
#include "library_cfd_coupling.h"

#include "liggghtsCouplingWrapper.h"
#include "latticeDecomposition.h"

using namespace plb;
using namespace std;

typedef double T;

#define DESCRIPTOR descriptors::D3Q19Descriptor //defining
   the model to be used
#define   DYNAMICS   IBcompositeDynamics<T,DESCRIPTOR>(new
   BGKdynamics<T,DESCRIPTOR>(parameters.getOmega()))
   //defining the dynamics of the model

   const T lx = 0.007, ly =0.007, lz = 0.030;     //defining
```

```
    the dimensions
    T g = 9.81;                          //defining      the
    gravity
    T r_part= 1e-4;                            //defining
    the radius of the particles
    T rho_s = 2650;                      //defining      the
    density of the solid particles as DOUBLE type
    const T rho_f = 1000;                     //defining the
    density of the fluid as DOUBLE type
    plint N=5;                       //defining the number of
    grids points per particle diameter as Palabos INTEGER
    type
    T uMax=0.004;                              //defining
    the maximum velocity in LB units as DOUBLE type
    T nu_f = 1e-6;                          //defining   the
    kinematic viscosity of the fluid as DOUBLE type
    T v_inf= 0.01;                             //defining
    the estimated settling velocity as DOUBLE type
        T CI = 600;                      //coupling interval

        const T maxT = 0.20;
        const T vtkT = 0.05;
        const T logT = 0.001;

void writeVTK(MultiBlockLattice3D<T,DESCRIPTOR>& lattice,
              IncomprFlowParam<T> const& parameters,
```

```
                PhysUnits3D<T> const& units, plint iter)
{

  T                          p_fact                          =
   units.getPhysForce(1)/pow(units.getPhysLength(1),2)/3.;

  std::string fname(createFileName("vtk", iter, 6));

  VtkImageOutput3D<T>                              vtkOut(fname,
   units.getPhysLength(1));
  vtkOut.writeData<3,float>(*computeVelocity(lattice),
   "velocity", units.getPhysVel(1));
  vtkOut.writeData<float>(*computeDensity(lattice),
   "density",units.getPhysDensity(1));

  MultiScalarField3D<T> p(*computeDensity(lattice));
  subtractInPlace(p,1.);
  vtkOut.writeData<float>(p,"pressure",p_fact );

  IBscalarQuantity sf = SolidFraction;
  applyProcessingFunctional(new
   GetScalarQuantityFromDynamicsFunctional<T,DESCRIPTOR,T>
   (sf),

   lattice.getBoundingBox(),lattice,p);
```

```
  vtkOut.writeData<float>(p,"solidfraction",1. );

  pcout << "wrote " << fname << std::endl;
}

void boundaryConditions( MultiBlockLattice3D<T,DESCRIPTOR>&
    lattice,   //boundary conditions are defined here
                              IncomprFlowParam<T>      const&
    parameters,

    OnLatticeBoundaryCondition3D<T,DESCRIPTOR>&
    boundaryCondition )
{
     const plint nx = parameters.getNx();
     const plint ny = parameters.getNy();
     const plint nz = parameters.getNz();

     Box3D inlet    = Box3D(0,    nx-1, 0,    ny-1, 0,    0);
     Box3D outlet = Box3D(0,    nx-1, 0,    ny-1, nz-1, nz-
    1);

     Box3D top    = Box3D(0,    nx-1, ny-1, ny-1, 0, nz-1);
     Box3D bottom = Box3D(0,    nx-1, 0,    0,    0, nz-1);

     Box3D left   = Box3D(0,    0,    1,    ny-2, 0, nz-1);
     Box3D right  = Box3D(nx-1, nx-1, 1,    ny-2, 0, nz-1);
```

```
boundaryCondition.setPressureConditionOnBlockBoundaries
( lattice, inlet);                    //create or define
pressure boundary condition at inlet and outlet


boundaryCondition.setPressureConditionOnBlockBoundaries
( lattice, outlet);

//boundaryCondition.setVelocityConditionOnBlockBoundari
es ( lattice, inlet);

 boundaryCondition.setVelocityConditionOnBlockBoundaries
( lattice, top );
 boundaryCondition.setVelocityConditionOnBlockBoundaries
( lattice, bottom );

 boundaryCondition.setVelocityConditionOnBlockBoundaries
( lattice, left );
 boundaryCondition.setVelocityConditionOnBlockBoundaries
( lattice, right );


//boundaryCondition.setVelocityConditionOnBlockBoundari
es ( lattice, top, boundary::freeslip );
```

```
//boundaryCondition.setVelocityConditionOnBlockBoundari
es ( lattice, bottom, boundary::freeslip );


//boundaryCondition.setVelocityConditionOnBlockBoundari
es ( lattice, left, boundary::freeslip );

//boundaryCondition.setVelocityConditionOnBlockBoundari
es ( lattice, right, boundary::freeslip );

setBoundaryVelocity(lattice,                          top,
 Array<T,3>((T)0.0,(T)0.0,(T)1e-10));
setBoundaryVelocity(lattice,                       bottom,
 Array<T,3>((T)0.0,(T)0.0,(T)1e-10));
setBoundaryVelocity(lattice,                         left,
 Array<T,3>((T)0.0,(T)0.0,(T)1e-10));
setBoundaryVelocity(lattice,                        right,
 Array<T,3>((T)0.0,(T)0.0,(T)1e-10));


//setBoundaryVelocity(lattice,                      inlet,
 Array<T,3>((T)0.0,(T)0.0,(T)5e-5));


setBoundaryDensity(lattice, inlet, 1.0456);


 setBoundaryDensity(lattice,        outlet,        1.);
```

```
    // specify the pressure boundary condition at OUTLET

    lattice.initialize();

}

int main(int argc, char* argv[]) {          //argc     and
    argv parameters are used to access the command line
    parameters to the main function

    plbInit(&argc, &argv);              //   necessary   to
    initialize Palabos in every program

    std::string outDir;

    try {
        global::argv(1).read(outDir);

}   catch(PlbIOException& exception) {
        pcout << "1 : outDir\n";
        exit(1);
    }

    std::string lbOutDir(outDir), demOutDir(outDir);
    lbOutDir.append("/tmp/"); demOutDir.append("/post/");
    global::directories().setOutputDir(lbOutDir);
```

```
 LiggghtsCouplingWrapper
wrapper(argv,global::mpi().getGlobalCommunicator());

 // particle size and volume fraction are handed over to
LIGGGHTS
 // as variables (see LIGGGHTS docu for details)
 wrapper.setVariable("r_part",r_part);
 wrapper.setVariable("rho_s",rho_s);
 wrapper.setVariable("rho_f",rho_f);
 wrapper.setVariable("lx",lx);
 wrapper.setVariable("ly",ly);
 wrapper.setVariable("lz",lz);

 wrapper.execFile("in.lbdem");

 T r_ = r_part;                  //defining the radius of
particles from the diameters as DOUBLE type

 T m = r_*r_*r_*4./3.*3.14*rho_s;          //calculating
the mass of each particle from its density and volume and
defining as DOUBLE type

 PhysUnits3D<T>
units(2.*r_,v_inf,nu_f,lx,ly,lz,N,uMax,rho_f);
```

```
 IncomprFlowParam<T> parameters(units.getLbParam());

 plint nx = parameters.getNx(), ny = parameters.getNy(),
nz = parameters.getNz();

 // get lattice decomposition from LIGGGHTS and create
lattice according to parallelization
 // given in the LIGGGHTS input script
 LatticeDecomposition
lDec(parameters.getNx(),parameters.getNy(),parameters.g
etNz(),
                            wrapper.lmp);
 SparseBlockStructure3D         blockStructure         =
lDec.getBlockDistribution();
 ExplicitThreadAttribution*     threadAttribution      =
lDec.getThreadAttribution();
 plint envelopeWidth = 1;

 MultiBlockLattice3D<T, DESCRIPTOR>
   lattice    (MultiBlockManagement3D    (blockStructure,
threadAttribution, envelopeWidth ),

defaultMultiBlockPolicy3D().getBlockCommunicator(),

defaultMultiBlockPolicy3D().getCombinedStatistics(),
```

```
defaultMultiBlockPolicy3D().getMultiCellAccess<T,DESCRI
PTOR>(),
            new DYNAMICS);

 defineDynamics(lattice,lattice.getBoundingBox(),new
DYNAMICS);

 const plint maxSteps = units.getLbSteps(maxT);
 const            plint            vtkSteps            =
max<plint>(units.getLbSteps(vtkT),1);
 const            plint            logSteps            =
max<plint>(units.getLbSteps(logT),1);

 writeLogFile(parameters,  "Hydraulic  Conductivity  and
Internal Instability");

 lattice.initialize();
 T dt_phys = units.getPhysTime(1);
 plint demSubsteps = CI;
 T dt_dem = dt_phys/((T)demSubsteps);


 pcout << "-------------------------------\n"
       << "tau: " << 1/parameters.getOmega() << "\n"
       << "dt_phys: " << dt_phys << "\n"
       << "maxT: " << maxT << " | maxSteps: " << maxSteps
```

```
    << "\n"
          << "v_inf: " << v_inf << "\n"
          << "Re : " << parameters.getRe() << "\n"
          << "vtkT: " << vtkT << " | vtkSteps: " << vtkSteps
    << "\n"
          << "grid size: " << nx << " " << ny << " " << nz
    << "\n"
          << "-----------------------------" << std::endl;

// set timestep and output directory
    wrapper.setVariable("t_step",dt_dem);
    wrapper.setVariable("dmp_stp",vtkSteps*demSubsteps);
    wrapper.setVariable("dmp_dir",demOutDir);

    wrapper.execFile("in2.lbdem");

    clock_t start = clock();
    clock_t loop = clock();
    clock_t end = clock();

// use the boundary conditions which are already defined

OnLatticeBoundaryCondition3D<T,DESCRIPTOR>*
    boundaryCondition
      = createLocalBoundaryCondition3D<T,DESCRIPTOR>();
```

```
boundaryConditions(lattice,                    parameters,
    *boundaryCondition);

//T previousIterationTime = T();

    // Loop over main time iteration.
    for (plint iT=0; iT<=maxSteps; ++iT) {

      bool initWithVel = false;

    setSpheresOnLattice(lattice,wrapper,units,initWithVel);

      if(iT%vtkSteps == 0 && iT > 0) // LIGGGHTS does not
    write at timestep 0
        writeVTK(lattice,parameters,units,iT);

      lattice.collideAndStream();

      getForcesFromLattice(lattice,wrapper,units);

      wrapper.run(demSubsteps);

      if(iT%logSteps == 0){
        end = clock();
        T time = difftime(end,loop)/((T)CLOCKS_PER_SEC);
        T                totaltime                =
```

```
    difftime(end,start)/((T)CLOCKS_PER_SEC);
         T              mlups              =              ((T)
    (lattice.getNx()*lattice.getNy()*lattice.getNz()*logSte
    ps))/time/1e6;
         pcout << "time: " << time << " " ;
         pcout << "calculating at " << mlups << " MLU/s"
               << " | total time running: " << totaltime <<
    std::endl;
         loop = clock();
       }
     }
     T totaltime = difftime(end,start)/((T)CLOCKS_PER_SEC);
     T              totalmlups              =              ((T)
    (lattice.getNx()*lattice.getNy()*lattice.getNz()*(maxSt
    eps+1)))/totaltime/1e6;
     pcout << " ********************** \n"
           << "total time: " << totaltime
           << " calculating at " << totalmlups << " MLU/s" <<
    std::endl;
    delete boundaryCondition;
}
variable  run1 equal 1e7
variable  run2 equal 5e6
variable        hz equal 0.012
variable  n_particles equal 22300
```

```
variable  v_limit equal 1e-14

#incremental radius values

variable  r1   equal     0.000239
variable  r2   equal     0.0002202
variable  r3   equal     0.0002049
variable  r4   equal     0.0001957
variable  r5   equal     0.0001919
variable  r6   equal     0.0001894
variable  r7   equal     0.0001857
variable  r8   equal     0.0001815
variable  r9   equal     0.0001773
variable  r10  equal     0.0001745
variable  r11  equal     0.0001722
variable  r12  equal     0.0001694
variable  r13  equal     0.0001672
variable  r14  equal     0.000165
variable  r15  equal     0.0001629
variable  r16  equal     0.0001602
variable  r17  equal     0.0001561
variable  r18  equal     0.000151
variable  r19  equal     0.0001438
variable  r20  equal     0.0001333

#incremental percent passing values
```

```
variable  pts1 equal     0.05
variable  pts2 equal     0.05
variable  pts3 equal     0.05
variable  pts4 equal     0.05
variable  pts5 equal     0.05
variable  pts6 equal     0.05
variable  pts7 equal     0.05
variable  pts8 equal     0.05
variable  pts9 equal     0.05
variable  pts10     equal     0.05
variable  pts11     equal     0.05
variable  pts12     equal     0.05
variable  pts13     equal     0.05
variable  pts14     equal     0.05
variable  pts15     equal     0.05
variable  pts16     equal     0.05
variable  pts17     equal     0.05
variable  pts18     equal     0.05
variable  pts19     equal     0.05
variable  pts20     equal     0.05

units          si
atom_style     granular
atom_modify    map array
```

```
communicate    single vel yes

boundary  f f f
newton         off
processors * * *
region         box block 0 ${lx} 0 ${ly} 0 ${lz} units box
create_box     1 box

region         delete_region block 0 ${lx} 0 ${ly} ${hz}
   ${lz} units box

variable  skin equal 1e-5
neighbor  ${skin} bin
neigh_modify   delay 0

fix grav all gravity 9.810  vector 0 0 -1

fix       m1 all property/global youngsModulus peratomtype
   70e9
fix       m2 all property/global poissonsRatio peratomtype
   0.3
fix       m3  all  property/global  coefficientRestitution
   peratomtypepair 1 0.70
fix       m4   all   property/global   coefficientFriction
   peratomtypepair 1 0
```

```
# lb coupling fix
fix lbcoupling all couple/lb/onetoone

pair_style     gran model hertz tangential history
pair_coeff     * *

fix  1 all nve/sphere

fix xwalls1 all wall/gran model hertz tangential history
   primitive type 1 xplane 0
fix xwalls2 all wall/gran model hertz tangential history
   primitive type 1 xplane ${lx}
fix ywalls1 all wall/gran model hertz tangential history
   primitive type 1 yplane 0
fix ywalls2 all wall/gran model hertz tangential history
   primitive type 1 yplane ${ly}
fix zwalls1 all wall/gran model hertz tangential history
   primitive type 1 zplane 0
fix zwalls2 all wall/gran model hertz tangential history
   primitive type 1 zplane ${lz}

fix pts1 all particletemplate/sphere 11593 atom_type
     1 density constant ${rho_s} volume_limit
     ${v_limit} radius constant ${r1}
fix pts2 all particletemplate/sphere 11701 atom_type
     1 density constant ${rho_s} volume_limit
```

```
     ${v_limit}     radius    constant  ${r2}
fixpts3   all  particletemplate/sphere  11807     atom_type
     1    density   constant  ${rho_s}  volume_limit
     ${v_limit}     radius    constant  ${r3}
fixpts4   all  particletemplate/sphere  11897     atom_type
     1    density   constant  ${rho_s}  volume_limit
     ${v_limit}     radius    constant  ${r4}
fixpts5   all  particletemplate/sphere  11969     atom_type
     1    density   constant  ${rho_s}  volume_limit
     ${v_limit}     radius    constant  ${r5}
fixpts6   all  particletemplate/sphere  12071     atom_type
     1    density   constant  ${rho_s}  volume_limit
     ${v_limit}     radius    constant  ${r6}
fixpts7   all  particletemplate/sphere  12157     atom_type
     1    density   constant  ${rho_s}  volume_limit
     ${v_limit}     radius    constant  ${r7}
fixpts8   all  particletemplate/sphere  12253     atom_type
     1    density   constant  ${rho_s}  volume_limit
     ${v_limit}     radius    constant  ${r8}
fixpts9   all  particletemplate/sphere  12347     atom_type
     1    density   constant  ${rho_s}  volume_limit
     ${v_limit}     radius    constant  ${r9}
fixpts10  all  particletemplate/sphere  12437     atom_type
     1    density   constant  ${rho_s}  volume_limit
     ${v_limit}     radius    constant  ${r10}
fixpts11  all  particletemplate/sphere  12517     atom_type
```

```
     1    density   constant  ${rho_s}  volume_limit
     ${v_limit}     radius    constant  ${r11}
fixpts12  all  particletemplate/sphere  12601     atom_type
     1    density   constant  ${rho_s}  volume_limit
     ${v_limit}     radius    constant  ${r12}
fixpts13  all  particletemplate/sphere  12689     atom_type
     1    density   constant  ${rho_s}  volume_limit
     ${v_limit}     radius    constant  ${r13}
fixpts14  all  particletemplate/sphere  12791     atom_type
     1    density   constant  ${rho_s}  volume_limit
     ${v_limit}     radius    constant  ${r14}
fixpts15  all  particletemplate/sphere  12899     atom_type
     1    density   constant  ${rho_s}  volume_limit
     ${v_limit}     radius    constant  ${r15}
fixpts16  all  particletemplate/sphere  12973     atom_type
     1    density   constant  ${rho_s}  volume_limit
     ${v_limit}     radius    constant  ${r16}
fixpts17  all  particletemplate/sphere  13049     atom_type
     1    density   constant  ${rho_s}  volume_limit
     ${v_limit}     radius    constant  ${r17}
fixpts18  all  particletemplate/sphere  13159     atom_type
     1    density   constant  ${rho_s}  volume_limit
     ${v_limit}     radius    constant  ${r18}
fixpts19  all  particletemplate/sphere  13249     atom_type
     1    density   constant  ${rho_s}  volume_limit
     ${v_limit}     radius    constant  ${r19}
```

```
fix pts20 all particletemplate/sphere 13339 atom_type
    1 density constant ${rho_s} volume_limit
    ${v_limit} radius constant ${r20}

fix pdd1 all particledistribution/discrete 32452843 20 pts1
   ${pts1} pts2 ${pts2} pts3 ${pts3} pts4 ${pts4} pts5
   ${pts5} pts6 ${pts6} pts7 ${pts7} pts8 ${pts8} pts9
   ${pts9} pts10 ${pts10} pts11 ${pts11} pts12 ${pts12}
   pts13 ${pts13} pts14 ${pts14} pts15 ${pts15} pts16
   ${pts16} pts17 ${pts17} pts18 ${pts18} pts19 ${pts19}
   pts20 ${pts20}

region  insreg block 0 ${lx} 0 ${ly} 0 ${lz} units box

fix ins all insert/pack seed 32452867 distributiontemplate
   pdd1 insert_every once overlapcheck yes
   particles_in_region ${n_particles} region insreg ntry_mc
   5000

compute cpgl all pair/gran/local pos id force
   force_normal force_tangential contactArea

run 1

timestep ${t_step}
```

```
fix euler all ave/euler nevery ${dmp_stp} cell_size_relative
   3 parallel no

compute              peratom all stress/atom pair
compute           p all reduce sum c_peratom[1] c_peratom[2]
   c_peratom[3]
variable            press              equal              -
   (c_p[1]+c_p[2]+c_p[3])/(3*vol)
#variable           sigmaxx equal -(c_p[1])/vol
#variable           sigmayy equal -(c_p[2])/vol
#variable           sigmazz equal -(c_p[3])/vol

# thermo settings
fix  ts all check/timestep/gran 10000 0.2 0.2
compute        contacts all contact/atom
thermo_style   custom ke step v_press
thermo         100000
thermo_modify  lost ignore norm no

#run with particle insertion
run ${run1}

delete_atoms region delete_region
run 20000

unfix m4
```

```
fix       m4   all   property/global   coefficientFriction
   peratomtypepair 1 0.30
run ${run2}

fix bu all buoyancy level ${lz} dim z density 1000

run 20000

# dumping start
dump      dmp_LIG       all       custom       ${dmp_stp}
   ${dmp_dir}LIG_*.liggghts id type type x y z ix iy iz vx
   vy vz fx fy fz omegax omegay omegaz radius c_contacts
   c_peratom[1]  c_peratom[2]  c_peratom[3]  c_peratom[4]
   c_peratom[5] c_peratom[6] f_dragforce[1] f_dragforce[2]
   f_dragforce[3]

dump dmp_cpgl all local ${dmp_stp} output/CPGL/cpgl_*.dump
   c_cpgl[1]  c_cpgl[2]  c_cpgl[3]  c_cpgl[4]  c_cpgl[5]
   c_cpgl[6]  c_cpgl[7]  c_cpgl[8]  c_cpgl[9]  c_cpgl[10]
   c_cpgl[11] c_cpgl[12] c_cpgl[13] c_cpgl[14] c_cpgl[15]
   c_cpgl[16] c_cpgl[17] c_cpgl[18] c_cpgl[19]

dump      dmp_euler      all      euler/vtk      ${dmp_stp}
   output/euler/eulerdump_*.vtk
```

APPENDIX D - SOURCE CODE FOR DIRECTIONAL DISTRIBUTION OF CONTACTS

This code calculates the orientation of the branch vectors and plots them in the form of a rose diagram using MATLAB. Note that the branch and contact normal vectors coincide in the case of spherical particles, and this code only applies to spherical particles

```
data_CPGL = xlsread('data_CPGL');      % dump file of
compute/pair/gran - LIGGGHTS

x1 = data_CPGL(:,1);   % centre "x" coordinate of particle
1
y1 = data_CPGL(:,2);   % centre "y" coordinate of particle
1
z1 = data_CPGL(:,3);   % centre "z" coordinate of particle
1
x2 = data_CPGL(:,4);   % centre "x" coordinate of particle
2
y2 = data_CPGL(:,5);   % centre "y" coordinate of particle
2
z2 = data_CPGL(:,6);   % centre "z" coordinate of particle
2
fx = data_CPGL(:,13);  % x component of "f_normal"
fy = data_CPGL(:,14);  % y component of "f_normal"
fz = data_CPGL(:,15);  % z component of "f_normal"
```

```
nbins = 36; % number of bins in 0 to 2pi limits

for i = 1:size(fx,1)

    fn(i,1) =sqrt(fx(i,1)^2+fy(i,1)^2+fz(i,1)^2); % normal
contact force

end

fn_avg = mean(fn); % mean normal contact force

n = size (fx,1); % maximum number of values = number of
contacts (Nc)

for i = 1 : n

    nx(i,1) = fx(i,1)/fn_avg;
    ny(i,1) = fy(i,1)/fn_avg;
    nz(i,1)= fz(i,1)/fn_avg;

    %Rose diagram (radians)- Branch Vector
    xy(i,1)=  atan(ny(i,1)/nx(i,1));  %angles  of  branch
vectors in xy plan
    xz(i,1)=  atan(nz(i,1)/nx(i,1));  %angles  of  branch
vectors in xz plan
```

```
    yz(i,1)=  atan(nz(i,1)/ny(i,1));  %angles  of  branch
vectors in yz plan

end

% transferring the data to 2pi values
XY1 = xy;
XY2 = xy+pi;
XY = [XY1; XY2];

XZ1 = xz;
XZ2 = xz+pi;
XZ = [XZ1; XZ2];

YZ1 = yz;
YZ2 = yz+pi;
YZ = [YZ1; YZ2];

figure(1);
h  =  polarhistogram(YZ,nbins);  %  plotting  the  number  of
contact normals
hold off

%Analytical solution

DNc = h.Values;
```

```
E = DNc/(n*(360/nbins));

thetai = (h.BinEdges(1:end-1) + h.BinEdges(2:end))/2;    %
angle of bin centers

DesignMatrix        =        (1/(2*pi))+[cos(2*thetai(:))
sin(2*thetai(:))]; %design the equation in the form of matrix
without the coefficients
Coefficients                                              =
inv(DesignMatrix'*DesignMatrix)*DesignMatrix'*E(:);       %
getting the coefficients
coeff1 = Coefficients(1);
coeff2 = Coefficients(2);

thetaA =(atan(coeff2/coeff1))/2; % derived by equating both
the coefficients as given in the book by O'Sullivan (in
radians)

a = 2*pi*coeff1/cos(2*thetaA);

for j = 1:nbins

   %Ethetai                      (1,j)                      =
(1/(2*pi))+coeff1*cos(2*(thetai(1,j)))+coeff2*sin(2*(thetai
(1,j)));
```

```
   Ethetai (1,j) = (1/(2*pi))*(1+a*cos(2*(thetai(1,j)-
thetaA)));

end

figure(2);
h1 = polarhistogram(YZ,nbins,'Normalization','pdf'); %
plotting the probability density functions of contact
normals
h1.DisplayStyle = 'stair'; % displays the figure h1 in the
form of stairs

hold on

polarplot(thetai,Ethetai); % plotting the analytical
solution of the probability density function
```

APPENDIX E - SOURCE CODE FOR COMPUTING COORDINATION NUMBER, GEOMETRIC COORDINATION NUMBER AND VOLUME-WEIGHTED COORDINATION NUMBER

This code calculates the coordination number, geometric coordination number, and volume-weighted coordination number using MATLAB. The data_LIG is the output file of LIGGGHTS.

```
V = 3.43e-7; %entire volume of the specimen in m3 for vol-
weighted coordination number only

data_LIG = xlsread('data_LIG');

radius = data_LIG(:,19);

contacts = data_LIG(:,20);

NOP=size(radius,1); %number of particles

%Coordination number (Thornton 2000)

NOC = sum (contacts); % total number of contacts x 2 - each
contact is shared between two particles

Z = NOC/NOP;

%Mechanical coordination number (Thornton 2000)

Np0 = sum(contacts(:)==0); % count the number of particles
with zero (0) contacts or number of zero contacts
Np1 = sum(contacts(:)==1); % count the number of particles
with one (01) contacts
```

```
Z_mech = (NOC - Np1)/(NOP-Np1-Np0); % Note: NOC = 2 x number
of contacts

%Geometric coordination number

Z_geo = NOC/(NOP-Np0); % Note: NOC = 2 x number of contacts

% Volume-Weighted Coordination Number (Shaebani et al.
(2012))

for i = 1:NOP
    Vp(i,1) = (4/3)*pi*(radius(i,1))^3;
end

for i = 1:NOP
    CpVp(i,1) = contacts(i,1)*Vp(i,1);
end

sumCpVp = sum(CpVp);

Z_vol_weighted = sumCpVp/V;

ZZs = [Z Z_geo Z_mech];
```

APPENDIX F - SOURCE CODE FOR COMPUTING STRESS REDUCTION FACTOR

This code calculates the stress reduction factor using MATLAB for the methods of Shire et al. (2014) and Sufian et al. (2021).

```
V = 1; %entire volume of the specimen in m3 - does not affect the alpha value

load r.txt; % radii of the finer fraction

data_LIG = xlsread('D:\PhD\MATLAB Codes\DEM-MAT\AllCodes\data_LIG');

radius = data_LIG(:,19);
psXXwv = -data_LIG(:,21);  %sigmaxx of individual particle multiplied by volume of the particle
psYYwv = -data_LIG(:,22);  %sigmayy of individual particle multiplied by volume of the particle
psZZwv = -data_LIG(:,23);  %sigmazz of individual particle multiplied by volume of the particle

NOP=size(radius,1); %number of particles

%stresses in the entire sample
sigmaxx = sum(psXXwv); %sigmaxx of the entire sample
```

```
sigmayy = sum(psYYwv); %sigmayy of the entire sample
sigmazz = sum(psZZwv); %sigmazz of the entire sample

meanstress = (sigmaxx+sigmayy+sigmazz)/(3*V); % mean stress
of entire sample

%finding the porosity

for i = 1:NOP

    Vp(i,1) = (4/3)*pi*(radius(i,1))^3;

end

Vs = sum(Vp); % total volume of the particles

SVF = Vs/V; % Solid Volume Fraction

n = 1 - SVF; % Porosity

% finding the rows containing the finer fraction

row1=find(radius(:)==r(1,1));
row2=find(radius(:)==r(2,1));
row3=find(radius(:)==r(3,1));
row4=find(radius(:)==r(4,1));
```

```
row5=find(radius(:)==r(5,1));
row6=find(radius(:)==r(6,1));

row = [row1;row2;row3;row4;row5;row6];

psXXwv_fines = psXXwv(row,1); % psXXwv values of fines

psYYwv_fines = psYYwv(row,1); % psZZwv values of fines

psZZwv_fines = psZZwv(row,1); % psZZwv values of fines

radius_fines= radius(row,1);  % radii of fines

for i = 1:size(radius_fines,1)

    Vp_fines(i,1) = (4/3)*pi*radius_fines(i,1)^3;

end

Vfines = (sum(Vp_fines))/(1-n);

% mean stress in the fines
meanstressfines
=(sum(psXXwv_fines)+sum(psYYwv_fines)+sum(psZZwv_fines))/(3
*Vfines);
```

```
% DEM stress reduction factor
alpha_DEM = meanstressfines./meanstress;

% calculations for the beta parameter

qf = (sum(psZZwv_fines)-sum(psXXwv_fines));
q = (sigmazz-sigmaxx);

beta_DEM = qf/q;

% calculation of the coordination number for fine to fine
and fine to
% coarse contacts only

contacts = data_LIG(:,20);

contacts = contacts (row,:);

NOP_FF = size(contacts,1);

NOC = sum(contacts);

CN_FF=NOC/NOP_FF;

%Alpha DEM Calculation based on the method by Sufian et al.
(2021)
```

```
% mean stress in the fines
meanstressfines_as
=(sum(psXXwv_fines)+sum(psYYwv_fines)+sum(psZZwv_fines))/(3
*V);
% DEM stress reduction factor
alpha_DEM_as = meanstressfines_as./meanstress;

OUTPUT =[alpha_DEM alpha_DEM_as beta_DEM CN_FF];

load r.txt; % radii of the finer fraction

if size(r,1) ==2
    SRF2radius
elseif size(r,1) ==3
    SRF3radius
elseif size(r,1) ==4
    SRF4radius
elseif size(r,1) ==5
    SRF5radius
elseif size(r,1) ==6
    SRF6radius
else
    SRF7radius
end
```

APPENDIX G - SOURCE CODE FOR COMPUTING PERCENTAGE OF SLIDING CONTACTS

This code calculates the percentage of sliding contacts using MATLAB.

```
Mu = 0.3; % coefficient of sliding friction

data_CPGL = xlsread('data_CPGL'); % dump file of compute/pair/gran - LIGGGHTS

fnx = data_CPGL(:,13);  % x-component of "f_normal"
fny = data_CPGL(:,14);  % y-component of "f_normal"
fnz = data_CPGL(:,15);  % z-component of "f_normal"
ftx = data_CPGL(:,16);  % x-component of "f_tangential"
fty = data_CPGL(:,17);  % y-component of "f_tangential"
ftz = data_CPGL(:,18);  % z-component of "f_tangential"

for i = 1:size(fnx,1) % normal contact force

    fn(i,1)    =sqrt(fnx(i,1)^2+fny(i,1)^2+fnz(i,1)^2);    % normal contact force

end

for i = 1:size(ftx,1)  % tangential contact force
```

```
ft(i,1)      =sqrt(ftx(i,1)^2+fty(i,1)^2+ftz(i,1)^2);      %
tangential contact force


end


for i = 1:size(fnx,1)


S(i,1)= (ft(i,1))./(Mu*fn(i,1));


end


S = sortrows(S);


%SlidingContacts = sum(S(:)>=1 & S(:)<=1.01); % number of
sliding contacts


SlidingContacts = sum(S(:)>=1); % number of sliding contacts


percentageSlidingContacts                                    =
100*SlidingContacts/size(fnx,1); % ratio of sliding contacts
to total number of contacts
```

APPENDIX H - SOURCE CODE FOR COMPUTING CONSTRAINT RATIO

This code computes the constraint ratio (ratio of the number of constraints to the number of degrees of freedom in a granular assembly) using MATLAB.

```
Mu = 0.3; % coefficient of sliding friction
```

```
data_CPGL  =  xlsread('data_CPGL');       %dump  file  of
compute/pair/gran - LIGGGHTS

data_LIG = xlsread('data_LIG');     %dump file of LIGGGHTS

contacts = data_LIG(:,20);

fnx = data_CPGL(:,13);  % x-component of "f_normal"
fny = data_CPGL(:,14);  % y-component of "f_normal"
fnz = data_CPGL(:,15);  % z-component of "f_normal"
ftx = data_CPGL(:,16);  % x-component of "f_tangential"
fty = data_CPGL(:,17);  % y-component of "f_tangential"
ftz = data_CPGL(:,18);  % z-component of "f_tangential"

for i = 1:size(fnx,1) % normal contact force

    fn(i,1)    =sqrt(fnx(i,1)^2+fny(i,1)^2+fnz(i,1)^2);    %
normal contact force

end

for i = 1:size(ftx,1)  % tangential contact force

    ft(i,1)    =sqrt(ftx(i,1)^2+fty(i,1)^2+ftz(i,1)^2);    %
tangential contact force
```

```
end

for i = 1:size(fnx,1)

    S(i,1)= (ft(i,1))./(Mu*fn(i,1));

end

S = sortrows(S);

SlidingContacts = sum(S(:)>=1); % number of sliding contacts

f = SlidingContacts/size(fnx,1); % fraction of sliding
contacts

NOP=size(contacts,1); %number of particles
NOC = sum (contacts); % total number of contacts x 2 - each
contact is shared between two particles
Np0 = sum(contacts(:)==0); % count the number of particles
with zero (0) contacts or number of zero contacts
Np1 = sum(contacts(:)==1); % count the number of particles
with one (01) contacts

Z = NOC/NOP;
```

```
Z_mech = (NOC - Np1)/(NOP-Np1-Np0); % Note: NOC = 2 x number
of contacts
Z_geo = NOC/(NOP-Np0); % Note: NOC = 2 x number of contacts


Ir_Z = Z*((3-2*f)/12);
Ir_Zgeo = Z_geo*((3-2*f)/12);
Ir_Zmech = Z_mech*((3-2*f)/12);
output = [Ir_Z Ir_Zgeo Ir_Zmech];
```

APPENDIX I - PERMISSION INFORMATION FROM THE JOURNAL

SPRINGER NATURE LICENSE

Jul 19, 2022

This Agreement between the University of Technology Sydney, Sydney, NSW, Australia -- Shay Haq ("You") and Springer Nature ("Springer Nature") consists of your license details provided by Springer Nature and Copyright Clearance Center.

License Number	5352821418800
License date	Jul 19, 2022
Licensed Content Publisher	Springer Nature
Licensed Content Publication	Acta Geotechnica
Licensed Content Title	Microscale boundaries of internally stable and unstable soils

Licensed Content Author	Buddhima Indraratna et al
Licensed Content Date	Aug 2, 2021
Type of Use	Thesis/Dissertation
Requestor type	non-commercial (non-profit)
Format	electronic
Portion	full article/chapter
Will you be translating?	no
Circulation/distribution	50000 or greater
Author of this Springer Nature content	yes
Title	Microscale investigations of hydromechanical failures of granular soils
Institution name	University of Technology Sydney, Sydney, Australia
Expected presentation date	Dec 2022
Requestor Location	University of Technology Sydney, Sydney, NSW, Australia Parcel Collect 10218 04930 The Broadway S/C, Shop G21, 1-21 Bay St Sydney, New South Wales 2037

Australia

Attn: University of Technology Sydney, Sydney, NSW, Australia